8-2005

The Mechanical and Electrochemical Properties of Bulk Metallic Glasses

Mark Lee Morrison
University of Tennessee - Knoxville

To the Graduate Council:

I am submitting herewith a dissertation written by Mark Lee Morrison entitled "The Mechanical and Electrochemical Properties of Bulk Metallic Glasses." I have examined the final electronic copy of this dissertation for form and content and recommend that it be accepted in partial fulfillment of the requirements for the degree of Doctor of Philosophy, with a major in Materials Science and Engineering.

Raymond A. Buchanan, Major Professor

We have read this dissertation and recommend its acceptance:

Peter K. Liaw, Charlie R. Brooks, Charles Feigerle

Accepted for the Council:
Dixie L. Thompson

Vice Provost and Dean of the Graduate School

(Original signatures are on file with official student records.)

To the Graduate Council:

I am submitting herewith a dissertation written by Mark Lee Morrison entitled "The Mechanical and Electrochemical Properties of Bulk Metallic Glasses." I have examined the final electronic copy of this dissertation for form and content and recommend that it be accepted in partial fulfillment of the requirements for the degree of Doctor of Philosophy, with a major in Materials Science and Engineering.

_____Raymond A. Buchanan_____
Major Professor

We have read this dissertation
and recommend its acceptance:

_Peter K. Liaw_____

_Charlie R. Brooks_____

_Charles Feigerle_____

Accepted for the Council:

_____Anne Mayhew_____
Vice Chancellor and Dean of
Graduate Studies

(Original signatures are on file with official student records.)

The Mechanical and Electrochemical Properties of Bulk Metallic Glasses

A Dissertation Presented
For the
Doctor of Philosophy
Degree
The University of Tennessee, Knoxville

Mark Lee Morrison
August, 2005

ACKNOWLEDGEMENTS

I am grateful to the National Science Foundation Integrative Graduate Education and Research Training (IGERT) Program in Materials Lifetime Science and Engineering, under Grant No. DGE-9987548; the Combined Research and Curriculum Development (CRCD) Program on Intermetallics and Composites, under EEC-9527527 and EEC-0203415; the International Materials Institutes (IMI) Program on Advanced Neutron Scattering Network for Education and Research (ANSWER), with a focus on Mechanical Behavior of Materials, under DHR-0231320, managed by Drs. Lenore Clesceri, Wyn Jennings, and Larry Goldberg, Ms. Mary Poats, and Dr. Carmen Huber, respectively; and to the Division of Materials Science and Engineering, Department of Energy under Contract DE-AC05-00OR22725 with the Oak Ridge National Laboratory (ORNL) operated by The University of Tennessee – Battelle, LLC, for the support of this research. Also, special thanks are given to Drs. R.A. Buchanan, P.K. Liaw, J.A. Horton, C.T. Liu, and C. Feigerle for their advice, assistance, and guidance during my graduate career. Furthermore, this work would not have been possible without the assistance of Douglas Fielden, Larry Smith, Dan Hackworth, Frank Holiway, Randy Stooksbury, Carla Lawrence, and Sandra Maples of The University of Tennessee and Cecil Carmichael of the Oak Ridge National Laboratory.

ABSTRACT

Bulk metallic glasses (BMGs) represent an emerging class of materials with an amorphous structure and a unique combination of properties. Some of these outstanding properties include exceptionally high strength, large elastic deformation, near-net-shape formability, and superplasticity. However, these materials are not commonly used in structural applications because of a lack of plasticity and a lack of clarity in terms of deformation and failure mechanisms. Furthermore, the electrochemical behavior of these materials with and without loading is not well defined. Thus, the objectives of this study were to define and model the electrochemical and mechanical behaviors of BMGs, in addition to the interactions between these.

The electrochemical behaviors of Zr-, Ti-, and Ca-based BMGs have been studied in various environments. Moreover, the electrochemical behaviors of several common, crystalline materials have also been characterized in the same environments to facilitate comparisons. In general, the Zr- and Ti-based BMG alloys demonstrated relatively good general corrosion resistance in all of the environments. Mean corrosion penetration rates (CPRs) were found to be less than 30 μm/year for these alloys. On the other hand, the Ca-based BMG alloys were found to be highly active with CPRs ranging from 300 – 5700 μm/year in a non-aggressive 0.05 M Na_2SO_4 electrolyte. Furthermore, most of these alloys were found to be susceptible to localized corrosion in these environments. However, the Zr- and Ti-based BMG alloys exhibited relatively high, positive values for both pitting overpotentials (η_{pit}) and protection overpotentials (η_{pp}).

The Zr-based BMG commonly known as Vitreloy 105 (Vit 105) was selected for further studies. This material was fabricated at the Oak Ridge National Laboratory by arc-melting and drop-casting into a water-cooled, copper mold. Mechanical characterization of this alloy was conducted through four-point bend fatigue testing, as well as tensile testing with *in situ* thermography.

Fatigue testing in air revealed that both the fatigue lives at various stresses and the fatigue endurance limit are similar to those reported for this material in uniaxial fatigue. This result alone demonstrates that the great differences in fatigue results reported in the literature are not due to differences in testing geometry. In fact, the larger scatter observed in four-point bend fatigue at a given stress range was found to be due to variations in material quality. Thus, material quality is believed to be the primary reason for the great differences in fatigue behavior of various BMG alloys that have been reported in the literature since 1995.

After the electrochemical and mechanical behaviors of the Vit 105 BMG alloy were defined separately, the corrosion-fatigue behavior of this alloy was studied. Corrosion-fatigue tests were conducted under identical conditions as those utilized during fatigue testing in air. However, in this case, the environment was a 0.6 M NaCl electrolyte, identical to one of the environments in which the electrochemical behavior was previously defined. The environmental effect was found to be significant at most stress levels, with decreasing effects at higher stress levels due to decreasing time in the detrimental environment. Furthermore, the corrosion-fatigue endurance limit was found to be severely depressed to a stress range of less than 400 MPa. Again, the variation in the corrosion-fatigue data at a given stress range was found to be primarily dependent

upon material quality. In addition, the crack-initiation locations were observed to shift from the inner span, in air, to the outer loading pins in the 0.6 M NaCl electrolyte. This shift in initiation locations was due to wear at the outer pins that removed the passive layer, which promoted pitting and crack initiation.

Cyclic-anodic-polarization tests were conducted during cyclic loading to elucidate the effect of cyclic stresses on the electrochemical behavior. It was found that a stress range of 900 MPa resulted in active pitting at the open-circuit potentials. Thus, η_{pit} had shifted from high, positive values in the static condition to low, negative values under cyclic loading. Next, the degradation mechanism was examined by anodic and cathodic polarization. While cathodic polarization extended the fatigue life, anodic polarization severely degraded the fatigue life. Based upon these dramatic shifts in the fatigue lives at 900 MPa, it was concluded that the degradation mechanism is stress-assisted dissolution, not hydrogen embrittlement.

Finally, tensile tests were conducted with the Vit 105 BMG alloy with *in situ* infrared (IR) thermography to observe the evolution of shear bands during deformation. More importantly, the length, location, sequence, temperature evolution, and velocity of individual shear bands have been quantified through the use of IR thermography. This study revealed that multiple shear bands can initiate, propagate, and arrest within the sample during a single tensile test, contrary to popular belief. After arrest, many shear bands were reactivated at a later time and higher stress and propagated before arresting again. The velocity of shear band propagation was estimated to be a minimum of 1 m/s. The temperature profiles along the axis of shear band propagation were found to continually decrease from the point of initiation to the point of arrest. This gradual

decrease in the temperature as the shear band propagates suggests that arrest occurs because the driving mechanism slowly decreases until it is exhausted. A maximum temperature increase of approximately 2.6°C was observed in association with the propagation of shear bands. However, this temperature change is likely an underestimate of the actual increase in temperature generated by the shear band due to the limited temporal and spatial resolution of the IR camera and rapid heat conduction in the sample. Finally, the maximum temperature of a shear band has been shown to be the best predictor of the shear band length out of all of the parameters examined in this study. Based upon this correlation, it can be concluded that the final failure must have occurred when a critical shear-band temperature was attained in one or more of the shear bands, preventing the arrest of the shear band before it attained a critical length.

Based upon all of these studies on a variety of BMG alloy systems, it is obvious that these materials are extremely sensitive to both material quality and surface defects. Therefore, future research on the improvement of BMG alloys should be focused on these areas. However, these materials possess a unique collection of desirable properties despite these drawbacks. Thus, it is possible that the shortcomings of this novel class of materials can be remedied through further study and understanding.

TABLE OF CONTENTS

LIST OF TABLES

LIST OF FIGURES

LIST OF ABBREVIATIONS

α	Level of significance
γ	Lu and Liu glass-forming ability criterion
σ	Stress
σ_L	Fatigue endurance limit
σ_r	Stress range
θ	Angle of incidence
ν	Frequency
η_{pit}	Pitting overpotential
η_{pp}	Protection overpotential
a	crack length
at.%	Atomic percent
ASTM	American Society for Testing and Materials
AES	Auger electron spectroscopy
AISI	American Iron and Steel Institute
ANOVA	Analysis of variance
ARIMA	AutoRegressive Integrated Moving Average
BMG	Bulk metallic glass
BAA	Bulk amorphous alloy
BAM	Bulk amorphous material
CI	Confidence interval
CPR	Corrosion penetration rate
CT	Compact-tension
DO	Dissolved oxygen
DSC	Differential scanning calorimetry
E	Potential
E_{oc}	Open-circuit potential
E_{corr}	Corrosion potential
E_{pit}	Pitting potential
E_{pp}	Protection potential
i	Current density
i_{cap}	Capacitive current density
i_{corr}	Corrosion current density
i_{far}	Faradaic current density
i_g	Oxide growth current density
IR	Infrared
E_{pit}	Pitting potential
E_{pp}	Protection potential
EDM	Electrical-discharge machining
EDS	Energy-dispersive spectroscopy
FBS	Fetal bovine serum
FEM	Finite element modeling
HAC	Hydrogen-assisted cracking

GFA	Glass-forming ability
IC_{50}	Inhibitory concentration 50%
L	Length
LM-001	Vitreloy 1
LM-010	Ti-based BMG [$Ti_{43.3}Zr_{21.7}Ni_{7.5}Be_{27.5}$ (at.%)]
ΔK_{TH}	Threshold stress-intensity range
K	Stress-intensity factor
m	Crack growth exponent
M	Molar
MEM	Miminum essential medium
MRI	Magnetic resonance imaging
N	Cycles
NDE	Non-destructive evaluation
p	Observed level of significance
PBS	Phosphate-buffered saline
PCA	Phosphate – citric-acid-buffered saline
PRESS	Prediction error sum of squares
R	Minimum stress / maximum stress
r^2	Coefficient of determination
R_a	Arithmetic average roughness
R_c	Critical cooling rate
R_p	Polarization resistance
RE	Rare-earth element
S-N	Stress-fatigue life
SAD	Stress-assisted dissolution
SB	Shear band
SCC	Stress corrosion cracking
SCE	Saturated calomel electrode
SEM	Scanning electron microscope
SiC	Silicon carbide
SS	Stainless steel
t	Time
T	Temperature
ΔT_{avg}	Mean change in temperature
ΔT_{max}	Maximum change in temperature
ΔT_x	Supercooled liquid region
T_{avg}	Mean temperature
T_g	Glass-transition temperature
T_m	Melting temperature
T_{max}	Maximum temperature
T_{rg}	Reduced glass-transition temperature
T_x	Crystallization temperature
TM	Transition metal
Vit 1	Vitreloy 1 [$Zr_{41.2}Ti_{13.8}Ni_{10}Cu_{12.5}Be_{22.5}$ (at.%)]
Vit 105	Vitreloy 105 [$Zr_{52.5}Cu_{17.9}Ni_{14.6}Al_{10}Ti_5$ (at.%)]

W	Width
wt.%	Weight percent
XPS	X-ray photoelectron spectroscopy
XRD	X-ray diffraction

1. INTRODUCTION

The term metallic glass or amorphous alloy describes a class of materials that have no long-range, periodic atomic order [1]. These amorphous alloys are fabricated through a variety of techniques all of which involve rapid solidification from the gas or liquid phase [1]. When the solidification of the melt or gas is rapid enough, the atoms of the alloy are essentially frozen in their liquid configuration. This novel microstructure results in unique mechanical, electrical, magnetic and corrosion behaviors not seen in typical crystalline materials [1]. Through years of research in alloy design, compositions were discovered that reduced the critical cooling rate necessary to produce the amorphous structure. These new materials with a minimum thickness of approximately 1 mm are commonly called bulk metallic glasses (BMGs), bulk amorphous alloys (BAAs), or bulk amorphous materials (BAMs).

Bulk metallic glasses (BMGs) are an emerging class of new materials with a unique collection of properties due to the amorphous microstructure. These novel properties include high strength [2, 3], low modulus [4, 5], good impact toughness [6], high fracture toughness [7-9], high hardness [10], low magnetic energy loss [11], near-net-shape formability [12-14], near-shape fabrication by injection molding and die casting [14, 15], microformability [12, 13, 16, 17], high fatigue limit [18-20], and high corrosion resistance [21-24]. Despite this appealing collection of properties, many aspects of BMGs have not been characterized or are not well understood. In particular, the electrochemical behavior has not been explored for many BMG compositions. Furthermore, localized corrosion has been reported in every BMG corrosion study published to date. This fact is unexpected for an ideally homogeneous material. Finally,

the mechanical behavior of many BMG compositions has not been characterized, and the actual deformation and failure mechanisms are not fully understood.

In order for BMGs to be used for structural applications in the future, the electrochemical and mechanical behaviors, and the interaction between these, must be clarified and thoroughly understood. Therefore, the general objectives of this study are to better characterize the electrochemical and mechanical behaviors of several BMG compositions and better elucidate the mechanisms involved. Specifically, the electrochemical and mechanical behavior of various BMGs will be examined through the following methods:

i. Characterization of the electrochemical behavior of these BMGs in several environments;

ii. Examination of the fatigue properties of these BMGs in air; and

iii. Evaluation of the interaction of corrosion and fatigue in an aqueous environment.

2. REVIEW OF RELATED LITERATURE

2.1. Historical Background of Amorphous Alloys

Prior to the discovery of amorphous alloys in the 20th century, solidified metallic materials were only known to exist in their crystalline states. Kramer claims to have first synthesized a metallic glass in the 1930's through vapor deposition [25, 26]. In 1950, Brenner et al. reported the fabrication of an amorphous nickel-phosphorus alloy through electrodeposition [27].

However, it was not until 1960 that Duwez, Klement and Willens at Caltech reported the formation of an amorphous solid by rapidly quenching a $Au_{70}Si_{30}$ [atomic percent (at.%)] alloy directly from the melt to liquid nitrogen temperature [28]. Almost simultaneously, Miroshnickenko and Salli reported the successful fabrication of an amorphous alloy as well [29]. Both amorphous alloys were fabricated through similar techniques that later acquired the designation of "splat-cooling" [1]. In the case of Duwez et al., they initially used what is commonly referred to as gun quenching. A schematic diagram of the apparatus used by Duwez et al. is presented in Figure 1 (All figures are located in Appendix II). In this technique, the metal alloy is melted in a crucible in an inert atmosphere. The melt is quickly ejected from the crucible by an acoustic shock wave and strikes a cold copper surface. The melt spreads out along the copper surface due to the force of impact and solidifies through rapid heat conduction. Through this innovative rapid cooling method, cooling rates of 10^6 – 10^8 K/s can be attained [30]. The technique utilized by Miroshnickenko and Salli once again begins with the metal alloy being melted in a crucible in an inert environment. However, in this case, the melt is dropped between an anvil and a pneumatically driven piston (Figure 2)

[29]. The melt is struck between the piston and the anvil and spread into a thin layer on the cooled surface of the anvil. Heat conduction out of this thin layer results in solidification with cooling rates in the range of $10^5 – 10^6$ K/s [30]. Duwez and his group at Caltech proceeded to demonstrate glass formation in other alloy systems such as Pd-Si and Pd-Cu-Si. All of these landmark discoveries were made through research on rapid cooling techniques to produce the necessary cooling rates greater than 10^5 K/s [30, 31].

Other important early contributors to the subject were Turnbull and Chen. Their research confirmed the glass transition in these alloy systems and others [32, 33]. Turnbull was also the first to develop a measure for the glass-forming ability (GFA) of an alloy system. He theorized that as the ratio of the glass transition temperature (T_g) to the melting temperature (T_m) increased to the range of 0.5 to 0.7, the nucleation of the undercooled melt should be slow enough to allow solidification of the melt without crystallization [34, 35]. This ratio (T_g/T_m) is known as the reduced glass transition temperature (T_{rg}) and is still utilized today as a measure of the glass-forming ability (GFA) of an alloy.

Both of the previously mentioned rapid quenching methods (Figures 1-2) were used by Duwez et al. and by Giessen and Grant at MIT throughout the 1960's for further research into amorphous alloys. It was through this research that two broad classes of amorphous alloys were identified. The Duwez group identified what is commonly termed the metal-metalloid amorphous alloy system. Generally, the metal-metalloid alloys contain about 80 at.% of a transition metal (i.e., Ni, Co, Fe, etc.) and approximately 20 at.% of a metalloid element (i.e., Si, P, B, C, etc.) [30]. During the 1960's Giessen et al. discovered a second class of glass-forming alloys that are now

referred to as the metal-metal system [30]. This system typically contains an early transition metal (TM) or rare earth (RE) (i.e., Zr, Nb, Ti, etc.) and a late transition element such as Ni, Co, Fe, Pd, etc. [30].

Innovation in this novel area of materials science continued in the 1970's after continuous casting processes were developed [31]. Pond and Maddin developed a technique, known as melt-spinning, for the preparation of continuous, long lengths of amorphous alloy ribbons [36]. This continuous fabrication process introduced the possibility of a large-scale production method and interest in metallic glass research increased [1].

However, the tremendous cooling rates necessary to produce these early amorphous alloys were a significant disadvantage. In order to produce cooling rates on the order of 10^4–10^5 K/s, the samples must be extremely thin [37]. In fact, amorphous alloys produced by the aforementioned techniques were typically less than 100 μm in thickness [30]. It was not until the 1980's that the next technological hurdle was surpassed in amorphous material research. Turnbull and others demonstrated that Pd-Ni-P alloys could be cast in rods with diameters of millimeters [38, 39]. Lee and Johnson also reported similar results with Au-Pb-Sb alloys at about the same time [40]. In the early 1990's, Inoue and other collaborators began to systematically investigate the glass-forming ability of a variety of multicomponent alloy systems [14]. These early bulk glass-forming compositions included the Zr-Al-Ni-Cu, Mg-Y-Ni-Cu, and La-Al-Ni-Cu systems [41-45]. Concurrently, Peker and Johnson also systematically investigated numerous Zr- and Ti-based alloy systems. This work resulted in the discovery of bulk-glass-forming alloys in the Zr-Ti-Ni-Cu-Be and Zr-Ti-Ni-Cu systems [46, 47].

While previous amorphous alloys required critical cooling rates (R_c) on the order of 10^4–10^5 K/s, these new multicomponent alloy systems that were designed by Inoue et al. and Johnson et al. required much lower critical cooling rates on the order of 10^{-1}–10^3 K/s, as demonstrated in Figure 3. Over the next decade, many glass-forming alloy systems were discovered. These multicomponent systems included Mg- [48], Ln- [49], Zr- [41, 46], Fe- [50, 51], Pd-Cu- [52], Pd-Fe- [53], Ti- [54, 55], Cu- [56], Co- [57, 58], Ca- [59, 60], Y- [61], and Ni-based [62] alloys. These alloy systems are summarized in Table 1 (All tables are located in Appendix I) along with the year in which the first paper or patent was published on each system. These advances meant that maximum sample thickness (t_{max}) and glass-forming ability (GFA) increased greatly with the advent of these new alloys, as graphically demonstrated in Figure 4. Finally, this new class of materials is distinctly unique, as can be seen in Figure 5. In terms of materials selection for a specific application, as one selects a crystalline material with higher strength, the trade-off is significantly greater stiffness. However, BMGs maintain their elasticity even with large increases in strength, as demonstrated by the distinctly different linear relationship in Figure 5.

2.2. Empirical Rules of Glass Formation

With the design and discovery of many bulk glass-forming systems, an understanding of the criteria necessary to avoid crystal nucleation on solidification began to take shape. Inoue et al. proposed three empirical rules for the achievement of a large glass-forming ability as follows: (a) a multicomponent system consisting of three or more elements, (b) atomic size ratios with differences of greater than 12% among the

constituent elements, and (c) negative heats of mixing among the constituent elements [41, 49, 63, 64]. Together, these rules increase the complexity of the alloy and result in the "frustration" of the crystallization process upon solidification [31].

In addition to these empirical rules for glass formation, various parameters were developed to describe / predict the glass-forming ability of various alloy systems. As previously mentioned, Turnbull was the first to suggest that, as the ratio of the glass-transition temperature to the melting temperature (T_m) increased, the homogeneous nucleation rate of crystals in the undercooled melt would decrease [34, 35]. This criterion is commonly known as the "Turnbull criterion" or the reduced glass-transition temperature (T_{rg}).

$$\text{Reduced glass transition temperature} = T_{rg} = T_g / T_m \quad (1)$$

Based upon this criterion, the GFA should increase as T_{rg} increases. In practice, T_{rg} values greater than 0.6 – 0.7 are generally necessary for bulk glass formation [31].

Masumoto and Inoue have used the size of the supercooled liquid region (ΔT_x) as a measure of the stability of the undercooled liquid above T_g [14]. The supercooled liquid region is defined as follows:

$$\text{Supercooled liquid region} = \Delta T_x = T_x - T_g \quad (2)$$

where T_x is the temperature at the onset of crystallization. As described by Masumoto and Inoue, the GFA of the alloy should increase as ΔT_x increases. However, several studies have demonstrated that this relationship is not valid for all BMG alloys [65-68].

More recently, Lu and Liu have systematically addressed the shortcomings of these criteria. They proposed a new, comprehensive criterion for the prediction of GFA as follows [69]:

$$\gamma = T_x / (T_g + T_L) \quad (3)$$

where T_L is the liquidus temperature. The denominator accounts for the liquid phase stability (thermodynamics) while the numerator describes the resistance to crystallization (kinetics). As T_L and T_g decrease, the supercooled liquid stability and GFA increase. On the other hand, higher values of T_x result in an increased resistance to crystallization and a higher GFA. Therefore, the best GFA is obtained when γ is equal to 0.5. This parameter was reportedly effective at predicting the relative GFAs for various glass-forming materials.

2.3. Electrochemical Properties of Bulk Metallic Glasses

Corrosion is dependent on both the chemistry of the electrolyte and the chemical composition of the material. Localized corrosion is particularly dependent upon physical damage or physical irregularities in the passive film such as grain boundaries, scratches, differing phases, crystal imperfections, etc. [70]. Therefore, it would be expected that amorphous alloys should exhibit improved resistance, or even immunity, to localized corrosion due to the inherent microstructural homogeneity and lack of these surface irregularities. With this in mind, several recent studies have compared the corrosion behavior of bulk metallic glasses in both the amorphous and crystalline states. In general, all of these studies have found a susceptibility of various BMG alloys to localized corrosion. Depending upon the particular components in the alloys, the general corrosion rates and resistances to localized corrosion have varied widely. However, the Zr-based BMGs have typically demonstrated reasonably low corrosion rates and moderate to high resistances to localized corrosion. Based upon various studies, it is believed that the

susceptibility to localized corrosion is due to inhomogeneities in the materials. Thus, the quality and homogeneity of the BMG material is of utmost importance for good electrochemical behavior. A brief summary of some of the various electrochemical studies will follow.

Peter et al. performed cyclic-anodic-polarization tests in 0.6 M NaCl on both amorphous and crystalline $Zr_{52.5}Cu_{17.9}Ni_{14.6}Ti_{5.0}Al_{10.0}$, commonly known as Vitreloy 105 (Vit 105) [21]. Both states exhibited passive corrosion behaviors at the natural corrosion potentials and pitting-corrosion susceptibilities. However, the amorphous alloy was found to be slightly more resistant to pitting corrosion than the crystalline alloy. Furthermore, the protective passive film was shown to reform quickly following mechanical damage with a diamond stylus.

Along the same lines, Schroeder et al. investigated the electrochemical properties of the Zr-based $Zr_{41.2}Ti_{13.8}Ni_{10.0}Cu_{12.5}Be_{22.5}$ (at.%) BMG alloy, commonly referred to as Vitreloy 1 (Vit 1) or Liquidmetal-001 (LM-001), in both the amorphous and crystalline states in 0.5 M NaCl and 0.5 M $NaClO_4$ [71]. The results indicated that the amorphous alloy was only slightly more resistant to pitting corrosion than the crystalline alloy in the NaCl electrolyte. In the $NaClO_4$ electrolyte, the amorphous and crystalline states did not demonstrate any significant differences in corrosion behavior.

Koster et al. studied the corrosion behavior of a crystalline and amorphous $Zr_{69.5}Cu_{12}Ni_{11}Al_{7.5}$ (at.%) melt-spun alloy [72]. Potentiodynamic polarization tests were conducted in a 0.1 N NaOH electrolyte at room temperature. They found that there was no significant difference in the corrosion behavior between the crystalline and amorphous alloys.

Finally, He et al. examined the corrosion behavior of the Vit 105 alloy in various states of crystallinity [73]. The electrochemical behavior of the as-cast amorphous alloy was compared to the same alloy annealed for 5, 20 and 60 minutes at 500°C in argon to produce samples with 11%, 63% and 100% volume fraction of nanocrystals, respectively. Electrochemical characterization was conducted in aerated 0.5 kmol / m^3 H_2SO_4 or 0.5 kmol / m^3 NaCl electrolytes. Compared to the crystalline samples, the amorphous samples exhibited good resistance to general corrosion in 0.5 kmol / m^3 H_2SO_4 and to pitting corrosion in 0.5 kmol / m^3 NaCl. Both general and pitting corrosion resistances were found to be inversely proportional to the volume fraction of nanocrystals.

Electrochemical studies have also been conducted to determine the effect of specific alloying elements on the corrosion behavior of BMGs and the resultant passive films. For example, Raju et al. examined the effect of Nb and Ti additions on the corrosion behavior of Zr-based BMGs in 0.1 M Na_2SO_4 and 0.01 M NaCl electrolytes [74]. In particular, Zr-Al-Cu-Ni-X alloys containing small amounts of X = Nb or Ti exhibited improved corrosion resistance in chloride containing electrolytes as compared to the quaternary alloy $Zr_{55}Al_{10}Cu_{30}Ni_5$ (at.%). However, the improvement in corrosion resistance was attributed to the higher GFA of these alloys and the resultant homogeneous single-phase amorphous material. In addition, Auger electron spectroscopy (AES) was also utilized to study the role of alloying elements in the formation of passivating films. The quaternary alloy exhibited the thickest oxide layer (approximately 18 nm) while the Nb-containing alloys produced relatively thin passive films (approximately 12-13 nm) significantly enriched in Cu and Ni near the oxide / alloy interface.

Pang et al. characterized the electrochemical behavior of melt-spun amorphous alloys with nominal compositions of $Zr_{60-x}Nb_xAl_{10}Ni_{10}Cu_{20}$ (x = 0, 5, 10, 15, 20 at%) [75]. These alloys were evaluated in 1 N HCl, 3 mass% NaCl and 1 N H_2SO_4. This study demonstrated that the addition of increasing amounts of Nb to this alloy resulted in decreasing supercooled liquid regions (ΔT_x), increasing equilibrium corrosion potentials, considerable improvements in the corrosion resistance in the 1 N HCl electrolyte, and increasing pitting potentials in the 3% NaCl electrolyte. For the 1 N $H2_5O_4$ electrolyte, all of the alloys investigated exhibited high corrosion resistance with wide passive regions and passive current densities lower than those of pure Zr and pure Ni metals.

Gebert et al. examined the electrochemical behavior of a $Zr_{55}Cu_{30}Al_{10}Ni_5$ (at.%) bulk metallic glass [76]. Potentiodynamic and potentiostatic polarization measurements were investigated in 0.1 M Na_2SO_4 and 0.001 M NaCl electrolytes at 150°C and 250°C. The results revealed accelerated corrosion with increases in temperature as compared to the room temperature behavior. The degradation of the corrosion resistance was attributed to enhanced metal dissolution and to changes in the oxide growth mechanisms. At higher temperatures, the oxide layer formed in thicker layers but was more permeable and, therefore, less protective. Pitting initiated primarily at crystalline inclusions in chloride-containing electrolytes at high temperatures.

Hiromoto et al. at the National Research Institute for Metals in Tsukuba, Japan have published multiple reports in the literature regarding electrochemical studies of Zr-based BMGs in biologically relevant environments. In one study, they characterized the influence of pH on the corrosion behavior of an amorphous $Zr_{65}Al_{7.5}Ni_{10}Cu_{17.5}$ (at.%) melt-spun ribbon [77]. Potentiodynamic polarization tests were conducted in a deaerated

phosphate – citric-acid-buffered solution (PCA) at various pH levels between 2.2 and 8.0 and in a deaerated phosphate-buffered-saline solution (PBS) at a pH of 7.5. This research demonstrated that the pitting potential of this Zr-based BMG was not influenced by the pH. Furthermore, chloride ions did not influence the open-circuit potential (E_{corr}). However, the quantity of metal ions released from the alloy increased with decreasing pH through a shift in E_{corr} and an increase in the solubility of the passivation layer. Although the pitting corrosion resistance decreased with decreasing pH, the repassivation potential was always higher than E_{corr}. Therefore, pitting corrosion is not likely to occur with this alloy in environments similar to those found in vivo.

In another study, Hiromoto et al. investigated the effect of the chloride ion concentration on the anodic polarization behavior of the same $Zr_{65}Al_{7.5}Ni_{10}Cu_{17.5}$ (at.%) melt-spun amorphous alloy [78]. Again, the electrolyte was a deaerated phosphate – citric-acid-buffered solution (PCA). However, in this study, the chloride ion [Cl-] concentration was varied from 0 to 1.0 M. With increasing chloride ion concentration, E_{corr} was constant and E_{pit} decreased logarithmically. The polarization resistance (R_p) decreased with increasing chloride concentration up to 6.8×10^{-2} mol / L and remained constant at higher concentrations.

Hiromoto et al. also evaluated the electrochemical behavior of this same $Zr_{65}Al_{7.5}Ni_{10}Cu_{17.5}$ melt-spun amorphous alloy in phosphate buffered solutions with varying amounts of chloride ions [Cl^-], pH, and dissolved oxygen [DO] in the electrolyte [22]. This alloy demonstrated high corrosion resistance in all of the electrolytes evaluated with polarization resistances similar to those of pure titanium. Both R_p and the pitting corrosion resistance decreased with decreasing pH and increasing chloride ion

concentrations. However, the pitting potential was higher than the open-circuit potential (E_{corr}) down to a pH of 2.2.

Furthermore, Hiromoto et al. examined the electrochemical behavior and surface composition of a $Zr_{60}M_5Al_{7.5}Cu_{27.5}$ (M = Pd, Ni, In, Mn, Cr, Ti, Nb and Zr) (at.%) melt-spun amorphous alloy [79]. Anodic polarization experiments were conducted in a deaerated phosphate-buffered saline solution at a pH of 7.5 at 37°C. XPS was utilized to characterize the surface composition of the alloys after immersion in the electrolyte for 1.8×10^3 seconds. XPS analysis revealed that Al is enriched in the surface oxide film while Cu is enriched in the substrate just below the surface oxide film. The anodic polarization behavior of the alloys was found to correlate with the [Zr] / [Zr+Al] ratio in the surface oxide film, where the R_p and E_{pit} decreased with an increase in the [Zr] / [Zr+Al] ratio. The alloys containing Pd, Ni and Nb demonstrated the highest values of R_p and the Pd-, In- and Zr-containing alloys exhibited the highest values of E_{pit}.

Finally, Hiromoto et al. have also conducted electrochemical studies of an amorphous powder consolidated $Zr_{65}Al_{10}Ni_{10}Cu_{15}$ (at.%) alloy immersed in cell culture medium [23, 80]. Anodic-polarization tests were conducted in the following deaerated electrolytes: Hanks' solution, Eagle's minimum essential medium (MEM) and cell culture medium (MEM + FBS) consisting of MEM and fetal bovine serum (FBS). The different solutions were used to determine the effect of various components on the electrochemical behavior. Hanks' solution contains only inorganic ions, MEM contains inorganic ions and amino acids, and MEM + FBS contains inorganic ions, amino acids and proteins [23]. Furthermore, short-term and long-term immersion in the electrolytes was conducted to evaluate the effect of the immersion time on the corrosion performance

of this alloy. The amino acids and proteins present in the MEM + FBS electrolyte were found to retard the cathodic reaction resulting in a decrease in E_{corr}. Independent of the presence of biomolecules, long-term immersion in the electrolyte prior to the polarization tests resulted in higher values of E_{corr}, R_p and E_{pit}. However, the difference between E_{corr} and E_{pit} decreased after long-term immersion.

2.4. Mechanical Properties of Bulk Metallic Glasses

2.4.1. Monotonic Loading

The monotonic deformation response of bulk metallic glasses can be classified as either inhomogeneous or homogeneous, depending upon the deformation conditions [15, 81, 82]. At low strain rates and high temperatures (e.g., $T > 0.70\ T_g$), BMGs typically demonstrate homogeneous deformation with significant plasticity [81]. For example, Nieh et al. reported that the Vit 105 BMG alloy exhibited a maximum tensile elongation of over 600% at 425 - 440°C and a high strain rate of $10^{-2}\ s^{-1}$ [82]. Photos of these BMG samples after the tensile tests and the stress-strain curves are shown in Figure 6(a) and 6(b), respectively. Furthermore, the temperature for the transformation from inhomogeneous to homogeneous deformation is strongly dependent upon the strain rate [15]. Depending upon the strain rate and temperature, the deformation of BMGs in the supercooled liquid region can be Newtonian viscous flow (lower strain rates) or non-Newtonian (higher strain rates) [15, 30]. Nieh et al. attributed the non-Newtonian behavior to glass instability in the form of stress-induced nanocrystallization [15]. In addition, Kawamura et al. reported superplasticity in a Pd-based BMG above T_g at strain rates from 10^{-4} to $100\ s^{-1}$ with a maximum elongation to failure of 1260% [83].

On the other hand, at high strain rates and low temperatures (e.g. room temperature), BMGs exhibit inhomogeneous deformation, which is characterized by the formation of localized shear bands that rapidly propagate and result in catastrophic failure. Wright et al. [84] and Schuh et al. [85] reported this behavior following nanoindentation studies in which they observed serrated flow upon loading. In addition, Nieh et al. have demonstrated that serrated flow is strongly dependent upon the rate of deformation, with rapid deformation rates suppressing the prominence of the serrations [81].

Two primary hypotheses exist in the literature regarding plastic flow and localized shear bands in monotonically-loaded BMGs [86]. The first theory suggests that the viscosity in the shear bands decreases due to the formation of free volume [87]. The second theory contends that the viscosity in the shear bands decreases due to local adiabatic heating [88]. Either way, the decrease in viscosity results in localized deformation and inhomogeneous flow within the shear bands.

Wright et al. studied the serrated plastic flow in $Zr_{40}Ti_{14}Ni_{10}Cu_{12}Be_{24}$ (at.%) and $Pd_{40}Ni_{40}P_{20}$ (at.%) during compressive loading [86]. Quantitative measurements of the serrated deformation during mechanical testing were used to estimate the temperature increase in a single shear band due to local adiabatic heating. The resultant estimation predicted temperature increases on the order of only a few degrees Celsius. Therefore, the authors conclude that localized heating is not likely the primary cause of shear banding.

Gilbert et al. investigated the light emission phenomenon observed during the fracture of the Vit 1 alloy [89]. Charpy V-notch impact tests in oxygen and nitrogen

were conducted in conjunction with spectroscopic measurements of the light emitted upon fracture. In oxygen, the spectra exhibited a single, broad peak that could be fit to an approximate blackbody temperature of 2900 K. In nitrogen, the intensity of the light emitted was reduced by more than four orders of magnitude and the effective blackbody temperature was estimated to be 1400 K. In addition, the fracture surfaces from both environments exhibited the vein morphology typically reported in the literature. Based upon these observations, the authors suggested that the light emission associated with the fracture of BMGs is due to pyrolysis of the newly created surfaces upon failure. Furthermore, the temperature measured in the nitrogen environment is proposed to be a direct measurement of the deformation-induced heating.

Zhang et al. examined the cyclic deformation and fatigue-crack propagation of the Vit 1 alloy in both the amorphous and partially crystalline states [90]. Both states demonstrated controlled crack growth prior to final fracture under fully reversed, stress-controlled loading. The amorphous and partially crystalline samples failed at an average of approximately 19,000 and 13,000 cycles, respectively. The fatigue exponent ranged between 1.43 and 1.66 in the Paris regime. Stages of crack initiation, stable crack propagation and overload fracture could be clearly discerned on the fracture surfaces of the amorphous samples. The crystalline phases were reported to act as sites for crack initiation as opposed to barriers against crack propagation under fully reversed stress control. However, under fully reversed load control, the acicular crystalline phases can retard crack growth or act as crack initiation sites, depending upon the orientation to the crack growth direction.

Li et al. examined the initiation and propagation of shear bands in Vit 1 and $Zr_{57}Cu_{15.4}Ni_{12.6}Al_{10}Nb_5$ (at.%), known as Vitreloy 106, through in situ tensile tests conducted in an SEM [91]. It was reported that both the normal and shear stresses played a role in the initiation and propagation of shear bands in BMGs. Mode II shear microcracks initiated and propagated along the shear bands. These mode II cracks opened and became mode I + II complex cracks with depths of 10-20 μm. Failure occurred as soon as the complex crack became a mode I crack that penetrated the thickness of the samples.

Hufnagel et al. also investigated shear-band kinetics through in situ three-point bend tests of an amorphous $Zr_{57}Ti_5Cu_{20}Ni_8Al_{10}$ (at.%) alloy in an SEM [92]. The initial shear bands were reported to coincide with the onset of plastic deformation. The density of shear bands increased dramatically with increasing load and serrated flow appeared to be correlated with the initiation of new shear bands. Final failure occurred on one of the primary shear bands on the surface of maximum tensile stress.

However, it is important to note that all of the aforementioned measured or estimated temperature increases were primarily associated with the final fracture or crack growth and not those associated with simple shear banding prior to failure. Wright et al. studied the serrated plastic flow in $Zr_{40}Ti_{14}Ni_{10}Cu_{12}Be_{24}$ (at.%) and $Pd_{40}Ni_{40}P_{20}$ (at.%) during compressive loading [86]. Quantitative measurements of the serrated deformation during mechanical testing were used to estimate the temperature increase in a single shear band due to local adiabatic heating. It was assumed that each serration was due to the formation of one shear band. The resultant estimation predicted temperature increases on the order of only a few degrees Celsius. Therefore, the authors concluded that localized

heating is not likely the primary cause of shear banding. On the other hand, Lewandowski et al. cleverly estimated the temperature rise associated with shear-banding by coating Cu-, Hf-, and Zr-based BMG samples with thin films of low-melting-point metals [93]. The authors reported temperature increases, in all cases, of at least 200ºC, based upon the melting of the thin films at the locations of shear bands.

The applications of these new materials are limited in many cases due to the lack of plasticity in tension. A multitude of studies on improving the plasticity of BMGs exist in the literature [2]. In fact, improvements in plasticity with a minimal loss of strength have been reported through the precipitation of various crystalline particles [2]. On the other hand, the deformation and failure mechanisms of BMGs are not well understood. The general consensus in the literature is that deformation occurs through highly localized shear bands near the plane of maximum shear within the material. Although more than 30 years have passed since Spaepen and Leamy proposed their respective theories, the exact mechanisms of shear band formation and propagation behavior still have not been clearly delineated.

2.4.2. Cyclic Loading

Theoretically, the absence of plastic deformation in BMG alloys suggests that a perfectly amorphous alloy, without constraint, could exhibit an ideal fatigue limit – one that approaches the ultimate tensile strength [19, 94]. However, this early theory has not been demonstrated. On the contrary, the first fatigue study of a BMG was conducted by Gilbert et al. on the Vit 1 alloy [95, 96]. Four-point bend tests at frequencies of 25 Hz, with a stress ratio ($R = \sigma_{min} / \sigma_{max}$) of 0.1, resulted in a fatigue endurance limit, in terms of the stress range (σ_r), of approximately 152 MPa, or a normalized stress range (stress

range / ultimate tensile strength) of 0.08. In contrast, conventional crystalline alloys, such as high-strength steels and titanium and aluminum alloys, typically exhibit fatigue endurance limits, in terms of the stress range, that are 30-50% of the ultimate tensile strengths [97]. However, the crack-propagation behavior of this alloy was found to be similar to that observed in ductile, crystalline alloys "in terms of (a) the dependence of crack-growth rates on the applied stress-intensity factor range, (b) the role of the load ratio and crack closure, and (c) the presence of ductile striation on fatigue fracture surfaces" [9, 96]. Thus, the authors concluded that the low fatigue endurance limit was due to the ease of crack initiation in the BMG alloy.

Peter et al. compared the uniaxial fatigue behavior ($R = 0.1$, $\nu = 10$ Hz) of the Vit 105 BMG alloy in both air and vacuum [18, 19]. Samples tested in air exhibited slightly longer lifetimes and less scatter than those tested in vacuum. More importantly, they reported a high fatigue endurance limit at a stress range of 907 MPa (Figure 7), approximately 53% of the ultimate tensile strength.

Likewise, Wang et al. also conducted uniaxial fatigue experiments ($R = 0.1$, $\nu =$ 10 Hz) on the $Zr_{50}Cu_{40}Al_{10}$ (at.%) and $Zr_{50}Cu_{30}Al_{10}Ni_{10}$ (at.%) BMG alloys in air and vacuum [20]. The authors reported fatigue-endurance limits at stress ranges of 752 MPa and 865 MPa, respectively, resulting in normalized stress ranges of 41% and 46%, respectively.

Gilbert et al. studied the mechanisms for fracture and fatigue-crack propagation through the use of compact-tension (CT) specimens of the Vit 1 alloy [96]. The mean fracture toughness of that composition was reported to be approximately 55 MPa $m^{0.5}$. This value decreased to 1 MPa $m^{0.5}$ upon partial crystallization. For the fully amorphous

samples, stable fatigue-crack growth was reported with rates that were comparable to those observed in traditional polycrystalline alloys (Figure 8). In addition, the crack growth behavior was consistent with Paris' law with a crack-growth exponent (m) in the range of 2 – 5, common values for ductile, crystalline materials. Furthermore, the values for ΔK_{TH} were determined to be in the range from 1 -3 MPa $m^{0.5}$, which is again comparable to crystalline materials such as aluminum alloys and high-strength steels.

Fatigue fracture surfaces have been analyzed in detail to gain insight into the cyclic crack-growth mechanisms. Through careful analysis, Tatschl et al. reported that the fatigue fracture surfaces contained striations with relatively constant spacing independent of crack-growth rate and stress intensity range [98]. The overload regions of the fracture surfaces consisted of the typical vein morphology that was generated by localized necking.

Despite a number of studies on the fatigue behavior of BMGs reported in the literature, great inconsistencies in the fatigue limit of these materials have been reported. The aforementioned results are summarized in Table 2 along with several high-strength alloys and pure Zr for comparison. Finally, the exact deformation and failure mechanisms in cyclic-loading conditions have not yet been clearly delineated.

2.5. Corrosion Fatigue

Corrosion fatigue is the damage to or failure of a metal due to corrosion combined with fluctuating stresses [99]. In general, corrosion fatigue can occur by one of three primary mechanisms: stress-assisted dissolution (SAD), hydrogen-assisted cracking

(HAC), or liquid metal embrittlement [97, 100]. Since this study is not concerned with a liquid metal environment, only the first two mechanisms will be discussed.

Stress-assisted dissolution, or anodic dissolution, occurs in materials that form passive films in a given environment. The applied, fluctuating stresses cause localized plastic deformation at the crack tip, resulting in rupture of the passive film. The exposed bare metal serves as the anode and the unbroken passive film can serve as the cathode. As a result, anodic dissolution of the exposed bare metal leads to crack growth [97]. Ironically, materials that have moderate repassivation rates are most vulnerable to this corrosion fatigue mechanism. Anodic dissolution associated with low repassivation rates results in rapid dissolution on the crack sides, resulting in blunting of the crack tip and a decrease in the crack growth rate. On the other hand, high repassivation rates result in little anodic dissolution per film-rupture event [97].

Hydrogen-assisted cracking, or hydrogen-induced embrittlement, occurs when the pH and the potential within the crack tip are sufficiently low to allow for the reduction of hydrogen ions or water to hydrogen. These hydrogen atoms can adsorb on the metal surface, combine, absorb, and rapidly diffuse to the crack-tip stress field, resulting in embrittlement ahead of the crack tip [97].

A primary technique for distinguishing between SAD and HAC is by studying the effect of applied potentials on the fatigue crack growth rate or fatigue life [100]. The basic idea for this technique was first theorized by Uhlig [101], followed by development by Phelps and Loginow [102]. According to the theory, if an applied cathodic potential increases the time to failure, the degradation mechanism operating at the open-circuit

potential is SAD. On the other hand, the operating mechanism is HAC if an applied anodic potential increases the time to failure.

Several studies have examined the environmental effect on the fatigue properties of BMG alloys. For instance, Schroeder et al. studied the effect of the environment on the fatigue behavior of the Vit 1 BMG alloy [103]. Fatigue and fatigue crack-growth studies were conducted in air, deionized water, and 0.5 M NaCl at a frequency of 25 Hz with R = 0.1. The authors reported that deionized water caused a marginal increase in the crack-growth rate, while 0.5 M NaCl caused a substantial increase of two to three orders of magnitude, in addition to a decrease in the threshold stress-intensity factor range (ΔK_{TH}). Sustained loading of the sample in the 0.5 M NaCl solution resulted in stress-corrosion cracking with crack-growth rates comparable to the cyclically-loaded condition.

Ritchie et al. reported similar results in fatigue tests of the Vit 1 BMG alloy in air, de-ionized water, and aerated 0.5 M NaCl [104, 105]. These results are presented in Figure 9. While fatigue striations were observed on the samples tested in air and de-ionized water, none were visible on the samples tested in the NaCl solution. Furthermore, the exponent in Paris' law for the samples tested in NaCl approached zero in the plateau region, compared to an exponent of approximately 1.6 in air. The authors conclude that this type of behavior that was observed in the NaCl solution is typical of stress-corrosion fatigue. The stress-corrosion fatigue behavior was further investigated by polarizing the samples during fatigue. For this material, the open-circuit potential (E_{corr}) lies between the pitting potential (E_{pit}) and the protection potential (E_{pp}). Therefore, immersion in the NaCl electrolyte without polarization led to elevated crack-

growth rates. However, when the samples were cathodically polarized, the fatigue crack-growth rates were reduced greatly, or the fatigue cracks were arrested completely at cathodic potentials below approximately -750 mV (Figure 10), as measured versus the saturated calomel electrode (SCE). Moreover, the authors conclude that the crack-growth mechanism is not hydrogen-based because anodic polarization did not affect the crack-growth rates in the NaCl solution. Finally, Ritchie et al. utilized the experimentally-measured crack-growth rates, over the time (t) of one cycle, in NaCl at the open-circuit potential, $[da/dt\ (K(t))]_{SCC}$, to evaluate the effect of a static load on the fatigue-crack growth. Using a superposition model, predictions of effective fatigue crack-growth rates, $(da/dN)_{eff}$, in the NaCl solution can be calculated according the following equation:

$$\left(\frac{da}{dN}\right)_{eff} = \int_0^{1/\nu}\left[\frac{da}{dt}\left(K(t)\right)\right]_{SCC} dt \qquad (4)$$

where ν is the frequency. The SCC model prediction, with an average value for the onset of SCC (K_{ISCC}) of 0.9 MPa $m^{0.5}$, was consistent with the experimentally-measured fatigue crack-growth rates observed in the NaCl solution, as demonstrated in Figure 11.

In addition, Maruyama et al. performed fatigue tests with the $Zr_{65}Cu_{15}Ni_{10}Al_{10}$ (at.%) BMG alloy, fabricated by dry-pressing of consolidated powder, in dry air at ambient temperature ($R = 0.1$, $\nu = 20$ Hz), and in a phosphate-buffered saline (PBS) electrolyte at 37°C with a pH of 7.5 ($R = 0.1$, $\nu = 2$ Hz) [106]. The PBS electrolyte was deaerated with a N_2 / O_2 gas mixture to produce a physiologically-relevant oxygen content. As shown in Figure 12, there was no difference between the stress-fatigue life (S-N) curves in air and PBS. Furthermore, testing in both environments resulted in

fatigue limits at stress ranges of 300 MPa at 10^7 cycles. These values result in a fatigue endurance limit that is 24% of the tensile strength. For comparison to crystalline Ti-based alloys, Ti-6Al-4V and pure Ti have fatigue ratios of 25% and 34%, respectively. Finally, the fracture surfaces of the samples tested in both environments were similar. Crack initiation reportedly occurred primarily at defects or impurity particles.

2.6. Biomedical Applications of Bulk Metallic Glasses

The unique properties of BMGs make these materials attractive alternatives in biomedical applications. BMGs have potential biomedical applications as screws due to their toughness and high strength. Moreover, certain BMG compositions have been reported to have a low magnetic susceptibility, which could be advantageous in applications of surgical instruments for interventional magnetic resonance imaging (MRI) [107-109]. The ease of micro-forming / fabrication of BMGs [13, 17] also lends itself to the production of gears for small, high-powered micromotors that could be of use in arthroscopy tools. Finally, one of the most promising biomedical applications of bulk metallic glasses is for bone fracture fixation and hip arthroplasty components. BMGs possess low moduli that are comparable to the modulus of bone as well as high strength to withstand the large forces generated within the skeletal system of the human body.

Bone is a living tissue that undergoes constant remodeling through simultaneous bone formation and resorption [110]. Bone formation is performed by osteoblasts while bone resorption is performed by osteoclasts. Current understanding suggests that the local mechanical environment affects this tissue remodeling process [110].

Traditionally, rigid internal fixation of bone fractures has been utilized to maintain alignment and promote "primary osseous union by stabilization and compression" of the fracture [111]. This type of internal fixation is commonly attained through the use of metallic plates, screws and rods. However, difficulties associated with this method of fixation arise due to the bone plate / bone mechanical mismatch. This mismatch in mechanical properties results in the relatively rigid plate "shielding" the underlying bone from the stress to which it is typically exposed [112]. This phenomenon is known as stress-shielding or stress protection atrophy. Multiple reports in the literature have demonstrated that stress-shielding results in bone remodeling causing cortical thinning or osteoporosis, or both [112-116]. The ability of bone to structurally adapt to loading conditions and form the optimal structure to support loads has been described by Wolff's Law [117-119].

Furthermore, it has also been demonstrated that the magnitude of this detrimental bone remodeling is a function of the flexural stiffness of the plate [112]. For example, Bradley et al. examined the effect of bone plates with a range of flexural stiffnesses on the bone healing and remodeling of osteotomized femora in dogs [112]. They found that decreased flexural rigidity of the plate used was associated with increased strength of the bone. In other words, the decreased stiffness of the plate resulted in a greater load on the bone and the formation of "denser, stronger bone" according to Wolff's Law [112]. Finally, they theorized that this effect might have been even more drastic had the study been conducted for a longer time.

In order to avoid stress-shielding of the bone during fracture healing, the stiffness of the fixation device should be closely matched to the stiffness of healthy bone. The

proper material initially would carry a majority of the load. However, as healing progressed, the bone would carry an increasing share of the stress. A fixation device such as a bone plate or intramedullary rod with an elastic modulus similar to bone would allow this to occur. For comparison, the pertinent mechanical properties of a BMG are compared to common biomaterials in Table 3. As demonstrated in the table, the modulus of the Vit 105 BMG alloy is approximately 10 – 28% less than that of the Ti-6Al-4V alloy.

2.7. Biocompatibility

Biocompatibility can be defined as "the ability of a material to perform with an appropriate host response in a specific application" [120]. All biomedical implant devices interact to some extent with the tissue environment in which they are placed [121]. In other words, "inert" materials do not exist. The extent and results of this interaction define, in part, the biocompatibility of the device. Furthermore, the dynamic interaction between the device and the tissue includes the effects of the implant on the host tissue (host response) as well as the effects of the tissue on the implanted device (material response) [122]. However, these effects are typically interrelated, dependent upon the location, time of implantation, and function of the material and must be considered as a whole [123]. Often, the physiological fluids cause an adverse effect on the material, leading to the release of soluble or particulate matter and, in turn, leading to an adverse response from the tissue. It is crucial that any biomedical implant be evaluated for biocompatibility before clinical trials are initiated.

The biocompatibility of metallic materials is partially determined by the electrochemical interaction that results in the release of metal ions into the surrounding tissue and the cytotoxicity of these substances [122]. In fact, the corrosion rate of a material is directly related to the total amount of the metal content introduced into the body as described by the Taylor equation [124, 125]. Furthermore, the biocompatibility of metallic materials is also partially determined by the cytotoxicity of the types and quantities of metal ions that are released into the surrounding environment. However, this variable must be determined through analytical methods (e.g., atomic absorption spectrometry) and can not be predicted from the nobility or the overall composition of an alloy [126, 127]. All metallic materials corrode and release metal ions in the physiological environment. Therefore, biocompatibility is improved by minimizing the corrosion rate and selecting materials whose corrosion products produce the lowest levels of cytotoxicity.

The cytotoxicity of the metal ions is difficult to characterize. The conclusions, in many cases, are contradictory or rather vague. For example, some elements that are considered to be cytotoxic (e.g., Co, Ni, V, Al) are commonly used in biomedical applications without many known, severe complications. Contradictions between various reports could be due to antagonistic or protective effects caused by various metal combinations, differences in cell types, differences in assays, differences in the particular cellular response monitored, differences in exposure duration, or because of differences in the valence and concentrations of the metal ions examined [126, 128].

Numerous *in vitro* studies on the cytotoxicity of metallic ions and salts are reported in the literature [126, 129-136]. In some of these studies, the metallic ions or

salts were added to various cell cultures (e.g., fibroblasts, macrophages, neuroblastomas, etc.) and various assays were utilized to evaluate the effects on the cells. The cytotoxicological potential of a tested substance was often expressed as an IC_{50} value (inhibitory concentration 50%), which is the concentration of the substance required to induce a 50% variation of a particular cellular response in comparison to that of untreated cells [134]. The results from several of these studies have been summarized in Table 4. In this table, each metal salt was ranked from most to least toxic, in terms of the IC_{50} values for each cell line and bioassay. Since the number of metal ions tested in each evaluation was different, these ranks were then divided by the total number of metal ions evaluated within each study to produce a normalized rank. These normalized ranks were then averaged to produce a mean normalized rank for each metal ion. In other words, the normalized ranks range from 0.0 to 1.0, with increasing values denoting decreasing cytotoxicity. In most cases, the authors evaluated cytotoxicity on multiple cell lines and / or with multiple bioassays. For comparison purposes, the ranks from each of these cell lines / assays within each study were included in the rank calculations. It is important to note that metal ion salt solutions have been shown to be consistently slightly more cytotoxic than extracts of metal ions from an electrolyte [137]. Thus, these types of in vitro cytotoxicity studies are slightly conservative. Nevertheless, numerous studies have also demonstrated that significant biological alterations can occur in vivo at non-cytotoxic concentrations [126, 138-142].

3. MATERIALS AND METHODS

3.1. Electrochemical Characterization of BMGs

Zr-based alloy ingots with a nominal composition of $Zr_{52.5}Cu_{17.9}Ni_{14.6}Al_{10.0}Ti_{5.0}$ (at.%) [143], commonly known as Vitreloy 105 (Vit 105), were prepared from a mixture of these elements with elemental purities ranging from 99.5% to 99.99%. Each ingot was prepared by arc-melting the charge materials at Oak Ridge National Laboratory on a water-cooled, copper hearth under a Zr-gettered, Ar atmosphere. Each alloy button was melted and flipped multiple times to promote homogeneity. The alloy button was then drop cast into a water-cooled, copper mold to produce a cylindrical BMG ingot with a length of 76 mm and a diameter of 6.4 mm. Corrosion samples (∅6.4 x 5 mm) were extracted from the ingots by electrical-discharge machining (EDM) so that the transverse cross-sections of the ingots were exposed to the electrolyte in the corrosion tests.

In addition, a Ti-based BMG alloy plate with a nominal composition of $Ti_{43.3}Zr_{21.7}Ni_{7.5}Be_{27.5}$ (at.%), commonly known as LM-010, and a Zr-based $Zr_{41.2}Ti_{13.8}Ni_{10}Cu_{12.5}Be_{22.5}$ (at.%) BMG were fabricated and donated by Liquidmetal Technologies (Lake Forest, CA). The latter composition is commonly known as the Vitreloy 1, or Liquidmetal-001 (LM-001), BMG. Corrosion samples with approximate dimensions of 10 x 10 x 2 mm were extracted from the plates so that the large surfaces of the plates were exposed to the electrolyte in the corrosion tests. Ca-based BMGs were also fabricated and donated by the Air Force Research labs with the following nominal compositions: $Ca_{65}Mg_{15}Zn_{20}$, $Ca_{55}Mg_{18}Zn_{11}Cu_{16}$, and $Ca_{50}Mg_{20}Cu_{30}$ (at.%).

Finally, various corrosion-resistant, crystalline materials were selected for electrochemical characterization under identical conditions to provide for direct

comparisons with the BMG alloys. These materials included (a) $Ti_{90}Al_6V_4$ (wt.%) [$Ti_{86.2}Al_{10.2}V_{3.6}$ (at.%), ASTM F136], denoted as Ti-6Al-4V; (b) $Co_{63}Cr_{28}Mo_6$ (wt.%) [$Co_{61.4}Cr_{30.9}Mo_{3.6}$ (at.%), ASTM F799], denoted as CoCrMo; (c) AISI 316L stainless steel [$Fe_{62.5}Cr_{19.3}Ni_{13.3}$ (at.%), ASTM F138], denoted as 316L SS; (d) a Zr-based alloy [$Zr_{98.3}Sn_{1.1}Fe_{0.2}$ (at.%)] similar to Zircaloy; and (e) Mg-based ZK60 alloy [$Mg_{97.6}Zn_{2.2}Zr_{0.2}$ (at.%)].

Prior to electrochemical testing, x-ray diffraction (XRD) was performed to verify the amorphous structure of all of the BMG samples (Philips X'pert X-Ray Diffractometer), within the resolution limits of XRD. Electrochemical cyclic-anodic-polarization tests were conducted using an EG&G Princeton Applied Research 263A potentiostat with EG&G Powercorr software (Princeton Applied Research, Oak Ridge, TN). The electrochemical cell consisted of the corrosion sample, a saturated calomel reference electrode, and a platinum counter electrode. Thus, all potentials cited in this study will henceforth be in reference to the saturated calomel electrode (SCE). Finally, a Luggin capillary was used to bridge between the SCE and the corrosion sample to minimize the effect of the solution resistance.

Electrochemical characterization was performed in three different electrolytes. First, a naturally aerated 0.6 M (3.5 wt.%) NaCl electrolyte at room temperature (~ 22ºC) was selected because this is an electrolyte commonly found in the literature, which provides for direct comparisons with many other materials. The mean pH (± 95% confidence intervals) of the electrolyte in these tests was 6.97 ± 0.02. When necessary, the pH of the electrolyte was increased to 7.00 by the addition of NaOH. Second, characterization was performed in a phosphate-buffered saline (PBS) electrolyte at 37°C.

The composition of the electrolyte is presented in Table 5. This electrolyte is intended to simulate surgical implant conditions similar to those found *in vivo*. The mean pH (± 95% confidence intervals) of the PBS electrolyte was 7.44 ± 0.02, which is near that found in the human body (7.0 - 7.4) [22]. The dissolved-oxygen content of this electrolyte was reduced to a physiologically-relevant value of 3.3 x 10^{-2} mol/m^3 by aerating the electrolyte with a 4% O_2/N_2 gas mixture for one hour prior to testing at a flow rate of 50 mL/min, according to the procedure developed by Hiromoto et al. [79]. Aeration was continued at this rate throughout the corrosion tests to maintain the reduced oxygen content. In addition, a series of tests were also conducted in the 0.6 M NaCl electrolyte at 37°C and in the PBS electrolyte at 22°C. These tests allowed the influence of electrolyte temperature and chloride ion content on the electrochemical behavior to be defined. Finally, the Ca-based BMGs and ZK60 alloy were tested in a naturally aerated, 0.05 M solution of sodium sulfate (Na_2SO_4) in distilled, de-ionized water at room temperature (~ 22ºC).

Immediately prior to electrochemical testing, each sample was ground to a 600 grit SiC surface finish (arithmetic average roughness = $R_a \approx 0.163$ μm). A polymer sample holder was used to repeatedly expose 30 mm^2 of each sample to the electrolyte during testing. Before each polarization scan was initiated, the corrosion sample was allowed to stabilize in the electrolyte until the open-circuit potential (E_{oc}) changed by no more than 2 mV over a five-minute time period. The E_{oc} at which this occurred was determined to be the open-circuit corrosion potential (E_{corr}). The scan was started at 20 mV below E_{corr} and continued in the positive direction at a scan rate of 0.17 mV/s until a corrosion current density (i) of 10^4 mA/m^2 was reached. At this point, the scan direction

was reversed and the potential was decreased at the same rate until a potential 50 mV below E_{corr} was reached.

Following electrochemical testing, multiple corrosion-related parameters were derived from the cyclic-anodic-polarization curves as previously delineated in the literature [21]. The controlled specimen potential can be regarded as the "driving force" for corrosion, and the anodic current density is directly related to the specimen corrosion rate. The potential at which the current density suddenly increased, signifying pit initiation, was determined to be the breakdown or pitting potential (E_{pit}), as demonstrated in Figure 13. Depending upon the shape of the polarization curve (Figure 13), the protection potential (E_{pp}) was considered to be either: (a) the potential at which the down-scan crossed the up-scan portion of the curve in the passive region, labeled as $E_{pp}(A)$, or (b) the potential at which the cyclic-polarization curve demonstrated a horizontal, plateau region on the potential down-scan, followed by a pronounced down-turn into a new anodic curve, labeled as $E_{pp}(B)$. The former criterion is the traditional method used to define E_{pp} and was sufficient on a majority of the tests. However, several of the tests did not exhibit this type of behavior and a secondary criterion was necessary. In these tests, the down-scan never crossed the up-scan, or crossed at an artificially low potential (Figure 13)**,** because the anodic curve and open-circuit corrosion current density (i_{corr}) shifted to higher potentials and current densities, respectively, on the down-scan (after pitting). Just as the sudden increase in the current density during the up-scan typically signifies localized corrosion due to a breakdown in the passive film, a sudden decrease in the current density during the down-scan should typically signify repassivation of the pits. Despite the difference in the appearance between the two types

of cyclic-anodic-polarization curves, these criteria proved to be approximately equivalent because all of the tests demonstrated consistent values for this plateau region with little variance, independent of whether the down-scan actually crossed the up-scan or not.

In terms of the overall resistance to localized (pitting) corrosion, two parameters are important: (a) the pitting overpotential (η_{pit}), or ($E_{pit} - E_{corr}$), and (b) the protection overpotential (η_{pp}), or ($E_{pp} - E_{corr}$). Higher, positive values of these quantities are desirable [144]. A high η_{pit} signifies an increased resistance to pitting, and a high η_{pp} signifies a high probability of repassivation if damage to the passive film should occur (e.g., scratches, mechanical damage due to stress, etc.).

The corrosion penetration rate (CPR) is an estimate of the uniform corrosion rate of a material at E_{corr} and can also be derived from cyclic-anodic-polarization tests. The CPR is dependent upon inherent material and electrolyte properties and can be determined from the open-circuit corrosion current density (i_{corr}) by the application of Faraday's Law [70]. In this study, i_{corr} and the polarization resistance (R_p) were calculated by the Stern-Geary, or polarization-resistance, method [145]. However, i_{corr} is the sum of three components:

$$i_{corr} = i_{far} + i_{cap} + i_g \quad (5)$$

where i_{far}, the faradaic current density, is the actual current density associated with the flux of metal cations released into the electrolyte (i.e., the true parameter of interest); i_{cap}, the capacitive current density, is due to the capacitance of the metal / oxide / electrolyte interfaces; and i_g is the component of the current density associated with the growth of the oxide film [125, 146]. It can reasonably be assumed that the passive film was relatively stable at E_{corr}, and that i_g was small because of the aforementioned criterion for

allowing the sample to come to a steady-state in the electrolyte prior to cyclic-anodic polarization [146]. Furthermore, i_{cap} is proportional to the potential scan rate [147], which was a low 0.17 mV/s in this study; therefore, this variable is assumed to be small. Nevertheless, Equation 5 demonstrates that the use of i_{corr}, instead of i_{far}, in the calculation of the CPR results in a conservative estimate of the corrosion rate. Finally, it is important to note that all of these values derived from electrochemical characterization can be dependent upon the potential scan rate and other test variables.

The i_{corr} and, similarly, the CPR values are particularly important because they are related to the biocompatibility and cytotoxicity of a biomaterial. Sziraki et al. [148] and Chen et al. [149] have demonstrated that ion concentrations in solution were consistent with corrosion rates calculated by linear polarization and electrochemical impedance spectroscopy (EIS). Bumgardner et al. reported that low corrosion rates were well correlated with low amounts of corrosion products released in cell-culture experiments [150]. Several other studies have noted this trend [151-153]. Moreover, Wataha et al. determined that, in general, materials that introduce more ions into solution exhibit greater cytotoxicity [153]. However, cytotoxicity is also dependent upon other complicating factors, such as the preferential corrosion of particular elements or phases, the potency of each alloy element, the time of exposure, the concentrations of each element in the material, and the probability of synergistic or antagonistic effects of combinations of elements, among others [128, 153].

All statistical analyses were conducted with JMP 5.1.1 software (SAS Institute Inc., Cary, NC). Initially, the data for each of the derived corrosion parameters was evaluated to determine if the parametric assumptions of residual normality and equality

of variances were met. These assumptions were verified through the Shapiro-Wilk [154] and Levene's tests [155], respectively. When these parametric assumptions were met, analysis of variance (ANOVA) and Tukey's post-hoc tests were utilized at a 0.05 level of significance (α) to determine which pairs of materials were statistically different. When necessary, the Box-Cox transformation was used to improve the compliance with the parametric assumptions among the test results within materials [156]. However, for some of the derived corrosion parameters, the parametric assumption of equal variance within a given material was not met even after using the Box-Cox transformation. In this case, the Welch ANOVA test [157], which does not assume equality of variances, was used, followed by Tukey's post-hoc tests. Furthermore, there were multiple cases where neither of the parametric assumptions was met even after the Box-Cox transformation. When the transformed data did not conform to either of these assumptions, the nonparametric Kruskal-Wallis test [158], followed by pairwise comparisons, was used for the untransformed data to determine which pairs of materials were statistically different ($\alpha = 0.05$).

Ninety-five percent confidence intervals (95% CIs) were calculated for all of the means presented in this study based on the Student's t-distribution. Finally, box-and-whisker plots were constructed with Origin 7.5 software (OriginLab Corporation, Northampton, MA), which uses Tukey's hinges[159] in place of quartiles. For each material, the partitioned data is plotted on the left, and the box-and-whisker plot is plotted on the right. The whiskers represent the lower- and upper-inner fences. Data points that lie outside of these fences are considered outliers and are denoted by asterisks.

3.2. Corrosion-Fatigue Behavior of the Vitreloy 105 BMG

Vit 105 BMG ingots were fabricated as previously delineated. Radiographs were made of the ingots to identify the location of any porosity and to minimize the amount of porosity in the testing sections of the bend specimens. Two rectangular bend specimens were machined from each ingot with nominal cross-sections of 3.5 x 3.5 mm and lengths of 30 mm. Each side of these samples was polished to a 1200 SiC grit surface finish ($R_a \approx 0.163$ μm) parallel to the longitudinal axis of the specimens using a polishing fixture (South Bay Technologies, San Clemente, CA) to keep the sides parallel and perpendicular.

Cyclic, constant-amplitude, four-point bend testing was conducted at room temperature (~22°C) in air. Sinusoidal, force-controlled tests were performed on a Material Test System 810 (MTS Systems Corporation, Eden Prairie, MN) hydraulic load frame at frequencies of 10 Hz with R = 0.1, where R is the ratio of minimum stress to maximum stress. The four-point bend fixture was designed with inner and outer spans of 5 mm and 20 mm, respectively. This geometry was selected based upon the research of Zhai et al. [160]. In their study, finite-element modeling (FEM) of various four-point bend geometries revealed that the assumption of constant stress between the inner span is only accurate for a particular range of fixture and sample geometries. Alumina pins with diameters of 4.78 mm were selected to electrically isolate the sample from the other components for the corrosion-fatigue studies. For consistency, these pins were also used in the tests conducted in air.

The corrosion-fatigue studies were also conducted in the naturally aerated, 0.6 M NaCl electrolyte that was used in the aforementioned electrochemical studies. After

polishing these samples, pure Ti wires were spot-welded to the ends (outside of the outer load span) of the corrosion-fatigue samples to facilitate electrical contact. Glyptal 1201 insulating enamel (Glyptal, Inc., Chelsea, MA) was applied to the spot-welded portions of the bend samples and the to Ti wires to insulate these areas from the electrolyte.

Similar to the procedure for corrosion testing, the samples were placed in the corrosion-fatigue chamber to allow them to come to a steady-state in the electrolyte prior to initiating the cyclic loading. Cyclic loading was started after the open-circuit potential changed by less than 2 mV in a five-minute time period. During a majority of the corrosion-fatigue tests at various stress ranges, the open-circuit potential was recorded as a function of time. This was achieved with an EG&G Princeton Applied Research 263A potentiostat with EG&G Powercorr software (Princeton Applied Research, Oak Ridge, TN). The electrochemical cell consisted of the bend sample (working electrode), a saturated calomel reference electrode, and two platinum counter electrodes, one on each side of the bend samples. A Luggin capillary was used to bridge between the SCE and the bend sample to minimize the effect of the solution resistance.

Three cyclic-anodic-polarization tests were conducted during cyclic loading at stress ranges of 900 MPa to determine the effect of cyclic stresses on the electrochemical behavior of the Vit 105 BMG alloy. These corrosion-fatigue polarization scans were conducted at potential scan rates of 0.5 mV/s instead of the 0.17 mV/s rates that were used during the static electrochemical studies, due to the limited test time available prior to fatigue failure and the transient nature of E_{corr} during cyclic loading. The effect of this increased potential scan rate is well known and typically leads to features on the

polarization curve being skewed toward more noble potentials [70]. However, the increased scan rate used in this study is still relatively low.

Once the polarization curve was defined, additional tests were performed at the same stress range with imposed cathodic [E = -900 mV (SCE)] and anodic potentials [E = -100 mV (SCE)] to define the corrosion-fatigue degradation mechanism. In both cases, the corrosion current was recorded as a function of time. Finally, all of the samples tested in both environments were examined by SEM after testing.

3.3. Tensile Testing of the Vitreloy 105 BMG

Again, Vit 105 BMG ingots were fabricated as previously delineated. Each Vit 105 ingot was cut by electrical discharge machining (EDM) into four rectangular tensile samples with gage lengths of 9.5 mm, gage widths of 2 mm, and gage thicknesses of 0.5 mm. Ten tensile specimens were tested according to the American Society for Testing and Materials (ASTM) standard E8 [161]. The front and back surfaces of each specimen were polished to a 1200 SiC grit ($R_a \approx 0.163$ μm) finish parallel to the loading direction. In the first round of testing, only the front and back faces of the samples were polished. The edges of each specimen were not polished and were tested with the as-cut EDM surface. These specimens will be referred to as “unpolished edge” specimens for the remainder of the paper. Subsequent rounds of testing were conducted on samples that had all surfaces, including edges, polished to the same 1200 SiC grit surface finish. These specimens will be referred to as “polished edge” specimens for the remainder of the paper.

Prior to mechanical testing, XRD was performed to verify that each tensile specimen was amorphous, within the resolution limits of XRD. The tensile tests were performed in air on a Material Test System 810 (MTS Systems Corporation, Eden Prairie, MN) hydraulic load frame in a load-control mode with loading rates of 147 N/s and 45 N/s. These loading rates corresponded to approximate strain rates of 1×10^{-2} s^{-1} and 1×10^{-3} s^{-1}, respectively. The displacements and strain rates were estimated through the servo-hydraulic ram-displacement transducer. Prior to testing, the load frame was aligned to within 15 μm / m to minimize misalignment and bending moments within the samples.

In situ thermography was performed using an Indigo Phoenix infrared (IR) camera (Indigo Systems Corporation, Goleta, CA) with a 320 × 256 pixel focal plane array InSb detector, which has a spectral range of 1.5 – 5.0 μm. The temperature sensitivity is 0.015°C at 23°C. During mechanical testing, IR images were acquired at rates of 725 Hz. These settings correspond to an image resolution of approximately 5200 μm^2 / pixel. A thin, sub-micron graphite coating was applied to the specimen gage section to reduce IR reflections. A temperature calibration was performed before testing by acquiring IR images at various sample temperatures, as measured by a thermocouple, and performing regression analysis to yield a temperature-calibration curve. After tensile testing, the samples were examined by optical and scanning electron microscopy (SEM). Images recorded by the IR camera were analyzed in detail to estimate the properties, kinetics, and temperatures associated with shear banding and fracture in the BMG. All statistical analyses were conducted with JMP 5.1.1 software (SAS Institute Inc., Cary,

NC). All confidence intervals (CIs) were calculated by the Student's t-distribution at a 0.05 level of significance (α).

4. RESULTS AND DISCUSSION

4.1. Electrochemical Behavior of Ca-based Bulk Metallic Glasses

X-ray diffraction patterns of the $Ca_{65}Mg_{15}Zn_{20}$, $Ca_{50}Mg_{20}Cu_{30}$, and $Ca_{55}Mg_{18}Zn_{11}Cu_{16}$ alloys are presented in Figure 14. Each pattern shows a broad diffraction peak (halo) indicating that the samples are fully amorphous, within the resolution limits. The position and width of the halo depend on the alloy composition, so that the maximums are observed at 2θ = 30.3°, 31.5°, and 32.6°, and the full-widths-at-half-maximum (FWHM) of the halos are estimated to be 4.9°, 6.4°, and 8.2° for the Ca-Mg-Zn, Ca-Mg-Zn-Cu, and Ca-Mg-Cu alloys, respectively. The shift of the halo peak indicates that the average radius of the first coordination shell decreases from ~ 0.296 nm for Ca-Mg-Zn to ~ 0.275 nm for Ca-Mg-Cu, while an increase in the halo width reflects wider distribution of distances between the nearest atoms with an increase in the amount of Cu [162]. Such behavior can be explained by the smaller size of Cu atoms relative to Zn and Mg atoms.

DSC thermograms obtained from the cast plates during continuous heating at a rate of 20 K/min are shown in Figure 15. An endothermic reaction, corresponding to the transition from a glassy state into a super-cooled liquid state, and the following exothermic reactions corresponding to crystallization are clearly seen. These parameters are labeled as the glass transition, T_g, and crystallization, T_x, temperatures, respectively. At higher temperatures, an endothermic reaction is detected due to melting. The characteristic temperatures, as well as heats of crystallization and fusion, are given in Table 1. The Ca-Mg-Zn alloy had the lowest glass transition (T_g = 364 K) and crystallization (T_x = 400 K) temperatures, and the Ca-Mg-Cu alloy was found to have the

highest glass transition (T_g = 399 K) and crystallization (T_x = 433 K) temperatures, while the Ca-Mg-Zn-Cu alloy exhibited the intermediate values. One may therefore conclude that the stability of the glassy state increases with a decrease in the amount of Zn and an increase in the amount of Cu in the alloys. On the other hand, the quaternary $Ca_{55}Mg_{18}Zn_{11}Cu_{16}$ alloy has the maximum value of the reduced glass transition temperature, T_{rg}, which may indicate that this alloy has the best glass forming ability among the three alloys studied [163].

Four electrochemical cyclic-anodic-polarization tests were conducted for each Ca-based BMG and the ZK60 alloy at room temperature in a naturally aerated, 0.05 M solution of sodium sulfate (Na_2SO_4) in distilled, de-ionized water. Sodium sulfate was added to improve the electrical conductivity of the electrolyte without affecting the electrochemical behavior of the material. The mean pH (± standard deviation) of the electrolyte for all tests was 6.96 ± 0.06. When necessary, the pH was adjusted to 7.00 ± 0.10 by the addition of NaOH prior to testing.

The average cyclic-anodic-polarization curves for each of the Ca-based BMG alloys and the ZK60 alloy are plotted in Figure 16. The average curve for the $Ca_{65}Mg_{15}Zn_{20}$ (at.%) demonstrates that this material was within the active region at E_{corr} with high open-circuit corrosion current densities. The mean (± 95% CIs) and median CPRs for this material were 5691 ± 1046 and 5849 μm/year, respectively (Figure 17). Furthermore, the $Ca_{55}Mg_{18}Zn_{11}Cu_{16}$ (at.%) alloy exhibited slight passivity at E_{corr} with high open-circuit corrosion current densities and mean (± 95% CIs) and median CPRs of 311 ± 184 and 299 μm/year, respectively (Figure 17). The $Ca_{50}Mg_{20}Cu_{30}$ (at.%) alloy

was passive at E_{corr} with high open-circuit corrosion current densities. The mean (± 95% CIs) and median CPRs for this material were 1503 ± 435 and 1515 μm/year, respectively (Figure 17). Finally, the ZK60 Mg-based alloy was also active at E_{corr} with high open-circuit corrosion current densities. The mean (± 95% CIs) and median CPRs for this material were 425 ± 321 and 454 μm/year, respectively (Figure 17).

The CPR for the $Ca_{65}Mg_{15}Zn_{20}$ BMG alloy was found to be greater than those of the $Ca_{55}Mg_{18}Zn_{11}Cu_{16}$ BMG and ZK60 alloys by a statistically significant difference. In both cases, the differences were greater than an order of magnitude. In fact, subsequent post-test analysis in the SEM revealed that active pitting occurred in this material at E_{corr}. Since CPR is an approximation that is only valid for uniform corrosion, it is likely that this CPR is a severe underestimate of the actual material being lost in this alloy.

On the other hand, the CPRs for the $Ca_{50}Mg_{20}Cu_{30}$, $Ca_{55}Mg_{18}Zn_{11}Cu_{16}$, and ZK60 alloys were considered to be equivalent, at the tested levels. As might be expected, all of these materials exhibited high chemical reactivity with highly negative E_{corr} values (Figure 18). However, upon immersion of the samples in the electrolyte, the open-circuit potentials gradually became more noble until E_{corr} was attained.

Both the $Ca_{55}Mg_{18}Zn_{11}Cu_{16}$ and $Ca_{65}Mg_{15}Zn_{20}$ alloys were found to be susceptible to localized corrosion in the form of pitting. The $Ca_{55}Mg_{18}Zn_{11}Cu_{16}$ alloy exhibited a brief passive region before E_{pit} with mean (± 95% CIs) and median η_{pit} values (Figure 19) of 128 ± 41 and 120 mV, respectively. Once pitting initiated on the surface of this alloy, repassivation did not occur until the potential was decreased well below E_{corr}. As a result, the mean (± 95% CIs) and median η_{pp} values were calculated to be -457 ± 329 and -440

mV, respectively (Figure 19). Thus, it can be assumed that localized corrosion would occur in this alloy, immersed in this electrolyte, after an incubation period or damage to the passive film. On the other hand, the $Ca_{65}Mg_{15}Zn_{20}$ BMG exhibited active localized corrosion at E_{corr}; therefore, η_{pit} and η_{pp} values could not be determined for this material. Neither the $Ca_{50}Mg_{20}Cu_{30}$ BMG nor the ZK60 alloy experienced localized corrosion. All of the derived corrosion parameters, with 95% CIs, are presented in Table 6.

Post-test SEM analyses revealed that all of the Ca-based BMG alloys demonstrated cracked surface layers within the region exposed to the electrolyte (Figure 20). Pitting in the $Ca_{65}Mg_{15}Zn_{20}$ alloy, in particular, appeared to initiate at small particles within the amorphous matrix [Figure 20(a)]. This pit morphology is similar to those observed in other BMGs [164, 165]. Furthermore, the $Ca_{55}Mg_{18}Zn_{11}Cu_{16}$ material appeared to have small holes or pockmarks within the pits [Figure 20(b)]. It is suggested that these features also could be due to small particles within the amorphous matrix. This theory seems to be supported by the current fluctuations in all of the polarization curves for this material. Instabilities in the polarization curve at elevated potentials are commonly associated with the initiation and propagation of pits at small inclusions, followed by repassivation after the particle is dissolved. Finally, the ZK60 alloy (Figure 21) did not exhibit any evidence of localized corrosion upon SEM analysis.

For comparison with other amorphous materials, several of the derived corrosion parameters from this study are presented with data from the literature in Table 7. Peter et al. studied the electrochemical behavior of the Vit 105 BMG alloy [$Zr_{52.5}Cu_{17.9}Ni_{14.6}Al_{10}Ti_5$ (at.%)] in the same 0.05 M Na_2SO_4 electrolyte and reported a low CPR of 0.4 μm/year [21]. On the other hand, Szewieczek and Baron conducted

electrochemical characterization of an Fe-based BMG in a 0.5 M Na_2SO_4 electrolyte and reported a CPR of 927 μm/year, comparable to the $Ca_{55}Mg_{18}Zn_{11}Cu_{16}$ and $Ca_{50}Mg_{20}Cu_{30}$ alloys [166].

Unfortunately, most of the electrochemical studies from the literature do not report i_{corr} or CPR values. However, it is often possible to estimate these values based upon the data that is reported. Raju et al. conducted cyclic-anodic polarization tests on various compositions of the Zr-Cu-Al-Ni, Zr-Cu-Al-Ni-Ti, and Zr-Cu-Al-Ni-Nb BMG alloys in a 0.1 M Na_2SO_4 electrolyte [74]. Based upon the i_{corr} values estimated from their polarization curves, it appears that the CPRs are on the order of 1 μm / year or less. These alloys did not seem to be susceptible to localized corrosion in that electrolyte. Furthermore, Baril and Pebere investigated the electrochemical behavior of pure Mg in 0.1 M and 0.01 M Na_2SO_4 electrolytes [167]. The estimated CPRs in both electrolytes appear to be on the order of 1000 μm / year. Based upon all of these comparisons, it seems that the $Ca_{55}Mg_{18}Zn_{11}Cu_{16}$ and $Ca_{50}Mg_{20}Cu_{30}$ alloys are comparable to some Fe-based BMGs and Mg-based crystalline alloys. On the contrary, all three of these Ca-based BMGs are not as corrosion resistant as the Zr-based BMG alloys.

In this study, the electrochemical behavior of three Ca-based BMGs has been examined and compared to a crystalline, Mg-based alloy, as well as other amorphous and crystalline materials reported in the literature. Based upon cyclic-anodic-polarization tests in a 0.05 M Na_2SO_4 electrolyte and these comparisons, the following conclusions were drawn. The $Ca_{65}Mg_{15}Zn_{20}$ alloy was active at the open-circuit potentials with the highest mean corrosion penetration rate of 5691 μm/year. Both the $Ca_{50}Mg_{20}Cu_{30}$ and

$Ca_{55}Mg_{18}Zn_{11}Cu_{16}$ BMG alloys demonstrated slight passivity at the open-circuit potentials with lower mean CPRs of 1503 and 311 μm/year, respectively. These CPRs were found to be statistically equivalent to that of the Mg-based, crystalline alloy (ZK60), at the tested levels. In addition, the $Ca_{65}Mg_{15}Zn_{20}$ and $Ca_{55}Mg_{18}Zn_{11}Cu_{16}$ alloys were found to be susceptible to localized corrosion in the form of pitting. While the former alloy underwent active pitting at E_{corr}, the latter alloy exhibited low, positive η_{pit} values and high, negative η_{pp} values. Thus, it can be assumed that localized corrosion would occur in this alloy, immersed in this electrolyte, after an incubation period or damage to the passive film. Post-test SEM analysis seemed to indicate that pitting was associated with small particles within the amorphous matrix. Based upon comparisons with studies from the literature, it seems that the $Ca_{55}Mg_{18}Zn_{11}Cu_{16}$ and $Ca_{50}Mg_{20}Cu_{30}$ alloys are comparable to some Fe-based BMGs and Mg-based crystalline alloys, while all three of these Ca-based BMGs are not as corrosion resistant as the Zr-based BMG alloys.

4.2. Electrochemical Characterization of Vitreloy 1 in 0.6 M NaCl and PBS Electrolytes

This section is a portion of a manuscript that was published in the journal *Intermetallics* in 2004 by Mark L. Morrison, Raymond A. Buchanan, Atakan Peker, William H. Peter, Joe A. Horton, and Peter K. Liaw:

Morrison ML, Buchanan RA, Peker A, Peter WH, Horton JA, Liaw PK. Cyclic-anodic polarization studies of a Zr-41.2, Ti-13.8, Ni-10, Cu-12.5, Be-22.5 bulk metallic glass, *Intermetallics*, 2004; 12(10-11):1177-1181.

My primary contributions to this paper were all of the experimental work and the writing of the manuscript. These excerpts have been reprinted from [24] with permission from Elsevier.

A series of five tests each was conducted on the Zr-based Vit 1 BMG in an aerated 0.6 M NaCl electrolyte at both room temperature (approximately 22°C) and at 37°C. In addition, a series of five tests was performed in a phosphate-buffered saline (PBS) electrolyte at 22°C. Finally, a series of four tests was conducted in the PBS electrolyte at 37°C.

A representative XRD spectrum from the corrosion samples is presented in Figure 22. As expected, each spectrum demonstrated a broad, diffuse peak characteristic of amorphous alloys. The average cyclic-anodic-polarization curves for both electrolytes at 22ºC and 37ºC are shown in Figure 23. The corrosion parameters derived from the polarization tests for both electrolytes are presented in Figure 24. Furthermore, several of the relevant corrosion parameters from this study and other reports in the literature are presented in Table 7 for comparison. However, it should be noted that comparisons between these results and others are dependent upon differing surface conditions, potential scan rates and other test parameters.

For the 0.6 M NaCl electrolyte at both temperatures, the alloy demonstrated passive behavior at the open-circuit potentials with low corrosion rates. The values of i_{corr} and CPR were determined to be 3.1±2.5 mA/m^2 and 2.8±1.5 μm/year, respectively, at 22°C; and 1.2±1.3 mA/m^2 and 1.3±1.3 μm/year, respectively, at 37°C. These values are relatively low and within the expected range for passive behavior. For comparison, Chieh et al. conducted polarization tests on the $Zr_{52.5}Cu_{17.9}Ni_{14.6}Al_{10}Ti_5$ (at.%) (Vitreloy 105) BMG and 304 stainless steel (304 SS) in a 0.6 M NaCl electrolyte at room temperature [168]. They reported corrosion penetration rates for the BMG and 304 SS of

1.47 μm/year and 1.17 μm/year, respectively. Moreover, Peter et al. found a CPR of 1.3±0.7 μm/year for the Vitreloy 105 BMG in a 0.6 M NaCl electrolyte at room temperature [21].

The Vit 1 BMG showed susceptibility to pitting corrosion at elevated potentials in the 0.6 M NaCl electrolyte at both temperatures. The mean η_{pit} values were 98±53 mV and 142±56 mV at 22°C and 37°C, respectively. These values are lower than those reported for the Vitreloy 105 BMG by Peter et al. [21] in a 0.6 M NaCl electrolyte (approximately 300 mV) and He et al. [73] in a 0.5 M NaCl electrolyte (225 mV). Schroeder et al. reported a difference of 207 mV for the Vit 1 alloy in a 0.5 M NaCl electrolyte [71]. Finally, Chieh et al. found η_{pit} values of 360 mV and 490 mV for Vitreloy 105 BMG and 304 SS, respectively, in a 0.6 M NaCl electrolyte [168]. All of these comparative studies were conducted at room temperature.

The mean η_{pp} values were determined to be 28±33 mV and 68±55 mV at temperatures of 22°C and 37°C, respectively. These relatively low differences between the protection potentials and the open-circuit corrosion potentials indicate that localized corrosion due to surface damage or after incubation times could be a concern if the local or bulk environment became more aggressive. This parameter calculated from the 22°C tests is comparable to the difference of approximately 20 mV between E_{pp} and E_{corr} reported by Peter et al. for the Vitreloy 105 alloy [21]. Comparisons between other reports in the literature are not possible because most of those studies did not reverse the potential scan direction to evaluate repassivation kinetics.

For the PBS electrolyte, the alloy demonstrated passive behavior at the open-circuit potential with low corrosion rates at both of the temperatures evaluated in this study. In fact, the mean corrosion rates were lower than those found in the 0.6 M NaCl electrolyte. The mean values of i_{corr} and CPR were determined to be 0.7±0.5 mA/m^2 and 0.8±0.6 μm/year, respectively, at 22°C; and 0.9±0.4 mA/m^2 and 1.0±0.5 μm/year, respectively, at 37°C. Again, the alloy exhibited a susceptibility to pitting corrosion at elevated potentials in both electrolytes at both temperatures. The mean η_{pit} values were calculated to be 478±268 mV at 22°C and 410±154 mV at 37°C. These differences were less than the differences reported by Hiromoto et al. for a $Zr_{65}Al_{7.5}Ni_{10}Cu_{17.5}$ BMG (approximately 1025 mV) [22] and a $Zr_{65}Al_{7.5}Cu_{27.5}$ BMG (approximately 880 mV) [79] tested under the same conditions. The mean η_{pp} values were 215±53 mV at 22°C and 184±70 mV at 37°C. These large differences indicate that localized corrosion due to surface damage or after incubation times is not as great of a concern in this electrolyte, as compared to the 0.6 M NaCl electrolyte.

For the 0.6 M NaCl electrolyte, the increase in temperature resulted in a statistically significant decrease in the CPR. However, in the PBS electrolyte, the CPR increased by a statistically significant amount with an increase in temperature. Besides CPR, the only significant changes in corrosion parameters observed upon an increase in test temperature were a slight decrease in E_{pp} in both electrolytes and a slight decrease in E_{corr} and E_{pit} in the NaCl electrolyte. Finally, at both temperatures, statistical analyses revealed that the Vit 1 BMG exhibited comparable or improved values for every parameter in the PBS electrolyte as compared to the NaCl electrolyte. This increased

resistance to corrosion in the PBS electrolyte is consistent with other studies that have demonstrated that pitting resistance increases with decreasing chloride ion (Cl^-) concentration [22].

Although thorough post-test, microstructural analysis has not yet been performed, it is believed that the variability in the corrosion parameters is due to inhomogeneities in the materials. These inhomogeneities within the material could result in localized imperfections in the passive film and lead to the localized corrosion observed in this study. However, it is currently not clearly understood if these inhomogeneities are due to local chemical ordering of the alloy or contaminant features in the material such as oxide/amorphous-matrix interfaces. Furthermore, the variability encountered in this study is not readily comparable to other studies in the literature because most of these studies do not report variability or discuss statistical analyses of the data.

Based upon the results of this investigation, the following conclusions were drawn. In an aerated 0.6 M NaCl electrolyte at both 22°C and 37°C, the $Zr_{41.2}Ti_{13.8}Ni_{10}Cu_{12.5}Be_{22.5}$ (at.%) (Vit 1) BMG exhibits passive behavior at the natural corrosion potentials and low mean corrosion penetration rates of 2.5 μm/year and 1.3 μm/year, respectively. Furthermore, this BMG exhibits passive behavior at the natural corrosion potentials and low mean corrosion penetration rates of 0.7 μm/year and 1.0 μm/year, respectively, in a deaerated phosphate-buffered saline (PBS) electrolyte with a physiologically-relevant oxygen content at both 22°C and 37˚C. Susceptibilities to pitting corrosion were seen in both electrolytes at both temperatures, with lower susceptibilities being observed for the PBS electrolyte. The Vit 1 alloy appears to be

more susceptible to pitting corrosion in both electrolytes than other alloys reported in the literature. For both electrolytes, the change in temperature did not result in a statistically significant change in the corrosion penetration rate and only caused small changes in several other parameters. At both temperatures, statistical analyses revealed that this BMG exhibited comparable or improved values for every corrosion parameter in the PBS electrolyte as compared to the NaCl electrolyte. Although pitting corrosion might be a concern for this alloy depending upon the local and bulk environments, the protection potential was found to be greater than the open-circuit potential in all of the tested conditions. Thus, the probability of pitting corrosion occurring due to surface irregularities or passive film damage is decreased.

4.3. Electrochemical Characterization of a Ti-based BMG in a PBS Electrolyte

Electrochemical characterization of the LM-010 BMG alloy was performed in a phosphate-buffered saline (PBS) electrolyte at 37°C, in which one test was conducted per sample for a total of 20 corrosion tests. A representative XRD spectrum from the LM-010 corrosion samples is shown in Figure 25. Each spectrum demonstrated a broad, diffuse peak characteristic of amorphous alloys. The average cyclic-anodic-polarization curve is plotted in Figure 26. This average curve demonstrates that the material was passive at E_{corr} and exhibited a low i_{corr} in the passive region. The mean (± 95% CIs) and median CPRs were calculated to be 2.9 ± 2.6 and 0.8 μm/year, respectively (Figure 27). These values are relatively low and within the expected range for passive behavior. However, the mean CPR was unexpectedly elevated due to one data point that was determined to be an outlier. In this case, the median, which is more resistant to outlier

effects, is a better measure of the CPR. With this outlier removed, the mean (± 95% CIs) and median CPRs were calculated to be 1.8 ± 1.2 and 0.8 μm/year, respectively. For a comparison to other corrosion-resistant materials in the same, or similar, electrolytes, these corrosion parameters and those reported in the literature are summarized in Table 7. Since the corrosion resistance of Ti-based BMGs has not been previously evaluated, this material was compared to Zr-based BMGs and other corrosion-resistant, crystalline materials. Furthermore, the original corrosion data was available for the Vit 1 BMG [24], Vit 105 BMG, 316L stainless steel (316L SS), CoCrMo, and Ti-6Al-4V materials tested in the same environment [169]. Therefore, a direct statistical comparison with this data was possible. These mean CPRs are also plotted with 95% CIs in Figure 27 for comparison. The differences between CPRs for all of these materials were found to be statistically insignificant at the tested levels. In addition, the E_{corr} values are presented in Figure 28 for comparison.

The LM-010 alloy exhibited a susceptibility to localized corrosion at elevated potentials with mean (± 95% CIs) and median E_{pit} values of 217 ± 17 and 206 mV (SCE), respectively (Figure 29). Based upon these values, the mean (± 95% CIs) and median η_{pit} values were calculated to be 589 ± 57 and 550 mV, respectively (Figure 30). Furthermore, the mean (± 95% CIs) and median E_{pp} values were determined to be 38 ± 32 and 70 mV (SCE), respectively (Figure 31). Therefore, the mean (± 95% CIs) and median η_{pp} values were 411 ± 70 and 366 mV, respectively (Figure 32). It should be noted that both η_{pit} and η_{pp} are relatively high, positive values; therefore, localized corrosion is not a concern at the open-circuit potential with this alloy in this environment.

Comparing these values once again to those reported in the literature for which direct statistical comparisons were possible (Table 7), the mean LM-010 η_{pit} value was significantly different from the mean η_{pit} reported for the Vit 105 BMG ($p = 0.0306$) [169]. This statistically significant difference represents a 24.3% increase in the mean η_{pit} value as compared to the Vit 105 BMG. All other differences between η_{pit} values were found to be statistically insignificant at the levels tested. The mean LM-010 η_{pp} value was also found to be significantly different from the mean values reported for the Vit 1 [24], 316L SS and Vit 105 alloys ($p \leq 0.0001$) [169]. These differences represent statistically significant increases of 123.4%, 179.6%, and 82.7% in the mean η_{pp} values, as compared to the Vit 1, 316L SS, and Vit 105 BMG, respectively. Both the CoCrMo and Ti6Al-4V materials were reportedly not susceptible to localized corrosion in the tested environment; therefore, η_{pit} and η_{pp} values could not be determined for these materials [169].

In addition, approximate comparisons can be made between these derived corrosion parameters and those reported in the literature for the same, or similar, electrolytes (Table 7). In a majority of the cases, the parameters from other reports in the literature were estimated based upon analyses of the polarization curves. Again, it should be noted that comparisons between these results and those conducted in other laboratories should be made with the knowledge that they are dependent upon differing test parameters. Nevertheless, it appears that the CPR for the LM-010 BMG alloy is comparable to these other materials, keeping in mind that the mean CPR was artificially elevated due to an outlier. In terms of the localized corrosion resistance, the LM-010

BMG was equivalent, or superior, to all of the BMGs. All of the studies by Hiromoto et al. in this same deaerated PBS electrolyte were conducted with melt-spun metallic glasses and are, therefore, not directly comparable [22, 77-79, 170]. Moreover, it is difficult to make comparisons with the reports by Hiromoto et al. on the corrosion resistance of the $Zr_{65}Al_{7.5}Ni_{10}Cu_{17.5}$ (at.%) in Hanks' solution, Eagle's mimimum essential medium (MEM), and MEM with fetal bovine serum (MEM + FBS). The Hanks' solution is the closest to PBS as they have the same chloride ion contents. Also, the MEM electrolyte contains amino acids while the MEM + FBS electrolyte contains both amino acids and proteins. In addition, both the MEM and MEM+ FBS electrolytes contain lower chloride ion concentrations than the PBS and Hanks' solution. The susceptibility to localized corrosion of BMGs has been shown to increase with increasing chloride-ion content [78]. On the other hand, the corrosion rates of various materials have been reported to increase, decrease or be unaffected by the presence of amino acids and proteins [144, 171]. Nevertheless, it would appear that the LM-010 BMG alloy is comparable to the $Zr_{65}Al_{7.5}Ni_{10}Cu_{17.5}$ (at.%) BMG alloy in terms of both the CPR and the resistance to localized corrosion.

All of the corrosion samples were examined by stereomicroscopy after corrosion testing. All of the samples exhibited corrosion in the form of localized pitting. With the exception of one sample, crevice corrosion at the sample / sample holder interface was not prevalent. In general, the samples predominantly exhibited many scattered, small pits (diameter $\leq$ 100 μm) in addition to several larger pits. The number of pits on each sample was estimated and subjectively classified into one of the following categories: extra-large (XL), large (L), medium (M), and small (S). A pitting score was calculated

for each sample by assigning values to each pit size (i.e., XL = 4, L = 3, M = 2, and S = 1) and summing the product of the pitting score and the quantity of pits within each category. The minimum, maximum, median, and mean scores were calculated to be 9, 54, 42, and 36, respectively. The pitting scores were not correlated to any other corrosion parameters examined in this study (coefficient of determination = $r^2 \geq 0.35$).

Furthermore, several corrosion samples with both high and low CPRs were selected for SEM analyses. Representative images of the pit morphology are presented in Figure 33. The pit shown in Figure 33(a) is approximately 90 μm in diameter and is typical of the small pits observed on all of the samples. A magnified image inside this pit at location A is shown in Figure 33(b). Multiple concave facets, such as these, from 1 – 10 μm in diameter were observed in many of the pits. BMG alloys are ideally homogeneous materials; therefore, localized corrosion and, particularly, faceted surfaces inside of pits would not be expected. Multiple reports from the literature have attributed the susceptibility of BMGs to localized corrosion to the presence of crystalline inclusions [172-174]. However, no evidence of crystalline inclusions was observed in this study. Thus, the cause of these concave faceted surfaces is currently unknown.

Based upon the results of this investigation, the following conclusions were made about the corrosion resistance of the LM-010 BMG alloy in a PBS electrolyte. The LM-010 BMG alloy exhibited passive behavior at the open-circuit potential with a low corrosion rate. The mean CPR (2.9 $\pm$ 2.6 μm/year) was low and within the expected range for corrosion-resistant materials. In this study, one CPR value was found to be an outlier that resulted in an elevated mean CPR. The median CPR, which is more resistant

to outlier effects, was 0.8 μm/year, with or without the outlier. This mean CPR value was determined to be statistically equivalent to those of other materials reported in the literature, at the tested levels, for which direct statistical comparisons were possible. This BMG exhibited a susceptibility to localized corrosion in the form of pitting. However, both the η_{pit} and η_{pp} were relatively high, positive values; therefore, localized corrosion is not a concern at the open-circuit potential with this alloy in this environment. The resistance of the LM-010 alloy to localized corrosion was statistically equal to, or better than, all of the BMG materials for which direct statistical comparisons were possible. Furthermore, the localized corrosion resistance was statistically equal to, or better than, the 316L SS. The LM-010 BMG alloy appears to be comparable, or superior, to the other BMG alloys from the literature in terms of CPRs and localized corrosion resistance. Microscopic examinations revealed that the samples predominantly exhibited many scattered, small pits (diameter $\leq$ 100 μm) in addition to several larger pits.

4.4. Electrochemical Characterization of Vitreloy 105 in a PBS Electrolyte

This section is a portion of a manuscript that is being published in the *Journal of Biomedical Materials Research A* in 2005 by Mark L. Morrison, Raymond A. Buchanan, Ramon A. Leon, C.T. Liu, Brandice A. Green, Peter K. Liaw, and Joe A. Horton:

Morrison ML, Buchanan RA, Leon RV, Liu CT, Green BA, Liaw PK, Horton JA. The electrochemical evaluation of a Zr-based bulk metallic glass in a phosphate-buffered saline electrolyte, *Journal of Biomedical Materials Research A*, 2005; In press.

My primary contributions to this paper were all of the experimental work and the writing of the manuscript. This excerpt has been reprinted from [169] with permission from John Wiley & Sons.

Five tests were conducted on each of three Vit 105 BMG samples for a total of 15 corrosion tests in the PBS electrolyte. For comparison, several common biomaterials were also selected for testing. These included: (a) four tests on one sample of $Ti_{90}Al_6V_4$ (wt.%) [$Ti_{86.2}Al_{10.2}V_{3.6}$ (at.%), ASTM F136], denoted as Ti-6Al-4V; (b) three tests on one sample of $Co_{63}Cr_{28}Mo_6$ (wt.%) [$Co_{61.4}Cr_{30.9}Mo_{3.6}$ (at.%), ASTM F799], denoted as CoCrMo; and (c) fifteen tests on two samples of AISI 316L stainless steel [$Fe_{62.5}Cr_{19.3}Ni_{13.3}$ (at.%), ASTM F138], denoted as 316L SS.

A representative XRD spectrum from the Vit 105 corrosion samples is shown in Figure 34. As expected, each spectrum demonstrated a broad, diffuse peak characteristic of amorphous alloys. The average cyclic-anodic-polarization curves for each of the materials tested are plotted in Figure 26. These average curves demonstrate that each material was passive at E_{corr} and exhibited low open-circuit corrosion current densities in the passive region. The derived corrosion parameters were compared between all of the materials tested to identify statistically significant differences. The results of these ANOVA and Tukey post-hoc tests are summarized in Table 8. Within each of the derived parameters, materials not connected by the same letter are significantly different at a 0.05 level of significance (α).

The BMG alloy demonstrated passive behavior at the open-circuit potentials with low mean ($\pm$ 95% CIs) and median CPR values of 0.8 ± 0.4 and 0.5 μm/year, respectively (Figure 27). These values are relatively low and within the expected range for passive behavior. For comparison, the mean ($\pm$ 95% CIs) and median CPR values were determined to be 0.3 ± 0.2 and 0.3 μm/year, respectively, for the CoCrMo alloy (Figure

27) and 0.3 ± 0.2 and 0.3 μm/year, respectively, for the Ti-6Al-4V alloy (Figure 27). Furthermore, the mean (± 95% CIs) and median CPR values for the 316L SS were 1.5 ± 0.4 and 1.3 μm/year, respectively (Figure 27). When comparing mean CPR values, the Vit 105, Ti-6Al-4V, and the CoCrMo alloys exhibited 47%, 80%, and 80% reductions in mean corrosion rates, respectively, as compared to the 316L SS ($p < 0.0001$). All other differences in the mean CPR values were found to be statistically insignificant. For comparison, the measured E_{corr} values as also plotted in Figure 28.

The BMG alloy exhibited a susceptibility to localized corrosion at elevated potentials with mean (± 95% CIs) and median E_{pit} values of 69 ± 53 mV (SCE) and 65 mV (SCE), respectively (Figure 29). Furthermore, the mean (± 95% CIs) and median η_{pit} values were determined to be of 474 ± 73 and 534 mV, respectively (Figure 30). The 316L SS also demonstrated a susceptibility to pitting corrosion with mean (± 95% CIs) and median η_{pit} values of 531 ± 75 and 509 mV, respectively (Figure 30). Both the CoCrMo and Ti-6Al-4V alloys were not susceptible to localized corrosion in the tested environment and, therefore, η_{pit} and η_{pp} values could not be determined for these materials. In this study, no statistically significant difference was found for the Vit 105 and 316L SS mean η_{pit} values. For the Vit 105 BMG, the mean (± 95% CIs) and median E_{pp} values were -180 ± 11 and -177 mV, respectively (Figure 31). Thus, the mean (± 95% CIs) and median η_{pp} values were calculated to be 225 ± 38 and 219 mV, respectively, for the Vit 105 alloy and 147 ± 18 and 140 mV, respectively, for the 316L SS (Figure 32). As compared to the 316L SS, this difference represented a statistically significant increase of 53% ($p = 0.0019$) for the Vit 105 alloy.

All of the corrosion samples were examined by stereomicroscopy after corrosion testing. For the Vit 105 BMG samples, every sample exhibited corrosion in the form of localized pitting in a few locations (~1-5) on the samples. The 316L stainless steel samples almost always exhibited localized corrosion in the form of large, connected pits at the edges of the area exposed to the electrolyte. This was likely due to crevice corrosion between the samples and the specimen holder. Therefore, it is expected that this material would exhibit improved localized corrosion resistance in an ideal situation without any crevices. Post-test microscopic examination of the CoCrMo and Ti-6Al-4V samples revealed that there were no pits on the surfaces of any of the tested samples. Therefore, the apparent breakdowns on the polarization curves (Figure 26) are likely associated with uniform passive film dissolution for the CoCrMo and water oxidation for the Ti-6Al-4V.

In addition, several of the relevant corrosion parameters from this study and other reports in the literature (for the same electrolyte) are presented in Table 7 for comparison. However, it should be noted that comparisons between these results and others should be made with the knowledge that they are dependent upon differing surface conditions, potential scan rates and other test parameters. The one exception was the corrosion evaluation of the Vit 1, for which the original data was available for direct statistical comparisons [24]. No statistically significant difference was found between the mean η_{pit} value for the Vit 105 alloy and that reported for the Vit 1 material, which was tested under identical conditions [24]. Furthermore, the mean η_{pit} value for the Vit 105 alloy appears to be lower than those reported for both the $Zr_{65}Al_{7.5}Ni_{10}Cu_{17.5}$ (at.%) [22] and $Zr_{65}Al_{7.5}Cu_{27.5}$ (at.%) [79] alloys. However, both of these materials were fabricated by

melt-spinning with sample thicknesses of 25 – 50 μm and were, thus, not bulk metallic glasses. Finally, all of the corrosion parameters derived in this study for the standard, crystalline biomaterials were within the wide range of results reported in the literature for other *in vitro* studies in physiologically-relevant electrolytes and *in vivo* studies [144, 175-181].

Unfortunately, most studies in the literature do not investigate repassivation kinetics. Therefore, comparisons with other amorphous alloys in the same electrolyte are limited. However, a direct statistical comparison was possible with the Vit 1 alloy. The mean η_{pp} value for the Vit 105 alloy is statistically equivalent to that reported for the Vit 1 BMG alloy [24]. Again, CPRs are typically not reported in the literature. However, the Ti-6Al-4V and CoCrMo alloys both demonstrated 70% decreases in mean CPR as compared to the Vit 1 alloy amorphous alloy ($p < 0.0001$) [24]. The CPR values for the Vit 105 BMG and 316L SS alloys were found to be statistically equivalent to the CPR for the LM-001 alloy.

The 316L stainless steel alloy has been used successfully in biomedical applications for more than 30 years [182]. Today, 316L SS is still utilized primarily for temporary components such as bone plates, bone screws and intramedullary rods [183]. Modern-day, long-term implants are more commonly fabricated from the CoCrMo and Ti-6Al-4V alloys due to their superior corrosion properties. Therefore, it is important to note that the Vit 105 BMG alloy demonstrated better general and localized corrosion resistances, as compared to the 316L SS. Moreover, this study revealed that, in the tested environment, this amorphous alloy showed equivalent CPR values, as compared to both the CoCrMo and Ti-6Al-4V alloys. Moreover, these excellent electrochemical properties

are combined with a low modulus and unparalleled strength. This unique combination of properties dramatically demonstrates the potential for amorphous alloys as a new generation of biomaterials. While these results are encouraging, much more work needs to be done to examine the electrochemical properties of this and other BMG alloy compositions in environments that better replicate the *in vivo* environment.

Based upon the results of this investigation, the following conclusions were drawn. All of the tested materials exhibited passive behavior at the open-circuit potentials with low corrosion rates in the phosphate-buffered saline (PBS) electrolyte. The CoCrMo and the 316L stainless steel alloys demonstrated the lowest and highest mean corrosion penetration rates (CPRs), respectively, of the tested materials. The Vit 105 BMG alloy exhibited a 47% decrease in CPR as compared to the 316L stainless steel and a statistically equivalent CPR as compared to the Ti-6Al-4V. As expected, the CoCrMo and Ti-6Al-4V materials did not exhibit susceptibilities to pitting corrosion in the PBS electrolyte. Susceptibilities to pitting corrosion were seen for the 316L stainless steel and Vit 105 BMG. The Vit 105 BMG alloy exhibited a 53% increase in the resistance to pitting corrosion as compared to the 316L stainless steel. Although pitting corrosion might be a concern for the 316L stainless steel and Vit 105 BMG alloy depending upon the local and bulk environments, the mean protection potentials were found to be greater than the open-circuit potentials in all of the tested conditions. These positive values of η_{pp} signify a high probability of repassivation due to the formation of surface irregularities or damage to the passive film by scratches or applied stresses.

4.5. Corrosion Behavior of the Vitreloy 105 BMG Alloy in a 0.6 M NaCl Electrolyte

Five cyclic-anodic-polarization tests were conducted on each of the three BMG samples for a total of 15 corrosion tests. For comparison, several crystalline, corrosion-resistant materials were also selected for testing. These included: (a) thirteen tests on four samples of AISI 316L stainless steel [$Fe_{62.5}Cr_{19.3}Ni_{13.3}$ (at.%), ASTM F138], denoted as 316L SS; (b) five tests on one sample of $Co_{63}Cr_{28}Mo_6$ (wt.%) [$Co_{61.4}Cr_{30.9}Mo_{3.6}$ (at.%), ASTM F799], denoted as CoCrMo; and (c) five tests on one sample of a Zr-based alloy [$Zr_{98.42}Sn_{1.4}Fe_{0.1}$ (at.%)], similar to the Zircaloy family of alloys.

A second round of tests was conducted in an attempt to identify the source of pitting initiation. In these tests, three samples of the Vit 105 BMG alloy were mounted in epoxy and polished to a 0.05 μm alumina-slurry surface finish. Scanning electron microscopic (SEM) examination was conducted to identify any visible defects, pits, or scratches that could influence the point of pit initiation. This pre-test analysis was accomplished through a systematic survey of the samples at low and high magnifications. Cyclic-anodic-polarization tests were conducted in a similar fashion as previously described. However, in these tests, the test was manually stopped at varying times after pit initiation. Post-test SEM examination and energy-dispersive spectroscopy (EDS) were performed.

The average cyclic-anodic-polarization curves for each of the materials tested are plotted in Figure 35. These average curves demonstrate that each material was passive at E_{corr} and exhibited relatively low open-circuit corrosion current densities (i_{corr}) in the passive region. The derived corrosion parameters for each material, with 95% CIs, are

presented in Table 6. The E_{corr} values (Figure 36) for each of the crystalline materials was statistically different from that of the Vit 105 alloy.

The Vit 105 BMG was found to have relatively low mean (± 95% CIs) and median CPRs of 29.3 ± 33.5 and 8.8 μm/year, respectively (Figure 37). While the mean CPR is moderately high for passive behavior of a corrosion-resistant material, this value was positively skewed due to one data point (236 μm/year) that was determined to be an outlier. In such a case, the median, which is more resistant to outlier affects, is a better measure of the CPR. With this single outlier removed, the mean (± 95% CIs) and median CPRs were calculated to be 14.6 ± 11.9 and 6.5 μm/year, respectively. The CPR for the Vit 105 BMG was found to be statistically different from those of the 316L SS, CoCrMo, and Zr-based alloys, with or without the outlier, at the tested levels.

For a comparison to other corrosion-resistant materials in the same, or similar, electrolytes, the corrosion parameters derived in this study and those reported in the literature are summarized in Table 7. Furthermore, the original corrosion data was available for the Vit 1 BMG [24] and a previous report on the Vit 105 BMG alloy [21] tested in the same environment. Therefore, direct statistical comparisons with the current data were possible. The CPR calculated in this study for the Vit 105 BMG was determined to be statistically equivalent to those reported for the LM-001 and Vit 105 materials, with or without the outliers, at the tested levels.

The Vit 105 BMG was also found to be susceptible to localized corrosion in the form of pitting. Partitioned scatter and box plots of the E_{pit} and E_{pp} values are presented in Figures 38 and 39, respectively. On the other hand, the Vit 105 BMG demonstrated a

large amount of variation in localized-corrosion resistance from test-to-test. For instance, the current densities in the passive region of the anodic curve ranged from 1 to 1000 mA/m^2. Furthermore, five of the fifteen tests (33%) exhibited immunity to localized corrosion, up to a potential of almost 4 V in one case. Therefore, the average polarization curve presented in Figure 35 and the derived localized-corrosion parameters are only applicable to the 66% of the tests that experienced pitting. The mean (± 95% CIs) and median η_{pit} values for the Vit 105 were 603 ± 409 and 231 mV, respectively (Figure 40). The mean (± 95% CIs) and median η_{pp} values for the Vit 105 were 91 ± 64 and 81 mV, respectively (Figure 41). In both cases, the Vit 105 BMG samples that experienced localized corrosion were determined to be statistically equivalent to the 316L SS and Zr-based materials at the tested levels, in terms of the localized-corrosion resistance. However, this high resistance to localized corrosion was not comparable to the CoCrMo alloy, which exhibit immunity to localized corrosion in this electrolyte. Post-test microscopic examination of the CoCrMo samples revealed that there were no pits on the surfaces of any of the tested samples. Therefore, the apparent breakdown on the average polarization curve (Figure 35) is likely associated with uniform passive film dissolution. Comparing these results to those reported in the literature (Table 7), the localized corrosion resistance of the Vit 105 BMG appears to be superior to that of the other BMGs that have been investigated in the same electrolyte. However, the mean CPR for the Vit 105 BMG, with or without the outlier, is significantly higher.

Prior to conducting the second round of tests, SEM analysis demonstrated that the mounted and polished samples were generally free of scratches and defects. On several

occasions, a limited amount of small porosity was observed with a size range of 1 – 5 μm (Figures 42a – 42b). Two cyclic-anodic-polarization tests were conducted in which the tests were stopped approximately 1 – 5 mV after E_{pit}. Multiple pits were observed on the surfaces of the samples (Figures 42c and 42d) upon examination in the SEM. Many of these pits exhibited morphologies that appeared to contain remnants of particles in the centers of the pits. Based upon these morphologies at the initial stages of pit growth, it appears that the pits initiated at inhomogeneities in the amorphous material and propagated at constant rates through the amorphous matrix to produce spherical pits. Thirty-five EDS spectra were collected at various points within the pits, and 11 spectra were collected in the amorphous matrix (away from the pits) for comparison. This data (Table 9) demonstrated that the pits were enriched in copper and depleted in the other elements in the alloy, particularly Zr. This pit morphology and high Cu-content is similar to that reported by Mudali et al. [184]. Based upon the Pourbaix diagram for Cu [185], it is possible that the high Cu content is due to the dissolution of Cu to Cu^{++} within the pit (at lower pH), followed by the precipitation of CuO or Cu because of a subsequent rise in pH within or outside of the pit, or saturation of the solution with Cu ions on the local level, respectively.

In this study, cyclic-anodic-polarization tests were conducted with the Vit 105 BMG alloy in a 0.6 M NaCl electrolyte. Several corrosion-resistant, crystalline alloys were also studied in the same electrolyte for comparison. Based upon the results of this investigation, the following conclusions were drawn. The Vit 105 BMG was passive at the open-circuit potentials and exhibited moderately low CPRs. This CPR was found to be higher than those calculated for the 316L SS, CoCrMo, and Zircaloy materials by a

statistically significant difference. Furthermore, the Vit 105 CPR was statistically equivalent to those reported in the literature for the Vit 1 and Vit 105 alloys, at the tested levels. The Vit 105 BMG was found to be susceptible to localized corrosion in the form of pitting. However, this alloy demonstrated a large amount of variation in localized-corrosion resistance from test-to-test. For instance, five of the fifteen tests (33%) exhibited immunity to localized corrosion, up to a potential of almost 4 V in one case. The Vit 105 BMG samples that experienced localized corrosion were determined to be statistically equivalent to the 316L SS and Zr-based materials at the tested levels, in terms of the localized-corrosion resistance. However, this high resistance to localized corrosion was not comparable to the CoCrMo alloy, which exhibit immunity to localized corrosion in this electrolyte.

4.6. Corrosion-Fatigue Studies of the Vitreloy 105 BMG Alloy

4.6.1. Mechanical Characterization

The cyclic, four-point bend testing in air resulted in a large amount of scatter at most stress ranges (Figure 43). However, the scatter decreased at higher stress ranges, as typically expected for S-N behavior. In general, the majority of the fatigue lives were greater than those reported by Peter et al. for the same material tested in uniaxial fatigue [18, 19]. It appears that the fatigue endurance limit is approximately equal to or greater than the 907 MPa reported by Peter et al. [18, 19].

The stress-life data for the Vit 105 BMG bend samples tested in the 0.6 M NaCl electrolyte is plotted in Figure 43 along with the air data for comparison. As can be seen in the plot, the environment had a large effect on the fatigue lives, resulting in fatigue

lives that were generally shorter than in air. Surprisingly, these fatigue lives in the 0.6 M NaCl electrolyte were still equal to or greater than the fatigue lives reported by Peter et al., above the uniaxial fatigue endurance limit of 907 MPa reported by Peter et al. [18, 19]. However, the fatigue endurance limit in the 0.6 M NaCl electrolyte is greatly reduced compared to both the four-point bending tests in air and the uniaxial tests conducted by Peter et al. In this study, it appears that the fatigue endurance limit in the corrosion-fatigue condition is below a stress range of 400 MPa (Figure 43).

4.6.2. Fractography

SEM fractography revealed that all of the samples tested in air and NaCl appeared to fail due to fractures that initiated on the tensile sides of the samples. Wear at both the inner and outer pin locations was evident in both environments on all of the samples. Most of the bend samples tested in air exhibited fracture surfaces with the typical fatigue regions for a BMG [Figure 44(a)]: a striated, slow crack-growth region [Figure 44(b)]; a transition region [Figure 44(c)]; and an overload, fast-fracture, region with areas containing the vein pattern [Figure 44(d)] typically observed in BMGs. On the other hand, most of the samples tested in NaCl exhibited a different fracture morphology [Figure 45(a)]. Although striations were observed at various locations on these samples, a majority of the fracture surfaces demonstrated alternating regions of smooth steps, separated by abrupt changes in fracture planes, as shown in Figure 45(b). In some cases, these abrupt changes between the smooth fracture regions also contained visible striations [Figure 45(c)].

In a few tests, interior initiation sites were observed (Figure 46) where it appeared that fracture initiated at inhomogeneities within the samples. Porosity was also observed

on several of the fracture surfaces, most commonly at the transition from the controlled, striated crack-growth region to the final fracture/overload region (Figure 47). Finally, multiple samples appeared to fail due to fractures that initiated on the tensile surface at surface defects not associated with the corners, as shown in Figure 48.

In air, the majority of the samples (62%) failed within the inner span from fractures that initiated at, or within, the inner pins, as demonstrated in the schematic diagram in Figure 49. This behavior is expected since both the shear and tensile stresses are at maximums within these inner load pins. There were no obvious correlations between stress ranges and initiation locations. It should be noted that this diagram is schematic in that the plotted lines do not reflect the exact fracture planes on the samples. Rather, these lines simply reflect the fracture locations on the tensile and compressive surfaces of the bend samples. In addition, a histogram of the initiation locations for the bend samples tested in air is presented in Figure 50. As demonstrated in the histogram, the most frequent initiation location (mode) was at one of the inner loading pins. SEM fractography demonstrated that most of the fractures in air (62%) initiated at the corners of the samples, similar to that shown in Figure 44(a). Finally, approximately 31% of the fractures appeared to initiate on the tensile surfaces at other surface defects not associated with the corners (Figure 48).

A schematic diagram of the failure locations for the bend samples tested in the 0.6 M NaCl electrolyte is presented in Figure 51. Based upon this diagram, a correlation between stress range and initiation location is evident. All of the samples tested at stress ranges of 1600 MPa failed within the inner span, similar to the samples tested in air, while the majority (67%) of those tested at lower stress ranges failed from cracks that

initiated at the outer pins. This correlation is likely due to the limited time per test at the higher stresses during which corrosion-fatigue can occur. Again, these lines simply reflect the fracture locations on the tensile and compressive surfaces of the bend samples, not the exact fracture planes. In addition, a histogram of the initiation locations for the bend samples tested in air is presented in Figure 52. The shift in failure locations in the 0.6 M NaCl electrolyte is probably due to increased corrosion in conjunction with a greater amount of wear at the outer pins, which resulted in removal of the passive film, localized corrosion, and crack initiation.

Moreover, many of the samples exhibited particles on the fracture surfaces (Figures 53-55), which would be unexpected in an ideally homogeneous, amorphous material. Generally, there were three types of particles observed on the fracture surfaces of the fatigue samples. First, there were particles with approximate diameters of 5 – 20 μm that formed in isolation or in small groups, as shown in Figure 53. Analysis of matching fracture surfaces indicated that the particles on one surface corresponded to craters on the opposite surface [Figures 53(c-d)]. Second, there were groups of particles that formed arcs across the fracture surfaces, as demonstrated in Figure 54. Some of the arcs were short [Figure 54(a-c)], while some of them stretched across most of the bend sample, as shown in Figure 54(d). In general, most of these arcs consisted of particles that were approximately 5 – 20 μm in diameter. Finally, there were also large sheets of smaller particles with diameters less than 3 – 5 μm (Figure 55). These networks of smaller particles were observed to form in concentric arcs across the samples in various locations, as can be observed in Figures 55(c-d). Based upon the appearance of these sheets of particles, it appears that the interfaces along the surfaces of the sheets are

weakened and facilitate fracture propagation. In general, these arcing sheets of particles appear to be similar to the swirl patterns previously observed on polished and etched samples (Figure 56). Furthermore, these morphologies are also similar to those reported by Yokoyama et al. in a Zr-Cu-Ni-Al BMG alloy [186]. The authors attributed these particle arrays to oxygen contamination of the cast ingots.

Upon further examination, a clear correlation was observed between the presence of the particles on the fracture surface and a decreased fatigue life at a given stress range. To illustrate this correlation between inhomogeneities and fatigue lives, the S-N plots for the samples tested in air and 0.6 M NaCl are presented in Figures 57 and 58, respectively, with the qualitative amount of particles and porosity observed in each sample superimposed onto the stress-life data. Based upon these plots, it is evident that these particles and porosity greatly influenced the fatigue performance of this BMG alloy at all stress ranges and in both environments. Furthermore, much of the scatter in the fatigue life data can be attributed to these inhomogeneities in the samples. It should be noted that the particles and craters were never observed to cause crack initiation. Thus, it is theorized that these defects resulted in faster crack growth rates, ultimately resulting in shorter fatigue lives. However, the resultant scatter in the NaCl electrolyte is drastically decreased, as compared to the data from the tests conducted in air. This is likely due to the environmental effects surpassing the inhomogeneities as the dominant life-limiting mechanism. Finally, it can safely be assumed that the fatigue lives presented in this study are very conservative estimates relative to the potential fatigue performance of a homogeneous Vit 105 BMG alloy.

4.6.3. Electrochemical Characterization

During all of the bending fatigue tests conducted in the 0.6 M NaCl electrolyte, the open-circuit potential (E_{oc}) was recorded as a function of time. Initially, each sample was placed in the electrolyte and allowed to come to a steady-state in the unstressed condition. The E_{oc} was allowed to stabilize according to the criteria previously outlined, and, once this was achieved, this E_{oc} was assumed to be E_{corr}. For most of the tests at each stress range, there was a general trend (Figure 59) of a large decrease in potential at the onset of cyclic loading and a gradual increase in E_{oc}, followed by a plateau once a steady-state was reached. The potential at which this plateau was observed for each sample was correlated with the stress range (coefficient of determination = $r^2 = 0.63$), where increasing stress ranges corresponded to lower, more active plateau potentials. After a period of time, the E_{oc} began to decrease until the sample fractured. After fracture, the sample was no longer under cyclic loading, and E_{oc} increased back up to a potential near the unstressed E_{corr}.

During some of these corrosion-fatigue tests, the samples and open-circuit potentials were observed during testing. It was noted that visible cracks on the samples corresponded to the potential downturns near the ends of the tests. While it is possible that crack initiation occurred prior to this point, the potential downturn likely represents bare metal being exposed to the electrolyte at the crack tip. Thus, this downturn represents the onset of significant crack propagation leading to failure. Moreover, the elapsed time at the potential downturn was recorded for each test and divided by the elapsed time at failure to determine the percent of the fatigue life at which significant crack propagation occurred. It was found that this downturn occurred at a mean (±

standard deviation) of 92% ± 4% of the total fatigue lives. The maximum and minimum values were calculated to be 98% and 86%, respectively.

The average cyclic-anodic-polarization curve at a stress range of 900 MPa (denoted as corrosion-fatigue) is presented in Figure 60 with the average polarization curve from the static electrochemical studies (unstressed condition) for comparison. Where the mean η_{pit} (± 95% CIs) in the static condition was 603 ± 409 mV, the cyclic loading reduced E_{pit} to a potential less than E_{corr}, resulting in a η_{pit} that is negative. Thus, the cyclically loaded samples actively undergo pitting at E_{corr}. Interestingly, the E_{pp} value remained unchanged, signifying that the repassivation mechanism does not change under cyclic loading. It is also significant that i_{corr} increased by approximately two orders of magnitude under the corrosion-fatigue conditions, as compared to the static condition. The mean CPR (± 95% CIs) in the corrosion-fatigue condition was calculated to be 1119 ± 284 μm/year, as compared to 29 ± 34 μm/year for the static condition. However, the CPR approximation is only valid for uniform corrosion. Since localized corrosion was occurring at E_{corr}, the actual CPR at the pits is likely much higher.

In an effort to determine the mechanism responsible for the environmental degradation in this material, several tests were conducted with imposed potentials on the bend samples. First, a cathodic potential of -900 mV (SCE) was imposed on the sample throughout cyclic loading at a stress range of 900 MPa. While the average unpolarized, corrosion-fatigue life at this stress range was 58,350 cycles, the cathodically polarized sample did not fail up to 650,000 cycles, an order of magnitude increase in the fatigue life at a minimum. At that point, the cathodic polarization was stopped, and an anodic potential of 100 mV (SCE) was then imposed on the sample. After the initiation of

anodic polarization, the sample failed after 2134 cycles. To further verify this effect, a second test was conducted in which an anodic potential of -100 mV (SCE) was imposed on the sample throughout cyclic loading at a stress range of 900 MPa. In this case, the sample failed after 2302 cycles, a 96.1% decrease as compared to the mean unpolarized fatigue life. Thus, based upon these results, it can be concluded that the environmental degradation mechanism is through anodic dissolution of the alloy, not hydrogen embrittlement. Furthermore, it is important to note that this type of degradation mechanism can be avoided by cathodic protection, as demonstrated in this study. These results are similar to those reported by Ritchie et al. for the Vit 1 alloy in similar environments [104, 105]. In recent studies, Peter et al. have found that the fatigue life of the Vit 105 BMG is particularly sensitive to surface conditions [187]. Thus, it is not surprising that crack initiation occurred at the location of this pin wear. However, it is reasonable to assume that the fatigue lives and fatigue-endurance limits reported in this study are conservative estimates. In the absence of porosity and pin wear, it is expected that fatigue lives would be longer and the fatigue-endurance limits could be higher.

The four-point-bending-fatigue performance of the Vit 105 alloy has been defined in both air and 0.6 M NaCl. In air, a direct comparison of four-point-bending and uniaxial fatigue was conducted using materials that were fabricated and tested in the same labs, and following the same testing procedures. The fatigue lifetimes in air were in four-point bending were found to be equal to or greater than those reported in uniaxial testing. Moreover, the bending fatigue endurance limit appears to be equal to or greater than that reported for uniaxial fatigue. Thus, the significant differences between studies reported in the literature are not likely to be due to this difference in testing geometry.

On the contrary, the fatigue lifetimes were found to be highly dependent upon surface defects and material quality. Therefore, it is theorized that these variables likely account for the greatly varying conclusions on the fatigue performance of BMGs. Furthermore, the environmental effect of 0.6 M NaCl on the fatigue behavior of the Vit 105 BMG alloy has been defined. Surprisingly, the bending fatigue lives in the 0.6 M NaCl electrolyte were still equal to or greater than those reported for uniaxial fatigue in air, above the uniaxial fatigue endurance limit of 907 MPa in air. However, the corrosion-fatigue endurance limit was severely reduced to a stress range less than 400 MPa. In addition, the scatter in the fatigue data was determined to be primarily due to the inhomogeneities observed in most of the samples. Finally, the shift in the polarization curve due to applied cyclic stresses was defined, and the degradation mechanism was found to be anodic dissolution, not hydrogen embrittlement.

4.7. Shear-Band Evolution in the Vitreloy 105 BMG Alloy

The relationship between temperature and material deformation has long been recognized. In 1853, Kelvin summarized the relationship between the temperature and elastic strain, which is commonly known as the thermoelastic effect [188]. Furthermore, Kratochvil and Dillon developed the thermoplastic theory in 1960s [189, 190]. These two theories directly relate the temperature with the stress–strain state of the material, which, in turn, determines the mechanical behavior. However, prior to the last two decades, further development of thermography as a non-destructive evaluation (NDE) technique was constrained by the resolution of the available instrumentation [191-193].

Recently, research has shown the potential of thermography for in situ monitoring deformation during mechanical testing [194-205]. In this study, the deformation and failure mechanisms of a BMG were examined during tension experiments through *in situ* monitoring with a high-speed, high-resolution infrared (IR) camera. The use of the IR camera during mechanical testing permitted the heat generated through deformation to be imaged in real time at high spatial and temperature resolutions. Quantitative measurements of shear band (SB) properties and kinetics are presented.

The XRD spectra of the tensile specimens showed broad, diffuse peaks that are characteristic of amorphous alloys (Figure 61). The first two tensile tests were conducted with a loading rate of 147 N/s (approximately 1 x 10^{-2} strain rate). However, few images of shear bands were acquired at these rates. Therefore, the loading rate was decreased to 45 N/s (approximately 1 x 10^{-3} strain rate) for the remaining eight tests. At the lower loading rate, multiple shear bands were imaged in a majority of the tests. However, shear bands were not visualized in all of the tests. In general, the "unpolished edge" specimens exhibited multiple shear bands in numerous locations throughout the gage section. In contrast, the "polished edge" specimens typically exhibited multiple shear bands in a concentrated location in the region of the final failure. This change in the shear-band evolution was likely due to the removal of numerous stress concentrators present along the "rough" edges of the gage section in the "unpolished edge" specimens. For all tests in which shear bands were observed, the IR images revealed that multiple shear bands initiated, propagated to various lengths, and arrested before reaching the opposite edges of the specimens. After arrest, many shear bands were reactivated at a later time (and higher stress) and propagated before arresting again. A shear-band-activation event was

defined as either: (i) the initiation, propagation, and arrest of a shear band (Type I), or (ii) the reactivation, propagation, and arrest of a previously observed shear band (Type II). This type of behavior is particularly surprising because the prevailing belief has been that BMGs loaded in uniaxial tension will fail by the initiation and propagation of a single shear band [206, 207].

A particular "unpolished edge" specimen, in which 59 shear bands were observed, was selected for extensive analysis and will be discussed in detail. This particular test was conducted at a loading rate of 45 N/s and an IR image size of 64 x 128 pixels. The first shear band was observed approximately 4.1 seconds before failure. Within this final 4.1 seconds of the test, a minimum of 59 shear bands was observed. In each case, the primary shear bands initiated along one edge of the specimen and propagated at an average 56° from the loading direction (Figure 62). This shear band angle was verified through post-test SEM examination. The minimum shear band propagation velocity was estimated to be approximately 1 m/s based upon the maximum shear band propagation distance observed between IR camera frames (1.368 mm) and the time between frames (1.4 ms).

Although there were regions with higher shear band densities than others, the shear bands were distributed along the entire length of the gage section. The location of each shear band was measured to determine the number of Type I and Type II shear bands. A histogram of the number of shear bands that were imaged as a function of location along the length of the gage section is presented in Figure 63(a). Type I shear bands accounted for 45 (76.3%) of the 59 shear bands imaged. Type II shear bands accounted for the remaining 14 (23.7%) shear bands. Among all of the shear bands

observed, 12 shear bands (20.3%) were reactivations of shear bands at locations that had already experienced one previous shear-band-activation event, while 2 shear bands (3.4%) were reactivations of shear bands at locations that had already experienced two previous shear-band-activation events. It is important to note that, on several occasions, two shear bands initiated from the same location along the gage section but propagated in opposing directions (+56° and -56° to the loading axis). Therefore, both of these shear bands would be classified as Type I shear bands. Furthermore, a distribution of the distance between adjacent shear bands is presented in Figure 63(b). Both the median and mode of the distribution was 0.072 mm, which is the spatial resolution limit of the IR camera. This value is similar to that reported by Conner et al. (~ 0.070 mm) for the tensile side of bend samples with a thickness of 0.5 mm [206].

A series of IR images depicting the initiation, propagation, and arrest of a major and minor shear band at 1.62 GPa is presented in Figure 64. Within this figure, each image is 64 x 128 pixels, or 4.6 x 9.2 mm. The full gage section of the tensile specimen is visible at the center of each image. Between Frames 1 and 2, a shear band initiates at the lower, right edge of the specimen and propagates a short distance into the interior of the specimen (as denoted by the arrow in Frame 2). In Frame 3, the shear band has further propagated and arrested. In Frame 4, a second, shorter shear band has already initiated, propagated, and arrested at a location immediately below the former shear band (as denoted by the arrow in Frame 4). The remaining images show the dissipation of the heat generated during initiation and/or propagation of the shear band. At stress levels below approximately 1.67 GPa, all of the heat generated by the shear bands gradually dissipated through conduction within approximately 30 frames (41 ms).

As the specimen approached the failure stress (1.69 GPa), this conductive cooling after shear band arrest no longer occurred at such a rapid rate. As seen in Figure 65, two shear bands at opposing angles have initiated, propagated, and arrested immediately prior to Frame 1. After the arrests of these shear bands, this region of the gage section (also the location of the final failure) exhibited conductive cooling at a much slower rate throughout the final 280 ms before failure (Frames 2 – 10 in Figure 65). It is believed that multiple shear bands initiated, or reactivated, and propagated in rapid succession in this region and prevented the faster heat dissipation rate that was observed at lower stress levels (Figure 64). After regional heating, the successive shear bands in this portion of the gage section were not visible in the IR data. Therefore, it is expected that the total number of shear bands generated in the gage section was significantly higher than those visualized by thermography. Frame 10 (Figure 65) was the final image obtained prior to failure.

The IR images were carefully analyzed frame-by-frame to determine the exact time and stress of each of the 59 shear-band-activation events. The elapsed time and stress at the time of the i^{th} shear-band-activation event is plotted in Figure 66. For instance, the third shear band occurred at a time of 33.2 s and a stress of 1.52 GPa. After shear banding began at 1.51 GPa, the shear bands occurred at various times with a relatively uniform distribution. However, the shear bands that occurred near the onset of shear banding and immediately prior to failure both deviate from the linear portion in the middle of the plot. For every shear band, the elapsed time since the previous shear-band-activation event was calculated. Once shear banding began, the mean (± 95% CIs) and median times between sequential shear-band-activation events were 0.070 ± 0.022 and

0.044 s, respectively. Linear regression revealed that the SB initiation rate was approximately 17 shear bands per second after the occurrence of the initial shear band. No correlation was observed between any of the variables analyzed in this study and the elapsed time between the shear-band-activation events ($0.00 \leq r^2 \leq 0.14$).

An AutoRegressive Integrated Moving Average (ARIMA) model was employed to analyze the time sequence data of the shear-band-activation events [208]. ARIMA time series analysis models patterns in time series data and predicts the occurrence of future events by using a linear combination of the past values and past errors in the data. This analysis revealed that no structure was present in the data except the distribution of the time between events (Figure 67). Based upon this distribution, a lognormal distribution was fit to the data but did not adequately explain the data.

Moreover, the evolution of each shear band was elucidated by analyzing sequential frames of the IR images. A schematic diagram of a shear band is presented in Figure 68(a) in order to better illustrate the data extracted from the IR images. A plot of temperature as a function of the distance along the axis of each shear band [Figure 68(b)] was made for 37 of the 59 shear bands. The remaining 21 shear bands were not included in the analysis because they were either too short or more than two shear bands intersected, complicating a detailed analysis. The distance in each profile was measured from the point of shear-band initiation (the edge of the gage section) to the point of shear band arrest. From this plot, the length (L), maximum temperature (T_{max}), and mean temperature (T_{avg}) of each shear band were determined. In addition, a "background" temperature was determined by averaging the temperature values along each line profile from the two previous frames prior to shear band initiation. The difference between each

sequential frame and this "background" temperature profile was determined to calculate the maximum temperature increase (ΔT_{max}) and mean temperature increase (ΔT_{avg}) for each shear band. Furthermore, a plot of the temperature as a function of the distance along a line profile perpendicular to the shear band axis [Figure 68(c)] was made for 41 of the 59 shear bands. The other 18 shear bands were not analyzed because the short lengths made detailed analyses difficult. From this plot, the width (W) of each shear band at a location near the middle of the shear bands (~ 0.5L) was obtained.

The temperature profiles along the axes of shear-band propagation were analyzed for the primary shear band discussed in Figure 64. The evolution of these temperature profiles as a function of time is presented in Figure 69(a). In addition, a plot of the change in temperature, as calculated from the difference between each frame and the "background", as a function of the distance from the point of shear band initiation is presented in Figure 69(b). The frame numbers in both plots also correspond to the frame numbers in Figure 64. As seen in the IR images (Figure 64), the temperature data confirms the previous analysis in that the shear band initiated and propagated a small distance (~ 0.3 mm) prior to Frame 2 (Figure 69). Between Frames 2 and 3, the shear band further propagated and arrested at a final length of approximately 1 mm. In Frame 3, the maximum temperature (T_{max}) of approximately 22.5°C was reached at the point of initiation [Figure 69(a)]. Furthermore, the maximum temperature increase (ΔT_{max}) of approximately 2.5°C was also attained in the same location [Figure 69(b)]. In the following frames, the peak temperature (left-half) decreases and the lower temperature region (right-half) of the shear band increases. These effects are likely due to the heat

conduction away from the shear band and along the direction of the shear band after arrest, respectively.

A plot of temperature as a function of the distance perpendicular to the axis of the primary shear band in Figure 64 is presented in Figure 70(a). This line profile was made near the middle (~ 0.5 mm from the point of initiation) of the full shear band length. Furthermore, a plot of the change in temperature as calculated from the difference between each sequential frame and the "background" is presented in Figure 70(b). Again, the frame numbers correspond to those in Figures 4 and 9. Since the shear band only propagates to a length of about 0.3 mm prior to Frame 2, the shear band is not visible in this temperature profile until Frame 3, at which point the shear band has already propagated and arrested. From the profile obtained in Frame 3, a width of approximately 0.45 mm was measured (Figure 70). In the following frames, the heat conduction away from the shear band results in a decrease in the maximum temperature and a widening of the visible hot band.

The temperature evolution in Figure 69 was typical of all of the shear bands in that the maximum temperature was observed at the point of initiation (the edge of the gage section) and the temperature gradually decreased along the entire length of the shear band to the point of arrest. Surprisingly, this trend was also observed for the reactivation of previously arrested shear bands (Type II). Thus, it can be concluded that heat, and presumably shear, is generated along the entire length of the shear band when propagation occurs.

The temperature [T (°C)] along the distance of shear-band propagation [x (mm)] was characterized by simple linear regression for each shear band. The decrease in the

temperature as a function of distance was rather constant for all of the shear bands analyzed with a mean slope (± 95% CIs) of -2.11 ± 0.24 °C / mm. This gradual decrease in the temperature as the shear band propagates suggests that arrest occurs because the driving mechanism for shear band propagation slowly decreases until it is exhausted.

The mean (± 95% CIs), median, maximum, and minimum values for some of the parameters derived from this study are summarized in Table 10. It should be noted again that it was not possible to analyze all 59 shear bands for the calculation of these mean and median values. While there were several large shear bands excluded from the analyses due to shear bands overlapping, these cases were few in number. More commonly, shear bands were excluded from the analyses because they were too short to accurately analyze. Therefore, it is expected that all of the values in Table 10 are the maximum estimates and would likely be lower if all of the shear bands were analyzed.

It should be noted that all of the IR images and data are measures of the temperature on the surface of the sample. In other words, all of the data analyzed in the current study is representative of these "hot bands" that result from shear banding. Although this data can be utilized to understand the deformation mechanisms occurring in the material, both the images and the data are subject to distortion primarily through heat conduction. For instance, the current data demonstrates that the actual temperature increase in the hot bands is small (~ 2.5°C). This temperature increase is consistent with that of Wright et al. [86]. However, the mean width of the hot bands analyzed in the current study was 0.42 mm. Reports in the literature have estimated that shear bands have a width of approximately 10 – 100 nm. If all of the heat were assumed to be generated within the shear band and constricted to an area with a width of 10 – 100 nm

[209], the temperature increase in the shear band could be much greater. Furthermore, there are finite resolution limitations inherent in the IR camera system. With a pixel size of 72 x 72 μm, a high temperature shear band with a width of 100 nm would be averaged over the area of the entire pixel. Thus, this significant difference between the shear band size and the resolution of the camera could cause the temperatures observed in this study to be significant underestimates of the temperatures generated during shear banding.

Finally, all of the aforementioned variables derived from the IR and mechanical data were sequentially added to or removed from a model to predict the length of the shear bands. The prediction error sum of squares (PRESS) was calculated for each iteration of the model. The only variable that demonstrated a significant contribution to the model, denoted by a minimum PRESS value, was the maximum temperature of each shear band (T_{max}). As shown in Figure 71, a scatter plot of shear band length [L (mm)] as a function of T_{max} (°C) demonstrates that approximately 70% of the variation in L is accounted for by T_{max} as follows:

$$L = 0.23\, T_{max} - 4.28 \quad (6)$$

The final failure likely occurred when a shear band grew to a critical length such that arrest was no longer possible. Based upon the correlation between length and T_{max} observed in this investigation, it can be concluded that final failure must have occurred when a critical shear band temperature (T_c) was attained in one or more of the shear bands. As previously mentioned, the region of final failure remained at an elevated temperature immediately prior to failure (Figure 65). This was likely due to a quick succession of shear bands at surface defects (stress concentrators) in close proximity, which did not allow time for heat dissipation. As the temperature of the bulk material

increased, the maximum shear band temperature probably increased proportionately until T_c was reached. Unfortunately, this failure mechanism cannot be verified by thermography because the localized heating of the sample prevents the individual shear bands from being observed. Surprisingly, little correlation ($0.14 \leq r^2 \leq 0.33$) was observed between the stress and any of the shear band variables investigated, including length and T_{max}. Thus, it can be concluded that the location and density of stress concentration factors at small surface defects (i.e., the weak links in the chain) exhibited a much greater influence on the final failure of the sample than the stress alone. Theoretical modeling of the data derived from this study has generated promising results [210-213].

In conclusion, i*n situ* IR thermography has been shown to be a viable tool for the study of shear band evolution in BMGs. The high spatial and thermal resolution of modern IR cameras provides a unique method for the examination of inhomogeneous deformation. The length, location, sequence, temperature evolution, and velocity of individual shear bands have been quantified through the use of IR thermography. For the first time, this study surprisingly revealed that multiple shear bands initiated, propagated to various lengths, and arrested before reaching the center opposite edges of the specimens during uniaxial tensile tests. After arrest, many shear bands were reactivated at a later time and higher stress and propagated before arresting again. The velocity of shear band propagation was estimated to be a minimum of 1 m/s. The temperature profiles along the axis of shear band propagation were found to continually decrease from the point of initiation to the point of arrest. This gradual decrease in the temperature as the shear band propagates suggests that arrest occurs because the driving mechanism

slowly decreases until it is exhausted. A maximum temperature increase of approximately 2.6°C was observed in association with the propagation of shear bands. However, this temperature change is likely an underestimate of the actual increase in temperature generated by the shear band due to the limited temporal and spatial resolution of the IR camera and rapid heat conduction in the sample. Finally, the maximum temperature of a shear band has been shown to be the best predictor of the shear band length out of all of the parameters examined in this study. Based upon this correlation, it can be concluded that the final failure must have occurred when a critical shear-band temperature was attained in one or more of the shear bands, preventing the arrest of the shear band before it attained a critical length.

5. CONCLUSIONS

Although BMGs possess a unique assortment of properties, the lack of electrochemical and mechanical characterization for many of the compositions has hindered these materials from being used in structural applications. Moreover, the lack of understanding of localized corrosion and the deformation and failure mechanisms associated with both monotonic and cyclic loading have been major impediments.

In the current study, the electrochemical behaviors of Zr-, Ti-, and Ca-based BMGs have been studied in various environments. Moreover, the electrochemical behaviors of several common, crystalline materials have also been characterized in the same environments to facilitate comparisons. In general, the Zr- and Ti-based BMG alloys demonstrated relatively good general corrosion resistance in all of the environments. Mean corrosion penetration rates (CPRs) were found to be less than 30 μm/year for these alloys. On the other hand, the Ca-based BMG alloys were found to be highly active with CPRs ranging from 300 – 5700 μm/year in a non-aggressive 0.05 M Na_2SO_4 electrolyte. Furthermore, most of these alloys were found to be susceptible to localized corrosion in these environments. However, the Zr- and Ti-based BMG alloys exhibited relatively high, positive values for both pitting overpotentials (η_{pit}) and protection overpotentials (η_{pp}).

The Zr-based BMG commonly known as Vitreloy 105 (Vit 105) was selected for further studies. This material was fabricated at the Oak Ridge National Laboratory by arc-melting and drop-casting into a water-cooled, copper mold. Mechanical

characterization of this alloy was conducted through four-point bend fatigue testing, as well as tensile testing with *in situ* thermography.

Fatigue testing in air revealed that both the fatigue lives at various stresses and the fatigue endurance limit are similar to those reported for this material in uniaxial fatigue. This result alone demonstrates that the great differences in fatigue results reported in the literature are not due to differences in testing geometry. In fact, the larger scatter observed in four-point bend fatigue at a given stress range was found to be due to variations in material quality. Thus, material quality is believed to be the primary reason for the great differences in fatigue behavior of various BMG alloys that have been reported in the literature since 1995.

After the electrochemical and mechanical behaviors of the Vit 105 BMG alloy were defined separately, the corrosion-fatigue behavior of this alloy was studied. Corrosion-fatigue tests were conducted under identical conditions as those utilized during fatigue testing in air. However, in this case, the environment was a 0.6 M NaCl electrolyte, identical to one of the environments in which the electrochemical behavior was previously defined. The environmental effect was found to be significant at most stress levels, with decreasing effects at higher stress levels due to decreasing time in the detrimental environment. Furthermore, the corrosion-fatigue endurance limit was found to be severely depressed to a stress range of less than 400 MPa. Again, the variation in the corrosion-fatigue data at a given stress range was found to be primarily dependent upon material quality. In addition, the crack-initiation locations were observed to shift from the inner span, in air, to the outer loading pins in the 0.6 M NaCl electrolyte. This

shift in initiation locations was due to wear at the outer pins that removed the passive layer, which promoted pitting and crack initiation.

Cyclic-anodic-polarization tests were conducted during cyclic loading to elucidate the effect of cyclic stresses on the electrochemical behavior. It was found that a stress range of 900 MPa resulted in active pitting at the open-circuit potentials. Thus, η_{pit} had shifted from high, positive values in the static condition to low, negative values under cyclic loading. Next, the degradation mechanism was examined by anodic and cathodic polarization. While cathodic polarization extended the fatigue life, anodic polarization severely degraded the fatigue life. Based upon these dramatic shifts in the fatigue lives at 900 MPa, it was concluded that the degradation mechanism is stress-assisted dissolution, not hydrogen embrittlement.

Finally, tensile tests were conducted with the Vit 105 BMG alloy with *in situ* infrared (IR) thermography to observe the evolution of shear bands during deformation. More importantly, the length, location, sequence, temperature evolution, and velocity of individual shear bands have been quantified through the use of IR thermography. This study revealed that multiple shear bands can initiate, propagate, and arrest within the sample during a single tensile test, contrary to popular belief. After arrest, many shear bands were reactivated at a later time and higher stress and propagated before arresting again. The velocity of shear band propagation was estimated to be a minimum of 1 m/s. The temperature profiles along the axis of shear band propagation were found to continually decrease from the point of initiation to the point of arrest. This gradual decrease in the temperature as the shear band propagates suggests that arrest occurs because the driving mechanism slowly decreases until it is exhausted. A maximum

temperature increase of approximately 2.6°C was observed in association with the propagation of shear bands. However, this temperature change is likely an underestimate of the actual increase in temperature generated by the shear band due to the limited temporal and spatial resolution of the IR camera and rapid heat conduction in the sample. Finally, the maximum temperature of a shear band has been shown to be the best predictor of the shear band length out of all of the parameters examined in this study. Based upon this correlation, it can be concluded that the final failure must have occurred when a critical shear-band temperature was attained in one or more of the shear bands, preventing the arrest of the shear band before it attained a critical length.

In conclusion, both the electrochemical and mechanical behaviors of various BMGs have been clarified. In addition, the interactions between corrosion and fatigue have been elucidated. Based upon all of these studies on a variety of BMG alloy systems, it is obvious that these materials are extremely sensitive to both material quality and surface defects. Therefore, future research on the improvement of BMG alloys should be focused on these areas.

REFERENCES

1. Luborsky FE, "Amorphous metallic alloys," in Amorphous Metallic Alloys, F. E. Luborsky, Eds., Butterworths, London, 1983,
2. Hays CC, Kim CP, Johnson WL. Microstructure controlled shear band pattern formation and enhanced plasticity of bulk metallic glasses containing in situ formed ductile phase dendrite dispersions. Phys Rev Lett, Mar 2000;84:2901-2904.
3. Inoue A, Kimura HM, Sasamori K, Masumoto T. Ultrahigh strength of rapidly solidified Al-(96-x), Cr-3, Ce-1, Co-x (x=1, 1.5 and 2%) alloys containing an icosahedral phase as a main component. Mater Trans, 1994;35:85.
4. Vaidyanathan R, Dao M, Ravichandran G, Suresh S. Study of mechanical deformation in bulk metallic glass through instrumented indentation. Acta Mater, 2001;49:3781-3789.
5. Bian Z, He G, Chen GL. Microstructure and mechanical properties of as-cast Zr-52.5, Cu-17.9, Ni-14.6, Al-10, Ti-5 bulky glass alloy. Scripta Mater, Nov 2000;43:1003-1008.
6. Inoue A, Zhang T. Impact Fracture Energy of Bulk Amorphous Zr-55, Al-10, Cu-30, Ni-5 Alloy. Mater Trans, 1996;37:1726-1729.
7. Flores KM, Dauskardt RH. Enhanced toughness due to stable crack tip damage zones in bulk metallic glass. Scripta Mater, 1999;41:937-943.
8. Schneibel JH, Horton JA, Munroe PR. Fracture toughness, fracture morphology, and crack-tip plastic zone of a Zr-based bulk amorphous alloy. Metall Mater Trans A, 2001;32:2819-2825.

9. Gilbert CJ, Ritchie RO, Johnson WL. Fracture toughness and fatigue-crack propagation in a Zr-Ti-Ni-Cu-Be bulk metallic glass. Appl Phys Lett, Jul 1997;71:476-478.

10. Inoue A, Zhang T, Chen MW, Sakurai T. Mechanical properties of bulk amorphous Zr-Al-Cu-Ni-Ag alloys containing nanoscale quasicrystalline particles. Mater Trans, Dec 1999;40:1382-1389.

11. Inoue A, Miyauchi Y, Masumoto T. Soft magnetic Fe-Zr-Si-B alloys with nanocrystalline structure. Mater Trans, 1995;36:689-692.

12. Saotome Y, Itoh K, Zhang T, Inoue A. Superplastic nanoforming of Pd-based amorphous alloy. Scripta Mater, 2001;44:1541-1545.

13. Saotome Y, Hatori T, Zhang T, Inoue A. Superplastic micro/nano-formability of La-60, Al-20, Ni-10, Co-5, Cu-5 amorphous alloy in supercooled liquid state. Mater Sci Eng A, 2001;304-306:716-720.

14. Johnson WL. Fundamental aspects of bulk metallic glass formation in multicomponent alloys. Mater Sci Forum, 1996;225-227:35-50.

15. Nieh TG, Wadsworth J, Liu CT, Ohkubo T, Hirotsu Y. Plasticity and structural instability in a bulk metallic glass deformed in the supercooled liquid region. Acta Mater, 2001;49:2887-2896.

16. Saotome Y, Zhang T, Inoue A. Microforming of MEMS parts with amorphous alloys. Mater Res Soc Symp Proc, 1999.

17. Inoue A, Zhang T, Takeuchi A. Micro-formability of bulk amorphous alloys. Proc Int Conference and Exhibition, Micro Mat'97, 1997.

18. Peter WH, Liaw PK, Buchanan RA, Liu CT, Brooks CR, Horton JA, Carmichael CA, Wright JL. Fatigue behavior of Zr-52.5, Al-10, Ti-5, Cu-17.9, Ni-14.6 bulk metallic glass. Intermetallics, Nov-Dec 2002;10:1125-1129.

19. Peter WH, Buchanan RA, Liu CT, Liaw PK. The fatigue behavior of a zirconium-based bulk metallic glass in vacuum and air. J Non-Crys Solids, Mar 2003;317:187-192.

20. Wang GY, Liaw PK, Peter WH, Yang B, Yokoyama A, Benson ML, Green BA, Kirkham MJ, White SA, Saleh T, McDaniels RL, Steward RV, Buchanan RA, Liu CT, Brooks CR. Fatigue behavior of bulk-metallic glasses. Intermetallics, 2004;12:885-892.

21. Peter WH, Buchanan RA, Liu CT, Liaw PK, Morrison ML, Horton JA, Carmichael CA, Wright JL. Localized corrosion behavior of a zirconium-based bulk metallic glass relative to its crystalline state. Intermetallics, Nov-Dec 2002;10:1157-1162.

22. Hiromoto S, Tsai AP, Sumita M, Hanawa T. Corrosion Behavior of Zr-65, Al-7.5, Ni-10, Cu-17.5 Amorphous Alloy for Biomedical Use. Mater Trans, 2001;42:656-659.

23. Hiromoto S, Tsai AP, Sumita M, Hanawa T. Polarization behavior of bulk Zr-base amorphous alloy immersed in cell culture medium. Mater Trans, 2002;43:3112-3117.

24. Morrison ML, Buchanan RA, Peker A, Peter WH, Horton JA, Liaw PK. Cyclic-anodic polarization studies of a Zr-41.2, Ti-13.8, Ni-10, Cu-12.5, Be-22.5 bulk metallic glass. Intermetallics, 2004;12:1177-1181.

25. Kramer J. J Annln Phys, 1934;19:37.

26. Kramer J. Phys, 1937;106:675.

27. Brenner A, Couch DE, Williams EK. J Res Natn Bur Stand, 1950;44:109.

28. Klement W, Willens RH, Duwez P. Non-crystalline structure in solidified gold-silicon alloys. Nature, Sep 1960;187:869-870.

29. Miroshnickenko IS, Salli IV. Ind Lab-USSR, 1959;25:1463.

30. Johnson WL, "Metallic Glasses," in ASM Handbook, 2, S. R. Lampman, Eds., ASM International, Materials Park, OH, 1990,

31. Johnson WL. Bulk glass-forming metallic alloys: Science and technology. MRS Bulletin, Oct 1999;24:42-56.

32. Chen HS, Turnbull D. Formation, stability and structure of palladium-silicon based alloy glasses. Acta Metall Mater, Aug 1969;17:1021-1031.

33. Chen HS, Turnbull D. Evidence of a glass-liquid transition in a gold-germanium-silicon alloy. J Chem Phys, Mar 1968;48:2560-2571.

34. Turnbull D, Fisher JC. Rate of nucleation in condensed systems. J Chem Phys, Jan 1949;17:71-73.

35. Turnbull D. Kinetics of heterogeneous nucleation. J Chem Phys, Feb 1950;18:198-203.

36. Pond R, Maddin R. TMS-AIME, 1969;245:2475.

37. Rao X, Xia Q, Li X, Si P. Foundation of bulk amorphous alloy database. Intermetallics, 2000;8:499-501.

38. Drehman AJ, Greer AL. Acta Metall, 1984;32:323.

39. Kui HW, Greer AL, Turnbull D. Appl Phys Lett, 1984;45:615.

40. Lee MC, Kendall JM, Johnson WL. Appl Phys Lett, 1982;40:382.

41. Inoue A, Zhang T, Masumoto T. Zr-Al-Ni amorphous alloys with high glass transition temperature and significant supercooled liquid region. Mater Trans, 1990;31:177-183.

42. Zhang T, Inoue A, Masumoto T. Amorphous Zr-Al-TM (TM=Co, Ni, Cu) alloys with significant supercooled liquid region of over 100K. Mater Trans, 1991;32:1005-1010.

43. Inoue A, Zhang T, Nishiyama N, Ohba K, Masumoto T. Preparation of 16 mm diameter rod of amorphous Zr-65, Al-7.5, Ni-10, Cu-17.5 alloys. Mater Trans, 1993;34:1234-1237.

44. Inoue A, Zhang T, Masumoto T. Production of amorphous cylinder and sheet of La-55, Al-25, Ni-20 alloy by a metallic mold casting method. Mater Trans, 1990;31:425-428.

45. Inoue A, Nakamura T, Nishiyama N. Mg-Cu-Y bulk amorphous alloys with high tensile strength produced by a high-pressure die casting method. Mater Trans, 1992;33:937-945.

46. Peker A, Johnson WL. A highly processable metallic glass: Zr-41.2, Ti-13.8, Cu-12.5, Ni-10.0, Be-22.5. Appl Phys Lett, Oct 1993;63:2342-2344.

47. Lin XH, Johnson WL. Formation of Ti-Zr-Cu-Ni bulk metallic glass. J Appl Phys, Dec 1995;78:6514-6519.

48. Inoue A, Ohtera K, Kita K, Masumoto T. Japan J Appl Phys, 1988;27:L2248.

49. Inoue A, Zhang T, Masumoto T. Al-La-Ni amorphous alloys with a wide supercooled liquid region. Mater Trans, 1989;30:965-972.

50. Inoue A, Gook JS. Fe-based ferromagnetic glassy alloys with a wide supercooled liquid region. Mater Trans, 1995;36:1180-1183.

51. Inoue A, Zhang T, Itoi T, Takeuchi A. New Fe-Co-Ni-Zr-B amorphous alloys with wide supercooled liquid regions and good soft magnetic properties. Mater Trans, 1997;38:359-362.

52. Inoue A, Nishiyama N, Matsuda T. Preparation of bulk glassy Pd-40, Ni-10, Cu-30, P-20 alloy of 40 mm in diameter by water quenching. Mater Trans, 1996;37:181-184.

53. Schwarz RB, He Y. Mater Sci Forum, 1997;235-238:231.

54. Zhang T, Inoue A. Thermal and mechanical properties of Ti-Ni-Cu-Sn amorphous alloys with a wide supercooled liquid region before crystallization. Mater Trans, 1998;39:1001-1006.

55. Zhang T, Inoue A. Preparation of Ti-Cu-Ni-Si-B amorphous alloys with a large supercooled liquid region. Mater Trans, 1999;40:301-306.

56. Adlwarth-Dieball R, Ryder PL. Crystallization kinetics of amorphous Cu-Ni-P alloys. Mater Sci Eng A, 1991;133:359-362.

57. Krutkina T, Reshetnikov S. Corrosion resistance of magnetically soft amorphous alloy of the base of cobalt. European Corrosion Congress, Trondheim, Norway, Sep 22-25, 1997.

58. Yokoyama K, Hamada K, Asaoka K. Mechanical and electro-chemical properties of Co-based glassy alloy as biomaterials. Trans 6th World Biomater Congress, Kamuela, HI, May 15, 2000.

59. Amiya K, Inoue A. Formation, thermal stability and mechanical properties of Ca-based bulk glassy alloys. Mater Trans, 2002;43:81-84.

60. Amiya K, Inoue A. Formation and thermal stability of Ca-Mg-Ag-Cu bulk glassy alloys. Mater Trans, 2002;43:2578-2581.

61. Guo FQ, Poon SJ, Shiflet GJ. Enhanced bulk metallic glass formability by combining chemical compatibility and atomic size effects. J Appl Phys, Jan 2004;97:013512.

62. Akatsuka R, Zhang T, Koshiba M, Inoue A. Mater Trans, 1999;40:258.

63. Inoue A, Nishiyama N, Amiya K, Zhang T, Masumoto T. Ti-based amorphous alloys with a wide supercooled liquid region. Mater Lett, 1994;19:131-135.

64. Inoue A, Zhang T, Nishiyama N, Ohba K, Masumoto T. Mater Sci Eng A, 1994;179-180:210.

65. Waniuk TA, Schroers J, Johnson WL. Critical cooling rate and thermal stability of Zr-Ti-Cu-Ni-Be alloys. Appl Phys Lett, Feb 2001;78:1213-1215.

66. Lu ZP, Liu CT. A new glass-forming ability criterion for bulk metallic glasses. Acta Mater, 2002;50:3501-3512.

67. Lu ZP, Liu CT. On the glass forming ability criteria of bulk metallic glasses. Mater Res Soc, 2003.

68. Lu ZP, Liu CT. Glass formation criterion for various glass-forming systems. Phys Rev Lett, 2003;91:115505.

69. Lu ZP, Liu CT. A new approach to understanding and measuring glass formation in bulk amorphous materials. Intermetallics, 2004;12:1035-1043.

70. Stansbury EE, Buchanan RA. *Fundamentals of Electrochemical Corrosion*. Materials Park, OH: ASM International, 2000.

71. Schroeder V, Gilbert CJ, Ritchie RO. Comparison of the corrosion behavior of a bulk amorphous metal, Zr-41.2, Ti-13.8, Cu-12.5, Ni-10, Be-22.5, with its crystallized form. Scripta Mater, 1998;38:1481-1485.

72. Koster U, Zander D, Triwikantoro, Rudiger A, Jastrow L. Environmental properties of Zr-based metallic glasses and nanocrystalline alloys. Scripta Mater, 2001;44:1649-1654.

73. He G, Bian Z, Chen GL. Corrosion behavior of a Zr-base bulk glassy alloy and its crystallized counterparts. Mater Trans, Jun 2001;42:1109-1111.

74. Raju VR, Kuhn U, Wolff U, Schneider F, Eckert J, Reiche R, Gebert A. Corrosion behaviour of Zr-based bulk glass-forming alloys containing Nb or Ti. Mater Lett, Nov 2002;57:173-177.

75. Pang S, Zhang T, Kimura H, Asami K, Inoue A. Corrosion behavior of Zr-(Nb-)Al-Ni-Cu glassy alloys. Mater Trans, 2000;41:1490-1494.

76. Gebert A, Buchholz K, El-Aziz AM, Eckert J. Hot water corrosion behaviour of Zr-Cu-Al-Ni bulk metallic glass. Mater Sci Eng A, 2001;316:60-65.

77. Hiromoto S, Tsai AP, Sumita M, Hanawa T. Effect of pH on the polarization behavior of Zr-65, Al-7.5, Ni-10, Cu-17.5 amorphous alloys in phosphate buffered solution. Corr Sci, 2000;42:2193-2200.

78. Hiromoto S, Tsai AP, Sumita M, Hanawa T. Effect of chloride ion on the anodic polarization behavior of Zr-65, Al-7.5, Ni-10, Cu-17.5 amorphous alloys in phosphate-buffered solution. Corr Sci, 2000;42:1651-1660.

79. Hiromoto S, Asami K, Tasi AP, Sumita M, Hanawa T. Surface composition and anodic polarization behavior of zirconium-based amorphous alloys in a phosphate-buffered saline solution. J Electrochem Soc, Apr 2002;149:B117-B122.

80. Hiromoto S, Noda K, Hanawa T. Development of electrolytic cell with cell-culture for metallic biomaterials. Corr Sci, 2002;44:955-965.

81. Nieh TG, Schuh C, Wadsworth J, Li Y. Strain rate-dependent deformation in bulk metallic glasses. Intermetallics, 2002;10:1177-1182.

82. Nieh TG, Mukai T, Liu CT, Wadsworth J. Superplastic behavior of a Zr, Al-10, Ti-5, Cu-17.9, Ni-14.6 metallic glass in the supercooled liquid region. Scripta Mater, 1999;40:1021-1027.

83. Kawamura Y, Nakamura T, Inoue A. Superplasticity in Pd-40, Ni-40, P-20 metallic glass. Scripta Mater, 1998;39:301-306.

84. Wright WJ, Saha R, Nix WD. Deformation mechanisms of the Zr-40, Ti-14, Ni-10, Cu-12, Be-24 bulk metallic glasses. Mater Trans, 2001;42:642-649.

85. Schuh CA, Nieh TG. A nanoindentation study of serrated flow in bulk metallic glasses. Acta Mater, 2003;51:87-99.

86. Wright WJ, Schwarz RB, Nix WD. Localized heating during serrated plastic flow in bulk metallic glasses. Mater Sci Eng A, 2001;319-321:229-232.

87. Spaepen F. Metall Trans, 1977;25:407.

88. Leamy HJ, Chen HS, Wang TT. Plastic flow and fracture of metallic glass. Metall Trans, Mar 1972;3:699-708.

89. Gilbert CJ, Ager III JW, Schroeder V, Ritchie RO. Light emission during fracture of a Zr-Ti-Ni-Cu-Be bulk metallic glass. Appl Phys Lett, Jun 1999;74:3809-3811.

90. Zhang H, Wang ZG, Qiu KQ, Zang QS, Zhang HF. Cyclic deformation and fatigue crack propagation of a Zr-based bulk amorphous metal. Mater Sci Eng A, Sep 2003;356:173-180.

91. Li JX, Shan GB, Gao KW, Qiao LJ, Chu WY. In situ SEM study of formation and growth of shear bands and microcracks in bulk metallic glasses. Mater Sci Eng A, 2003;354:337-343.

92. Hufnagel TC, El-Deiry P, Vinci RP. Development of shear band structure during deformation of a Zr-57, Ti-5, Cu-20, Ni-8, Al-10 bulk metallic glass. Scripta Mater, 2000;43:1071-1075.

93. Lewandowski JJ, Stelmashenko NA, Greer AL. Experimental observations of shear banding in bulk metallic glasses. TMS Annual Meeting, Charlotte, NC, March 14-18, 2004.

94. Davis L. *Metallic Glasses*. Metals Park, OH: American Society for Metals, 1978.

95. Gilbert CJ, Lippmann JM, Ritchie RO. Fatigue of a Zr-Ti-Cu-Ni-Be bulk amorphous metal: stress/life and crack-growth behavior. Scripta Mater, 1998;38:537-542.

96. Gilbert CJ, Schroeder V, Ritchie RO. Mechanisms for fracture and fatigue-crack propagation in a bulk metallic glass. Metall Mater Trans A, Jul 1999;30:1739-1753.

97. Hertzberg R. *Deformation and Fracture Mechanics of Engineering Materials*. New York, NY: John Wiley & Sons, Inc., 1996.

98. Tatschl A, Gilbert CJ, Schroeder V, Pippan R, Ritchie RO. Stereophotogrammetric investigation of overload and cyclic fatigue fracture surface morphologies in a Zr-Ti-Ni-CU-Be bulk metallic glass. J Mater Res, Apr 2000;15:898-903.

99. Parker SP, Ed., Dictionary of Scientific and Technical Terms, McGraw-Hill, Inc., New York, 1994.

100. Shipilov SA. Mechanisms for corrosion fatigue crack propagation. Fatigue Fract Eng M, 2002;25:243-259.

101. Uhlig HH. Action of corrosion and stress on 13% Cr stainless steel. Met Prog, 1950;57:486-487.

102. Phelps EH, Loginow AW. Stress corrosion of steels for aircraft and missles. Corr, 1960;16:325-335.

103. Schroeder V, Gilbert CJ, Ritchie RO. Effect of aqueous environment on fatigue-crack propagation behavior in a Zr-based bulk amorphous metal. Scripta Mater, 1999;40:1057-1061.

104. Ritchie RO, Schroeder V, Gilbert CJ. Fracture, fatigue and environmentally-assisted failure of a Zr-based bulk amorphous metal. Intermetallics, 2000;8:469-475.

105. Schroeder V, Gilbert CJ, Ritchie RO. A comparison of the mechanisms of fatigue-crack propagation behavior in a Zr-based bulk amorphous metal in air and an aqueous chloride solution. Mater Sci Eng A, 2001;317:145-152.

106. Maruyama N, Nakazawa K, Hanawa T. Fatigue properties of Zr-based bulk amorphous alloy in phosphate buffered saline solution. Mater Trans, 2002;43:3118-3121.

107. Seifert V, Zimmermann M, Trantakis C, Vitzthum HE, Kuhnel K, Raabe A, Bootz F, Schneider JP, Schmidt F, Dietrich J. Open MRI-guided neurosurgery. Acta Neurochir, 1999;141:455-464.

108. Horton JA, Parsell DE. Biomedical potential of a zirconium-based bulk metallic glass. Mater Res Soc Symp Proc, 2003.

109. Schenck JF. The role of magnetic susceptibility in magnetic resonance imaging: MRI magnetic compatibility of the first and second kinds. Med Phys, Jun 1996;23:815-850.

110. Chao EYS, Aro HT, "Biomechanics of fracture fixation," in Basic Orthopaedic Biomechanics, 2nd, V. C. Mow and W. C. Hayes, Eds., Lippincott-Raven Publishers, Philadelphia, PA, 1997,

111. Alexander H, "Composites," in Biomaterials Science: An Introduction to Materials in Medicine, B. D. Ratner, A. S. Hoffman, F. J. Schoen and J. E. Lemons, Eds., Academic Press, San Diego, CA, 1996,

112. Bradley GW, McKenna GB, Dunn HK, Daniels AU, Statton WO. Effects of flexural rigidity of plates on bone healing. J Bone Joint Surg A, Sep 1979;61:866-872.

113. Coutts RD, Harris WH, Weinberg EH. Compressing plating: Experimental study of the effect on bone formation rates. Acta Orthop Scand, 1973;44:256-262.

114. Tonino AJ, Davidson CL, Klopper PJ, Linclau LA. Protection from stress in bone and its effects: Experiments with stainless steel and plastic plates in dogs. J Bone Joint Surg B, Feb 1976;58:107-113.

115. Uhthoff HK, Dubuc FL. Bone structure changes in the dog under rigid internal fixation. Clin Orthop, 1971;81:165-170.

116. Woo SLY, Akeson WH, Coutts RD, Rutherford L, Doty D, Jemmott GF, Amiel D. A comparison of cortical bone atrophy secondary to fixation with plates with large differences in bending stiffness. J Bone Joint Surg A, Mar 1976;58:190-195.

117. Wolff J. *Das Gesetz der Transformation der Knochen [The Law of Bone Remodeling]*. Berlin: Springer-Verlag, 1892.

118. Huiskes R, Verdonschot N, "Biomechanics of artificial joints: The hip," in Basic Orthopaedic Biomechanics, 2, V. C. Mow and W. C. Hayes, Eds., Lippincott-Raven Publishers, Philadelphia, PA, 1997, 317-351.

119. Roesler H. The history of some fundamental concepts in bone biomechanics. J Biomech, 1987;20:1025-1034.

120. Williams D, Ed., Concise Encyclopedia of Medical and Dental Materials, Pergamon Press, Oxford, UK, 1990.

121. Schoen FJ, "Host reactions to biomaterials and their evaluation," in Biomaterials Science: An introduction to materials in medicine, B. D. Ratner, A. S. Hoffman, F. J. Schoen and J. E. Lemons, Eds., Academic Press, San Diego, CA, 1996,

122. Williams DF, "Biomaterials and biocompatibility: An introduction," in Fundamental Aspects of Biocompatibility, 1, D. F. Williams, Eds., CRC Press, Inc., Boca Raton, FL, 1981, 1-10.

123. Wataha JC. Principles of biocompatibility for dental practitioners. J Prosthet Dent, Aug 2001;86:203-209.

124. Taylor DM. Trace metal patterns and disease. J Bone Joint Surg B, 1973;55:422-423.

125. Bundy KJ, Luedemann R. Factors which influence the accuracy of corrosion rate determination of implant materials. Ann Biomed Mater, 1989;17:159-175.

126. Geurtsen W. Biocompatibility of dental casting alloys. Crit Rev Oral Biol Med, 2002;13:71-84.

127. Wataha JC, Lockwood PE, Khajotia SS, Turner R. Effect of pH on element release from dental casting alloys. J Prosthet Dent, 1998;80:691-698.

128. Wataha JC, Hanks CT, Craig RG. In vitro synergistic, antagonistic, and duration of exposure effects of metal cations on eukaryotic cells. J Biomed Mater Res, 1992;26:1297-1309.

129. Yamamoto A, Honma R, Sumita M. Cytotoxicity evaluation of 43 metal salts using murine fibroblasts and osteoblastic cells. J Biomed Mater Res, 1998;39:331-340.

130. Shettlemore MG, Bundy KJ. Assessment of dental material degradation product toxicity using a bioluminescent bacterial assay. Dent Mater, 2002;18:445-453.

131. Niinomi M. Recent titanium R&D for biomedical applications in Japan. JOM, Jun 1999;51:32-34.

132. Wataha JC. Alloys for prosthodontic restorations. J Prosthet Dent, Apr 2002;87:351-363.

133. Wataha JC. Biocompatibility of dental casting alloys: A review. J Prosthet Dent, Feb 2000;83:223-234.

134. Sauvant MP, Pepin D, Bohatier J, Groliere CA, Guillot J. Toxicity assessment of 16 inorganic environmental pollutants by six bioassays. Ecotox Environ Safe, 1997;37:131-140.

135. Schmalz G, Arenholt-Bindslev D, Pfuller S, Schweikl H. Cytotoxicity of metal cations used in dental cast alloys. ATLA, May/Jun 1997;25:323-330.

136. Matsuno H, Yokoyama A, Watari F, Uo M, Kawasaki T. Biocompatibility and osteogenesis of refractory metal implants, titanium, hafnium, niobium, tantalum and rhenium. Biomaterials, 2001;22:1253-1262.

137. Schmalz G, Langer H, Schweikl H. Cytotoxicity of dental alloy extracts and corresponding metal salt solutions. J Dent Res, Oct 1998;77:1772-1778.

138. Klein CL, Kohler H, Kirkpatrick CJ. Increased adhesion and activation of polymorphonuclear neutrophis granulocytes to endothelial cells under heavy metal exposure in vitro. Pathobiology, 1994;62:90-98.

139. Puleo DA, Huh WW. Acute toxicity of metal ions in cultures of osteogenic cells derived from bone marrow stromal cells. J Appl Biomater, 1995;6:109-116.

140. Smith KL, Lawrence DA. Immunomodulation of in vitro antigen presentation by cations. Toxicol Appl Pharm, 1988;96:476-484.

141. Sun ZL, Wataha JC, Hanks CT. Effects of metal ions on osteoblast-like metabolism and differentiation. J Biomed Mater Res, 1997;34:29-37.

142. Wagner M, Klein CL, van Kooten TG, Kirkpatrick CJ. Mechanisms of cell activation by heavy metal ions. J Biomed Mater Res A, 1998;42:443-452.

143. Lin XH, Johnson WL, Rhim WK. Effect of oxygen impurity on crystallization of an undercooled bulk glass forming Zr-Ti-Cu-Ni-Al alloy. Mater Trans, 1997;38:473-477.

144. Bundy KJ. Corrosion and other electrochemical aspects of biomaterials. Crit Rev Biomed Engr, 1994;22:139-251.

145. Stern M, Geary AL. Electrochemical polarization: A theoretical analysis of the shape of polarization curves. J Electrochem Soc, 1957;104:56-63.
146. Keddam M, "Anodic Dissolution," in Corrosion Mechanisms in Theory and Practice, P. Marcus and J. Oudar, Eds., Marcel Dekker, Inc., New York, 1995,
147. Mansfeld F, Kendig M. Concerning the choice of scan rate in polarization measurements. Corr, 1981;37:545-546.
148. Sziraki L, Csontos H, Varsanyi ML, Kiss L. Corrosion mechanism of tin-zinc alloys in neutral medium. Corr Sci, 1993;35:371-376.
149. Chen G, Wen X, Zhang N. Corrosion resistance and ion dissolution of titanium with different surface microroughness. Bio-med Mater Eng, 1998;8:61-74.
150. Bumgardner JD, Lucas LC. Corrosion and cell culture evaluations of nickel-chromium dental casting alloys. J Appl Biomater, 1994;5:203-213.
151. Lappalainen R, Yli-Urpo A. Release of elements from some gold alloys and amalgams in corrosion. Scand J Dent Res, 1987;95:364-368.
152. Wataha JC, Malcolm CT, Hanks CT. Correlation between cytotoxicity and the elements released by dental casting alloys. Int J Prosthodont, 1995;8:9-14.
153. Wataha JC, Craig RG, Hanks CT. The release of elements of dental casting alloys into cell-culture medium. J Dent Res, Jun 1991;70:1014-1018.
154. Shapiro SS, Wilk MB. An analysis of variance test for normality. Biometrika, 1965;52:591-611.
155. Levene H, "Robust tests for the equality of variances," in Contributions to probability and statistics, I. Olkin, Eds., Stanford University Press, Stanford, CA, 1960,

156. Box GEP, Cox DR. An analysis of transformations. J Royal Stat Soc B, 1964;26:211-243.

157. Welch BL. On the comparison of several mean values: an alternative approach. Biometrika, 1951;38:330-336.

158. Tamhane AC, Dunlop DD. *Statistics and Data Analysis*. Upper Saddle River, NJ: Prentice Hall, 2000.

159. Hoaglin D, Mosteller F, Tukey J. *Understanding Robust and Exploratory Data Analysis*. New York: Wiley, 1983.

160. Zhai T, Xu YG, Martin JW, Wilkinson AJ, Briggs GAD. A self-aligning four-point bend testing rig and sample geometry effect in four-point bend fatigue. Inter J Fatigue, 1999;21:889-894.

161. *Annual Book of ASTM Standards*. Philadelphia: ASTM, 2003.

162. Klug HP, Alexander LE. *X-ray Diffraction Procedures for Polycrystalline and Amorphous materials*. New York: John Wiley & Sons, 1962.

163. Inoue A. Stabilization of metallic supercooled liquid and bulk amorphous alloys. Acta Mater, 2000;48:279-306.

164. Morrison ML, Buchanan RA, Peker A, Liaw PK, Horton JA. Electrochemical behavior of a Ti-based bulk metallic glass. Submitted to Intermetallics, 2005;

165. Morrison ML, Buchanan RA, Liu CT, Green BA, Liaw PK, Horton JA. Corrosion behavior of a Zr-based bulk metallic glass in a 0.6 M NaCl electrolyte. Unpublished research, 2005;

166. Szewieczek D, Baron A. Electrochemical corrosion and its influence on magnetic properties of Fe-75.5, Zi-13.5, B-9, Nb-3, Cu-1 alloy. J Mater Proc Tech, 2005;164-165:940-946.

167. Baril G, Pebere N. The corrosion of pure magnesium in aerated and deaerated sodium sulphate solutions. Corr Sci, 2001;43:471-484.

168. Chieh TC, Chu J, Liu CT, Wu JK. Corrosion of Zr-52.5, Cu-17.9, Ni-14.6, Al-10, Ti-5 bulk metallic glasses in aqueous solutions. Mater Lett, 2003;57:3022-3025.

169. Morrison ML, Buchanan RA, Leon RV, Liu CT, Green BA, Liaw PK, Horton JA. The electrochemical evaluation of a Zr-based bulk metallic glass in a phosphate-buffered saline electrolyte. J Biomed Mater Res A, 2005;In press:

170. Hiromoto S, Tsai AP, Sumita M, Hanawa T. Effects of surface finishing and dissolved oxygen on the polarization behavior of the Zr-65, Al-7.5, Ni-10, Cu-17.5 amorphous alloy in phosphate buffered solution. Corr Sci, 2000;42:2167-2185.

171. Clark GCF, Williams DF. The effects of proteins on metallic corrosion. J Biomed Mater Res, 1982;16:125-134.

172. Buchholz K, Gebert A, Mummert K, Eckert J, Schultz L. Corrosion behavior of bulk amorphous and crystalline Zr-55, Al-10, Cu-30, Ni-5 alloys at ambient and elevated temperature. Mater Sci Forum, 2000;343-346:213-218.

173. Gebert A, Mummert K, Eckert J, Schultz L, Inoue A. Electrochemical investigations on the bulk glass forming Zr-55, Cu-30, Al-10, Ni-5 alloy. Mater Corr, 1997;48:293-297.

174. Buchholz K, Gebert A, Mummert K, Eckert JS, L. Investigations on the electrochemical behavior of Zr-Al-Cu-Ni bulk metallic glass. Fall, 1998.

175. Pan J, Karlen C, Ulfvin C. Electrochemical study of resistance to localized corrosion of stainless steels for biomaterial applications. J Electrochem Soc, Mar 2000;147:1021-1025.

176. Escudero ML, Lopez MF, Ruiz J, Garcia-Alonso MC, Canahua H. Comparative study of the corrosion behavior of MA-956 and conventional metallic biomaterials. J Biomed Mater Res, Jul 1996;31:313-317.

177. Bolton J, Hu X. In vitro corrosion testing of PVD coatings applied to a surgical grade Co-Cr-Mo alloy. J Mater Sci - Mater M, 2002;13:567-574.

178. Metikos-Hukovic M, Kwokal A, Piljac J. The influence of niobium and vanadium on passivity of titanium-based implants in physiological solution. Biomaterials, 2003;24:3765-3775.

179. Okazaki Y, Ito Y, Kyo K, Tateishi T. Corrosion resistance and corrosion fatigue strength of new titanium alloys for medical implants without V and Al. Mater Sci Eng A, 1996;213:138-147.

180. Kuroda D, Hiromoto S, Hanawa T, Katada Y. Corrosion behavior of nickel-free high nitrogen austenitic stainless steel in simulated biological environments. Mater Trans, 2002;43:3100-3104.

181. Buchanan RA, Lemons JE. In vivo corrosion-polarization behavior of titanium-base and cobalt-base surgical alloys. Orlando, Florida, April 24-27, 1982.

182. Katz JL, "Orthopedic applications," in Biomaterials Science, B. D. Ratner, A. S. Hoffman, F. J. Schoen and J. E. Lemons, Eds., Academic Press, San Diego, 1996, 335-346.

183. Donachie M. Biomedical alloys. Advanced Mater Proc, Jul 1998;63-65.

184. Mudali UK, Baunack S, Eckert J, Schultz L, Gebert A. Pitting corrosion of bulk glass-forming zirconium-based alloys. J Alloys Compounds, 2004;377:290-297.

185. Pourbaix M. *Atlas of Electrochemical Equilibria in Aqueous Solutions*. Houston: National Association of Corrosion Engineers, 1974.

186. Yokoyama Y, Shinohara T, Fukaura K, Inoue A. Characterization of crystalline inclusions in cast bulk Zr-Cu-Ni-Al glassy alloy. Mater Trans, 2004;45:1819-1823.

187. Peter WH, Liaw PK, Buchanan RA, Liu CT. Unpublished research. 2005;

188. Thomson W. Trans R Soc, Edinb, 1853;20:261.

189. Dillon OW. J Mech Phys Solids, 1963;11:21.

190. Kratochvil J, Dillon OW. J Appl Phys, 1969;40:3207.

191. Henneke EG, Reifsnider KL, Strinchcomb WW. J Metals, 1979;31:11.

192. Blanc RH, Giacometti E. Stress Analysis by Thermoelastic Technics, 1984.

193. Nayroles B, Bouc R, Caumon H, Chezeaux JC, Giacornetti E. Int J Eng Sci, 1981;19:929.

194. Yang B. Thermographic detection of fatigue damage of reactor pressure vessel (RPV) steels. J Mater Eng Perform, 2003;12:345-353.

195. Liaw PK, Wang H, Jiang L, Yang B, Huang JY, Kuo RC, Huang JG. Thermographic detection of fatigue damage of pressure vessel steels at 1,000 Hz and 20 Hz. Scripta Mater, 2000;42:389-395.

196. Chen L, Liaw PK, Wang H, He YH, McDaniels RL, Jiang L, Yang B, Klarstrom DL. Cyclic deformation behavior of Haynes HR-120 superalloy under low-cycle fatigue loading. Mech Mater, 2004;36:85-98.

197. Jiang L, Wang H, Liaw PK, Brooks CR, Chen L, Klarstrom DL. Temperature evolution and life prediction in fatigue of superalloys. Met Mater Trans A, 2004;35:839-848.

198. Jiang L, Wang H, Liaw PK, Brooks CR, Klarstrom DL. Characterization of the temperature evolution during high-cycle fatigue of the ULTIMET superalloy: Experiment and theoretical modeling. Mater Trans A, 2001;32:2279-2296.

199. Jiang L, Wang H, Liaw PK, Brooks CR, Klarstrom DL. Effects of cyclic loading on temperature evolution of ULTIMET superalloy: Experiment and theoretical modeling. Trans Nonferrous Met Soc China, 2002;12:734-747.

200. Jiang L, Wang H, Liaw PK, Brooks CR, Klarstrom DL. Temperature evolution during low-cycle fatigue of ULTIMET alloy: Experiment and modeling. Mech Mater, 2004;36:73-84.

201. Wang H, Jiang L, He Y, Chen L, Liaw PK, Seeley R, Klarstrom DL. Infrared imaging during low-cycle fatigue of HR-120 alloy. Met Mater Trans A, 2002;33:1287-1292.

202. Wang H, Jiang L, Liaw PK, Brooks CR, Klarstrom DL. Infrared temperature mapping of ULTIMET alloy during high-cycle fatigue tests. Met Mater Trans A, 2000;31:1307-1310.

203. Yang B, Liaw PK, Wang H, Jiang L, Huang JY, Kuo RC, Huang JG. Thermographic investigation of the fatigue behavior of reactor pressure vessel steels. Mater Sci Eng A, 2001;314:131-139.

204. Yang B, Liaw PK, Wang G, Peter WH, Buchanan RA, Yokoyama Y, Huang JY, Kuo RC, Huang JG, Fielden DE, Klarstrom DL. Thermal-imaging technologies for

detecting mechanical damage during high-cycle fatigue. Met Mater Trans A, 2004;35:15-23.

205. Liaw PK, Yang B, Tian H, Jiang L, Wang H, Huang JY, Kuo RC, Huang JG, Fielden D, Strizak JP, Mansur LK, "Frequency effects on fatigue behavior and temperature evolution of steels," in Fatigue and Fracture Mechanics, 33, ASTM STP1417, W. G. Reuter and R. S. Piascik, Eds., ASTM International, West Conshohocken, PA, 2002, 524-556.
206. Conner RD, Li Y, Nix WD, Johnson WL. Shear band spacing under bending of Zr-based metallic glass plates. Acta Mater, May 2004;52:2429-2434.
207. Hufnagel TC, Fan C, Ott RT, Li J, Brennan S. Controlling shear band behavior in metallic glasses through microstructural design. Intermetallics, 2002;10:1163-1166.
208. Brockwell PJ, Davis RA. *Introduction to Time Series and Forecasting*. New York: Springer-Verlag, 1996.
209. Pekarskaya E, Kim CP, Johnson WL. In situ transmission electron microscopy studies of shear bands in a bulk metallic glass based composite. J Mater Res, Sep 2001;16:2513-2518.
210. Yang B, Liaw PK, Morrison M, Liu CT, Buchanan RA, Huang JY, Kuo RC, Huang JG, Fielden DE. Temperature evolution during fatigue damage. Intermetallics, 2005;13:419-428.
211. Edwards BJ, Feigl K, Morrison ML, Yang B, Liaw PK, Buchanan RA. Modeling the dynamic propagation of shear bands in bulk metallic glasses. Scripta Mater, 2005;In press:

212. Yang B, Morrison M, Nieh TG, Liaw PK, Liu CT, Buchanan RA. Temperature evolution of nanoscale shear bands and a new criterion of the glass transition temperature in bulk metallic glasses. 2005;

213. Yang B, Morrison ML, Liaw PK, Liu CT, Buchanan RA, Wang GY, Denda M. Dynamic evolution of nanoscale shear bands in a bulk-metallic glass. Appl Phys Lett, 2005;86:141904.

214. Inoue A. Bulk amorphous and nanocrystalline alloys with high functional properties. Mater Sci Eng A, 2001;304-306:1-10.

215. James RS, "Aluminum-Lithium Alloys," in ASM Handbook - Properties and Selections: Nonferrous Alloys and Special Purpose Materials, 2, Eds., ASM International, Metals Park, OH, 1990,

216. Wataha JC, Hanks CT, Craig RG. The in vitro effects of metal cations on eukaryotic cell metabolism. J Biomed Mater Res, 1991;25:1133-1149.

217. Yamamoto A, Honma R, Tanaka A, Sumita M. Generic tendency of metal salt cytotoxicity for six cell lines. J Biomed Mater Res, 1999;47:396-403.

218. Wataha JC, Hanks CT, Sun ZL. In vitro reaction of macrophages to metal ions from dental biomaterials. Dent Mater, Jul 1995;11:239-245.

219. Schedle A, Samorapoompichit P, Rausch-Fan XH, Franz A, Fureder W, Sperr WR, Sperr W, Ellinger A, Slavicek R, Boltz-Nitulescu G, Valent P. Response of L-929 fibroblasts, human gingival fibroblasts, and human tissue mast cells to various metal cations. J Dent Res, Aug 1995;74:1513-1520.

220. Wataha JC, Hanks CT, Sun Z. Effect of cell line on in vitro metal ion cytotoxicity. Dent Mater, May 1994;10:156-161.

221. Kappert HF, Kroll M, Schwickerath H, "Cell culture studies," in Compatibility of dental alloys with special reference to alternative methods in diagnosis, H. Schwickerath, Eds., Deutscher Arzteverlag, Cologne, Germany, 1998, 45-76.

222. Wang C, Zhang Q, Jiang F, Zhang H, Hu Z. Electrochemical behavior of amorphous alloy Zr-55, Al-10, Cu-30, Ni-5 in 3.5% NaCl solution. Acta Metall Sinica, Jul 2002;38:765-769.

223. Qin FX, Zhang HF, Deng YF, Ding BZ, Hu ZQ. Corrosion resistance of Zr-based bulk amorphous alloys containing Pd. J Alloys Compounds, 2004;375:318-323.

224. Qin FX, Zhang HF, Chen P, Chen FF, Qiao DC, Hu ZQ. Corrosion behavior of bulk amorphous Zr-55, Al-10, Cu-30, Ni-(5-x), Pd-x alloys. Mater Lett, 2004;58:1246-1250.

225. Pang S, Zhang T, Asami K, Inoue A. Formation, corrosion behavior, and mechanical properties of bulk glassy Zr-Al-Co-Nb alloys. J Mater Res, Jul 2003;18:1652-1658.

226. Qin C, Asami K, Zhang T, Zhang W, Inoue A. Corrosion behavior of Cu-Zr-Ti-Nb bulk glassy alloys. Mater Trans, 2003;44:749-753.

227. Qin C, Asami K, Zhang T, Zhang W, Inoue A. Effects of additional elements on the glass formation and corrosion behavior of bulk glassy Cu-Hf-Ti alloys. Mater Trans, 2003;44:1042-1045.

228. Qin C, Zhang W, Kimura H, Asami K, Inoue A. New Cu-Zr-Al-Nb bulk glassy alloys with high corrosion resistance. Mater Trans, 2004;45:1958-1961.

229. Yamamoto T, Qin C, Zhang T, Asami K, Inoue A. Formation, thermal stability, mechanical properties and corrosion resistance of Cu-Zr-Ti-Ni-Nb bulk glassy alloys. Mater Trans, 2003;44:1147-1152.

230. Asami K, Qin CL, Zhang T, Inoue A. Effect of additional elements on the corrosion behavior of a Cu-Zr-Ti bulk metallic glass. Mater Sci Eng A, Jul 2004;375-377:235-239.

231. Hiromoto S, Hanawa T, Ogawa K. Thermodynamic structural stability and polarization behavior of cast amorphous alloy. Mater Trans, 2003;44:1824-1829.

232. Morrison ML, Buchanan RA, Miracle DB, Senkov ON, Liaw PK. Electrochemical behavior of Ca-based bulk metallic glasses. Submitted to Acta Mater, 2005;

233. Inoue A, Takeuchi A. Recent progress in bulk glassy, nanoquasicrystalline and nanocrystalline alloys. Mater Sci Eng A, Jul 2004;375-377:16-30.

APPENDICES

APPENDIX I

Table 1. Bulk metallic glass alloy systems with the calendar years when the first paper or patent was published. (Adapted from [214] with permission from Elsevier.)

BMG Composition	Year
Mg–Ln–M (Ln = lanthanide metal; M = Ni, Cu, Zn)	1988
Ln–Al–TM (TM = Fe, Co, Ni, Cu)	1989
Ln–Ga–TM	1989
Zr–Al–TM	1990
Ti–Zr–TM	1993
Zr–Ti–TM–Be	1993
Zr–(Ti, Nb,Pd)–Al–TM	1995
Fe–(Al, Ga)–(P, C, B, Si, Ge)	1995
Fe–(Nb, Mo)–(Al, Ga)–(P, B, Si)	1995
Pd–Cu–Ni–P	1996
Pd–Ni–Fe–P	1996
Co–(Al, Ga)–(P, B, Si)	1996
Fe–(Zr, Hf, Nb)–B	1996
Co–(Zr, Hf, Nb)–B	1996
Ni–(Zr, Hf, Nb)–B	1996
Pd–Cu–B–Si	1997
Ti–Ni–Cu–Sn	1998
Fe–Co–Ln–B	1998
Fe–Ga–(Cr, Mo)–(P, C, B)	1998
Fe–(Nb, Cr, Mo)–(C, B)	1999
Ni–(Nb, Cr, Mo)–(P, B)	1999
Co–Ta–B	1999
Fe–Ga–(P, B)	2000
Ni–Zr–Ti–Sn–Si	2001
Cu–(Zr, Hf)–Ti	2001
Cu–(Zr, Hf)–Ti–(Y, Be)	2001
Cu–(Zr, Hf)–Ti–(Fe, Co, Ni)	2002
Ni–(Nb, Ta)–Zr–Ti	2002
Fe–Si–B–Nb	2002
Co–Fe–Si–B–Nb	2002
Ca–Mg–Ag–Cu	2002
Ca–Mg–Cu	2002
Ni–Si–B–Ta	2002
Y–Al–Ni	2004

Table 2. Comparison of pertinent properties of a bulk metallic glass (BMG) with those of bone and common biomaterials. (Reprinted from [169] with permission from John Wiley & Sons.)

	Cortical Bone	**CoCrMo**	**Ti-6Al-4V**	**316L SS**	**BMG (Vit 105)**
Tensile Yield Strength (MPa)	130 - 150	450 - 1030	760 - 1050	190 - 690	1900
Elastic Strain Limit (%)	1	0.18	.67	.34	2.0-2.2
Plastic Strain to Failure (%)	2	8 - 28	8 - 15	12 - 40	<1
Young's Modulus (GPa)	3 - 50	210 - 255	101 - 125	193 - 210	90
Hardness (Vickers)	63 - 75	345 - 390	320	365	590
Toughness (MPa $m^{0.5}$)	3.2 - 8.0	--	65 - 92	100	55 - 60
Fatigue Limit at 10^7 cycles (MPa)	20 - 60	207 - 970	598 - 816	200 - 800	910
Density (g/cm^3)	0.7 – 1.85	8.3	4.4	7.9	5.9

Table 3. Fatigue endurance limits and fatigue ratios based on the stress ranges of high-strength alloys, Zr-based BMGs and pure zirconium. (Reprinted from [20] with permission from Elsevier.)

Material	Yield Strength (MPa)	Ultimate Tensile Strength (MPa)	Fatigue-Endurance Limit (MPa)	Fatigue Ratio
$Zr_{50}Cu_{40}Al_{10}$ [20]	1821	1821	752	0.413
$Zr_{50}Cu_{30}Al_{10}Ni_{10}$ [20]	1900	1900	865	0.455
$Zr_{52.5}Cu_{17.9}Ni_{14.6}Al_{10}Ti_5$ (Vit 105) [18]	1700	1700	907	0.534
$Zr_{41.2}Ti_{13.8}Cu_{12.5}Ni_{10}Be_{22.5}$ (LM-001 or Vit 1) [95]	1900	1900	152	0.080
300 M Steel [97]	1670	2000	800	0.400
Ti-6Al-4V [97]	885	1035	515	0.498
2090-T81 Al-Li Alloy [215]	483	517	250	0.484
Zirconium (Grade 702) [215]	310	430	145	0.337

Table 4. Summary of cytotoxicology studies of metal salts from the literature [129, 134, 135, 216-221]. The metal ions were ranked from most to least toxic, in terms of the IC_{50} values for each cell line and bioassay. These ranks were then divided by the total number of metal ions evaluated within each study to produce a normalized rank. These normalized ranks were averaged to produce a mean normalized rank for each metal ion. In other words, the normalized ranks range from 0.0 to 1.0, with increasing values denoting decreasing cytotoxicity. The metal ions have been ranked from most toxic to least toxic.

Metal Ion	Mean Normalized Rank	Metal Ion	Mean Normalized Rank
Cr^{6+}	0.14	Sn^{4+}	0.61
Cd^{2+}	0.15	Mn^{2+}	0.62
Hg^{2+}	0.17	Ge^{4+}	0.64
Ag^{+}	0.18	Be^{2+}	0.66
V^{3+}	0.22	In^{3+}	0.67
Hg^{+}	0.23	Ti^{4+}	0.68
Tl^{3+}	0.28	Hf^{4+}	0.71
Ir^{4+}	0.34	Pd^{2+}	0.73
Sb^{3+}	0.35	Cs^{+}	0.76
Zn^{2+}	0.38	Cr^{3+}	0.76
Pt^{4+}	0.42	Fe^{3+}	0.79
Bi^{3+}	0.43	Fe^{2+}	0.80
Rh^{3+}	0.44	Pb^{2+}	0.81
V^{5+}	0.45	Sn^{2+}	0.82
Au^{3+}	0.45	Zr^{4+}	0.83
Tl^{+}	0.48	Ru^{3+}	0.83
Co^{2+}	0.48	Ta^{5+}	0.83
Cu^{+}	0.49	Mo^{5+}	0.83
Cu^{2+}	0.53	Sr^{2+}	0.86
Y^{3+}	0.53	Cr^{2+}	0.88
Nb^{5+}	0.54	Rb^{+}	0.90
Ga^{3+}	0.57	Al^{3+}	0.94
W^{6+}	0.59	Ba^{2+}	0.95
Ni^{2+}	0.60	Li^{+}	0.99

Table 5. Composition of the phosphate-buffered saline (PBS) electrolyte.

	NaCl	KCl	Na_2HPO_4	KH_2PO_4
Concentration (g / L H_2O)	8.01	0.20	1.15	0.20
Concentration (mol / L H_2O)	1.37×10^{-1}	2.68×10^{-3}	8.10×10^{-3}	1.47×10^{-3}

Table 6. Glass transition, T_g, crystallization, T_x, solidus, T_m, and liquidus, T_l, temperatures, heat of crystallization, ΔH_x, and heat of fusion, ΔH_m, as well as a reduced glass transition temperature, $T_{rg}=T_g/T_l$, for $Ca_{65}Mg_{15}Zn_{20}$, $Ca_{55}Mg_{18}Zn_{11}Cu_{16}$, and $Ca_{50}Mg_{20}Cu_{30}$ alloys, as obtained from DSC at a heating rate of 20 K/min.

Materials	**T_g (K)**	**T_x (K)**	**T_m (K)**	**T_l (K)**	**ΔH_x (J/g)**	**ΔH_m (J.g)**	**T_{rg}**
$Ca_{65}Mg_{15}Zn_{20}$	364	400	608	621	128	147	0.586
$Ca_{55}Mg_{18}Zn_{11}Cu_{16}$	391	432	597	610	110	165	0.641
$Ca_{50}Mg_{20}Cu_{30}$	399	433	628	688	138	184	0.580

Table 7. The mean corrosion parameters as determined from the cyclic-anodic polarization tests. The error ranges are 95% confidence intervals. All potentials are in reference to the saturated calomel electrode (SCE).

Materials	Electrolyte	E_{corr} (mV)	E_{pit} (mV)	E_{pp} (mV)	η_{pit} (mV)	η_{pp} (mV)	CPR (μm/year)
$Ca_{65}Mg_{15}Zn_{20}$	0.05 Na_2SO_4	-1535 ± 31	--[b]	--[b]	--[b]	--[b]	5691 ± 1046
$Ca_{55}Mg_{18}Zn_{11}Cu_{16}$	0.05 Na_2SO_4	-479 ± 320	-352 ± 340	-936 ± 256	128 ± 41	-457 ± 329	311 ± 184
$Ca_{50}Mg_{20}Cu_{30}$	0.05 Na_2SO_4	-1165 ± 17	--[a]	--[a]	--[a]	--[a]	1503 ± 435
$Mg_{97.6}Zn_{2.2}Zr_{0.2}$ (ZK60)	0.05 Na_2SO_4	-1501 ± 82	--[a]	--[a]	--[a]	--[a]	425 ± 321
Vit 1	0.6 M NaCl	-250 ± 44	-152 ± 26	-222 ± 5	98 ± 70	28 ± 44	2.8 ± 2.0
Vit 105	0.6 M NaCl	-264 ± 30	324 ± 399	-188 ± 66	603 ± 409	91 ± 64	29.3 ± 33.5
316L SS	0.6 M NaCl	-133 ± 27	264 ± 55	-135 ± 29	397 ± 63	-2 ± 39	4.2 ± 7.0
CoCrMo	0.6 M NaCl	-186 ± 41	--[a]	--[a]	--[a]	--[a]	0.5 ± 0.3
Zircaloy	0.6 M NaCl	-397 ± 95	258 ± 134	28 ± 46	661 ± 222	440 ± 52	0.6 ± 0.5
Vit 1	PBS	-391 ± 105	19 ± 119	-207 ± 11	410 ± 209	184 ± 94	1.0 ± 0.6
Vit 105	PBS	-405 ± 35	69 ± 53	-180 ± 11	474 ± 73	225 ± 38	0.8 ± 0.4
LM-010	PBS	-372 ± 62	217 ± 17	38 ±32	589 ± 57	411 ± 70	2.9 ± 2.6
316L SS	PBS	-221 ± 7	310 ± 75	-74 ± 19	531 ± 75	147 ± 18	1.5 ± 0.4
Ti-6Al-4V	PBS	-435 ± 44	--[a]	--[a]	--[a]	--[a]	0.3 ± 0.2
CoCrMo	PBS	-444 ± 135	--[a]	--[a]	--[a]	--[a]	0.3 ± 0.2

a. no localized corrosion occurred; b. Active pitting at E_{corr}

Table 8. Relevant corrosion parameters from this study and other reports in the literature. A majority of the values from the literature (particularly the CPR values) were estimated from the reported data. Error ranges signify 95% confidence intervals. All compositions are presented in atomic percent.

Authors	Material	Minimum Dimension (mm)	T (°C)	Electrolyte	Mean η_{pit}[a] (mV)	Mean η_{pp}[b] (mV)	Mean CPR[c] (μm/year)
Morrison et al. [24]	$Zr_{41.2}Ti_{13.8}Ni_{10}Cu_{12.5}Be_{22.5}$ (Vit 1)	2	22	0.6 M NaCl	97 ±70	26 ± 44	2.5 ± 2.0
Morrison et al. [24]	$Zr_{41.2}Ti_{13.8}Ni_{10}Cu_{12.5}Be_{22.5}$ (Vit 1)	2	37	0.6 M NaCl	142 ± 73	68 ± 72	1.3 ± 1.7
Morrison et al. [165]	316L Stainless Steel	NA	22	0.6 M NaCl	401 ± 61	15 ± 48	4.2 ± 7.0
Morrison et al. [165]	Ti-6Al-4V	NA	22	0.6 M NaCl	--[d]	--[d]	
Morrison et al. [165]	CoCrMo	NA	22	0.6 M NaCl	--[d]	--[d]	0.5 ± 0.3
Morrison et al. [165]	Zircaloy	NA	22	0.6 M NaCl	661 ± 222	440 ± 52	0.6 ± 0.5
Morrison et al. [165]	$Zr_{52.5}Cu_{17.9}Ni_{14.6}Al_{10}Ti_5$ (Vit 105)	6.5	22	0.6 M NaCl	603 ± 409	91 ± 64	29.3 ± 33.5
Chieh et al. [168]	$Zr_{52.5}Cu_{17.9}Ni_{14.6}Al_{10}Ti$ (Vit 105)	7	22	0.6 M NaCl	360	--[e]	1.5
Chieh et al. [168]	304 Stainless Steel	NA	22	0.6 M NaCl	490	--[e]	1.2
Peter et al. [21]	$Zr_{52.5}Cu_{17.9}Ni_{14.6}Al_{10}Ti_5$ (Vit 105)	6.5	22	0.6 M NaCl	300	20	1.3
Wang et al. [222]	$Zr_{55}Al_{10}Cu_{30}Ni_5$	2	22	0.6 M NaCl	200 – 300	--[e]	--[e]
Qin et al. [223]	$Zr_{55}Al_{10}Cu_{30}Ni_5$	2	25	0.6 M NaCl	180	--[e]	--[e]
Qin et al. [223]	$Zr_{55}Al_{10}Cu_{30}Ni_4Pd_1$	2	25	0.6 M NaCl	70	--[e]	--[e]
Qin et al. [223]	$Zr_{55}Al_{10}Cu_{30}Ni_2Pd_3$	2	25	0.6 M NaCl	55	--[e]	--[e]
Qin et al. [223]	$Zr_{55}Al_{10}Cu_{30}Pd_5$	2	25	0.6 M NaCl	50	--[e]	--[e]
Qin et al. [224]	$Zr_{55}Al_{10}Cu_{30}Ni_5$	2	25	0.6 M NaCl	175	--[e]	--[e]
Qin et al. [224]	$Zr_{55}Al_{10}Cu_{30}Pd_5$	2	25	0.6 M NaCl	45	--[e]	--[e]
Schroeder et al. [71]	$Zr_{41.2}Ti_{13.8}Ni_{10}Cu_{12.5}Be_{22.5}$ (Vit 1)	7	22	0.5 M NaCl	207	--[e]	--[e]
Pang et al. [225]	$Zr_{55}Al_{20}Co_{25}$	2.5	25	0.5 M NaCl	500	--[e]	--[e]
Pang et al. [225]	$Zr_{55}Al_{17.5}Co_{25}Nb_{2.5}$	2.5	25	0.5 M NaCl	535	--[e]	--[e]
Pang et al. [225]	$Zr_{55}Al_{15}Co_{25}Nb_5$	2.5	25	0.5 M NaCl	840	--[e]	--[e]
Pang et al. [75]	$Zr_{60}Al_{10}Ni_{10}Cu_{20}$	MS[f]	25	0.5 M NaCl	>135	--[e]	2
Pang et al. [75]	$Zr_{55}Al_{10}Ni_{10}Cu_{20}Nb_5$	MS[f]	25	0.5 M NaCl	>200	--[e]	0.5

Table 8. Continued.

Authors	Material	Minimum Dimension (mm)	T (°C)	Electrolyte	Mean η_{pit}[a] (mV)	Mean η_{pp}[b] (mV)	Mean CPR[c] (μm/year)
Pang et al. [75]	$Zr_{50}Al_{10}Ni_{10}Cu_{20}Nb_{10}$	MS[f]	25	0.5 M NaCl	>150	--[e]	--[e]
Pang et al. [75]	$Zr_{45}Al_{10}Ni_{10}Cu_{20}Nb_{15}$	MS[f]	25	0.5 M NaCl	>120	--[e]	0.4
Pang et al. [75]	$Zr_{40}Al_{10}Ni_{10}Cu_{20}Nb_{20}$	MS[f]	25	0.5 M NaCl	>240	--[e]	0.3
He et al. [73]	$Zr_{52.5}Cu_{17.9}Ni_{14.6}Al_{10}Ti_5$ (Vit 105)	2	22	0.5 M NaCl	225	--[e]	--[e]
Qin et al. [226]	$Cu_{58.2}Zr_{29.1}Ti_{9.7}Nb_3$	1.5	25	0.5 M NaCl	--[e]	--[e]	30
Qin et al. [226]	$Cu_{57.6}Zr_{28.8}Ti_{9.6}Nb_4$	1.5	25	0.5 M NaCl	--[e]	--[e]	20
Qin et al. [226]	$Cu_{57}Zr_{28.5}Ti_{9.5}Nb_5$	1.5	25	0.5 M NaCl	--[e]	--[e]	17
Qin et al. [226]	$Cu_{60}Zr_{30}Ti_{10}$	1.5	25	0.5 M NaCl	--[e]	--[e]	290
Qin et al. [226]	$Cu_{59.4}Zr_{29.7}Ti_{9.9}Nb_1$	1.5	25	0.5 M NaCl	--[e]	--[e]	120
Qin et al. [226]	$Cu_{58.8}Zr_{29.4}Ti_{9.8}Nb_2$	1.5	25	0.5 M NaCl	--[e]	--[e]	80
Qin et al. [227]	$Cu_{60}Hf_{25}Ti_{15}$	1.5	25	0.5 M NaCl	--[e]	--[e]	100
Qin et al. [227]	$Cu_{58.8}Hf_{24.5}Ti_{14.7}Mo_2$	1.5	25	0.5 M NaCl	75	--[e]	1
Qin et al. [227]	$Cu_{58.8}Hf_{24.5}Ti_{14.7}Ta_2$	1.5	25	0.5 M NaCl	70	--[e]	1
Qin et al. [227]	$Cu_{58.8}Hf_{24.5}Ti_{14.7}Nb_2$	1.5	25	0.5 M NaCl	65	--[e]	1
Qin et al. [228]	$Cu_{55}Zr_{40}Al_5$	1.5	25	0.5 M NaCl	--[e]	--[e]	200
Qin et al. [228]	$Cu_{50}Zr_{45}Al_5$	1.5	25	0.5 M NaCl	--[e]	--[e]	120
Qin et al. [228]	$Cu_{50}Zr_{40}Al_5Nb_5$	1.5	25	0.5 M NaCl	--[e]	--[e]	10
Yamamoto et al. [229]	$Cu_{55.8}Zr_{27.9}Ti_{9.3}Ni_7$	1.5	25	0.5 M NaCl	--[e]	--[e]	7
Yamamoto et al. [229]	$Cu_{57}Zr_{28.5}Ti_{9.5}Nb_5$	1.5	25	0.5 M NaCl	--[e]	--[e]	18
Asami et al. [230]	$Cu_{60}Zr_{30}Ti_{10}$	1.5	25	0.5 M NaCl	--[e]	--[e]	290
Asami et al. [230]	$Cu_{59.4}Zr_{29.7}Ti_{9.9}Nb_1$	1.5	25	0.5 M NaCl	--[e]	--[e]	120
Asami et al. [230]	$Cu_{59.4}Zr_{29.7}Ti_{9.9}Mo_1$	1.5	25	0.5 M NaCl	--[e]	--[e]	140
Asami et al. [230]	$Cu_{58.8}Zr_{29.4}Ti_{9.8}Ta_2$	1.5	25	0.5 M NaCl	--[e]	--[e]	200
Raju et al. [74]	$Zr_{60}Cu_{20}Al_{10}Ni_8Nb_2$	3	22	0.01 M NaCl	420	--[e]	--[e]
Raju et al. [74]	$Zr_{59}Cu_{20}Al_{10}Ni_8Nb_3$	3	22	0.01 M NaCl	620	--[e]	--[e]

Table 8. Continued.

Authors	Material	Minimum Dimension (mm)	T (°C)	Electrolyte	Mean η_{pit}[a] (mV)	Mean η_{pp}[b] (mV)	Mean CPR[c] (μm/year)
Raju et al. [74]	$Zr_{57}Cu_{15.4}Al_{10}Ni_{12.6}Nb_5$	3	22	0.01 M NaCl	730	--[e]	--[e]
Raju et al. [74]	$Zr_{59}Cu_{20}Al_{10}Ni_8Ti_3$	3	22	0.01 M NaCl	640	--[e]	--[e]
Raju et al. [74]	$Zr_{52.5}Cu_{17.9}Ni_{14.6}Al_{10}Ti_5$ (Vit 105)	3	22	0.01 M NaCl	505	--[e]	--[e]
Morrison et al.	$Ti_{43.3}Zr_{21.7}Ni_{7.5}Be_{27.5}$ (LM-010)	2	37	Deaerated PBS [g]	589 ± 57	411 ± 70	2.9 ± 2.6
Morrison et al. [24]	$Zr_{41.2}Ti_{13.8}Ni_{10}Cu_{12.5}Be_{22.5}$ (Vit 1)	2	22	Deaerated PBS [g]	478 ± 348	215 ± 69	0.8 ± 0.7
Morrison et al. [24]	$Zr_{41.2}Ti_{13.8}Ni_{10}Cu_{12.5}Be_{22.5}$ (Vit 1)	2	37	Deaerated PBS [g]	410 ± 209	184 ± 94	1.0 ± 0.6
Hiromoto et al. [22]	$Zr_{65}Al_{7.5}Ni_{10}Cu_{17.5}$	MS[f]	37	Deaerated PBS [g]	850	--[e]	--[e]
Hiromoto et al. [77]	$Zr_{65}Al_{7.5}Ni_{10}Cu_{17.5}$	MS[f]	37	Deaerated PBS [g]	630	--[e]	--[e]
Hiromoto et al. [78]	$Zr_{65}Al_{7.5}Ni_{10}Cu_{17.5}$	MS[f]	37	Deaerated PBS [g]	800	--[e]	0.001
Kuroda et al. [180]	316L Stainless Steel	NA	37	Deaerated PBS [g]	575	--[e]	--[e]
Morrison et al. [169]	$Zr_{52.5}Cu_{17.9}Ni_{14.6}Al_{10}Ti_5$ (Vit 105)	6.5	37	Deaerated PBS [g]	474 ± 73	225 ± 38	0.8 ± 0.4
Morrison et al. [169]	316L Stainless Steel	NA	37	Deaerated PBS [g]	531 ± 75	147 ± 18	1.5 ± 0.4
Morrison et al. [169]	CoCrMo	NA	37	Deaerated PBS [g]	--[d]	--[d]	0.3 ± 0.2
Morrison et al. [169]	$Zr_{52.5}Cu_{17.9}Ni_{14.6}Al_{10}Ti_5$ (Vit 105)	6.5	37	Deaerated PBS [g]	474 ± 73	225 ± 38	0.8 ± 0.4
Morrison et al. [169]	316L Stainless Steel	NA	37	Deaerated PBS [g]	531 ± 75	147 ± 18	1.5 ± 0.4
Morrison et al. [169]	CoCrMo	NA	37	Deaerated PBS [g]	--[d]	--[d]	0.3 ± 0.2
Morrison et al. [169]	Ti-6Al-4V	NA	37	Deaerated PBS [g]	--[d]	--[d]	0.3 ± 0.2
Pan et al.[175]	316LVM Stainless Steel	NA	25	Deaerated PBS [g]	835	315	--[e]
Hiromoto et al. [231]	$Zr_{65}Al_{7.5}Ni_{10}Cu_{17.5}$	2	22	Deaerated Hanks' Solution	400 – 810	--[e]	--[e]
Hiromoto et al. [231]	$Zr_{65}Al_{7.5}Ni_{10}Cu_{17.5}$	2.5	22	Deaerated Hanks' Solution	370 – 460	--[e]	--[e]
Hiromoto et al. [23]	$Zr_{65}Al_{7.5}Ni_{10}Cu_{17.5}$	3	37	Deaerated Hanks' Solution	410 – 730	--[e]	0.03 – 0.13
Hiromoto et al. [23]	$Zr_{65}Al_{7.5}Ni_{10}Cu_{17.5}$	3	37	Deaerated MEM [h]	310 – 570	--[e]	0.004 – 0.08

Table 8. Continued.

Authors	Material	Minimum Dimension (mm)	T (°C)	Electrolyte	Mean η_{pit}[a] (mV)	Mean η_{pp}[b] (mV)	Mean CPR[c] (μm/year)
Hiromoto et al. [23]	$Zr_{65}Al_{7.5}Ni_{10}Cu_{17.5}$	3	37	Deaerated MEM + FBS [i]	530 – 550	--[e]	0.005 – 0.09
Morrison et al. [232]	$Ca_{65}Mg_{15}Zn_{20}$	3	22	0.05 M Na_2SO_4	--[j]	--[j]	5691 ± 1046
Morrison et al. [232]	$Ca_{55}Mg_{18}Zn_{11}Cu_{16}$	3	22	0.05 M Na_2SO_4	128 ± 41	-457 ± 329	311 ± 184
Morrison et al. [232]	$Ca_{50}Mg_{20}Cu_{30}$	3	22	0.05 M Na_2SO_4	--[d]	--[d]	1503 ± 435
Morrison et al. [232]	$Mg_{97.6}Zn_{2.2}Zr_{0.2}$ (ZK60)	NA	22	0.05 M Na_2SO_4	--[d]	--[d]	425 ± 321
Peter et al. [21]	$Zr_{52.5}Cu_{17.9}Ni_{14.6}Al_{10}Ti_5$ (Vit 105)	6.5	22	0.05 M Na_2SO_4	--[d]	--[d]	0.4
Szewieczek et al. [166]	$Fe_{73.5}Si_{13.5}B_9Nb_9Cu_1$[f]			0.5 M Na_2SO_4	--[d]	--[d]	927
Raju et al. [74]	$Zr_{60}Cu_{20}Al_{10}Ni_8Nb_2$	3	22	0.1 M Na_2SO_4	--[d]	--[d]	~1
Raju et al. [74]	$Zr_{59}Cu_{20}Al_{10}Ni_8Nb_3$	3	22	0.1 M Na_2SO_4	--[d]	--[d]	~1
Raju et al. [74]	$Zr_{57}Cu_{15.4}Al_{10}Ni_{12.6}Nb_5$	3	22	0.1 M Na_2SO_4	--[d]	--[d]	~1
Raju et al. [74]	$Zr_{59}Cu_{20}Al_{10}Ni_8Ti_3$	3	22	0.1 M Na_2SO_4	--[d]	--[d]	~1
Raju et al. [74]	$Zr_{52.5}Cu_{17.9}Ni_{14.6}Al_{10}Ti_5$ (Vit 105)	3	22	0.1 M Na_2SO_4	--[d]	--[d]	~1
Baril and Pebere [167]	Pure Mg	NA		0.1 M Na_2SO_4	--[d]	--[d]	~1000
Baril and Pebere [167]	Pure Mg	NA		0.01 M Na_2SO_4	--[d]	--[d]	~1000

a. Pitting overpotential ($E_{pit} - E_{corr}$); b. Protection overpotential ($E_{pp} - E_{corr}$); c. Corrosion penetration rate; d. No pitting observed; e. Not investigated / reported; f. Melt-spun ribbons; g. Phosphate-buffered saline; h. Eagle's minimum essential medium; i. Eagle's minimum essential medium + fetal bovine serum; j. Active at E_{corr}

Table 9. Results from the ANOVA and Tukey post-hoc tests. Within each parameter derived from the electrochemical tests, materials not connected by the same letter are significantly different. No pitting was observed on the Ti-6Al-4V or the CoCrMo samples. (Reprinted from [169] with permission from John Wiley & Sons.)

Materials	**E_{corr}**	**E_{pit}**	**E_{pp}**	**$E_{pit} - E_{corr}$**	**$E_{pp} - E_{corr}$**	**CPR**
Vit 105 BMG	B	B	B	A	B	A B
316L SS	A	A	A	A	A	C
Ti-6Al-4V	B					A
CoCrMo	B					A
Vit 1[24]	B	B	B	A	A B	B C

Table 10. The nominal composition of the Vit 105 BMG alloy and the mean elemental compositions as measured by energy-dispersive spectroscopy (EDS). The error ranges are 95% confidence intervals. All compositions are given in atomic percent (at.%).

Element	Nominal Composition	Amorphous Matrix	Pits
Zr	52.5	53.6 ± 0.7	11.8 ± 6.3
Cu	17.9	16.8 ± 0.5	78.7 ± 8.9
Ni	14.6	15.2 ± 0.3	6.3 ± 1.4
Al	10.0	9.9 ± 0.5	2.3 ± 1.2
Ti	5.0	4.5 ± 0.4	1.1 ± 0.5

Table 11. Summary of shear-band parameters derived from analyses of the IR data.

Parameter	Mean ± 95% CIs*	Median	Maximum	Minimum
Length (mm)	0.50 ± 0.06	0.50	1.01	0.22
Width (mm)	0.42 ± 0.03	0.43	0.72	0.14
T_{max} (°C)	20.71 ± 0.21	20.69	22.30	19.92
ΔT_{max} (°C)	0.91 ± 0.19	0.91	2.58	0.20
T_{avg} (°C)	20.20 ± 0.14	20.15	21.26	19.66
ΔT_{avg} (°C)	0.53 ± 0.11	0.51	1.39	0.09

* 95% confidence intervals (CIs)

APPENDIX II

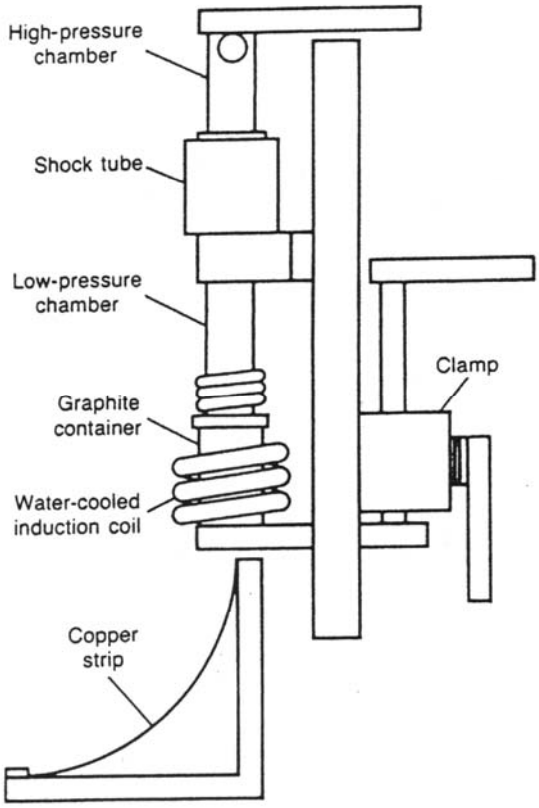

Figure 1. Schematic drawing of gun quenching device used by Duwez et al. for glass formation experiments. (Reprinted from [30] with permission from ASM International.)

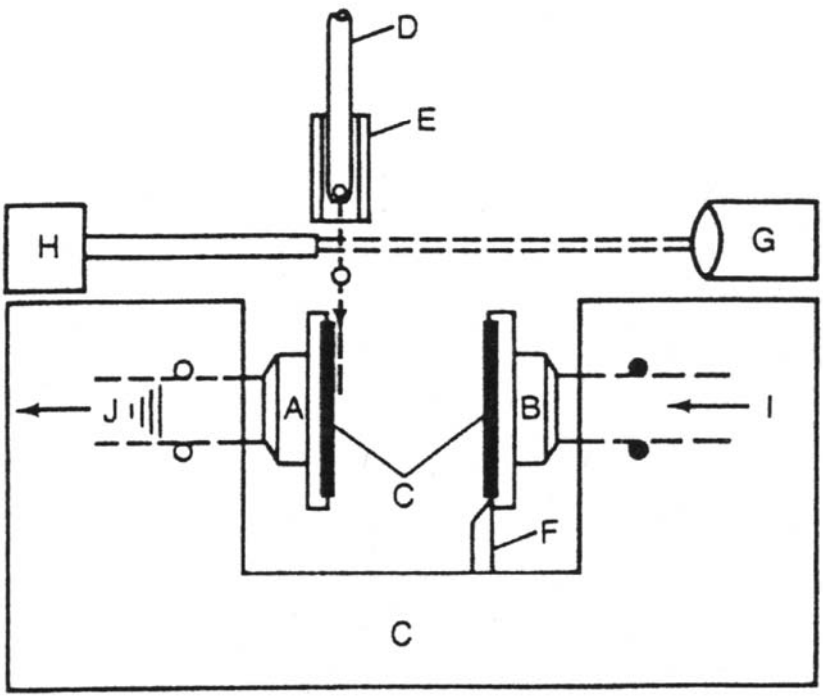

Figure 2. Schematic drawing of the piston and anvil device used by Duwez et al. and Miroshnickenko and Salli for rapid solidification of liquid metal drops. A, anvil; B, piston; C, chassis; D, crucible containing the sample droplet; E, heating element; F, latch to release piston; G, light source; H, photocell and timing circuits; I, pneumatic piston system; and J, pneumatic cushion for anvil. (Reprinted from [30] with permission from ASM International.)

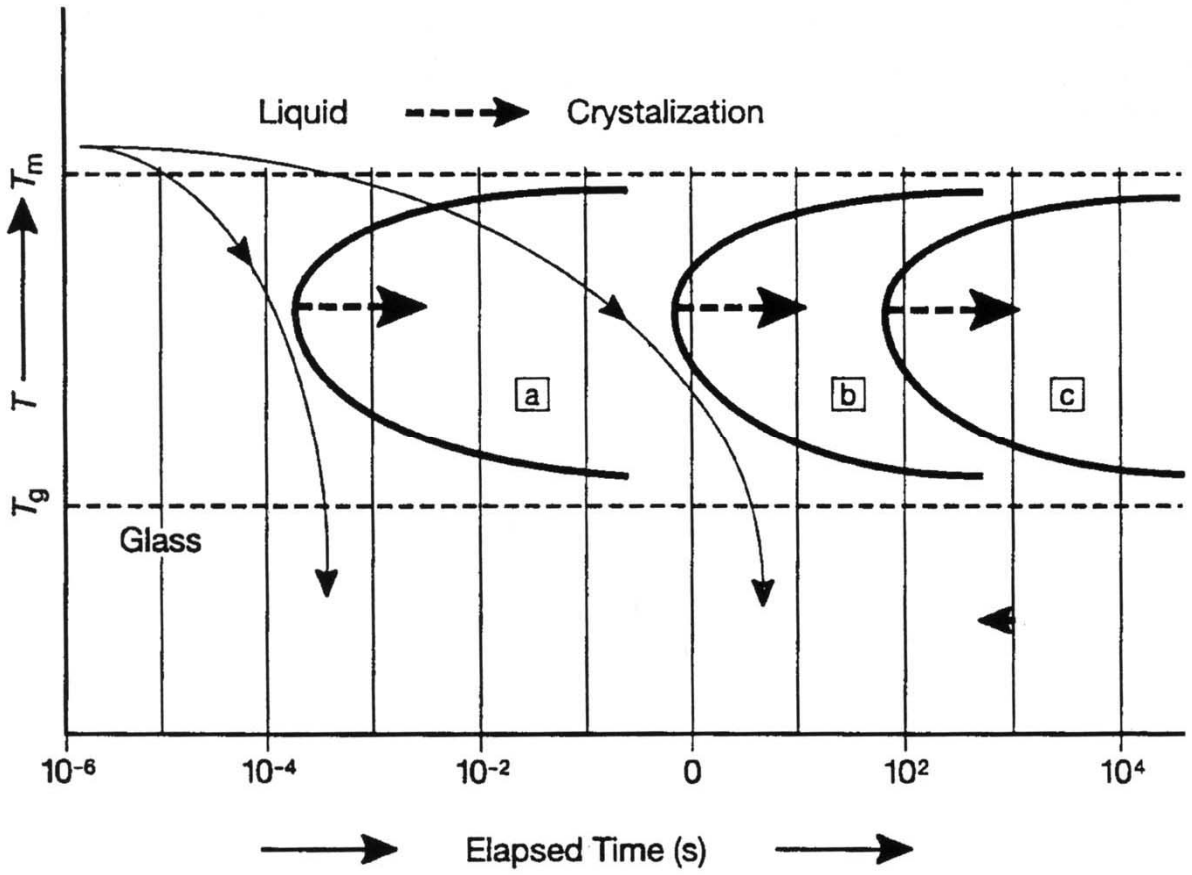

Figure 3. Time-temperature-transformation (TTT) diagram demonstrating decrease in critical cooling rate (R_c), from a to c, necessary for glass formation.

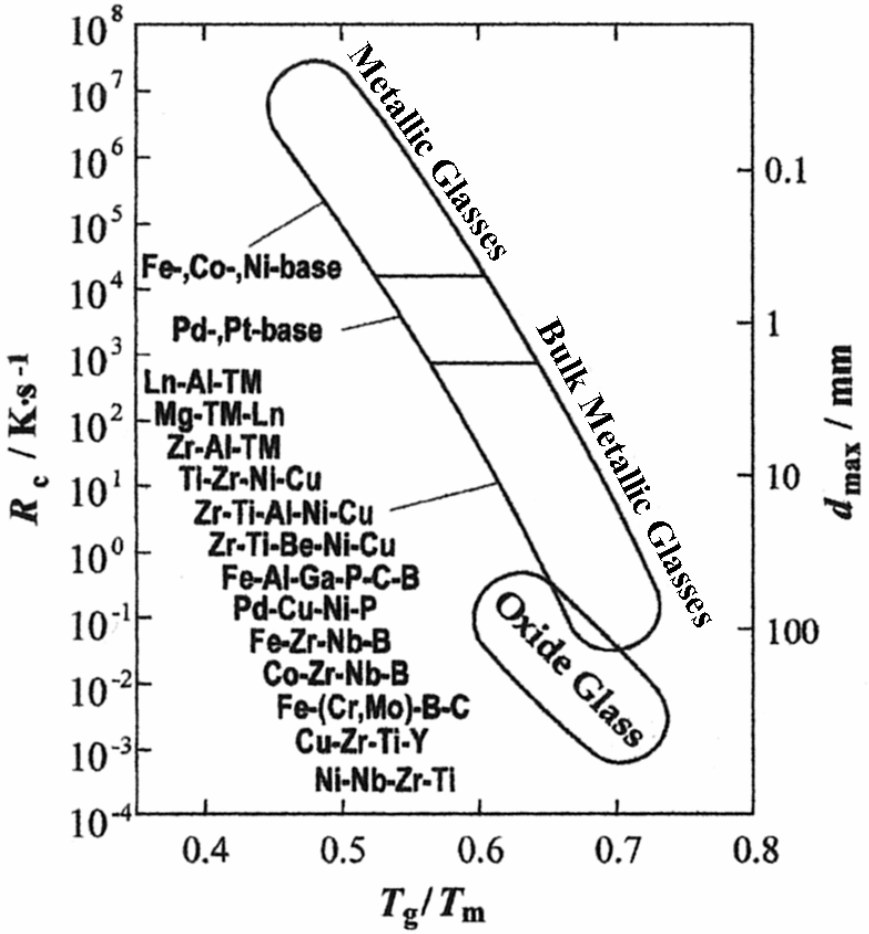

Figure 4. Relationship among the reduced glass transition temperature ($T_r = T_g / T_m$), the critical cooling rate for glass formation (R_c), and the maximum sample thickness for glass formation (d_{max}). (Reprinted from [233] with permission from Elsevier.)

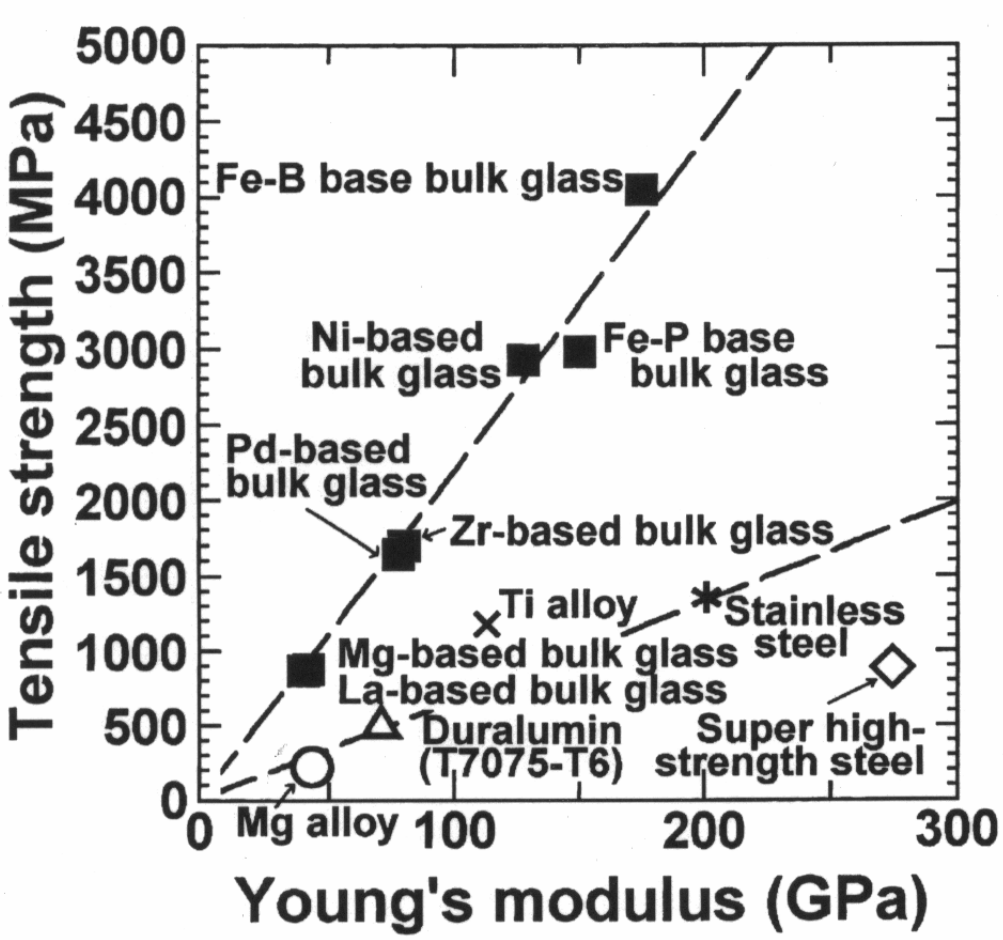

Figure 5. Relationship between Young's modulus and tensile strength for bulk metallic glasses and conventional, crystalline alloys. The data for the Fe-based BMGs is based on compression tests. (Reprinted from [214] with permission from Elsevier.)

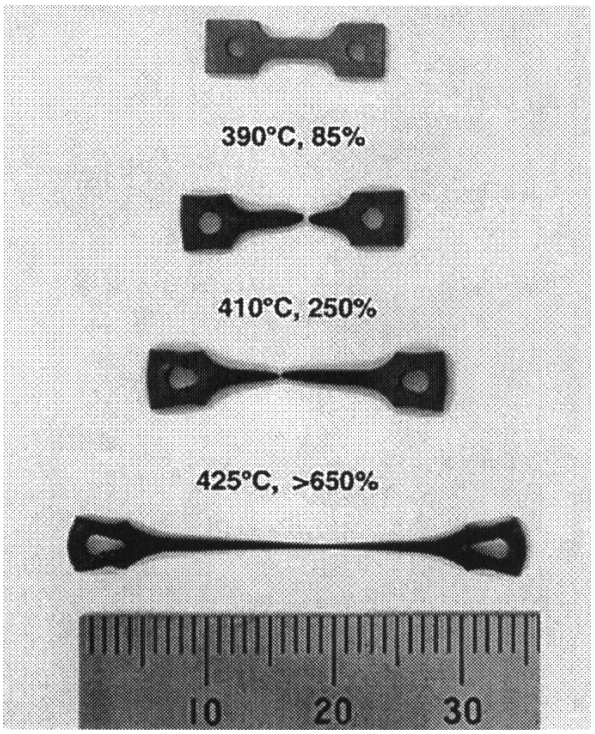

(a)

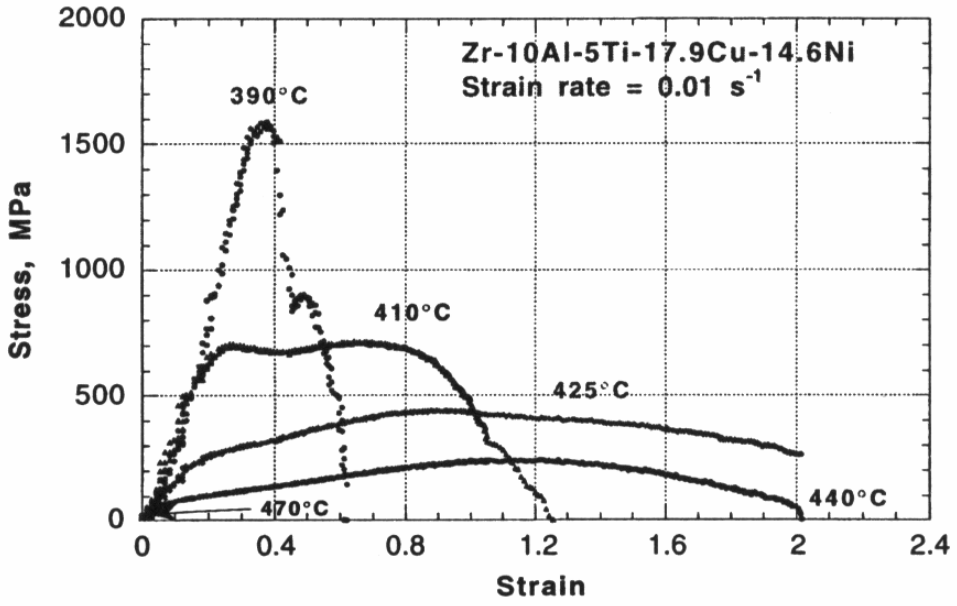

(b)

Figure 6. Data demonstrating superplasticity in the $Zr_{52.5}Cu_{17.9}Ni_{14.6}Al_{10.0}Ti_{5.0}$ (at.%) BMG alloy, also known as Vitreloy 105 (Vit 105), (a) Samples fractured at different temperatures at strain rates of 10^{-2} s^{-1}, and (b) stress-strain curves of Vit 105 at temperatures near the supercooled liquid region. (Reprinted from [82] with permission from Elsevier.)

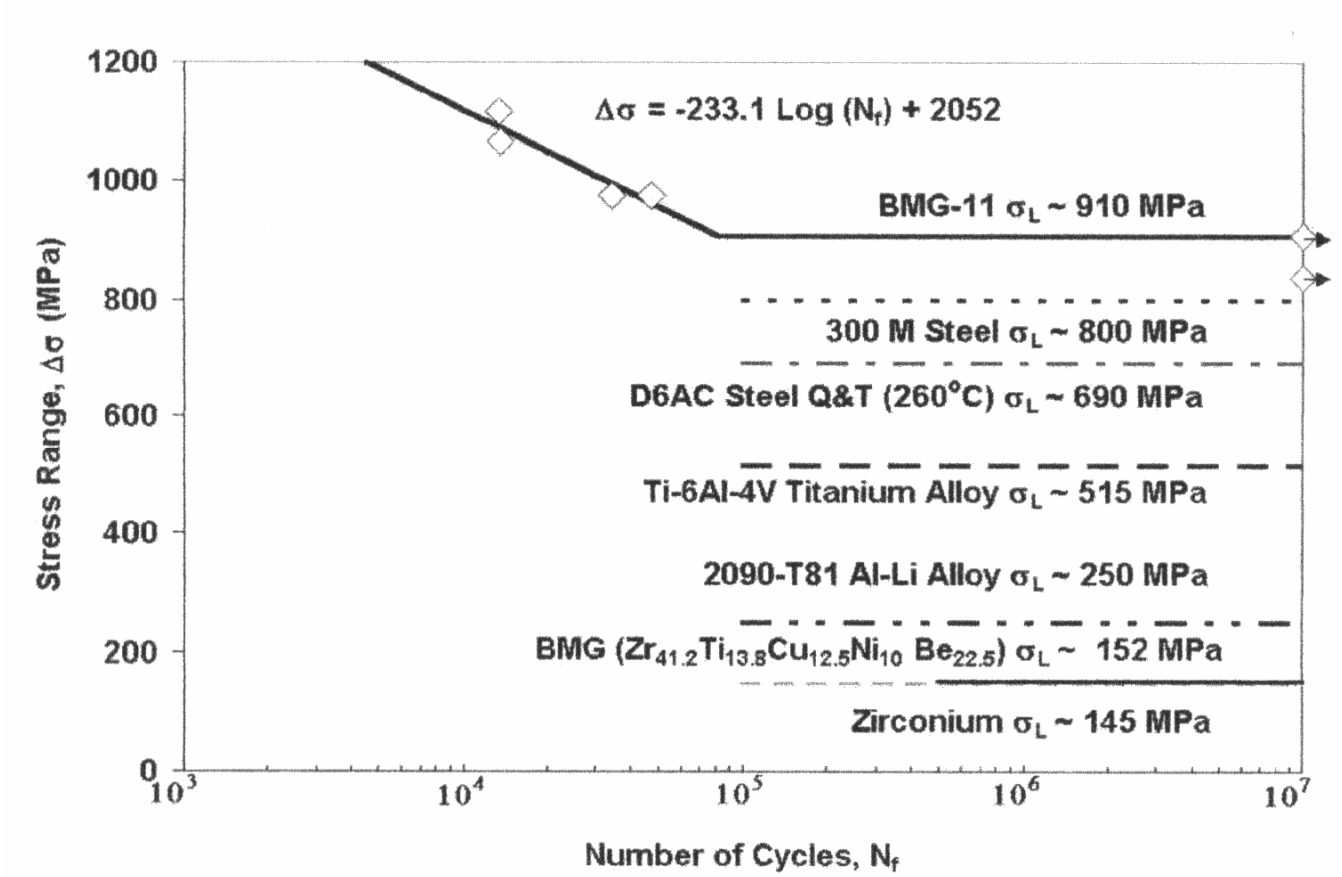

Figure 7. Stress-range / fatigue-life data of notched Vit 105 specimens tested in air compared with the fatigue endurance limits (σ_L) of the Vit 1 BMG and crystalline, high-strength alloys. (Reprinted from [18] with permission from Elsevier.)

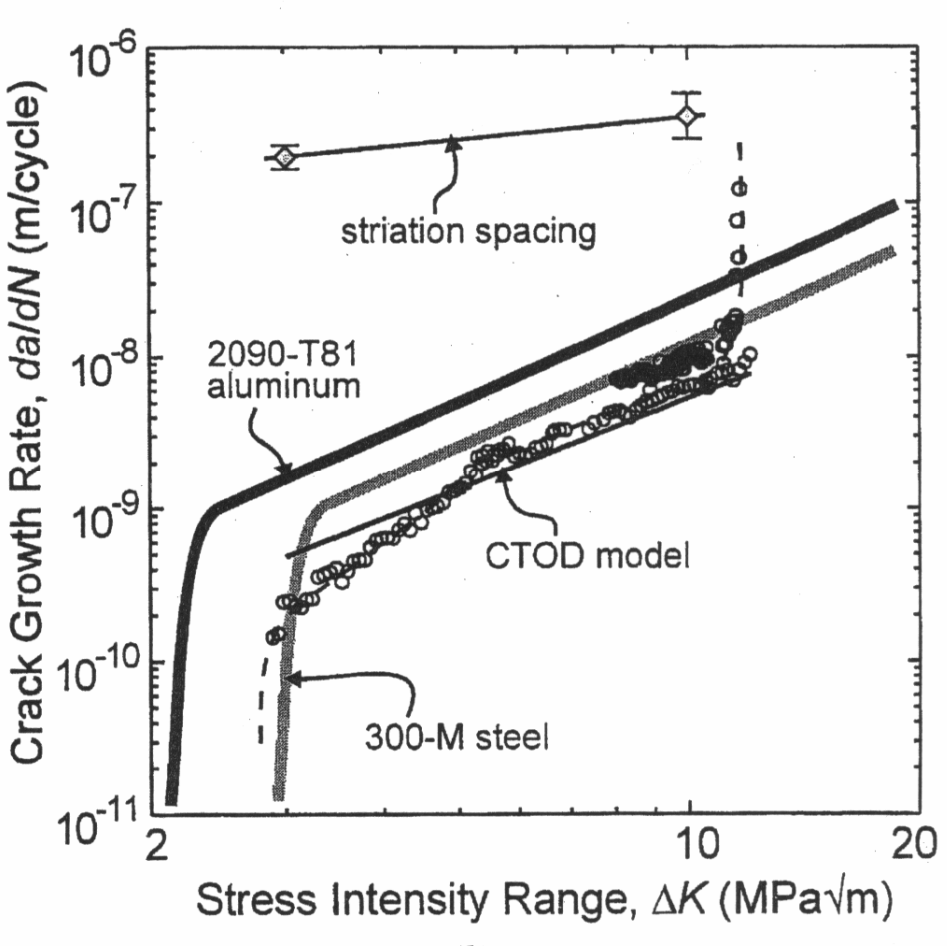

Figure 8. Fatigue crack-growth rates plotted as a function of the stress intensity range (ΔK) for the Vit 1 BMG alloy (R = 1, ν = 25 Hz). (Reprinted from [9] with permission from Elsevier.)

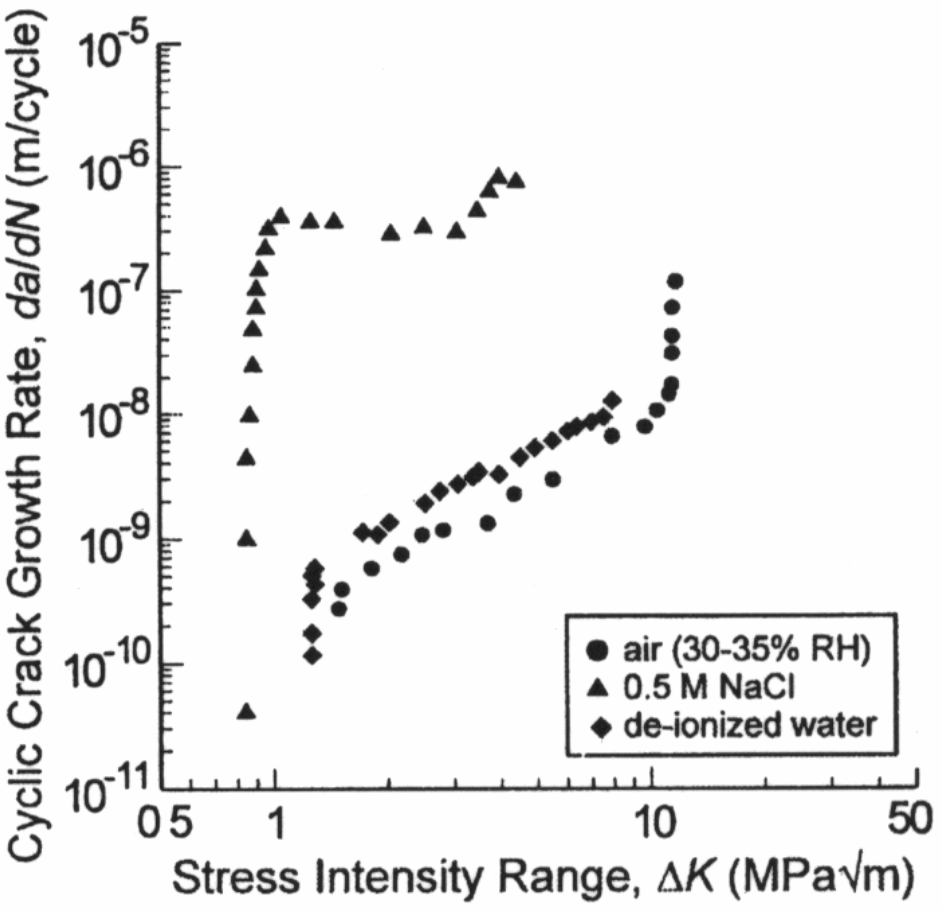

Figure 9. Fatigue crack-growth rates plotted as a function of stress intensity range (ΔK) in air, de-ionized water, and 0.5 M NaCl for the Vit 1 BMG alloy (R = 1, ν = 25 Hz). (Reprinted from [104] with permission from Elsevier.)

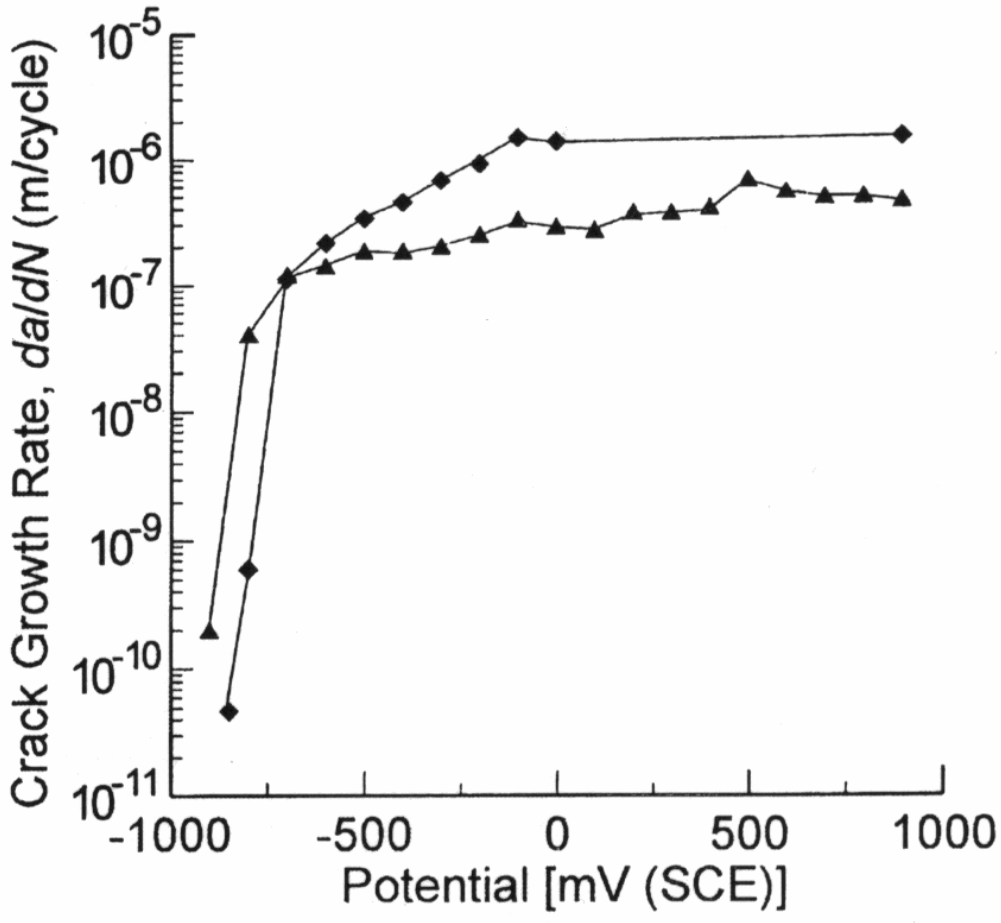

Figure 10. Fatigue crack-growth rates at constant ΔK = 1.5 MPa $m^{0.5}$ plotted as a function of potential in 0.5 M NaCl. Each potential was held for 300 – 500 μm of crack growth. (Reprinted from [104] with permission from Elsevier.)

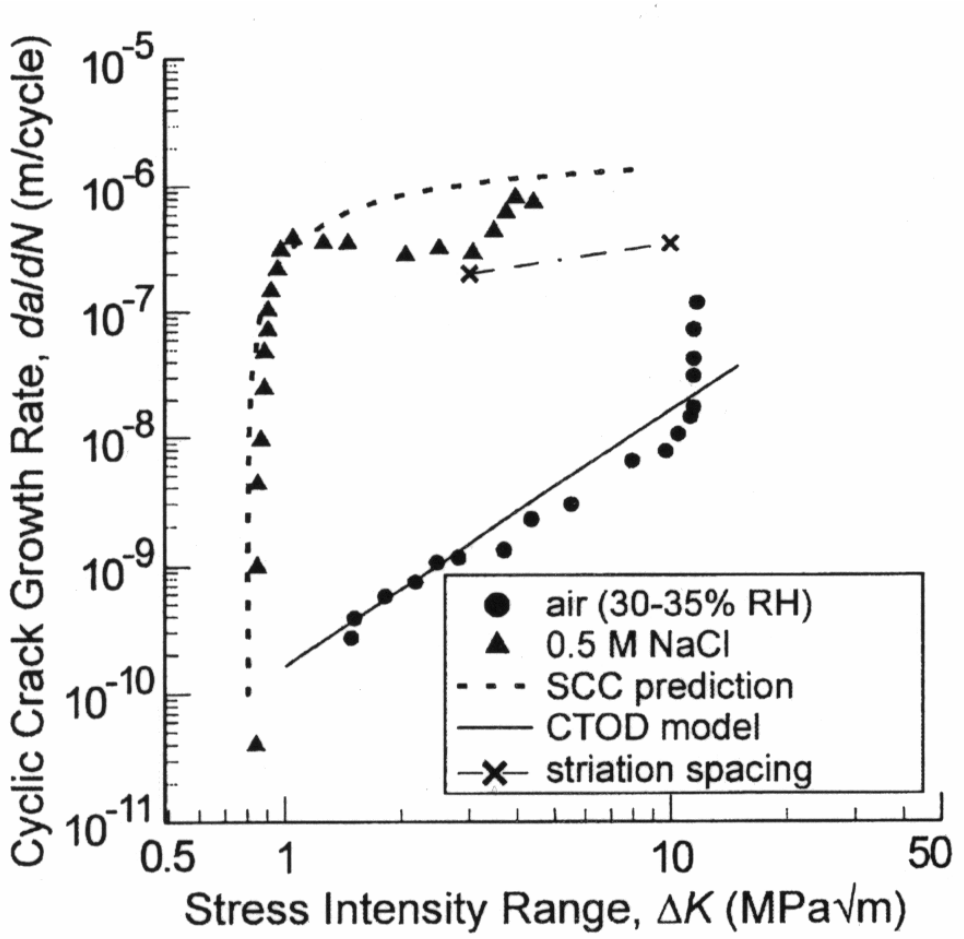

Figure 11. Fatigue crack-growth rates plotted as a function of stress intensity range (ΔK) in air and 0.5 M NaCl for the Vit 1 BMG alloy (R = 1, ν = 25 Hz). The experimental data is compared to the growth rates predicted by the stress-corrosion cracking (SCC) model in Equation 4. (Reprinted from [104] with permission from Elsevier.)

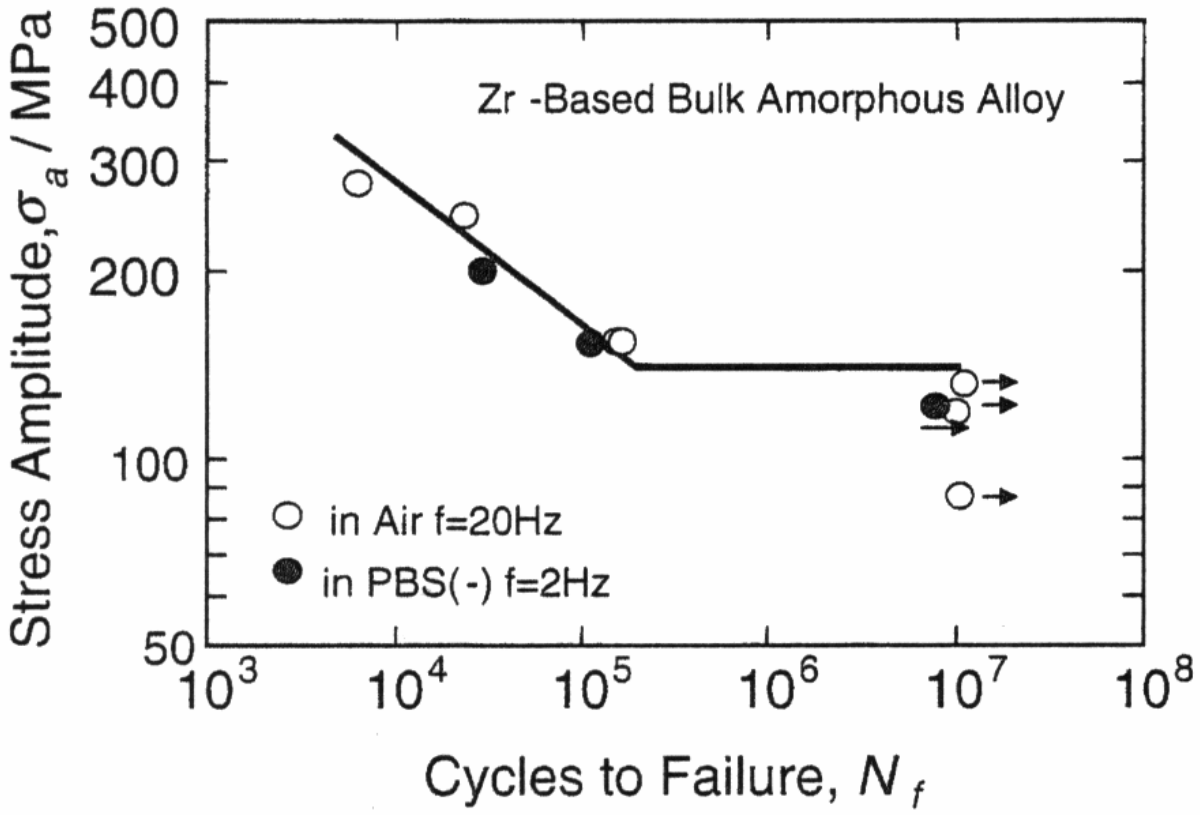

Figure 12. S-N curves of the $Zr_{65}Cu_{15}Ni_{10}Al_{10}$ (at.%) BMG alloy (consolidated powder) in dry air at ambient temperature (R = 0.1, ν = 20 Hz) and a phosphate-buffered saline (PBS) electrolyte at 37°C with a pH of 7.5 (R = 0.1, ν = 2 Hz). (Reprinted from [106] with permission from Elsevier.)

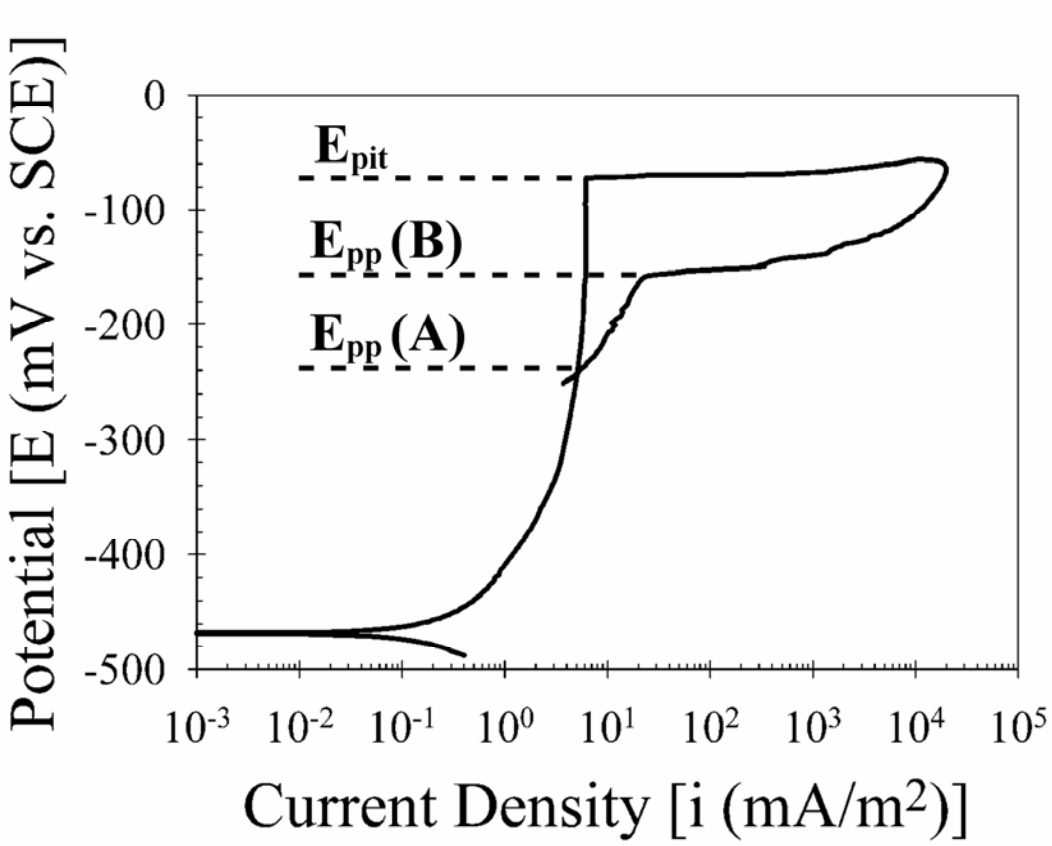

Figure 13. An example of a cyclic-anodic polarization curve in which the down-scan crossed the up-scan at an artificially low potential because the anodic curve and open-circuit corrosion current density (i_{corr}) shifted to higher potentials and current densities, respectively, on the down-scan (after pitting). The traditional criterion for the definition of the protection potential, denoted as E_{pp}(A), is contrasted with the modified criterion, denoted as E_{pp}(B), proposed in the current study. Epit represents the potential at which pitting occurs. (Reprinted from [169] with permission from John Wiley & Sons.)

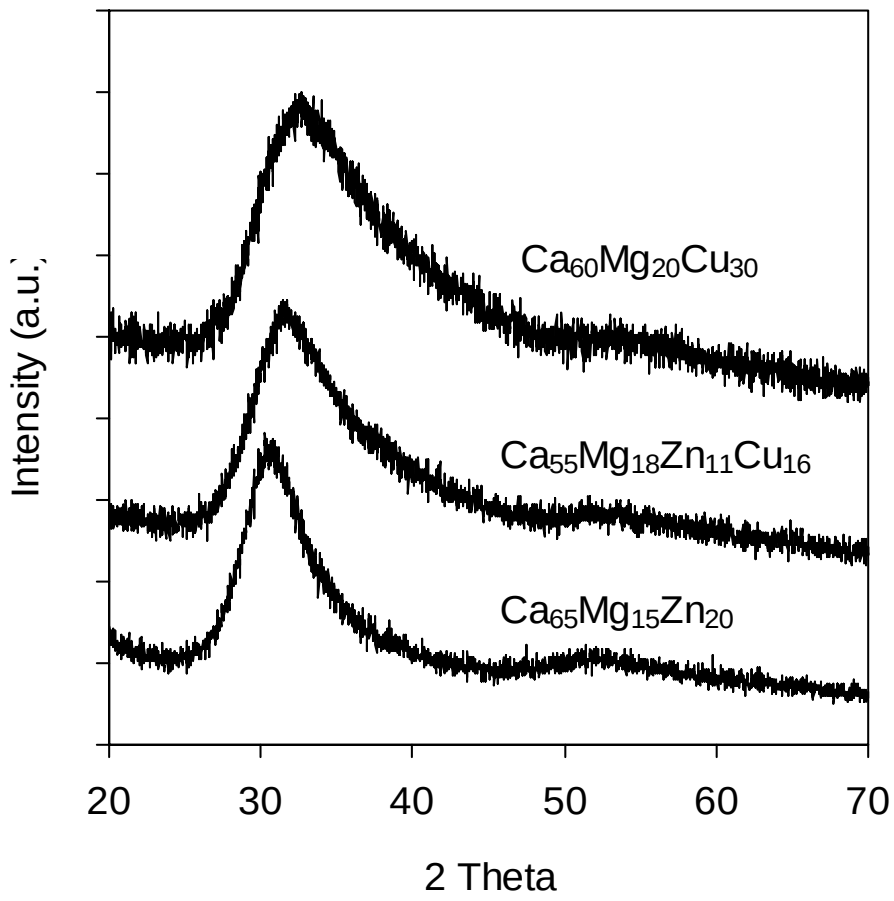

Figure 14. X-ray diffraction patterns of powdered samples extracted from 4-mm thick cast plates of $Ca_{65}Mg_{15}Zn_{20}$, $Ca_{50}Mg_{20}Cu_{30}$, and $Ca_{55}Mg_{18}Zn_{11}Cu_{16}$ alloys indicating fully amorphous state of the plates.

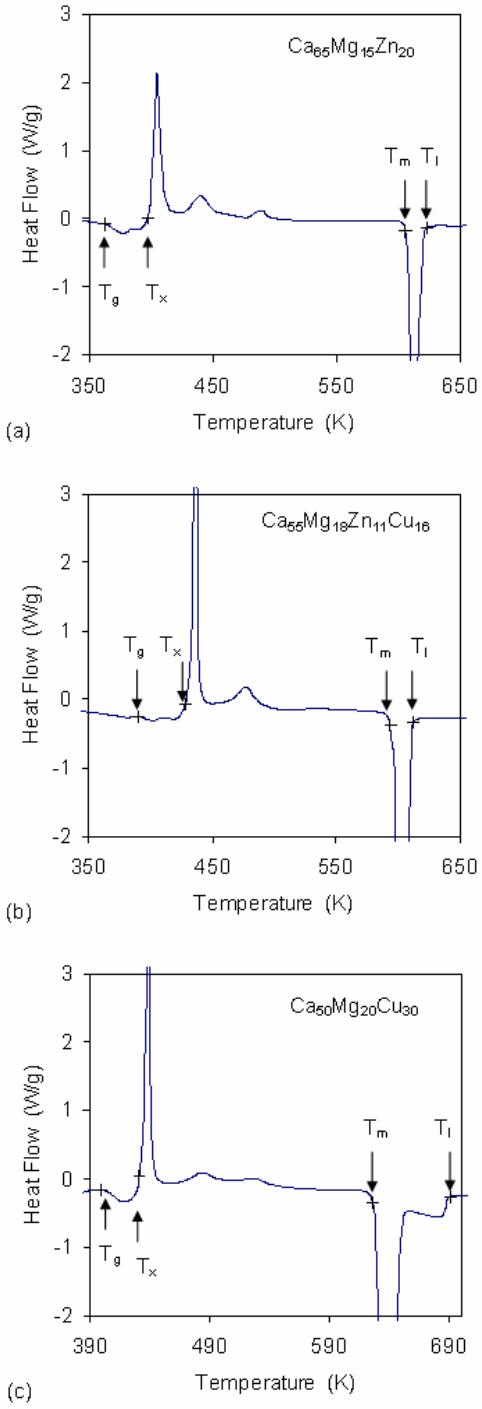

Figure 15. DSC thermograms of the (a) $Ca_{65}Mg_{15}Zn_{20}$, (b) $Ca_{55}Mg_{18}$ $Zn_{11}Cu_{16}$ and (c) $Ca_{50}Mg_{20}Cu_{30}$ glassy alloys. The exothermic reactions are positive. The heating rate was 20 K/min. Locations of the characteristic temperatures (T_g, T_x, T_m and T_l) are indicated by arrows.

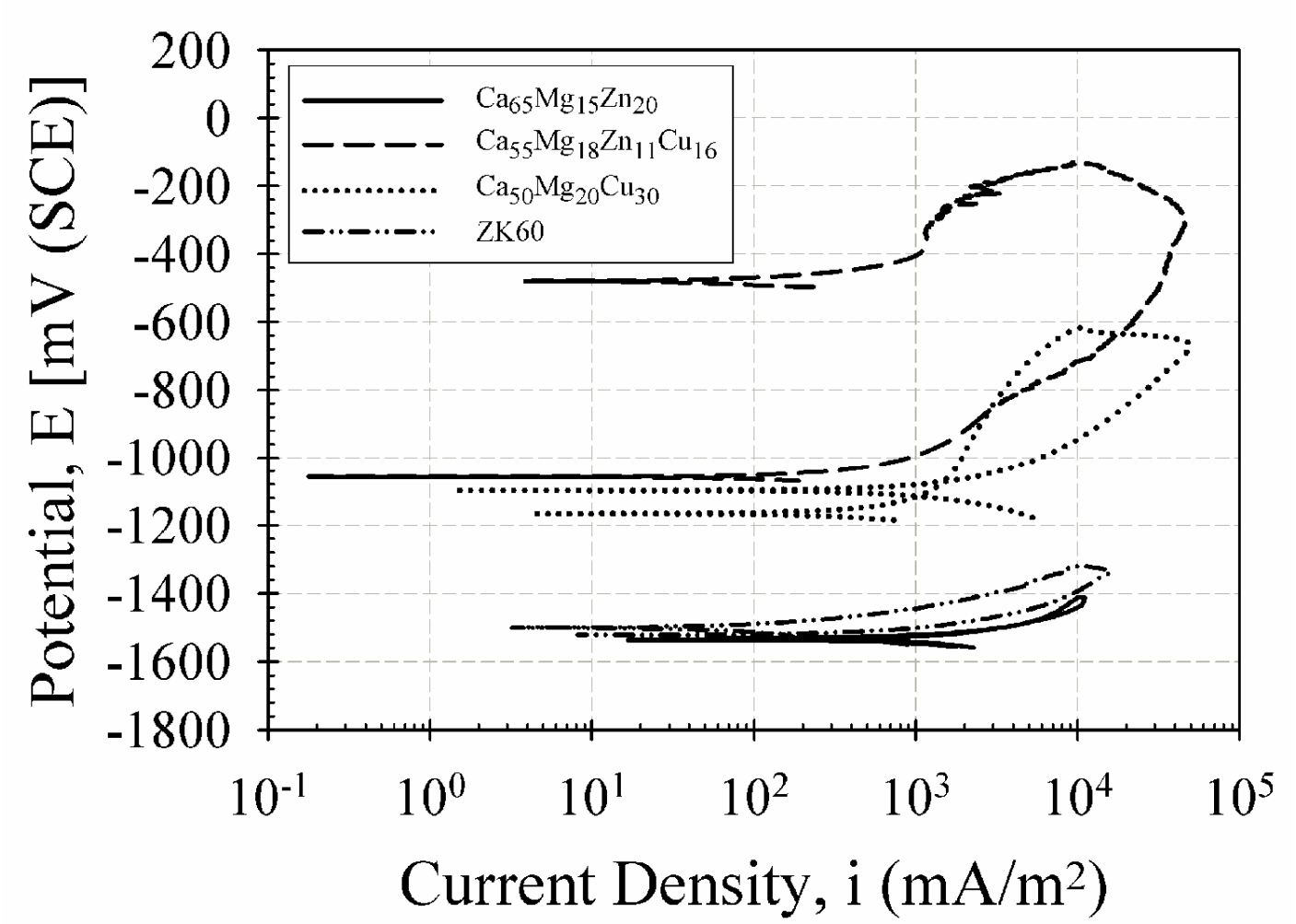

Figure 16. The average cyclic-anodic-polarization curves for the $Ca_{65}Mg_{15}Zn_{20}$, $Ca_{55}Mg_{18}Zn_{11}Cu_{16}$, $Ca_{50}Mg_{20}Cu_{30}$ BMG alloys, and the crystalline, Mg-based ZK60 alloy ($Mg_{97.6}Zn_{2.2}Zr_{0.2}$). All compositions are presented in atomic percent.

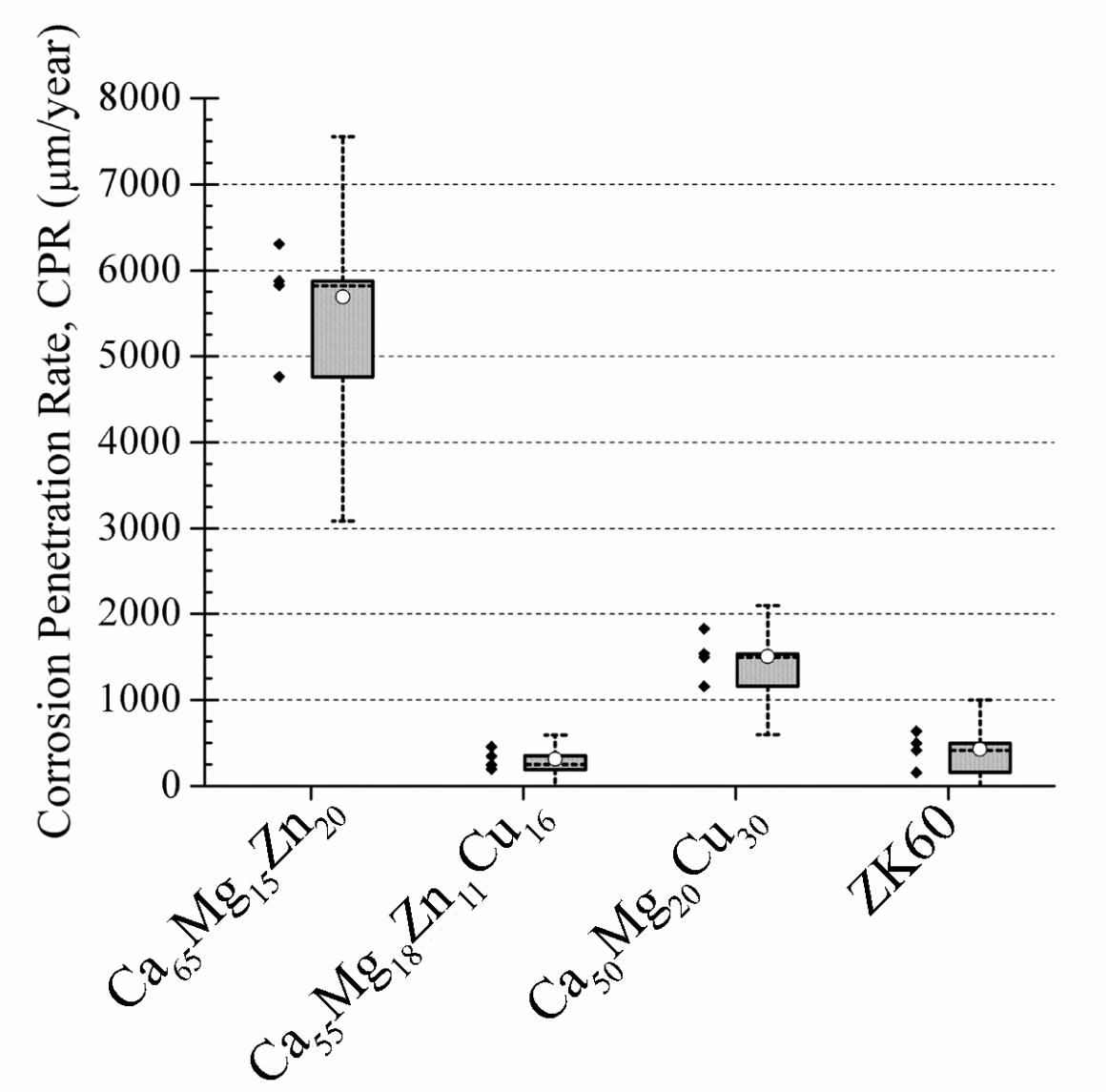

Figure 17. The mean corrosion penetration rates (CPRs) for the $Ca_{65}Mg_{15}Zn_{20}$, $Ca_{55}Mg_{18}Zn_{11}Cu_{16}$, $Ca_{50}Mg_{20}Cu_{30}$ BMG alloys, and the crystalline, Mg-based ZK60 alloy ($Mg_{97.6}Zn_{2.2}Zr_{0.2}$). All compositions are presented in atomic percent. The open-circle represents the mean CPR for each material, while the dashed line inside the box represents the median. The whiskers represent the lower and upper inner fences.

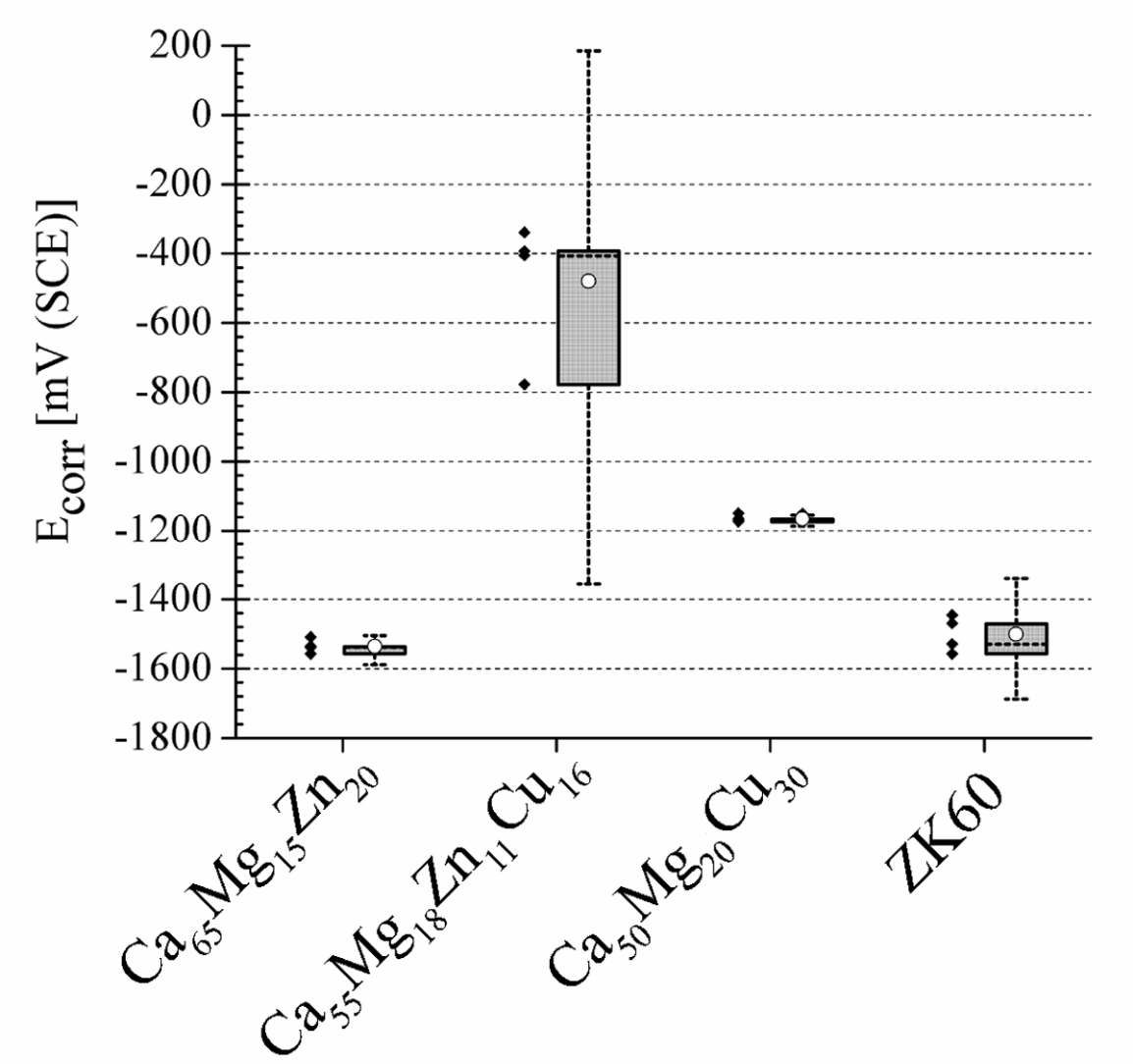

Figure 18. The open-circuit corrosion potentials (E_{corr}) derived from the cyclic-anodic-polarization tests of the $Ca_{65}Mg_{15}Zn_{20}$, $Ca_{55}Mg_{18}Zn_{11}Cu_{16}$, $Ca_{50}Mg_{20}Cu_{30}$ BMG alloys, and the crystalline, Mg-based ZK60 alloy ($Mg_{97.6}Zn_{2.2}Zr_{0.2}$). All compositions are presented in atomic percent. The open-circle represents the mean E_{corr} for each material, while the dashed line inside the box represents the median. The whiskers represent the lower and upper inner fences.

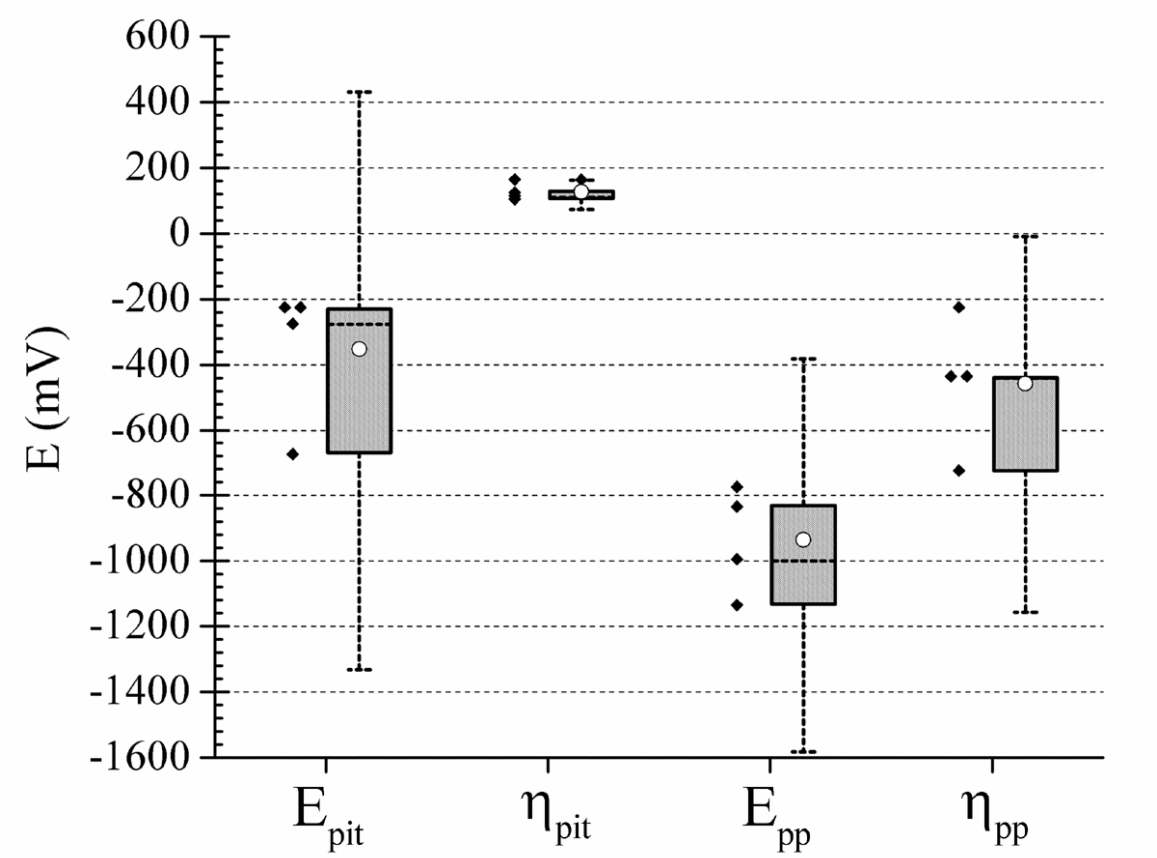

Figure 19. The localized corrosion parameters derived from the cyclic-anodic-polarization tests of the $Ca_{55}Mg_{18}Zn_{11}Cu_{16}$ (at.%) BMG alloy. All of the other materials that were evaluated did not exhibit localized corrosion. The open-circle represents the mean parameter, the dashed line inside the box represents the median, and the whiskers represent the lower and upper inner fences. The pitting potential (E_{pit}) and protection potential (E_{pp}) are in reference to the saturated calomel electrode (SCE). The overpotentials at E_{pit} and E_{pp} are designated η_{pit} and η_{pp}, respectively.

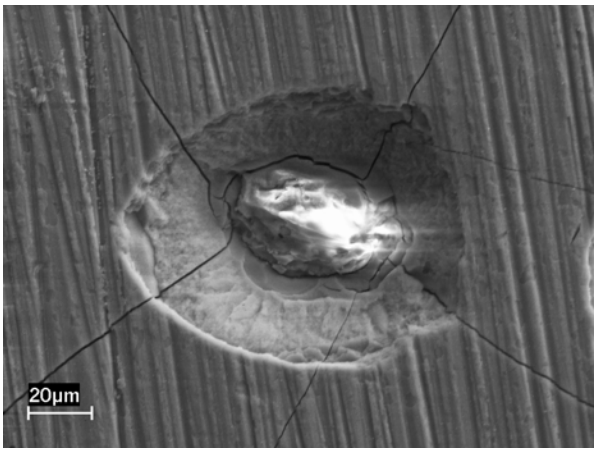

(a)

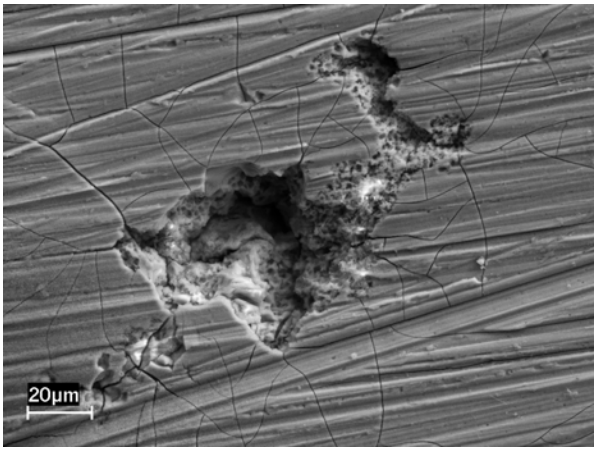

(b)

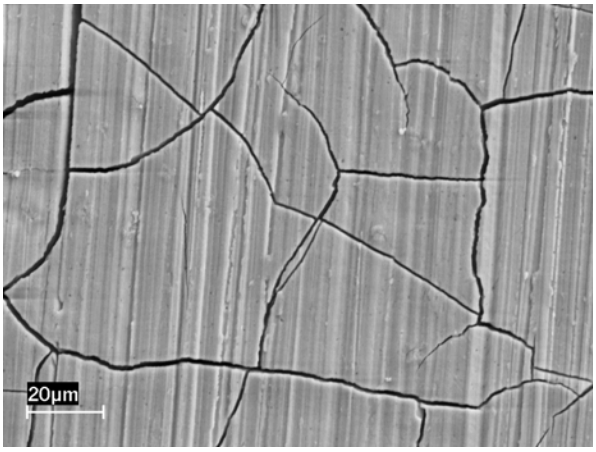

(c)

Figure 20. SEM photomicrographs of the (a) $Ca_{65}Mg_{15}Zn_{20}$, (b) $Ca_{55}Mg_{18}Zn_{11}Cu_{16}$, and (c) $Ca_{50}Mg_{20}Cu_{30}$ BMG alloys after cyclic-anodic-polarization tests in 0.05 M Na_2SO_4. All compositions are presented in atomic percent (at.%).

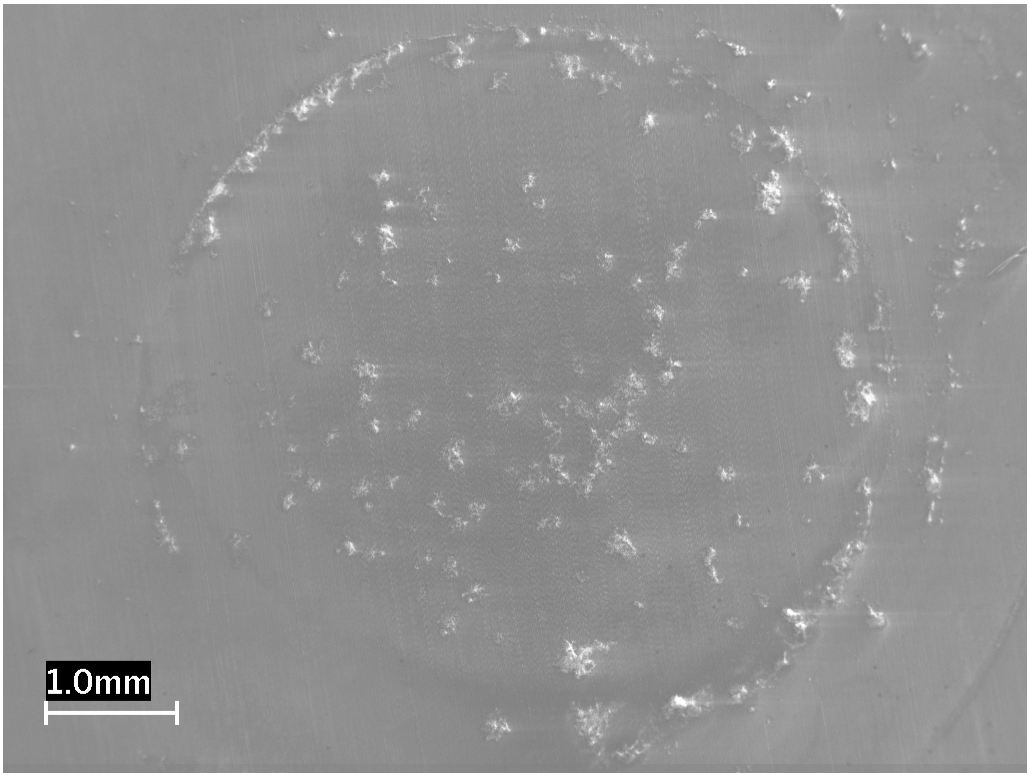

Figure 21. SEM photomicrographs of the crystalline, Mg-based ZK60 alloy ($Mg_{97.6}Zn_{2.2}Zr_{0.2}$) after cyclic-anodic-polarization tests in 0.05 M Na_2SO_4.

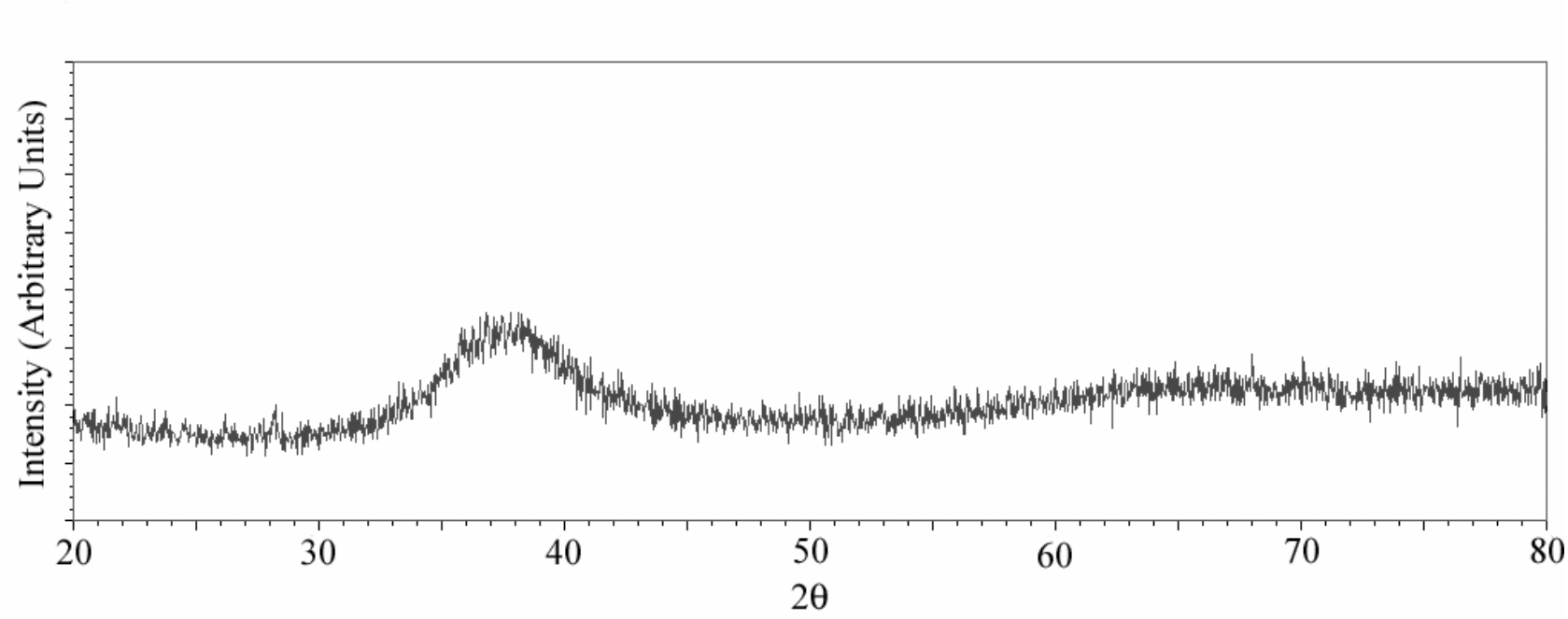

Figure 22. A representative X-ray diffraction spectrum of the Vitreloy 1 BMG [$Zr_{41.2}Ti_{13.8}Ni_{10}Cu_{12.5}Be_{22.5}$ (at.%)] corrosion samples. All spectra demonstrated broad, diffuse peaks characteristic of amorphous alloys.

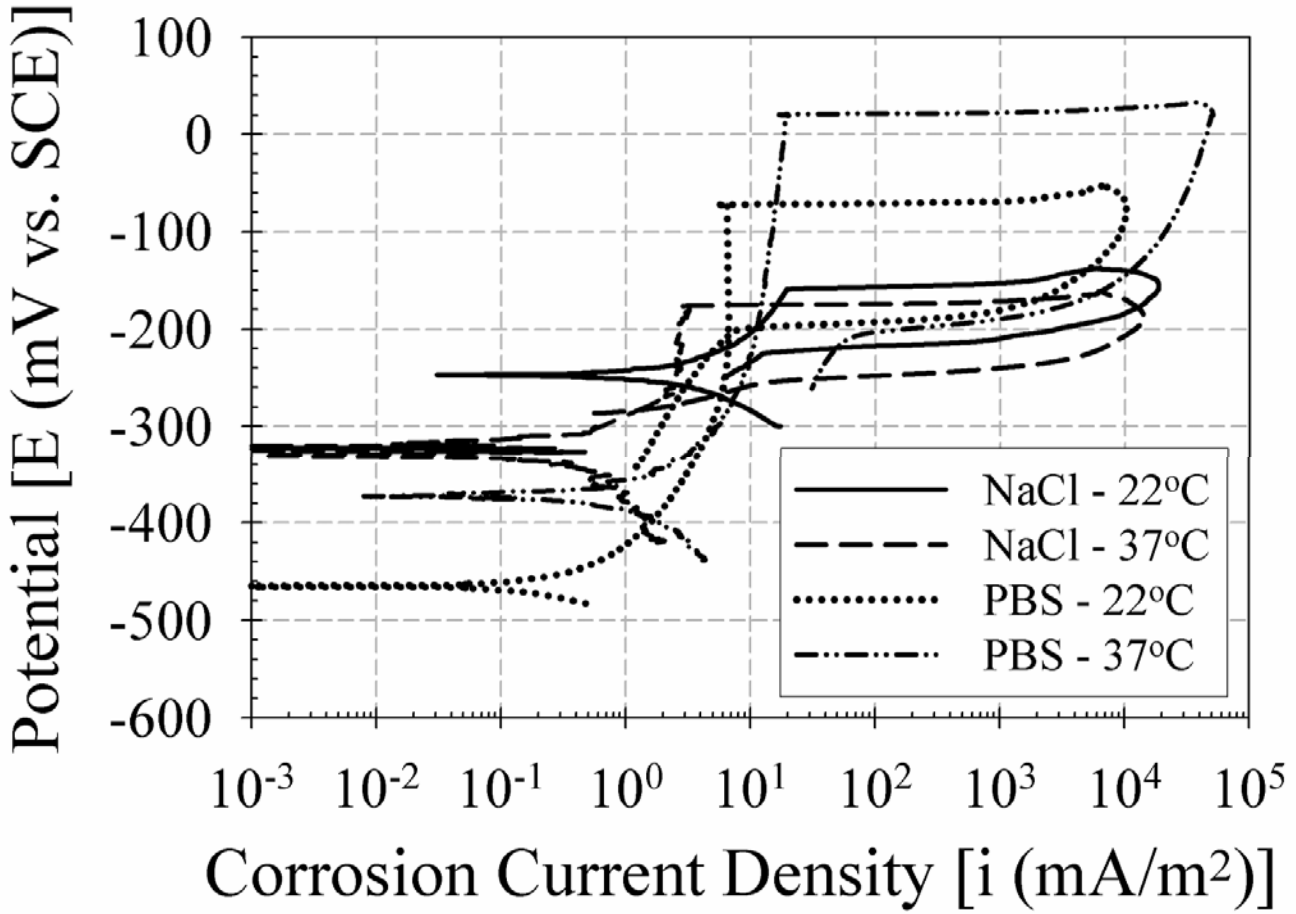

Figure 23. The average cyclic-anodic-polarization curves for the Vitreloy 1 BMG [$Zr_{41.2}Ti_{13.8}Ni_{10}Cu_{12.5}Be_{22.5}$ (at.%)] in an aerated 0.6 M NaCl electrolyte at 22ºC and 37°C, and in a phosphate-buffered saline (PBS) electrolyte, at 22ºC and 37°C, with a physiologically-relevant dissolved oxygen content.

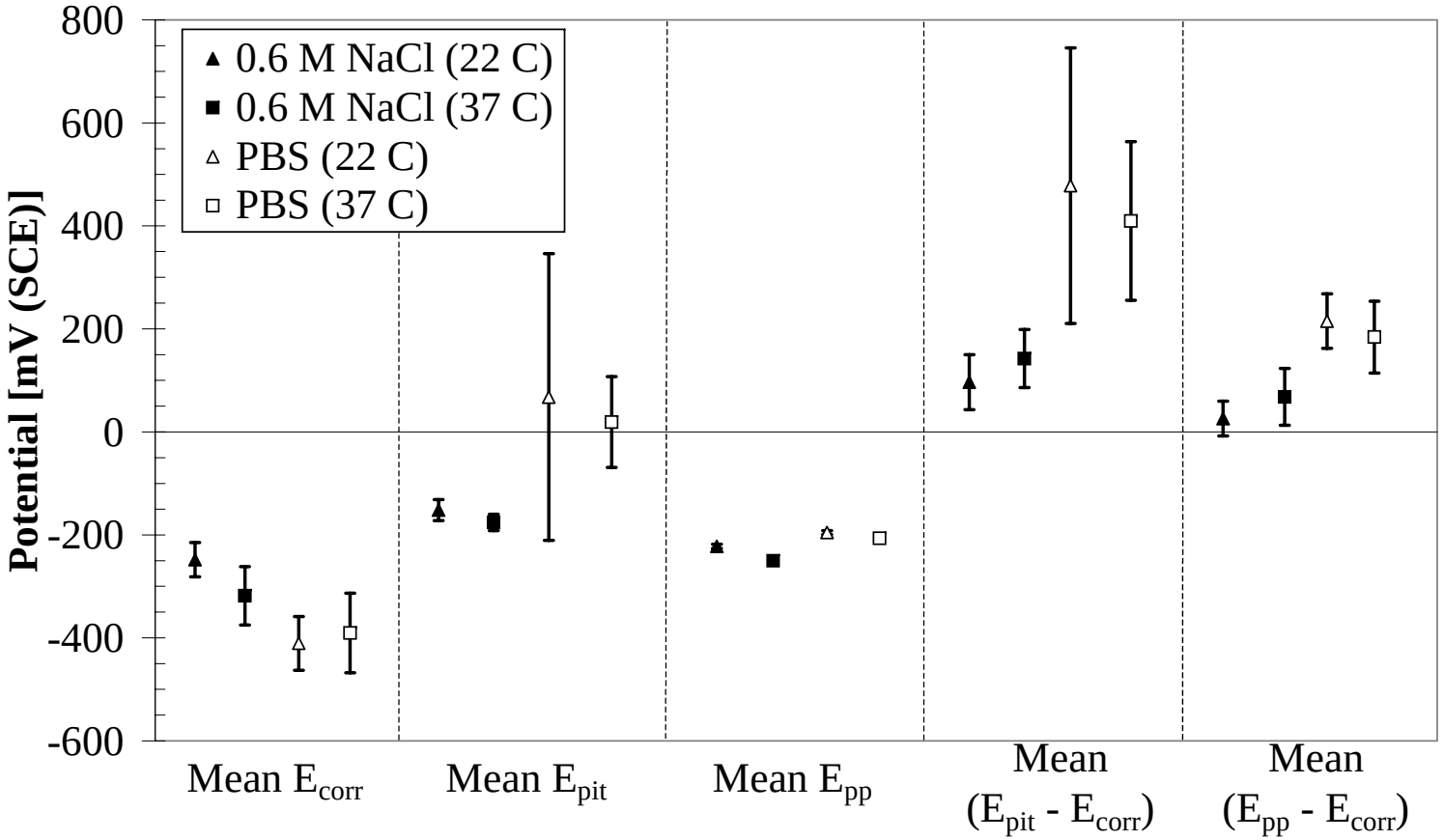

Figure 24. Corrosion parameters derived from the cyclic-anodic-polarization tests of the Vitreloy 1 BMG [$Zr_{41.2}Ti_{13.8}Ni_{10}Cu_{12.5}Be_{22.5}$ (at.%)] in an aerated 0.6 M NaCl electrolyte at 22ºC and 37ºC, and in a phosphate-buffered saline (PBS) electrolyte with a physiologically-relevant dissolved oxygen content at 22ºC and 37°C. Error bars represent 90% confidence intervals. (Reprinted from [24] with permission from Elsevier.)

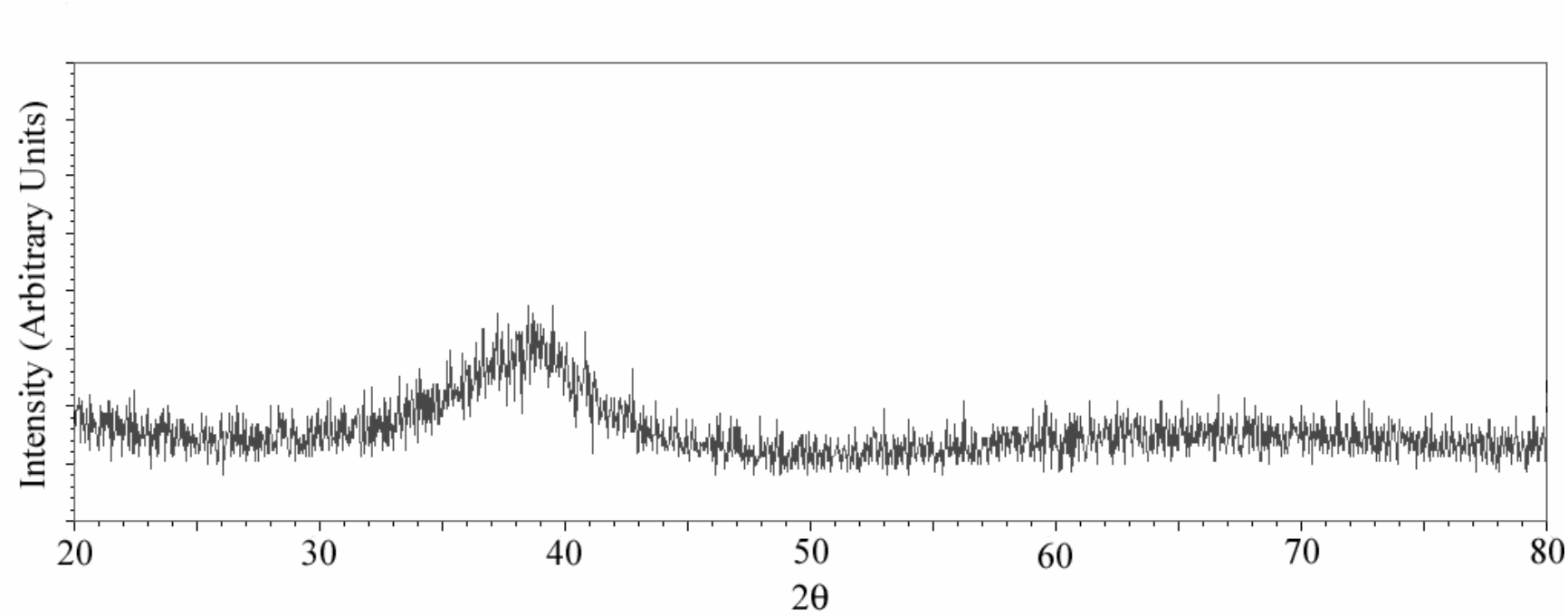

Figure 25. A representative x-ray diffraction spectrum of the LM-010 BMG [$Ti_{43.3}Zr_{21.7}Ni_{7.5}Be_{27.5}$ (at.%)] corrosion samples. All spectra demonstrated broad, diffuse peaks characteristic of amorphous alloys.

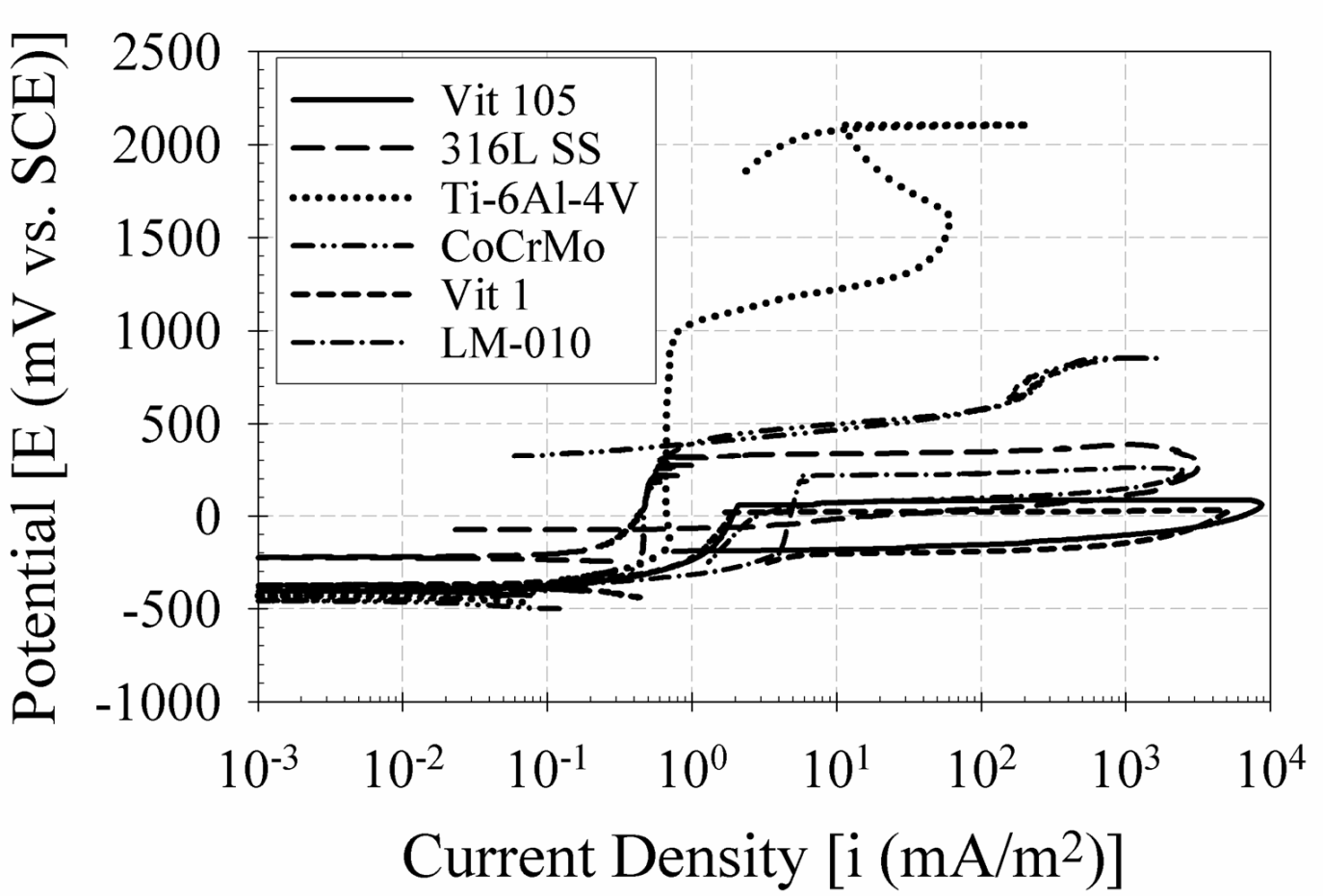

Figure 26. The average cyclic-anodic-polarization curves for the Vit 105 BMG [$Zr_{52.5}Cu_{17.9}Ni_{14.6}Al_{10.0}Ti_{5.0}$ (at.%)], AISI 316L stainless steel [$Fe_{62.5}Cr_{19.3}Ni_{13.3}$ (at.%), ASTM F138], Ti-6Al-4V [$Ti_{86.2}Al_{10.2}V_{3.6}$ (at.%), ASTM F136], CoCrMo [$Co_{61.4}Cr_{30.9}Mo_{3.6}$ (at.%), ASTM F799], Vit 1 BMG [$Zr_{41.2}Ti_{13.8}Ni_{10}Cu_{12.5}Be_{22.5}$ (at.%)], and LM-010 BMG [$Ti_{43.3}Zr_{21.7}Ni_{7.5}Be_{27.5}$ (at.%)] alloys in the PBS electrolyte at 37°C.

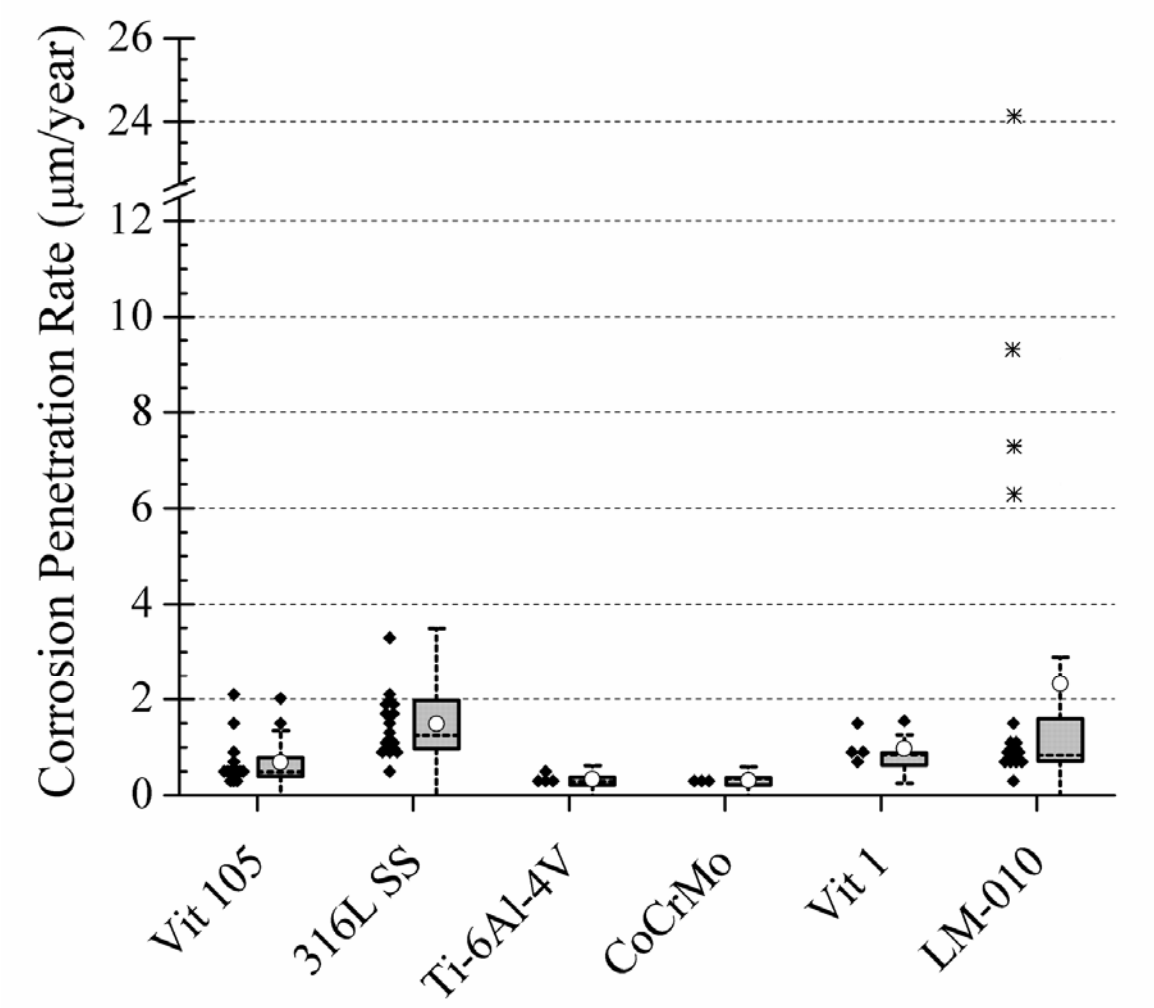

Figure 27. The corrosion penetration rates (CPRs) for the Vit 105 BMG [$Zr_{52.5}Cu_{17.9}Ni_{14.6}Al_{10.0}Ti_{5.0}$ (at.%)], AISI 316L stainless steel [$Fe_{62.5}Cr_{19.3}Ni_{13.3}$ (at.%), ASTM F138], Ti-6Al-4V [$Ti_{86.2}Al_{10.2}V_{3.6}$ (at.%), ASTM F136], CoCrMo [$Co_{61.4}Cr_{30.9}Mo_{3.6}$ (at.%), ASTM F799], Vit 1 BMG [$Zr_{41.2}Ti_{13.8}Ni_{10}Cu_{12.5}Be_{22.5}$ (at.%)], and LM-010 BMG [$Ti_{43.3}Zr_{21.7}Ni_{7.5}Be_{27.5}$ (at.%)] alloys in the PBS electrolyte at 37°C. The open-circle represents the mean CPR for each material, while the dashed line inside the box represents the median. The whiskers represent the lower and upper inner fences, and asterisks designate outliers.

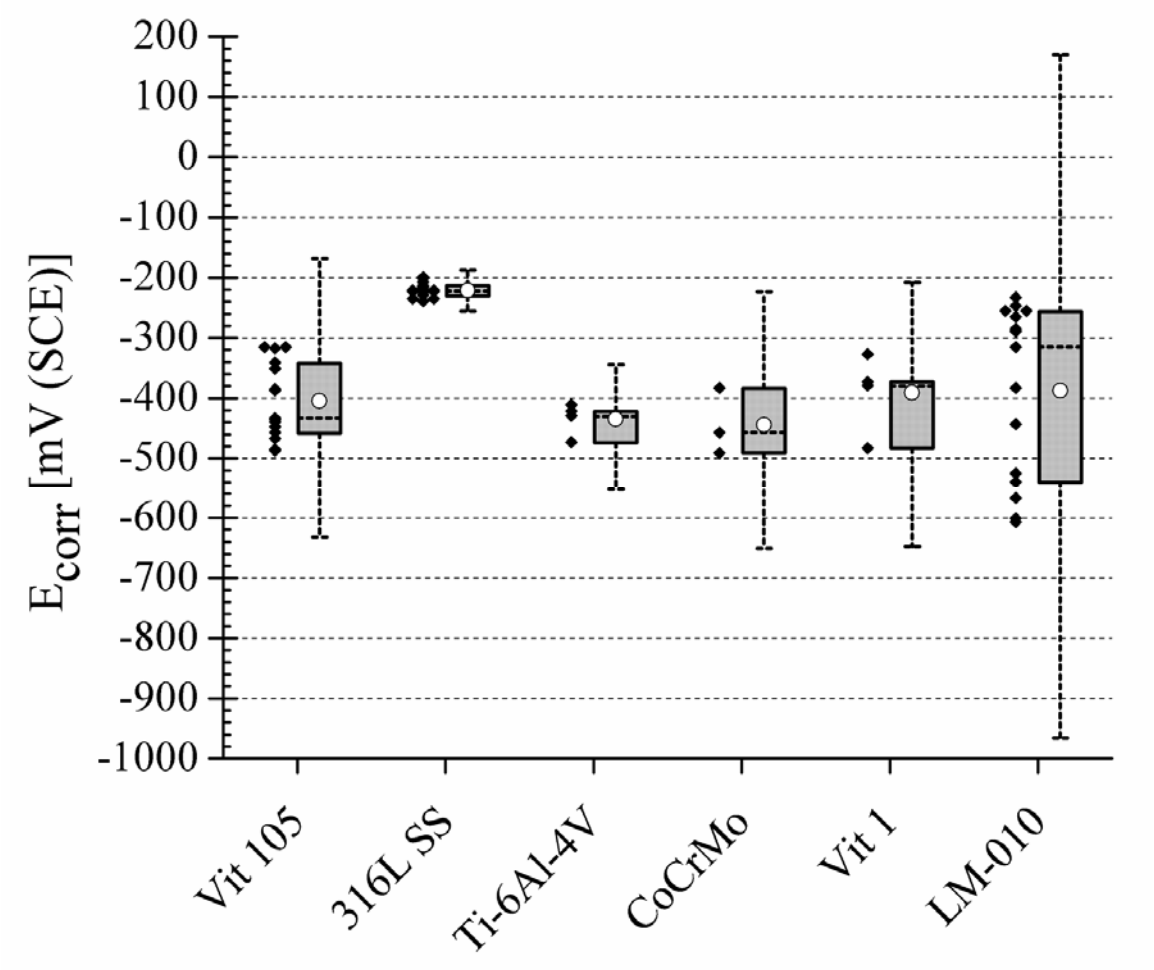

Figure 28. The corrosion potentials (E_{corr}) for the Vit 105 BMG [$Zr_{52.5}Cu_{17.9}Ni_{14.6}Al_{10.0}Ti_{5.0}$ (at.%)], AISI 316L stainless steel [$Fe_{62.5}Cr_{19.3}Ni_{13.3}$ (at.%), ASTM F138], Ti-6Al-4V [$Ti_{86.2}Al_{10.2}V_{3.6}$ (at.%), ASTM F136], CoCrMo [$Co_{61.4}Cr_{30.9}Mo_{3.6}$ (at.%), ASTM F799], Vit 1 BMG [$Zr_{41.2}Ti_{13.8}Ni_{10}Cu_{12.5}Be_{22.5}$ (at.%)], and LM-010 BMG [$Ti_{43.3}Zr_{21.7}Ni_{7.5}Be_{27.5}$ (at.%)] alloys in the PBS electrolyte at 37°C. The open-circle represents the mean E_{corr} for each material, while the dashed line inside the box represents the median. The whiskers represent the lower and upper inner fences.

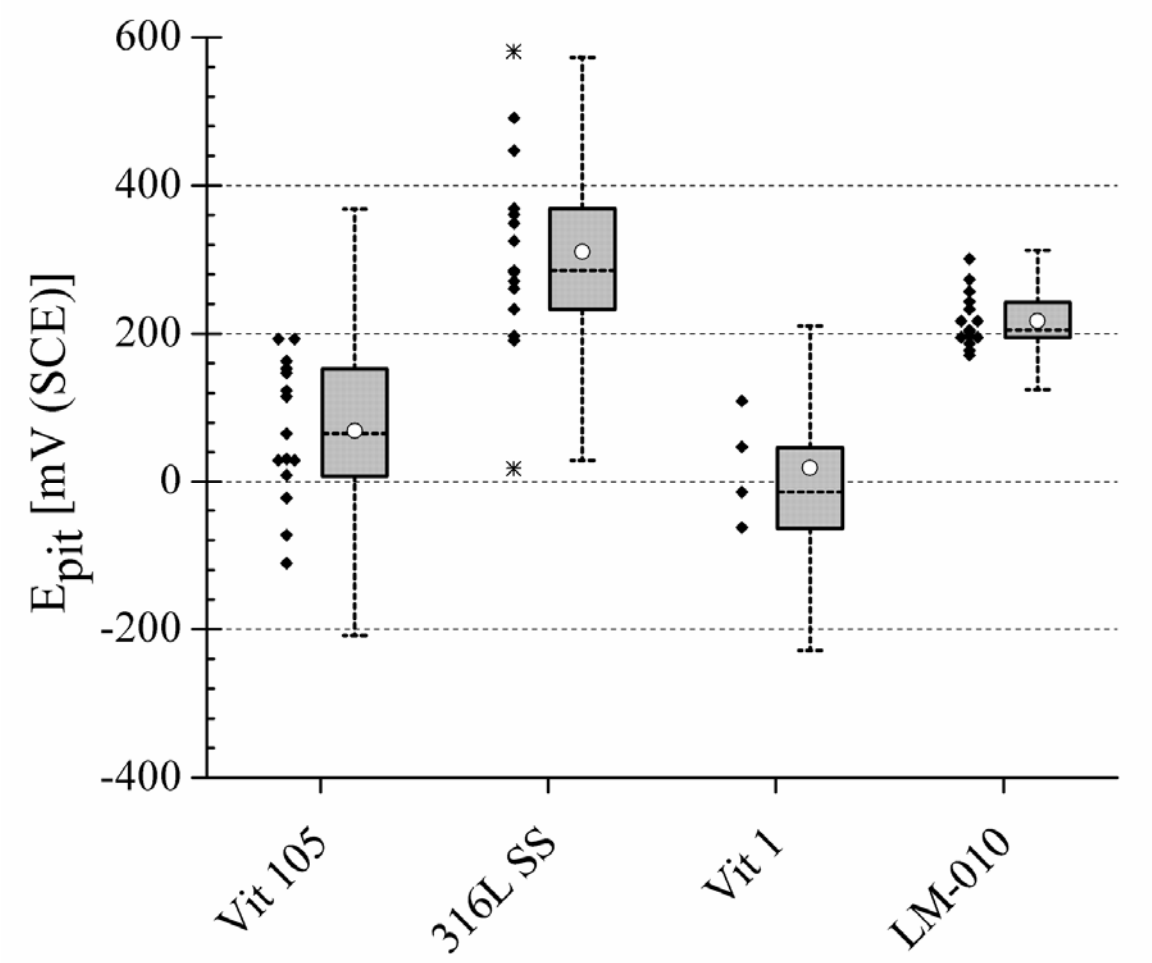

Figure 29. The pitting potentials (E_{pit}) for the Vit 105 BMG [$Zr_{52.5}Cu_{17.9}Ni_{14.6}Al_{10.0}Ti_{5.0}$ (at.%)], AISI 316L stainless steel [$Fe_{62.5}Cr_{19.3}Ni_{13.3}$ (at.%), ASTM F138], Vit 1 BMG [$Zr_{41.2}Ti_{13.8}Ni_{10}Cu_{12.5}Be_{22.5}$ (at.%)], and LM-010 BMG [$Ti_{43.3}Zr_{21.7}Ni_{7.5}Be_{27.5}$ (at.%)] alloys in the PBS electrolyte at 37°C. The Ti-6Al-4V and CoCrMo materials were not susceptible to localized corrosion. The open-circle represents the mean E_{pit} for each material, while the dashed line inside the box represents the median. The whiskers represent the lower and upper inner fences, and asterisks designate outliers.

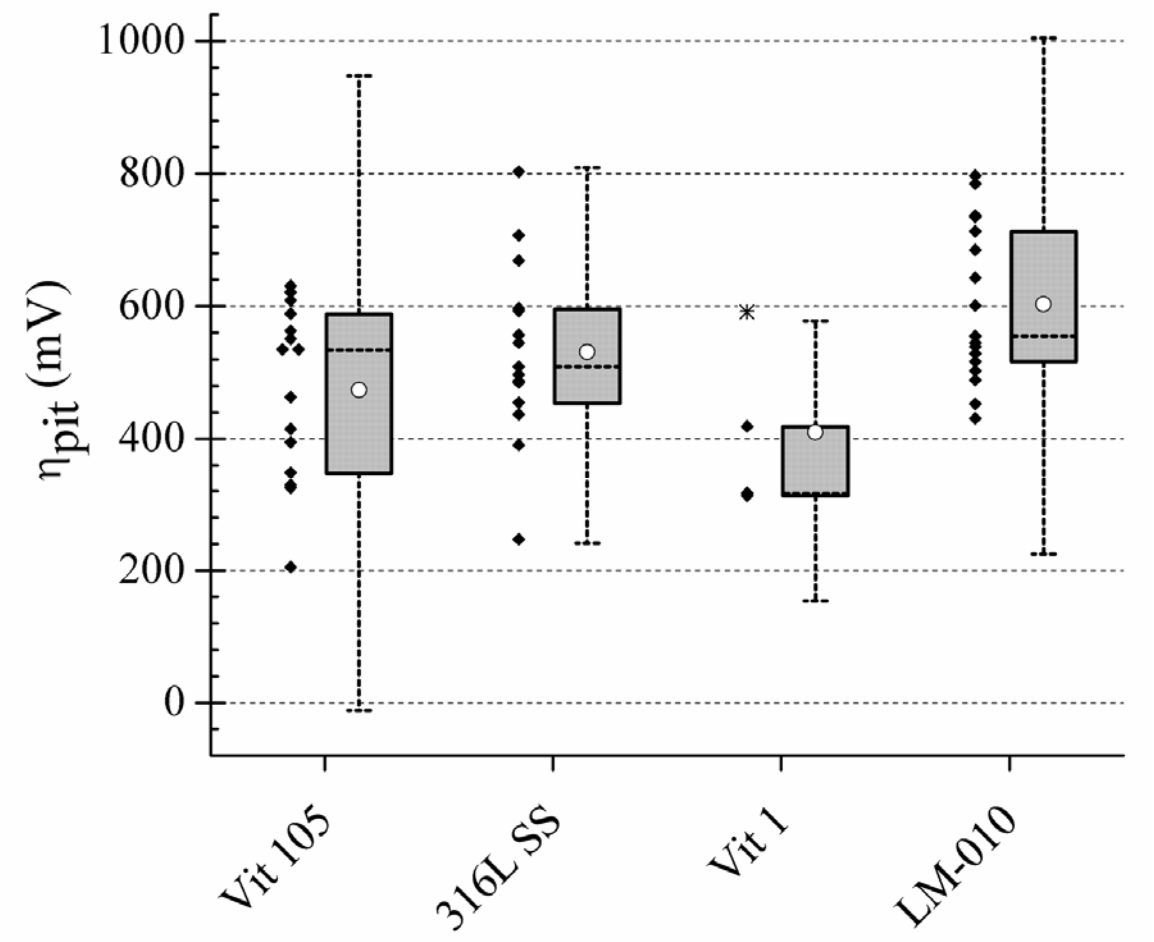

Figure 30. The pitting overpotentials (η_{pit}) for the Vit 105 BMG [$Zr_{52.5}Cu_{17.9}Ni_{14.6}Al_{10.0}Ti_{5.0}$ (at.%)], AISI 316L stainless steel [$Fe_{62.5}Cr_{19.3}Ni_{13.3}$ (at.%), ASTM F138], Vit 1 BMG [$Zr_{41.2}Ti_{13.8}Ni_{10}Cu_{12.5}Be_{22.5}$ (at.%)], and LM-010 BMG [$Ti_{43.3}Zr_{21.7}Ni_{7.5}Be_{27.5}$ (at.%)] alloys in the PBS electrolyte at 37°C. The Ti-6Al-4V and CoCrMo materials were not susceptible to localized corrosion. The open-circle represents the mean η_{pit} for each material, while the dashed line inside the box represents the median. The whiskers represent the lower and upper inner fences, and asterisks designate outliers.

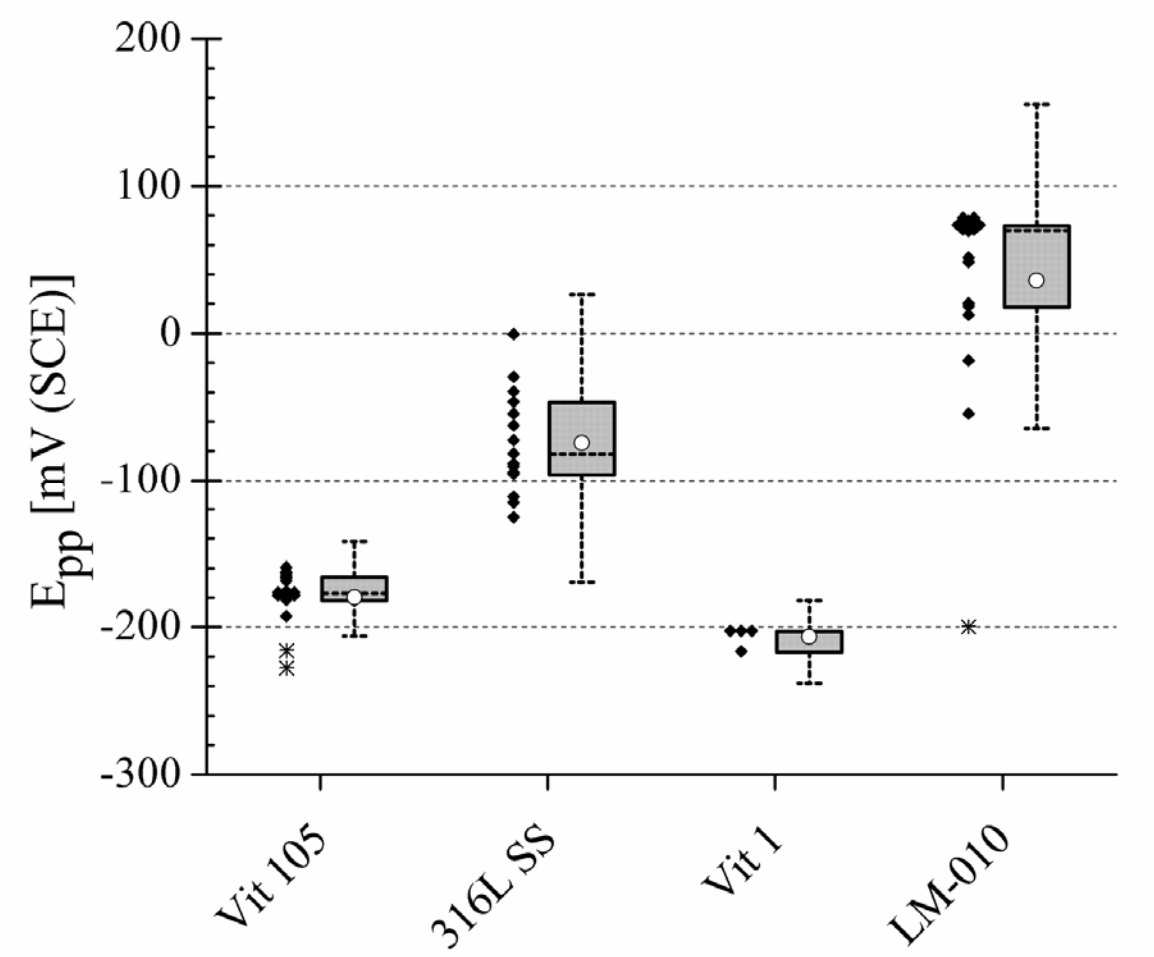

Figure 31. The protection potentials (E_{pp}) for the Vit 105 BMG [$Zr_{52.5}Cu_{17.9}Ni_{14.6}Al_{10.0}Ti_{5.0}$ (at.%)], AISI 316L stainless steel [$Fe_{62.5}Cr_{19.3}Ni_{13.3}$ (at.%), ASTM F138], Vit 1 BMG [$Zr_{41.2}Ti_{13.8}Ni_{10}Cu_{12.5}Be_{22.5}$ (at.%)], and LM-010 BMG [$Ti_{43.3}Zr_{21.7}Ni_{7.5}Be_{27.5}$ (at.%)] alloys in the PBS electrolyte at 37°C. The Ti-6Al-4V and CoCrMo materials were not susceptible to localized corrosion. The open-circle represents the mean E_{pp} for each material, while the dashed line inside the box represents the median. The whiskers represent the lower and upper inner fences, and asterisks designate outliers.

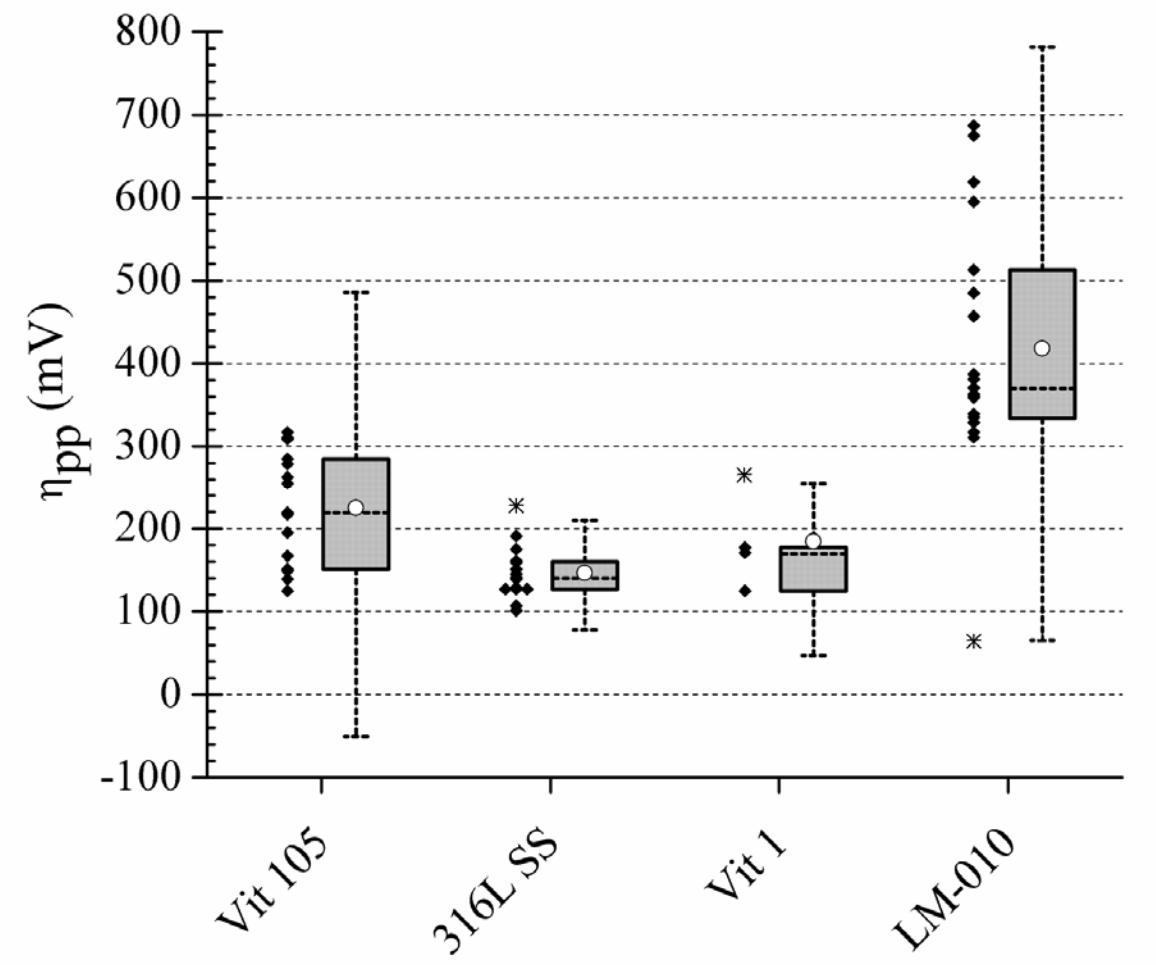

Figure 32. The protection overpotentials (η_{pp}) for the Vit 105 BMG [$Zr_{52.5}Cu_{17.9}Ni_{14.6}Al_{10.0}Ti_{5.0}$ (at.%)], AISI 316L stainless steel [$Fe_{62.5}Cr_{19.3}Ni_{13.3}$ (at.%), ASTM F138], Vit 1 BMG [$Zr_{41.2}Ti_{13.8}Ni_{10}Cu_{12.5}Be_{22.5}$ (at.%)], and LM-010 BMG [$Ti_{43.3}Zr_{21.7}Ni_{7.5}Be_{27.5}$ (at.%)] alloys in the PBS electrolyte at 37°C. The Ti-6Al-4V and CoCrMo materials were not susceptible to localized corrosion. The open-circle represents the mean η_{pp} for each material, while the dashed line inside the box represents the median. The whiskers represent the lower and upper inner fences, and asterisks designate outliers.

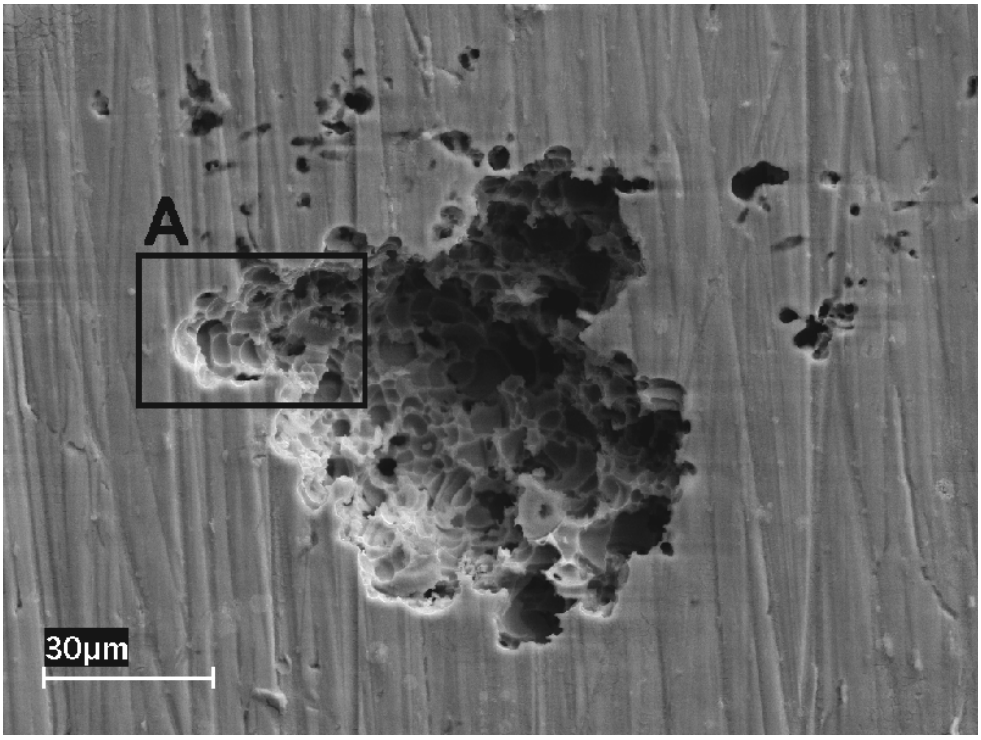

(a)

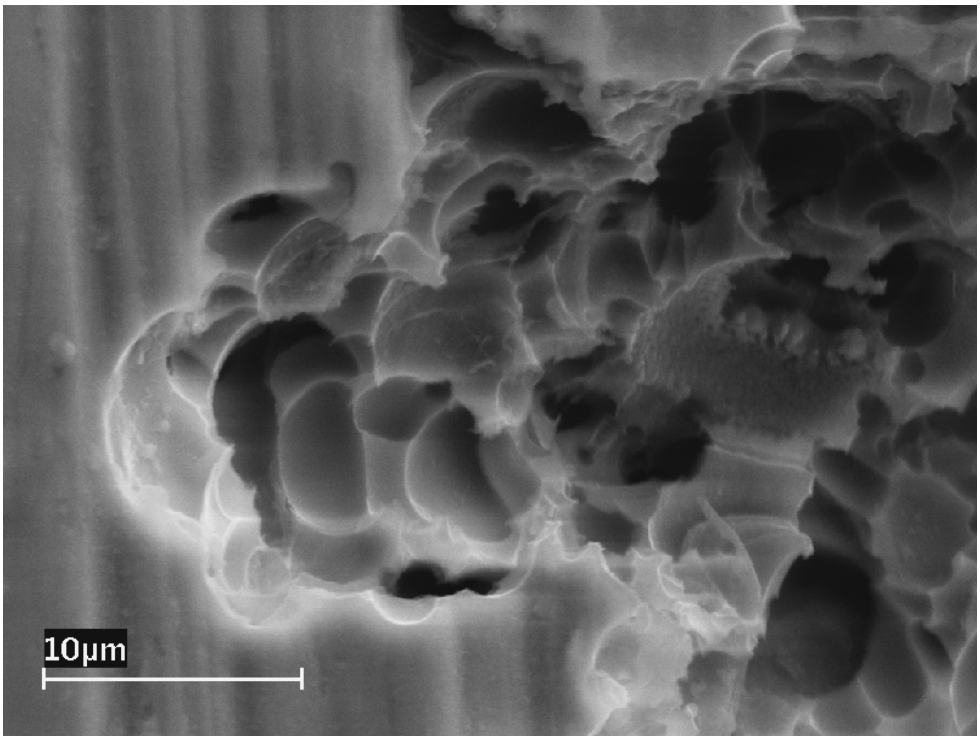

(b)

Figure 33. Representative SEM photomicrographs of the LM-010 BMG alloy after corrosion testing. (a) Typical appearance of a pit; (b) Magnified image of the pit at location A demonstrating faceted appearance of an interior pit surface.

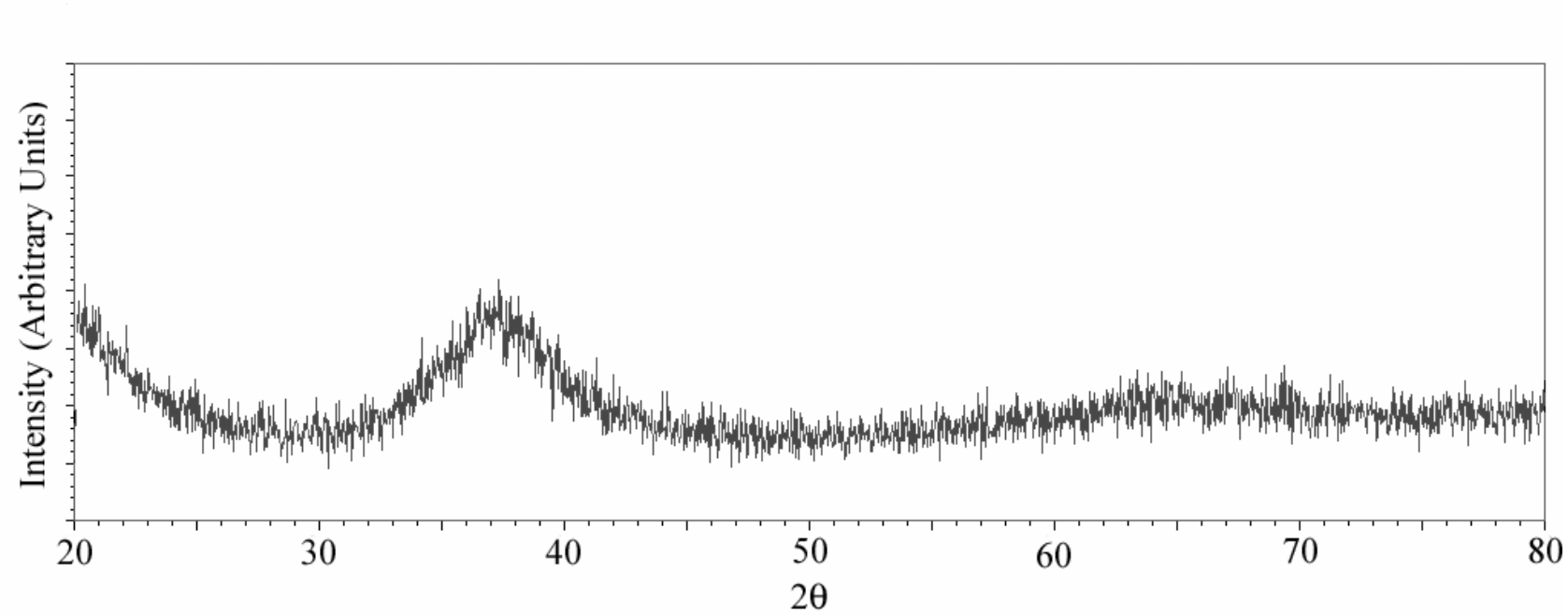

Figure 34. A representative X-ray diffraction spectrum of the Vit 105 BMG [$Zr_{52.5}Cu_{17.9}Ni_{14.6}Al_{10.0}Ti_{5.0}$ (at.%)] corrosion samples. All spectra demonstrated broad, diffuse peaks characteristic of amorphous alloys.

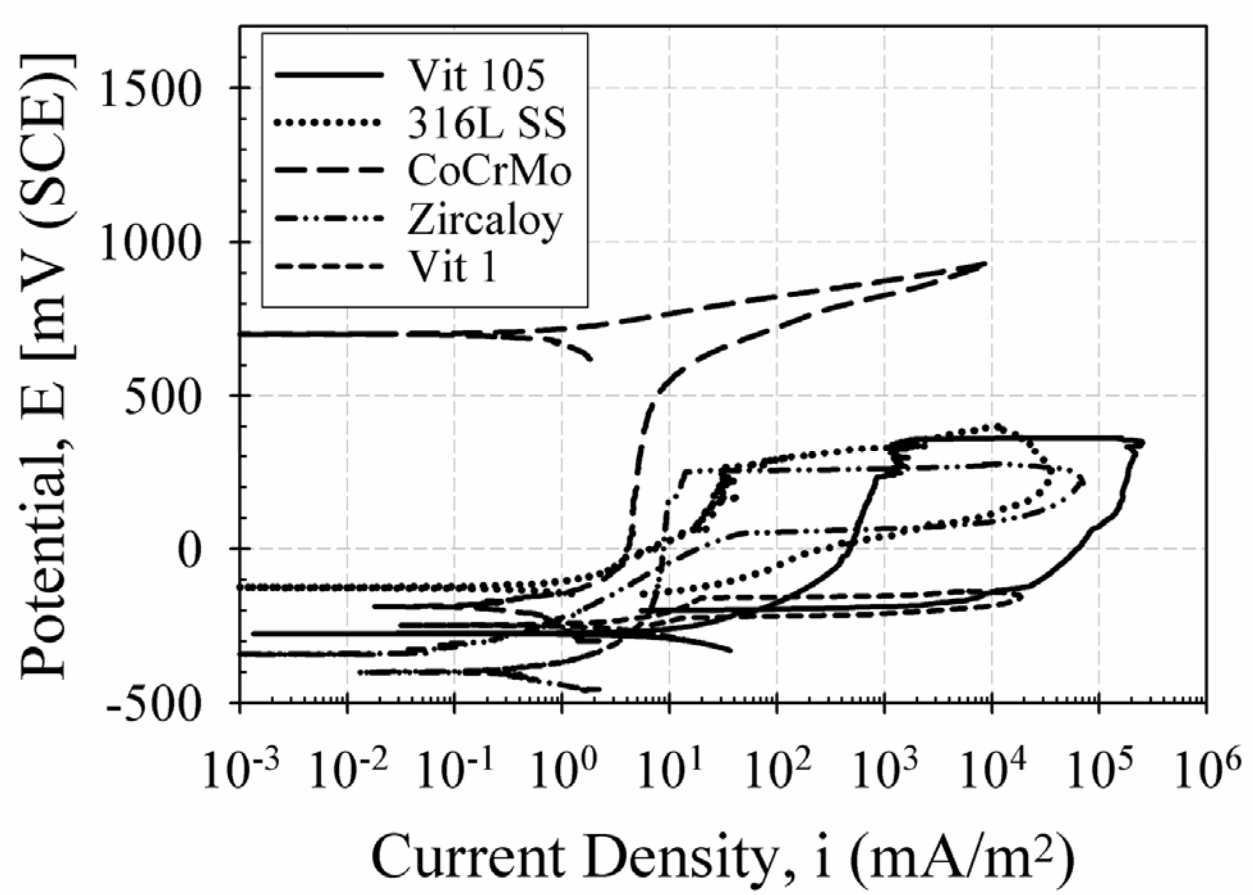

Figure 35. The average cyclic-anodic-polarization curves for the Vit 105 BMG [$Zr_{52.5}Cu_{17.9}Ni_{14.6}Al_{10.0}Ti_{5.0}$ (at.%)], AISI 316L stainless steel [$Fe_{62.5}Cr_{19.3}Ni_{13.3}$ (at.%), ASTM F138], CoCrMo [$Co_{61.4}Cr_{30.9}Mo_{3.6}$ (at.%), ASTM F799], Zr-based [$Zr_{98.42}Sn_{1.4}Fe_{0.1}$ (at.%)], and Vit 1 BMG [$Zr_{41.2}Ti_{13.8}Ni_{10}Cu_{12.5}Be_{22.5}$ (at.%)] alloys in the naturally aerated 0.6 M NaCl electrolyte.

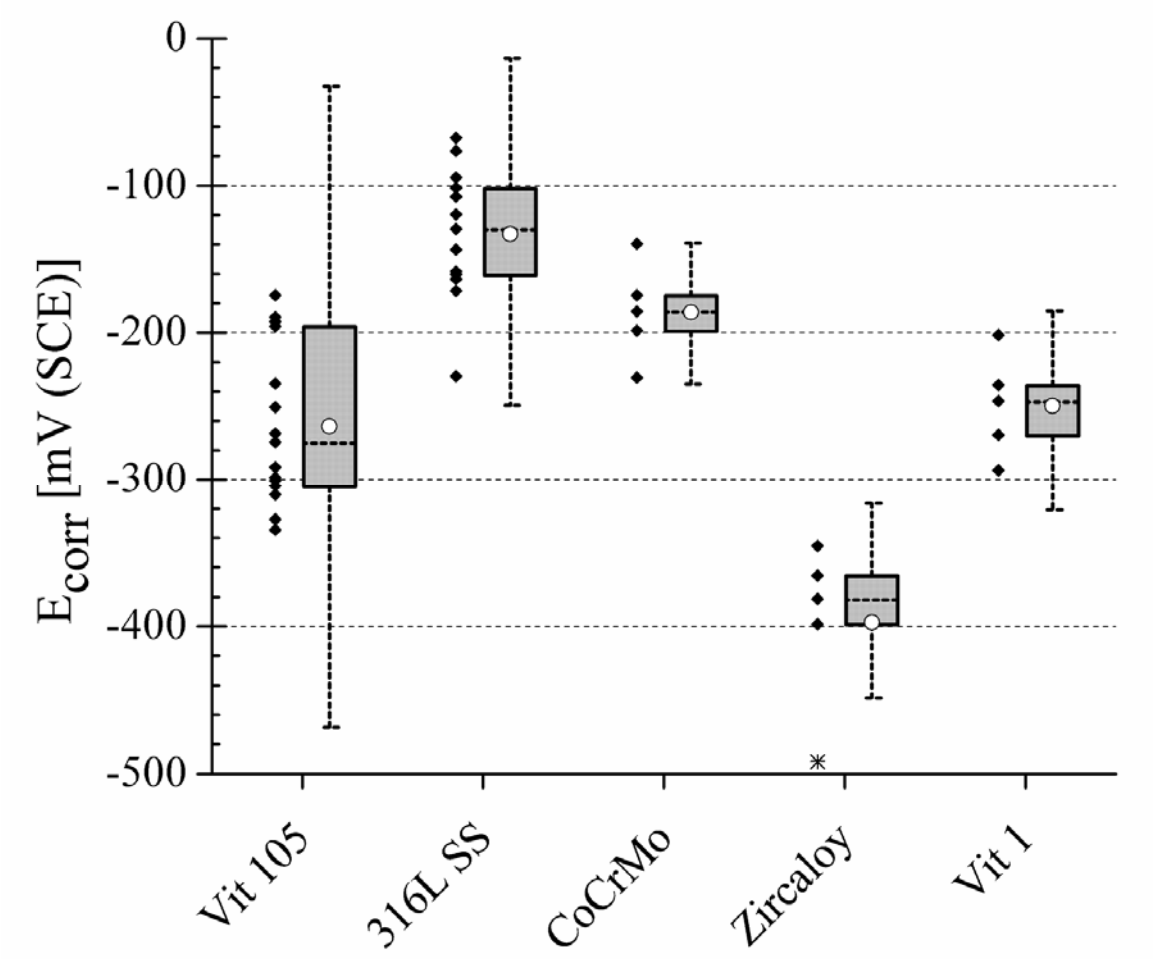

Figure 36. Partitioned scatter and box plots of the corrosion potential (E_{corr}) for the Vit 105 BMG [$Zr_{52.5}Cu_{17.9}Ni_{14.6}Al_{10.0}Ti_{5.0}$ (at.%)], AISI 316L stainless steel [$Fe_{62.5}Cr_{19.3}Ni_{13.3}$ (at.%), ASTM F138], CoCrMo [$Co_{61.4}Cr_{30.9}Mo_{3.6}$ (at.%), ASTM F799], Zr-based [$Zr_{98.42}Sn_{1.4}Fe_{0.1}$ (at.%)], and Vit 1 BMG [$Zr_{41.2}Ti_{13.8}Ni_{10}Cu_{12.5}Be_{22.5}$ (at.%)] alloys in the naturally aerated 0.6 M NaCl electrolyte. The open-circle represents the mean E_{corr} for each material, while the dashed line inside the box represents the median value. The whiskers represent the lower and upper inner fences, and asterisks designate outliers.

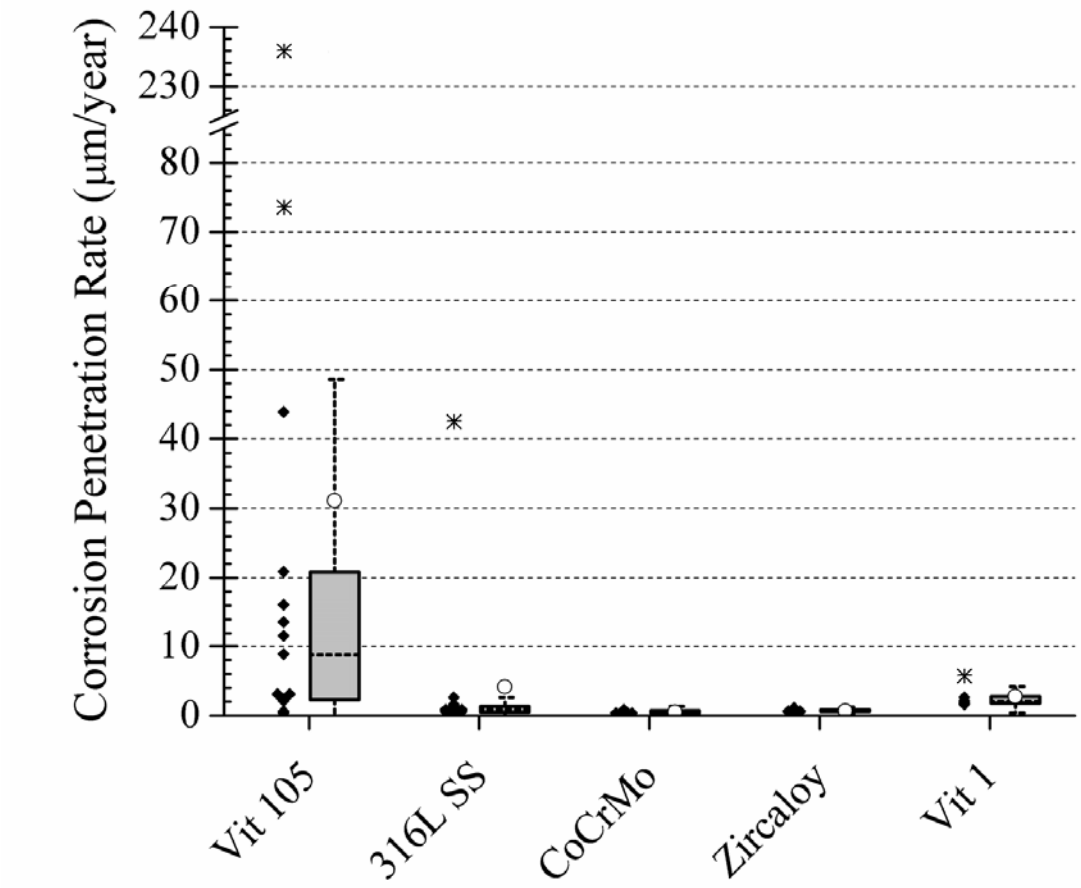

Figure 37. Partitioned scatter and box plots of the corrosion penetration rates (CPRs) for the Vit 105 BMG [$Zr_{52.5}Cu_{17.9}Ni_{14.6}Al_{10.0}Ti_{5.0}$ (at.%)], AISI 316L stainless steel [$Fe_{62.5}Cr_{19.3}Ni_{13.3}$ (at.%), ASTM F138], CoCrMo [$Co_{61.4}Cr_{30.9}Mo_{3.6}$ (at.%), ASTM F799], Zr-based [$Zr_{98.42}Sn_{1.4}Fe_{0.1}$ (at.%)], and Vit 1 BMG [$Zr_{41.2}Ti_{13.8}Ni_{10}Cu_{12.5}Be_{22.5}$ (at.%)] alloys in the naturally aerated 0.6 M NaCl electrolyte. The open-circle represents the mean CPR for each material, while the dashed line inside the box represents the median value. The whiskers represent the lower and upper inner fences, and asterisks designate outliers.

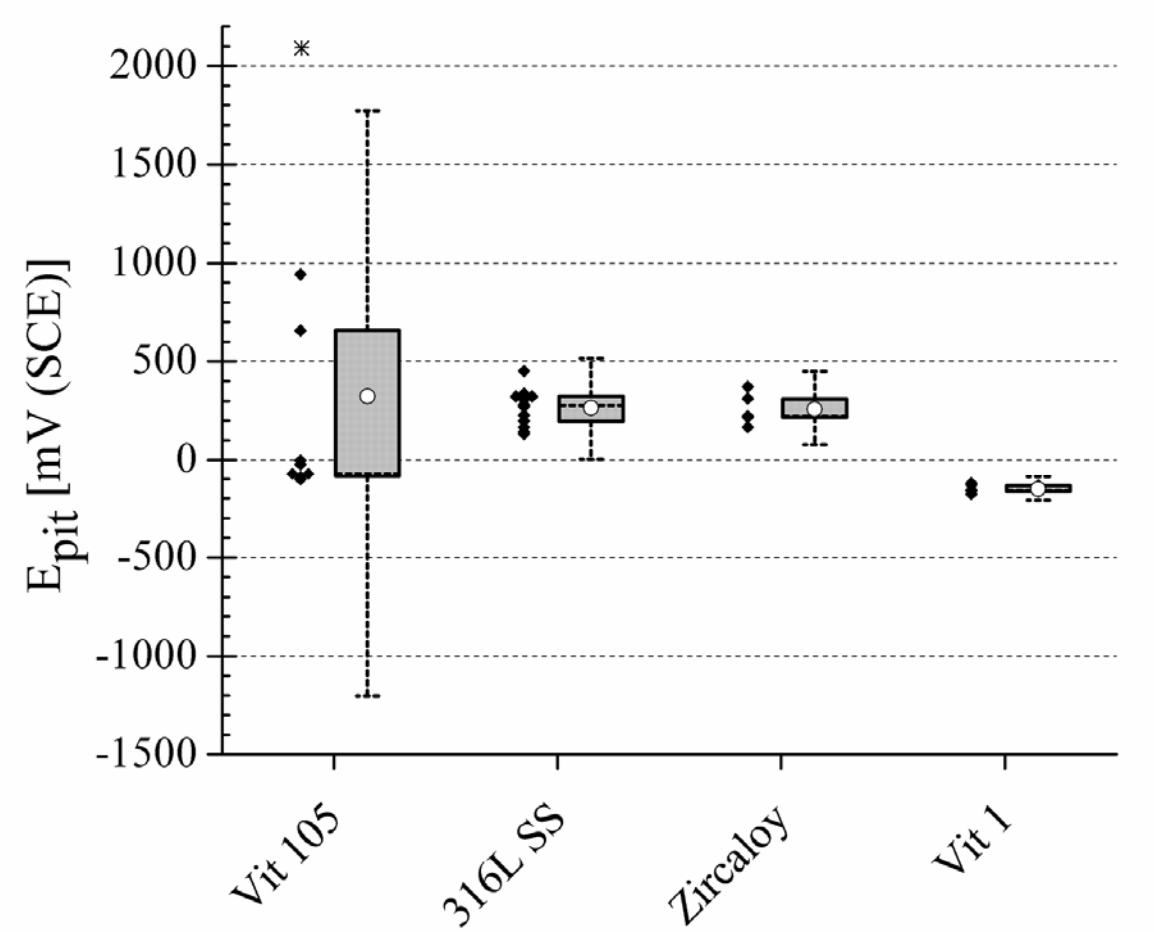

Figure 38. Partitioned scatter and box plots of the pitting potential (E_{pit}) for the Vit 105 BMG [$Zr_{52.5}Cu_{17.9}Ni_{14.6}Al_{10.0}Ti_{5.0}$ (at.%)], AISI 316L stainless steel [$Fe_{62.5}Cr_{19.3}Ni_{13.3}$ (at.%), ASTM F138], Zr-based [$Zr_{98.42}Sn_{1.4}Fe_{0.1}$ (at.%)], and Vit 1 BMG [$Zr_{41.2}Ti_{13.8}Ni_{10}Cu_{12.5}Be_{22.5}$ (at.%)] alloys in the naturally aerated 0.6 M NaCl electrolyte. The CoCrMo material was not susceptible to localized corrosion. The open-circle represents the mean E_{pit} for each material, while the dashed line inside the box represents the median value. The whiskers represent the lower and upper inner fences, and asterisks designate outliers.

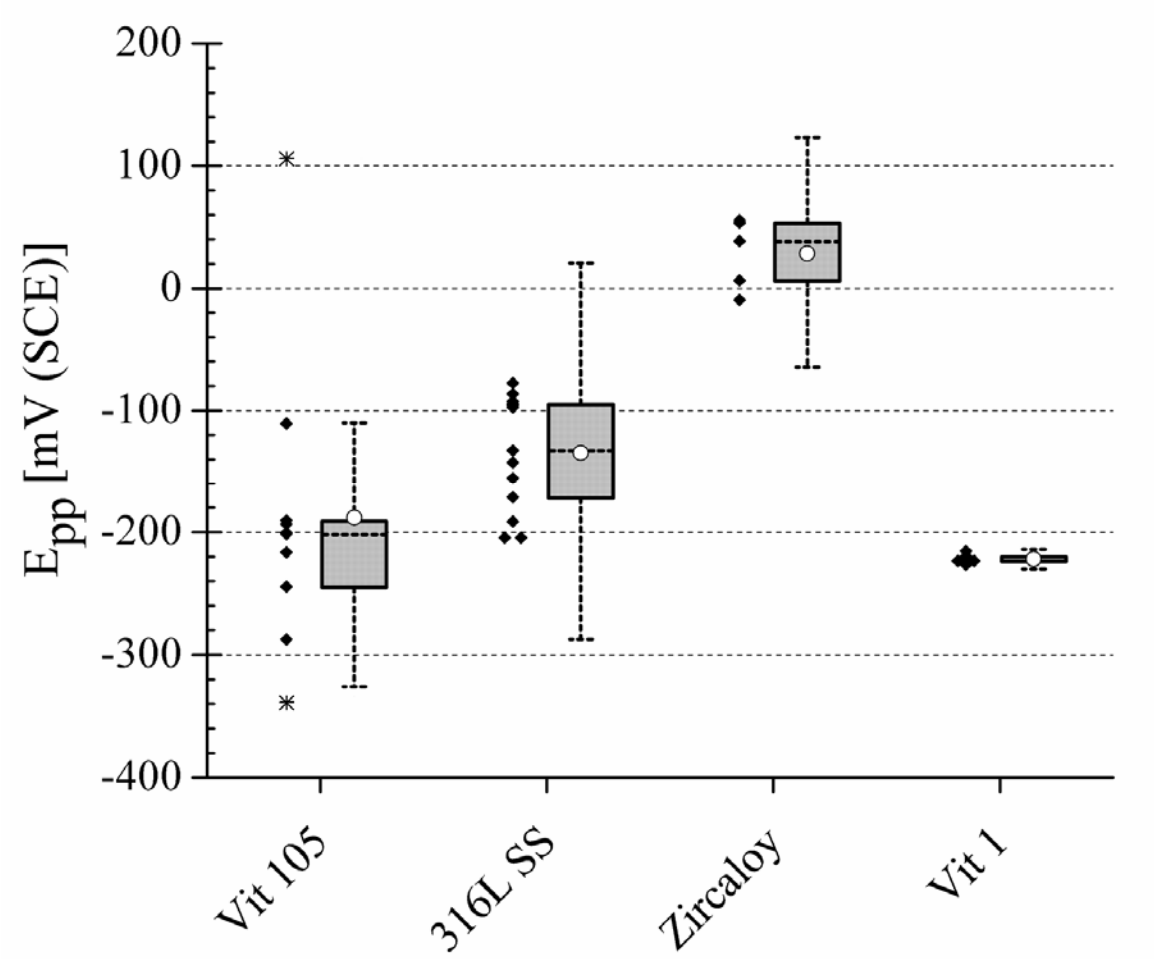

Figure 39. Partitioned scatter and box plots of the pitting overpotential (E_{pp}) for the Vit 105 BMG [$Zr_{52.5}Cu_{17.9}Ni_{14.6}Al_{10.0}Ti_{5.0}$ (at.%)], AISI 316L stainless steel [$Fe_{62.5}Cr_{19.3}Ni_{13.3}$ (at.%), ASTM F138], CoCrMo [$Co_{61.4}Cr_{30.9}Mo_{3.6}$ (at.%), ASTM F799], Zr-based [$Zr_{98.42}Sn_{1.4}Fe_{0.1}$ (at.%)], and Vit 1 BMG [$Zr_{41.2}Ti_{13.8}Ni_{10}Cu_{12.5}Be_{22.5}$ (at.%)] alloys in the naturally aerated 0.6 M NaCl electrolyte. The CoCrMo material was not susceptible to localized corrosion. The open-circle represents the mean E_{pp} for each material, while the dashed line inside the box represents the median value. The whiskers represent the lower and upper inner fences, and asterisks designate outliers.

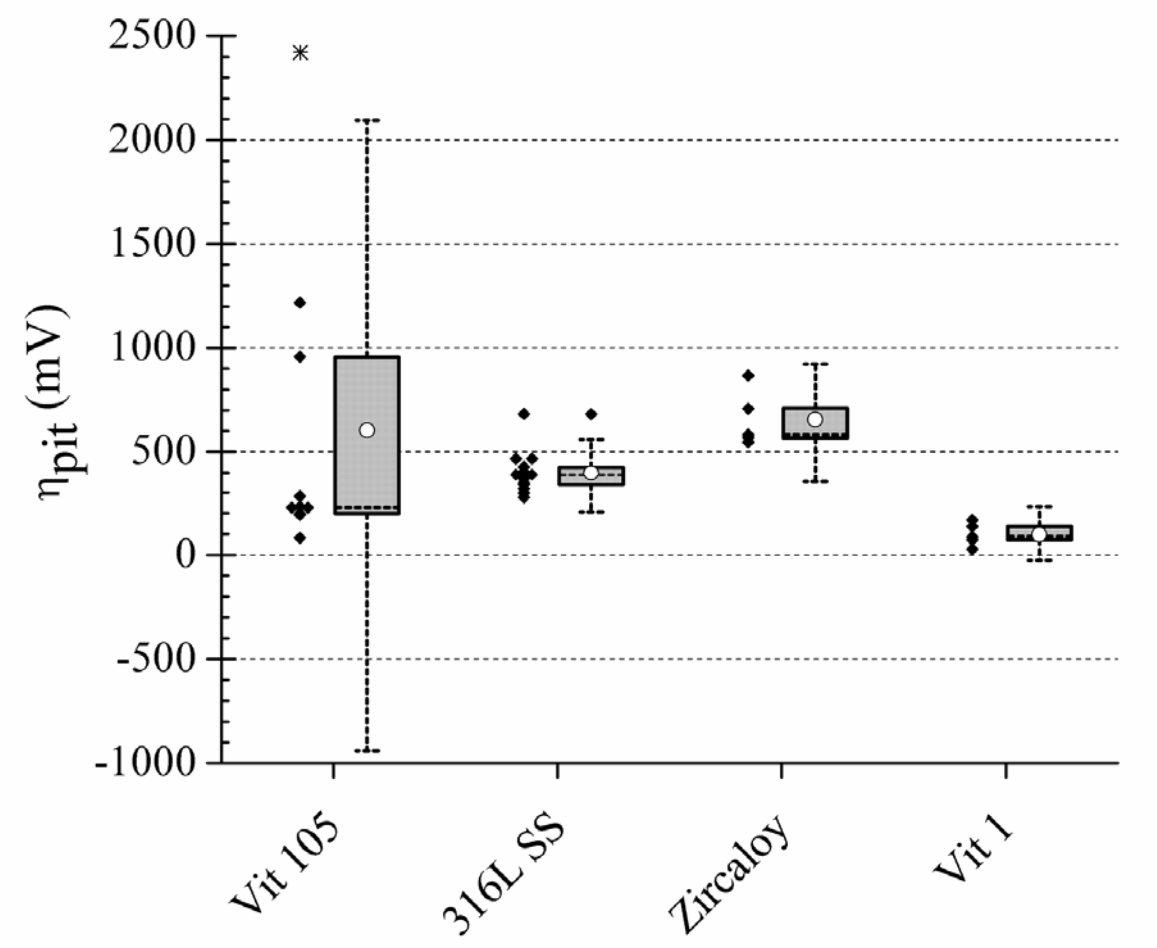

Figure 40. Partitioned scatter and box plots of the passivation potential (η_{pit}) for the Vit 105 BMG [$Zr_{52.5}Cu_{17.9}Ni_{14.6}Al_{10.0}Ti_{5.0}$ (at.%)], AISI 316L stainless steel [$Fe_{62.5}Cr_{19.3}Ni_{13.3}$ (at.%), ASTM F138], CoCrMo [$Co_{61.4}Cr_{30.9}Mo_{3.6}$ (at.%), ASTM F799], Zr-based [$Zr_{98.42}Sn_{1.4}Fe_{0.1}$ (at.%)], and Vit 1 BMG [$Zr_{41.2}Ti_{13.8}Ni_{10}Cu_{12.5}Be_{22.5}$ (at.%)] alloys in the naturally aerated 0.6 M NaCl electrolyte. The CoCrMo material was not susceptible to localized corrosion. The open-circle represents the mean η_{pit} for each material, while the dashed line inside the box represents the median value. The whiskers represent the lower and upper inner fences, and asterisks designate outliers.

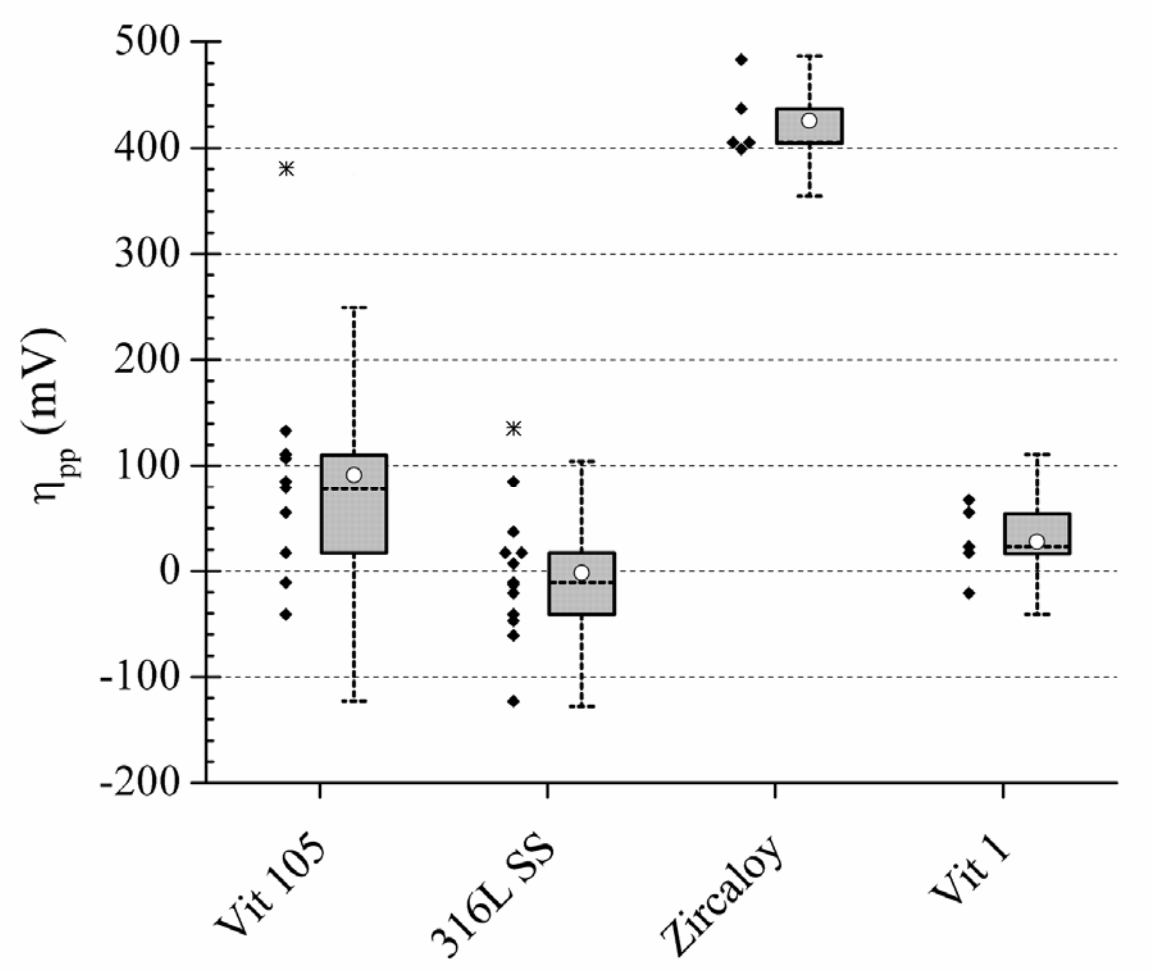

Figure 41. Partitioned scatter and box plots of the passivation overpotential (η_{pp}) for the Vit 105 BMG [$Zr_{52.5}Cu_{17.9}Ni_{14.6}Al_{10.0}Ti_{5.0}$ (at.%)], AISI 316L stainless steel [$Fe_{62.5}Cr_{19.3}Ni_{13.3}$ (at.%), ASTM F138], CoCrMo [$Co_{61.4}Cr_{30.9}Mo_{3.6}$ (at.%), ASTM F799], Zr-based [$Zr_{98.42}Sn_{1.4}Fe_{0.1}$ (at.%)], and Vit 1 BMG [$Zr_{41.2}Ti_{13.8}Ni_{10}Cu_{12.5}Be_{22.5}$ (at.%)] alloys in the naturally aerated 0.6 M NaCl electrolyte. The CoCrMo material was not susceptible to localized corrosion. The open-circle represents the mean η_{pp} for each material, while the dashed line inside the box represents the median value. The whiskers represent the lower and upper inner fences, and asterisks designate outliers.

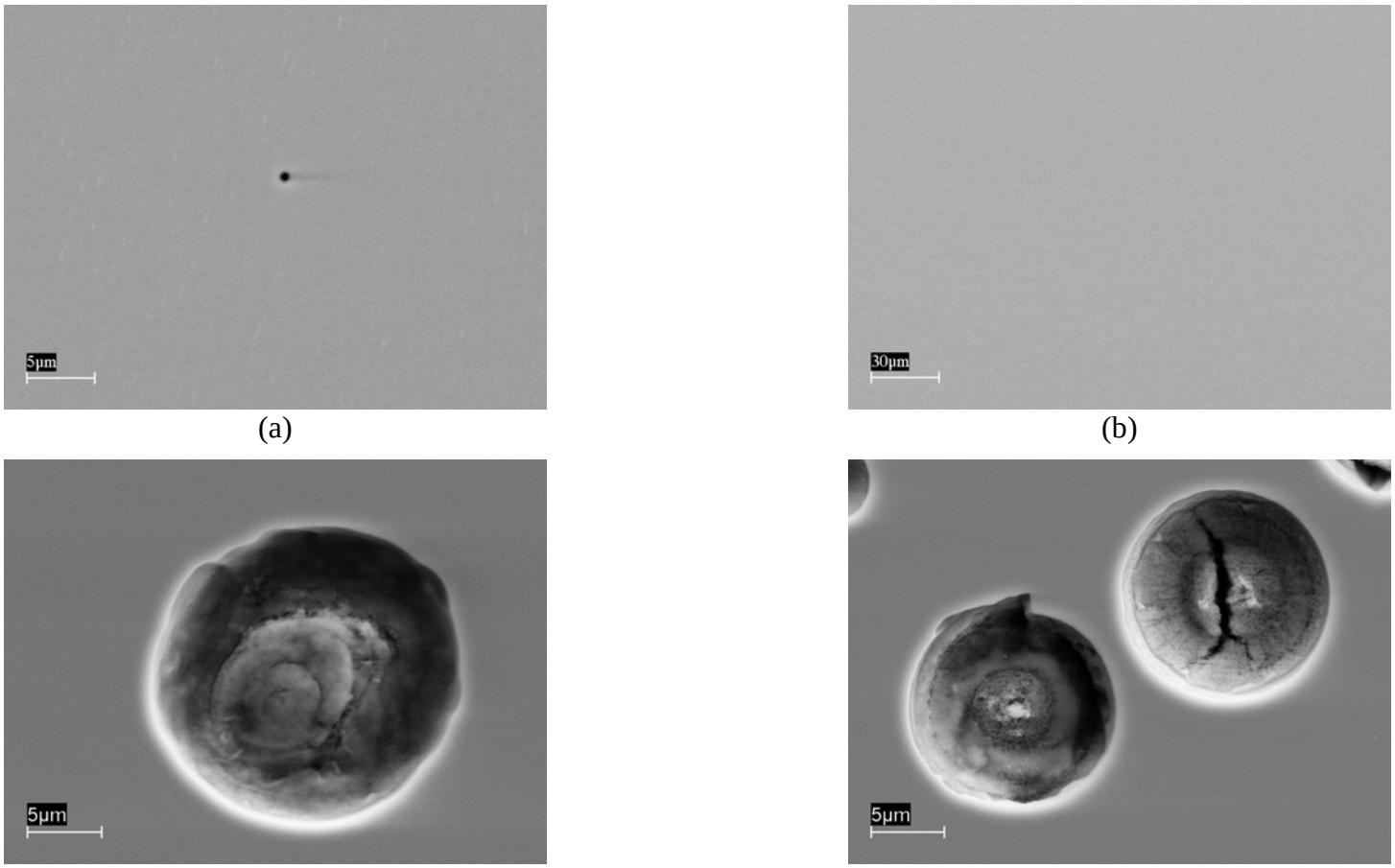

Figure 42. SEM photomicrographs of the Vit 105 BMG samples before (a-b) and after (c-d) the cyclic-anodic-polarization tests in 0.6 M NaCl that were manually stopped at varying times after pit initiation.

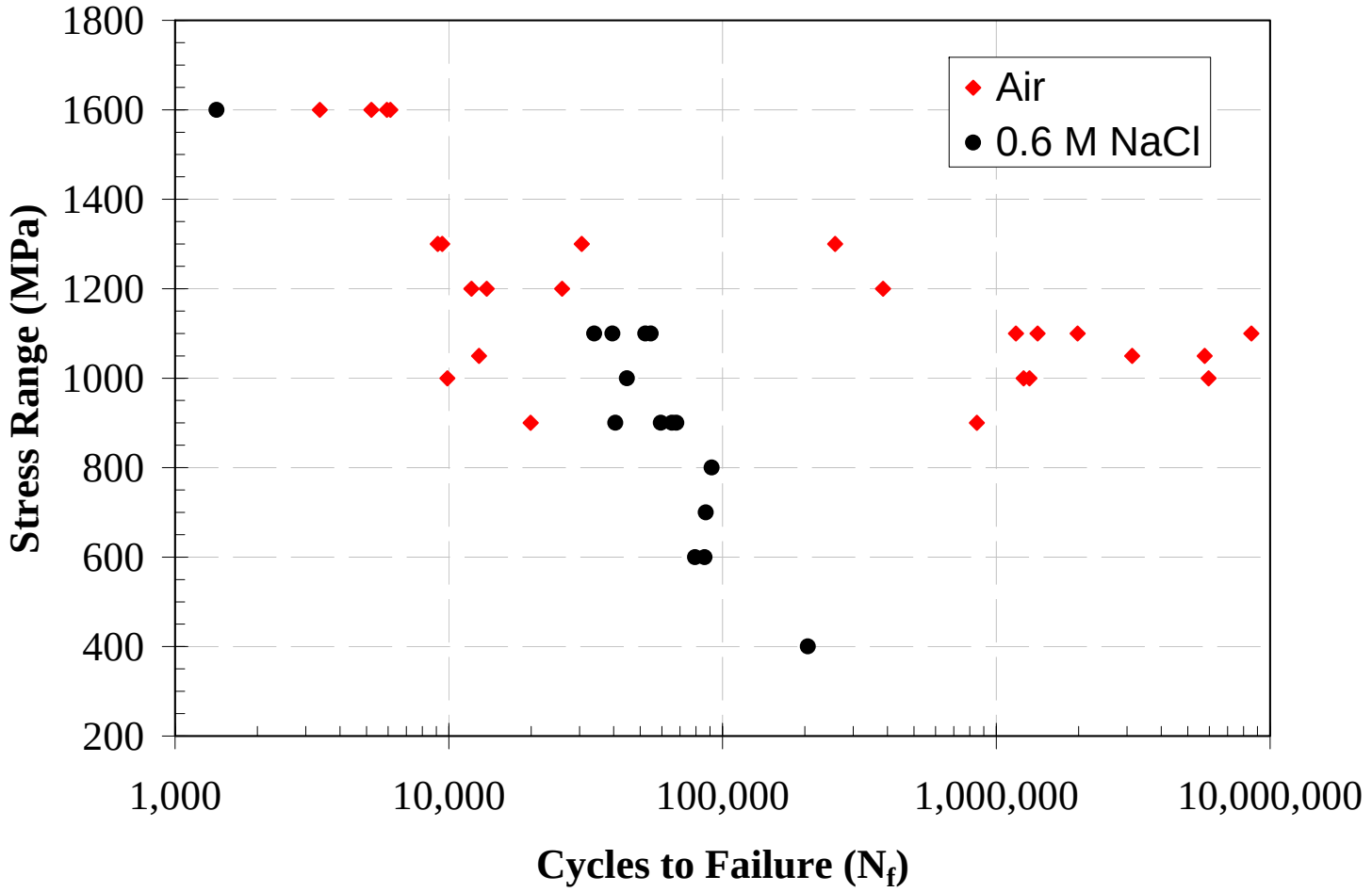

Figure 43. Plot of cycles to failure as a function of stress range for the four-point bending of Vit 105 BMG in air and a naturally aerated, 0.6 M NaCl electrolyte at a frequency of 10 Hz and R = 0.1.

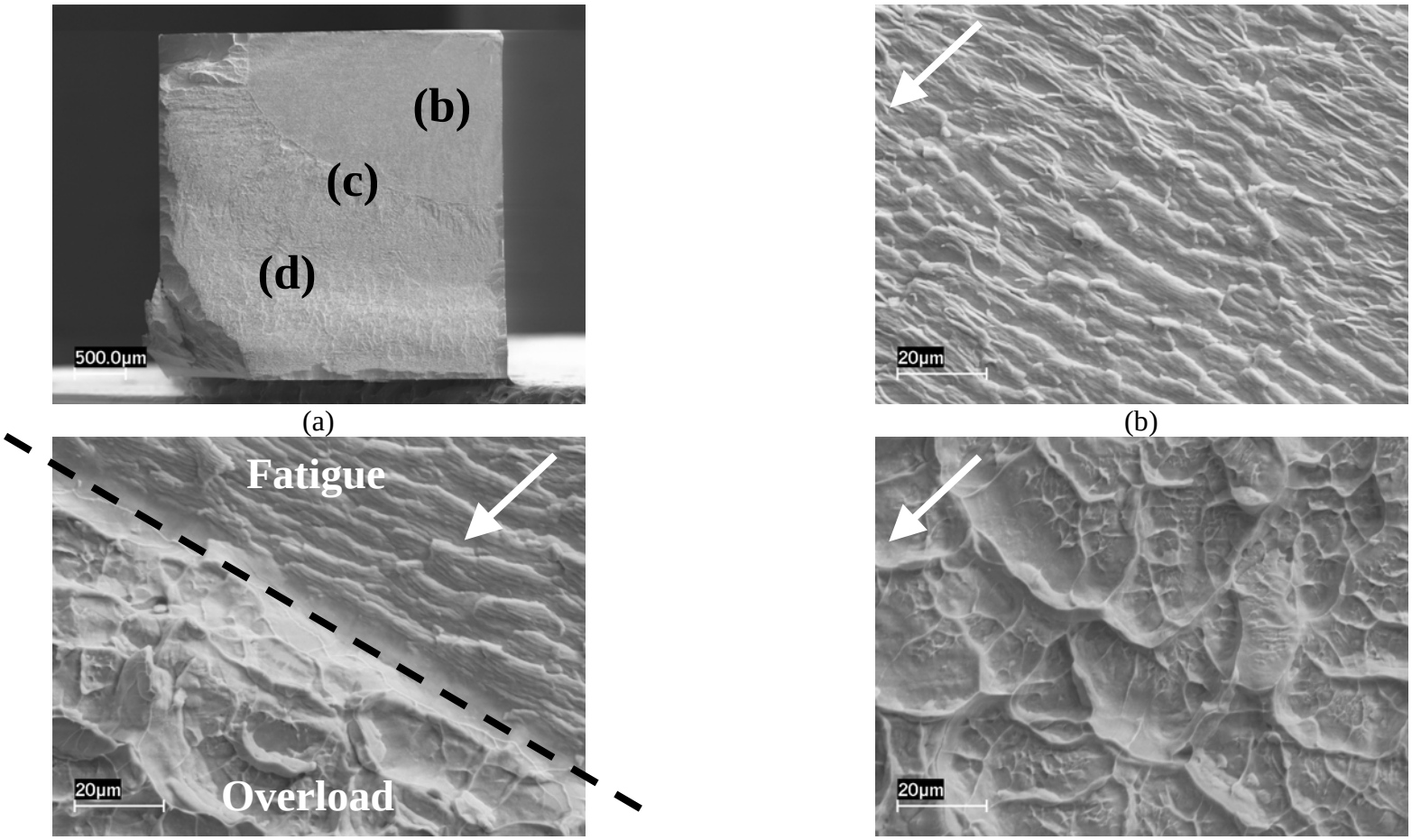

Figure 44. SEM fractographs demonstrating the typical fracture surface in air on which (a) the fracture initiated at the corner of the sample on the side subjected to tensile loading (top), (b) the striations of the fatigue crack-growth region, (c) the transition region from the fatigue to overload regions, and (d) the overload region. The arrows indicate the crack-growth direction.

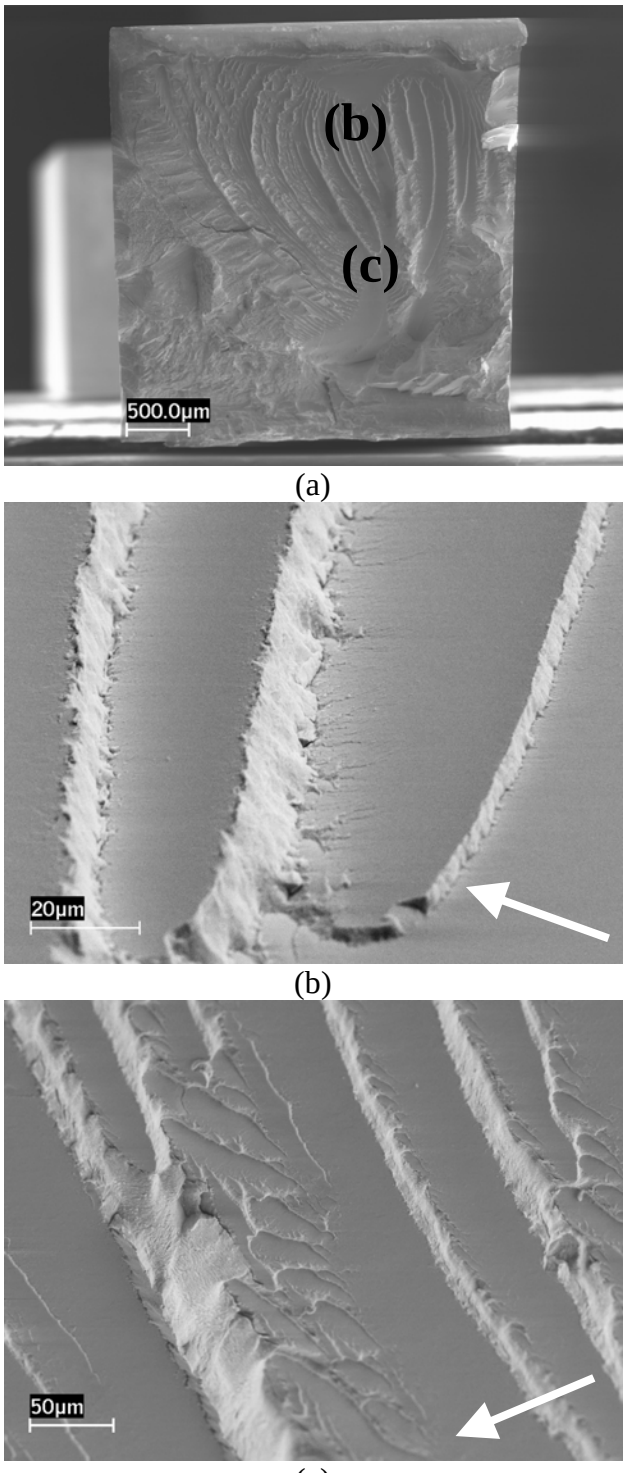

Figure 45. Fractographs demonstrating (a) the typical fracture surface in 0.6 M NaCl, (b) alternating regions of smooth steps, separated by abrupt changes in fracture planes, and (c) abrupt changes between the smooth fracture regions containing visible striations. The arrows indicate the crack-growth direction.

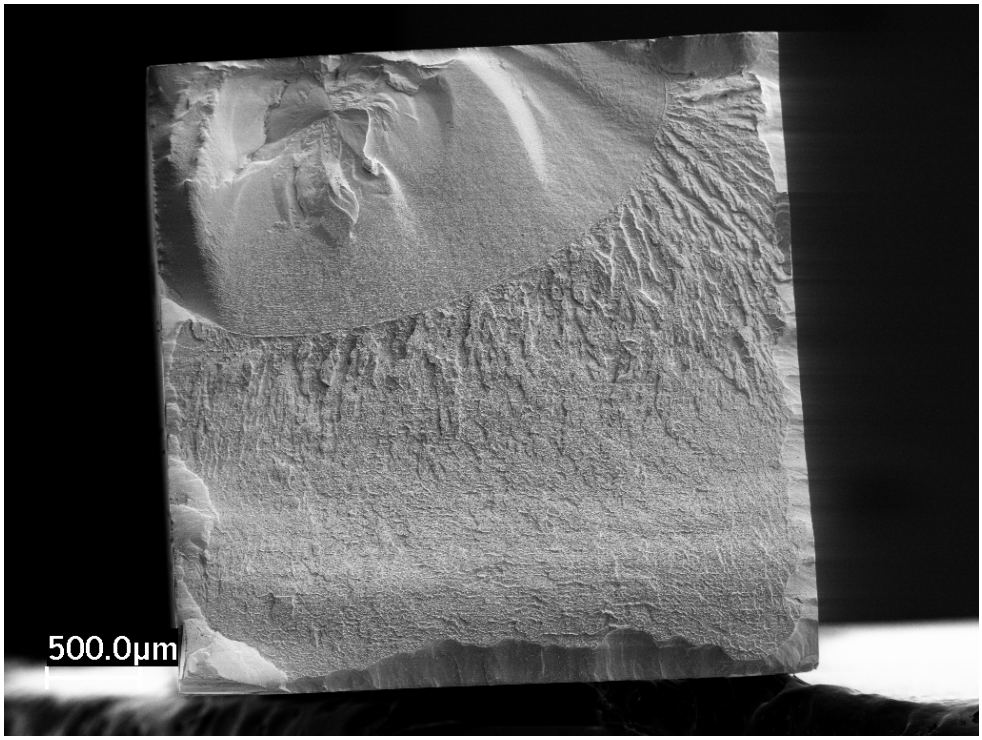

(a)

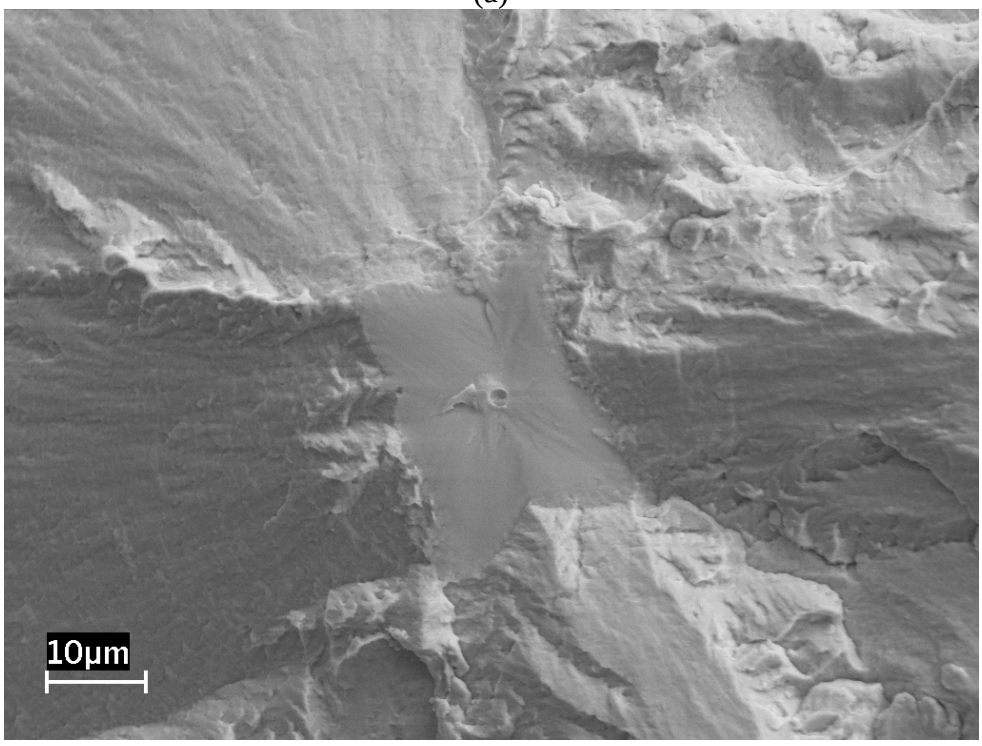

(b)

Figure 46. Fractograph of bend sample that fractured due to crack initiation at an interior inhomogeneity. (a) Low magnification, and (b) high magnification.

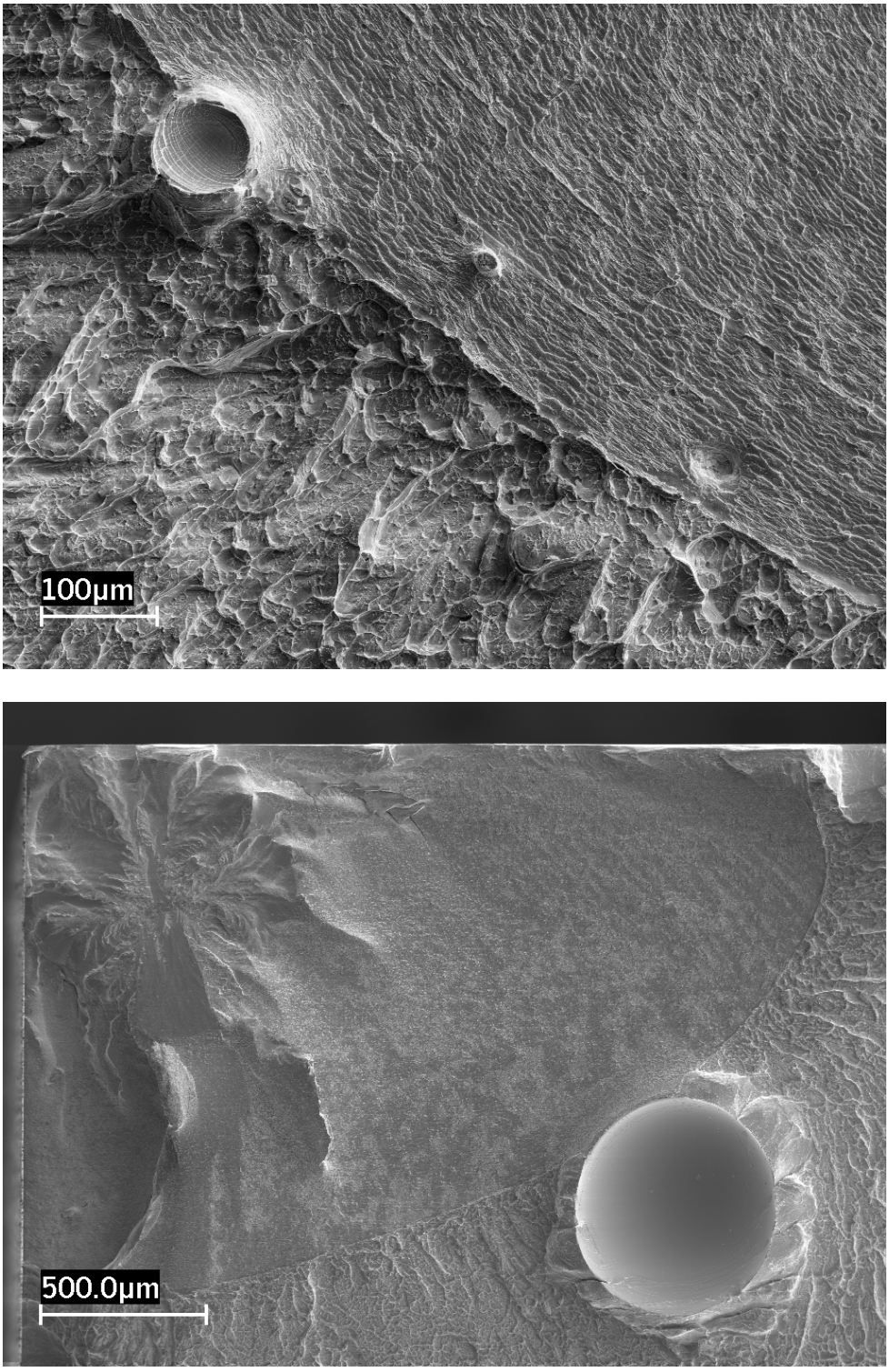

Figure 47. Fractographs demonstrating porosity at the transition from the controlled, striated crack-growth region to the final fracture/overload region.

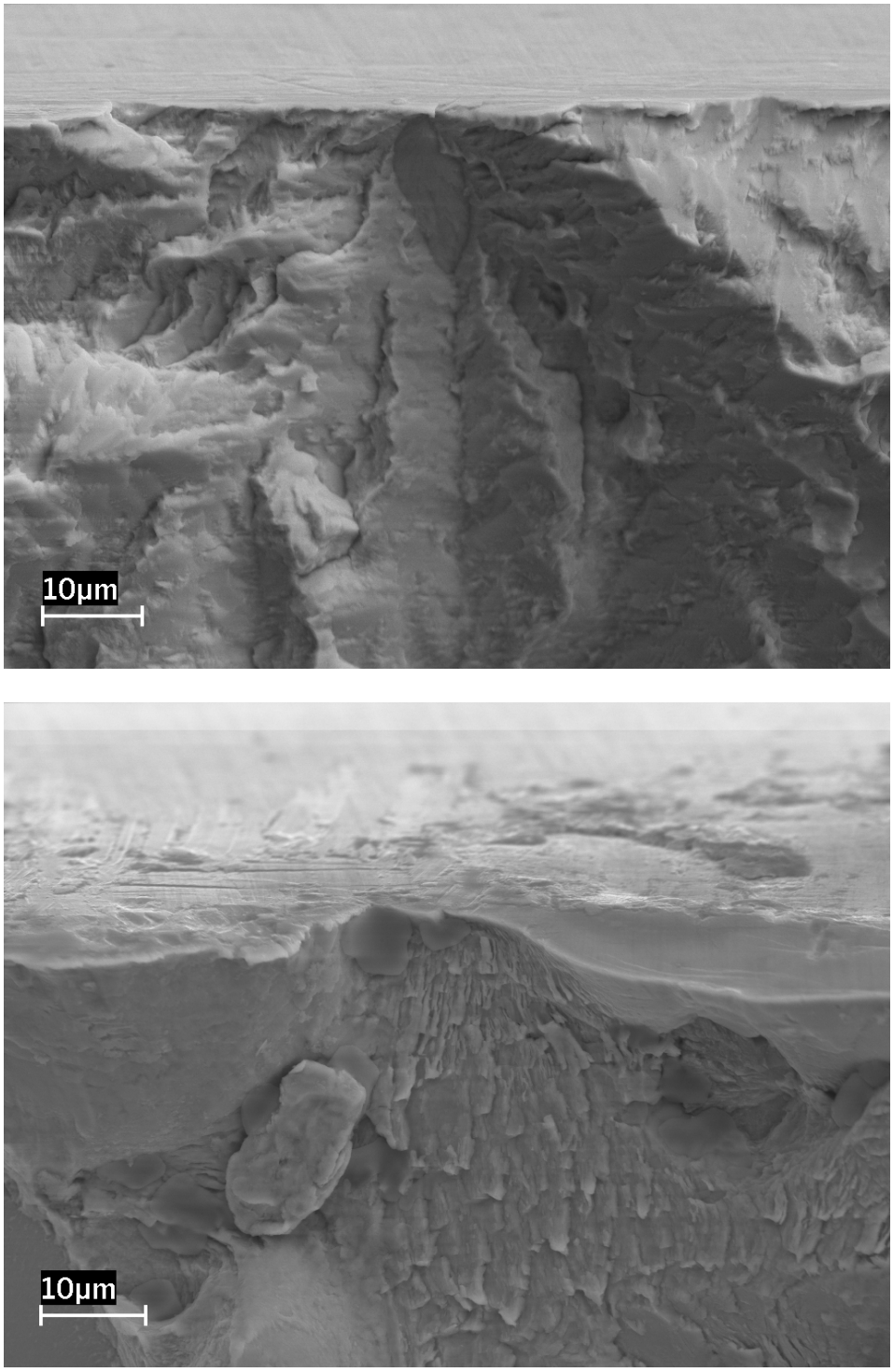

Figure 48. SEM photomicrographs illustrating examples of samples that failed due to fractures that initiated at particles or surface defects at the tensile surfaces of the bend samples.

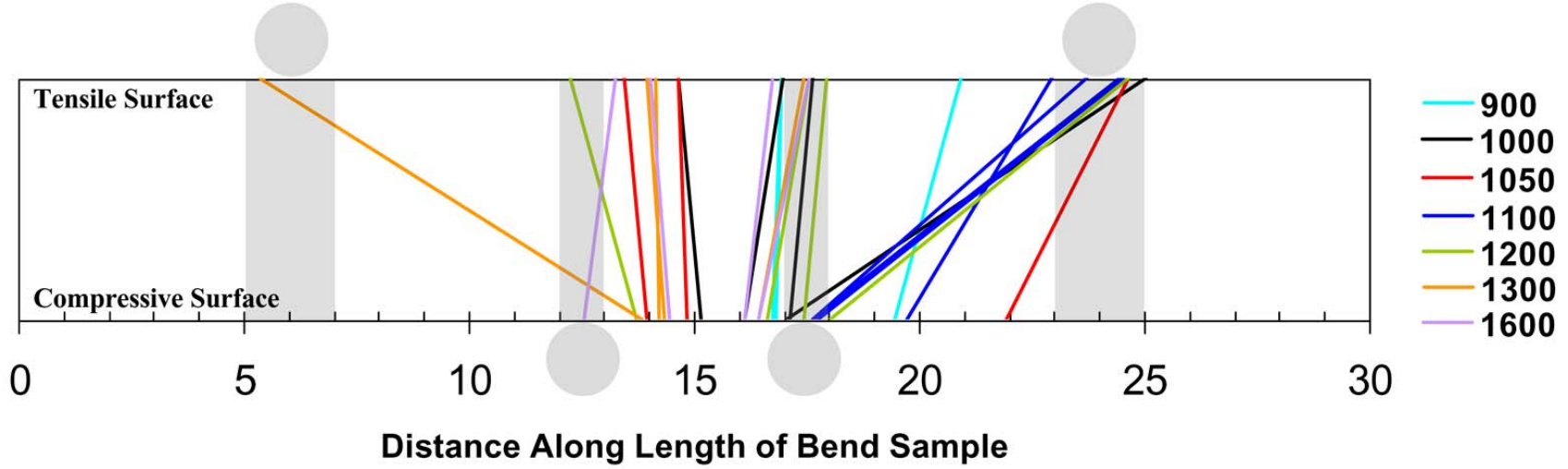

Figure 49. Schematic diagram illustrating the locations of the loading pins and fractures for the four-point bend samples tested in air at various stress levels. The shaded circles and areas represent the loading pins and the portions of the sample lengths that typically exhibited wear due to contact with the pins, respectively.

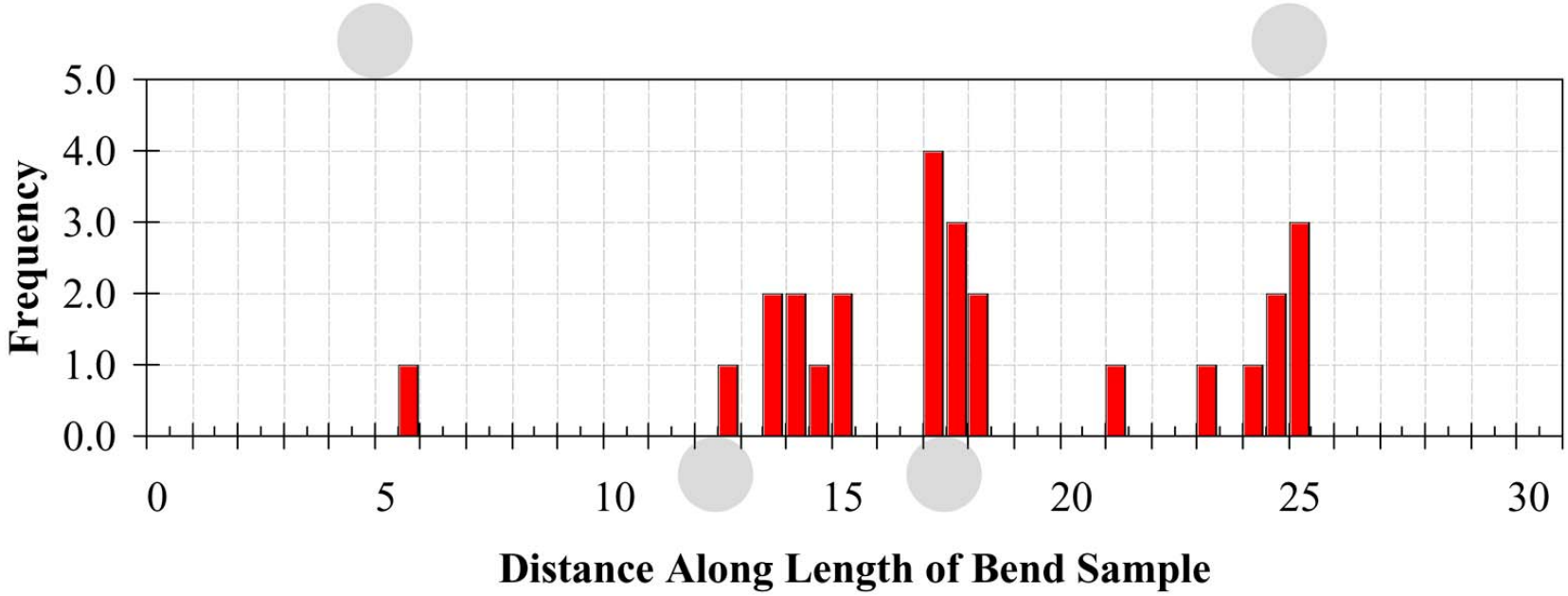

Figure 50. Histogram illustrating the location of crack initiation for the four-point bend samples tested in air at all stress levels. The gray circles represent the locations of the loading pins.

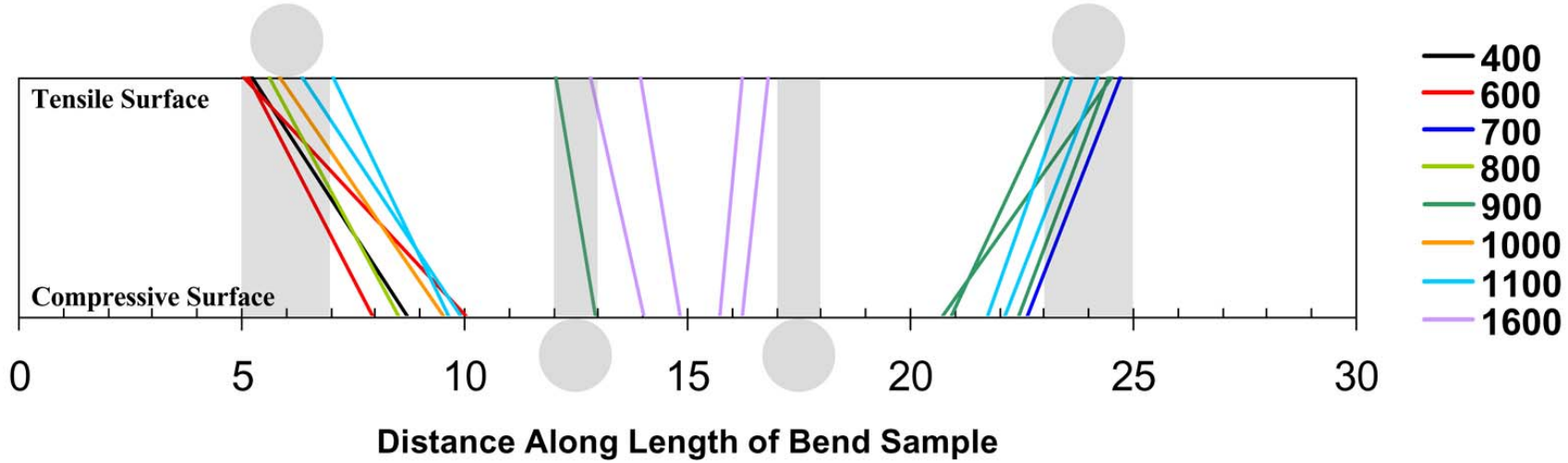

Figure 51. Schematic diagram illustrating the locations of the loading pins and fractures for the four-point bend samples tested in 0.6 M NaCl at various stress levels. The shaded circles and areas represent the loading pins and the portions of the sample lengths that typically exhibited wear due to contact with the pins, respectively.

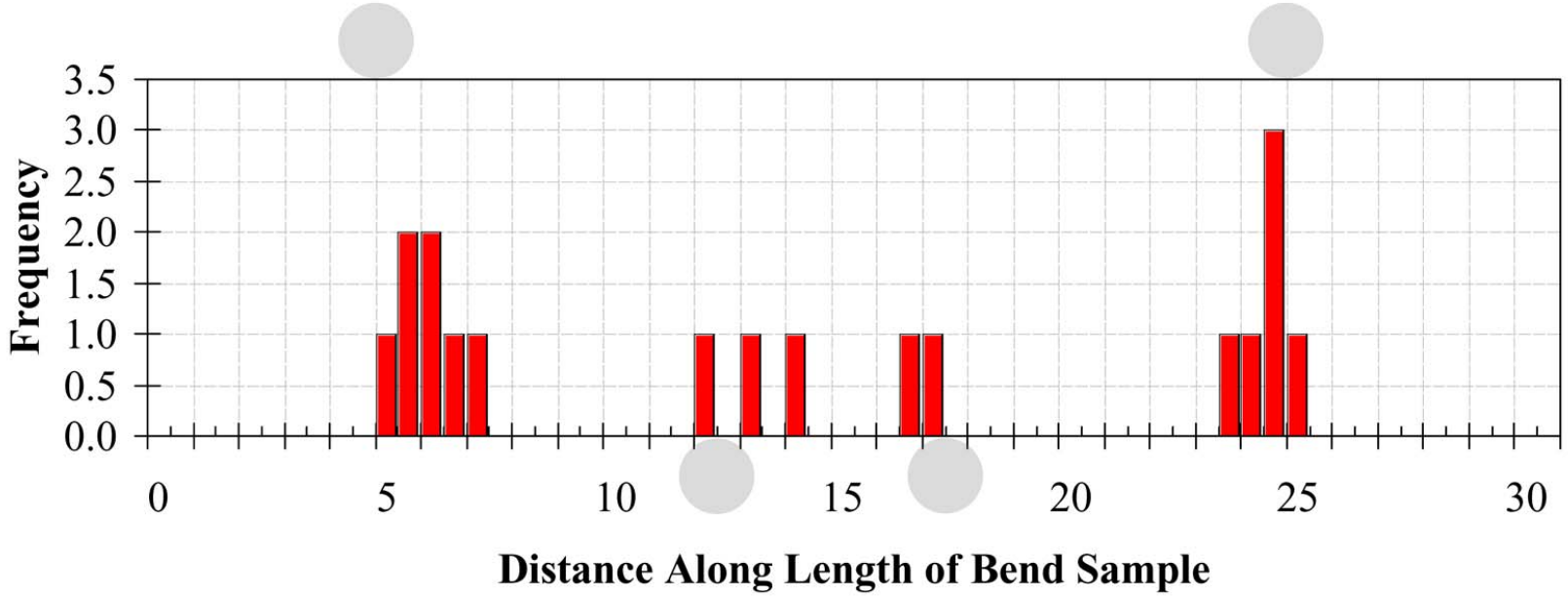

Figure 52. Histogram illustrating the location of crack initiation for the four-point bend samples tested in 0.6 M NaCl at all stress levels. The gray circles represent the locations of the loading pins.

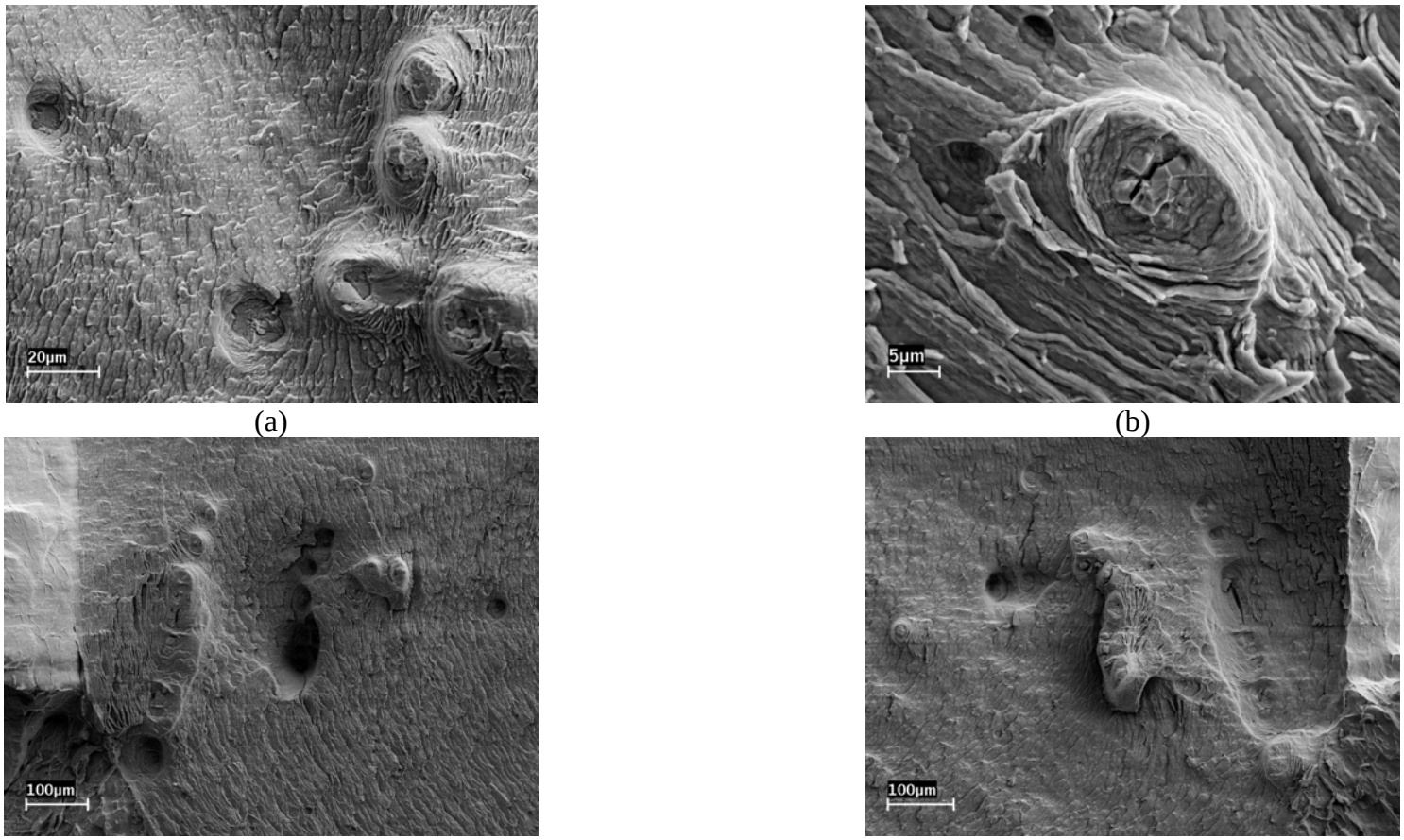

Figure 53. Fractographs of the particle-and-crater morphology in (a) small groups, and (b) in isolation. The particles on the fracture surface in (c) corresponded to craters on the opposite surface in (d), and vice-versa.

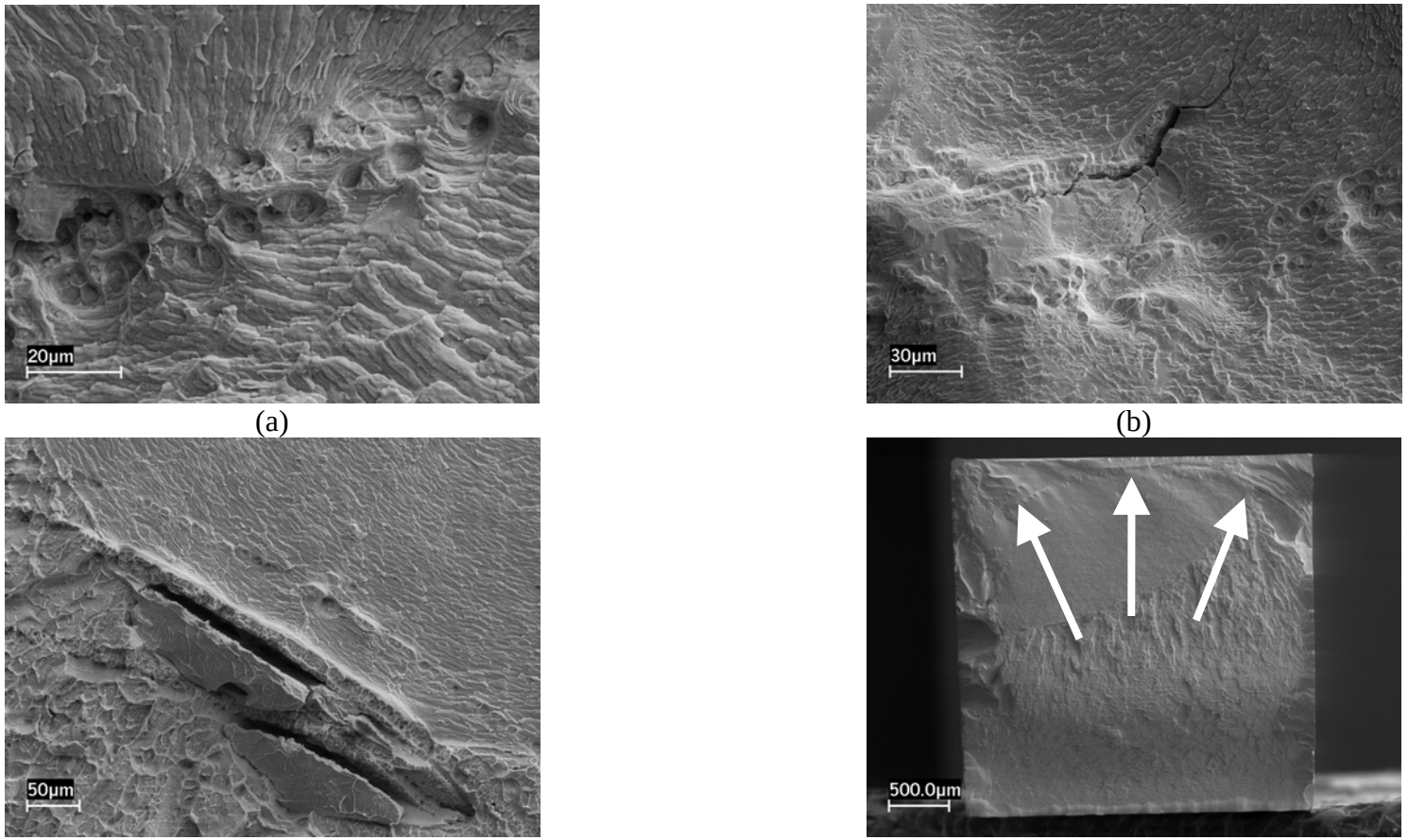

Figure 54. Fractographs of (a-c) short and (d) long arcs of particles observed on the fracture surfaces of the bend samples. The arrows in (d) denote the arc of particles across the top portion of the bend sample.

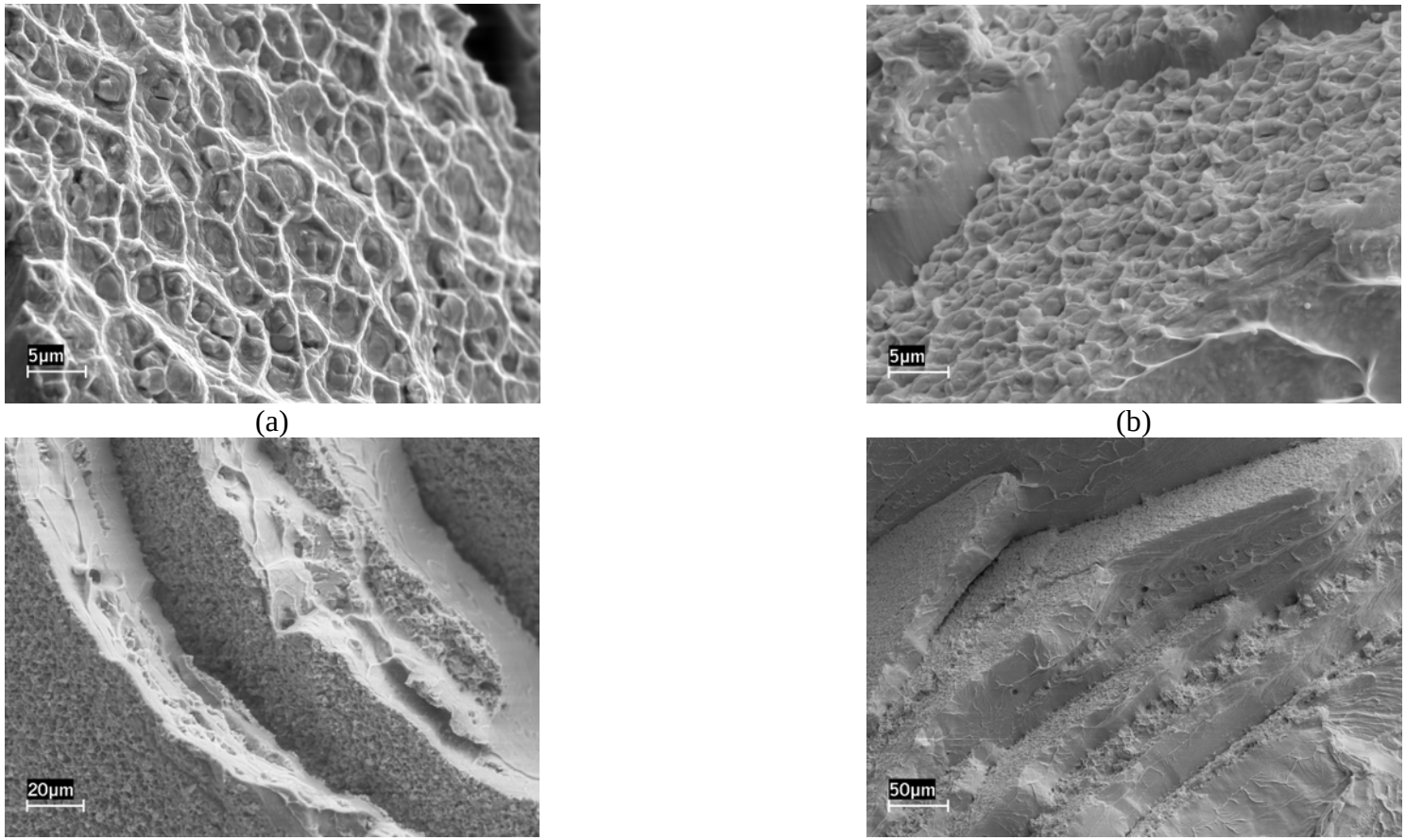

Figure 55. SEM fractographs illustrating morphology of the large sheets of small particles that form concentric arcs across the fracture surfaces in various locations.

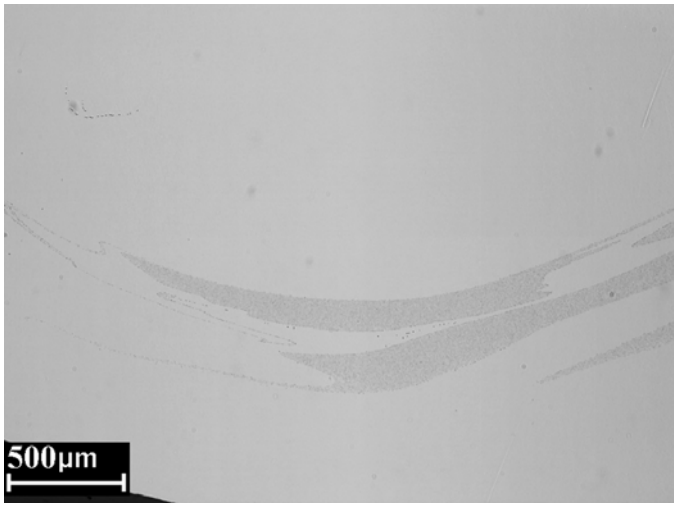

Figure 56. Optical microscopic photomicrograph of the “swirl pattern” commonly observed on polished and etched metallographic samples.

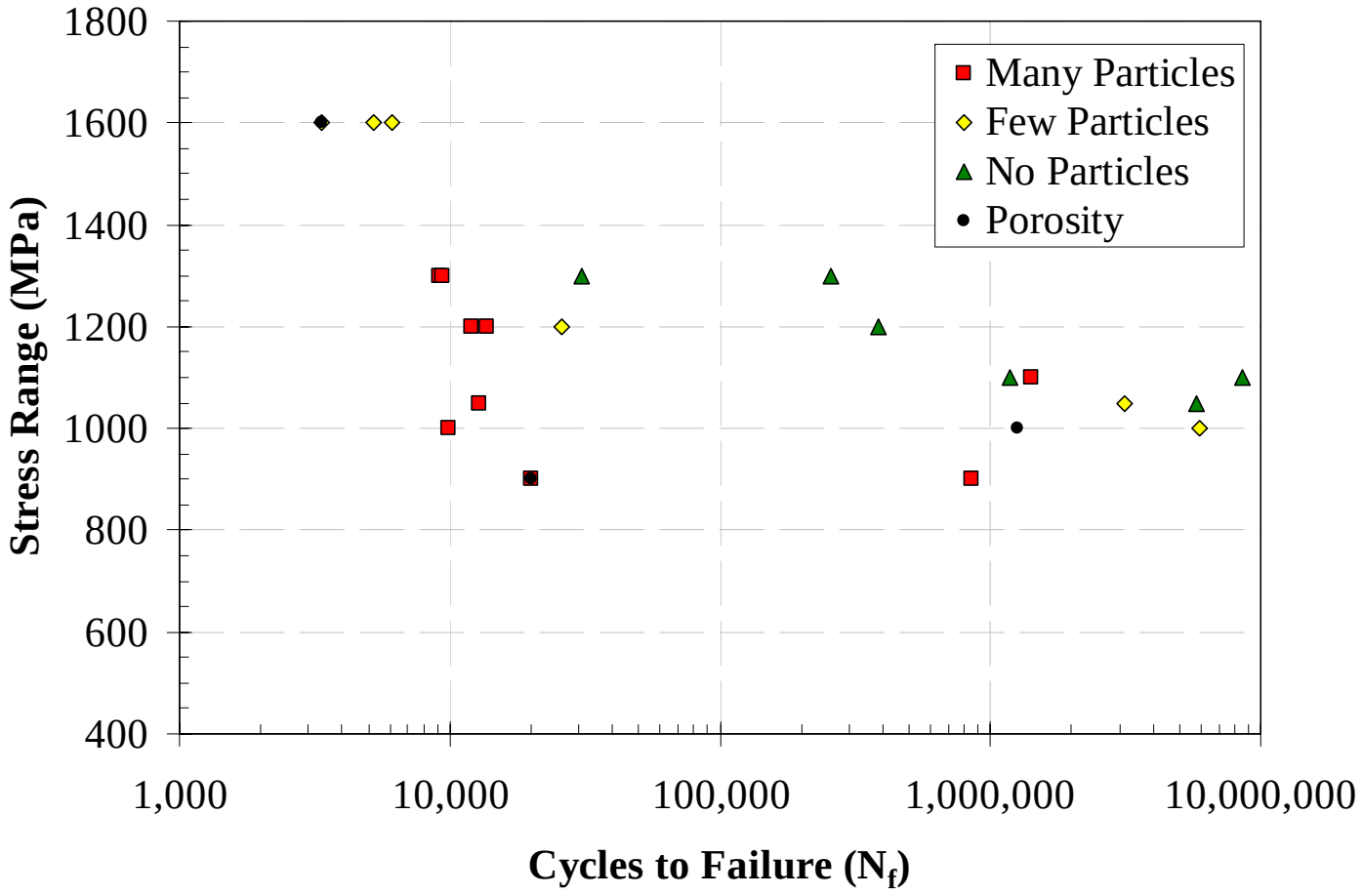

Figure 57. Plot of cycles to failure as a function of stress range (S-N) for the four-point bending of Vit 105 BMG in air. The qualitative amount of inhomogeneities and porosity observed in each sample is superimposed onto the stress-life data to demonstrate the correlation between inhomogeneities, porosity, and fatigue lives.

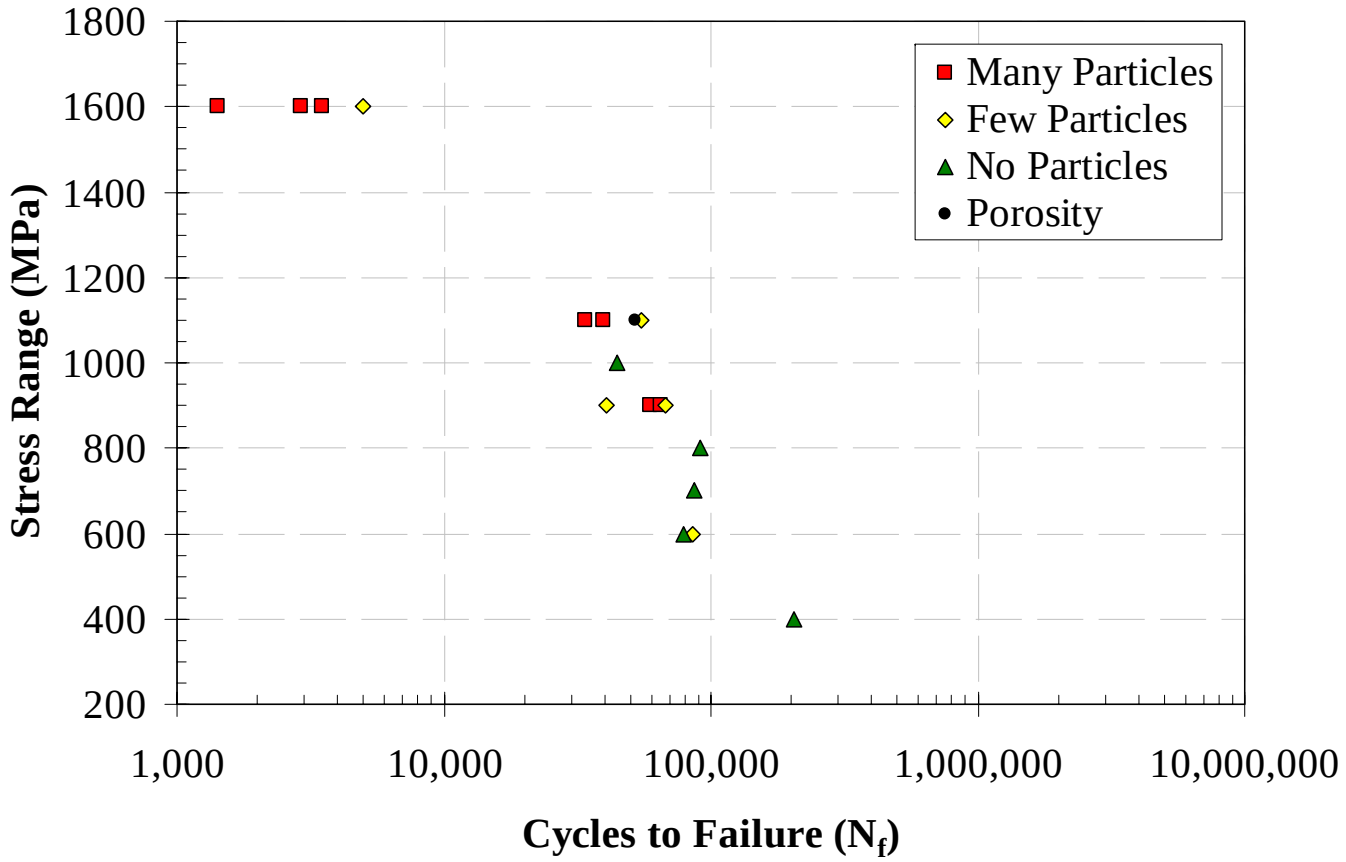

Figure 58. Plot of cycles to failure as a function of stress range (S-N) for the four-point bending of Vit 105 BMG in air. The qualitative amount of inhomogeneities and porosity observed in each sample is superimposed onto the stress-life data to demonstrate the correlation between inhomogeneities, porosity, and fatigue lives.

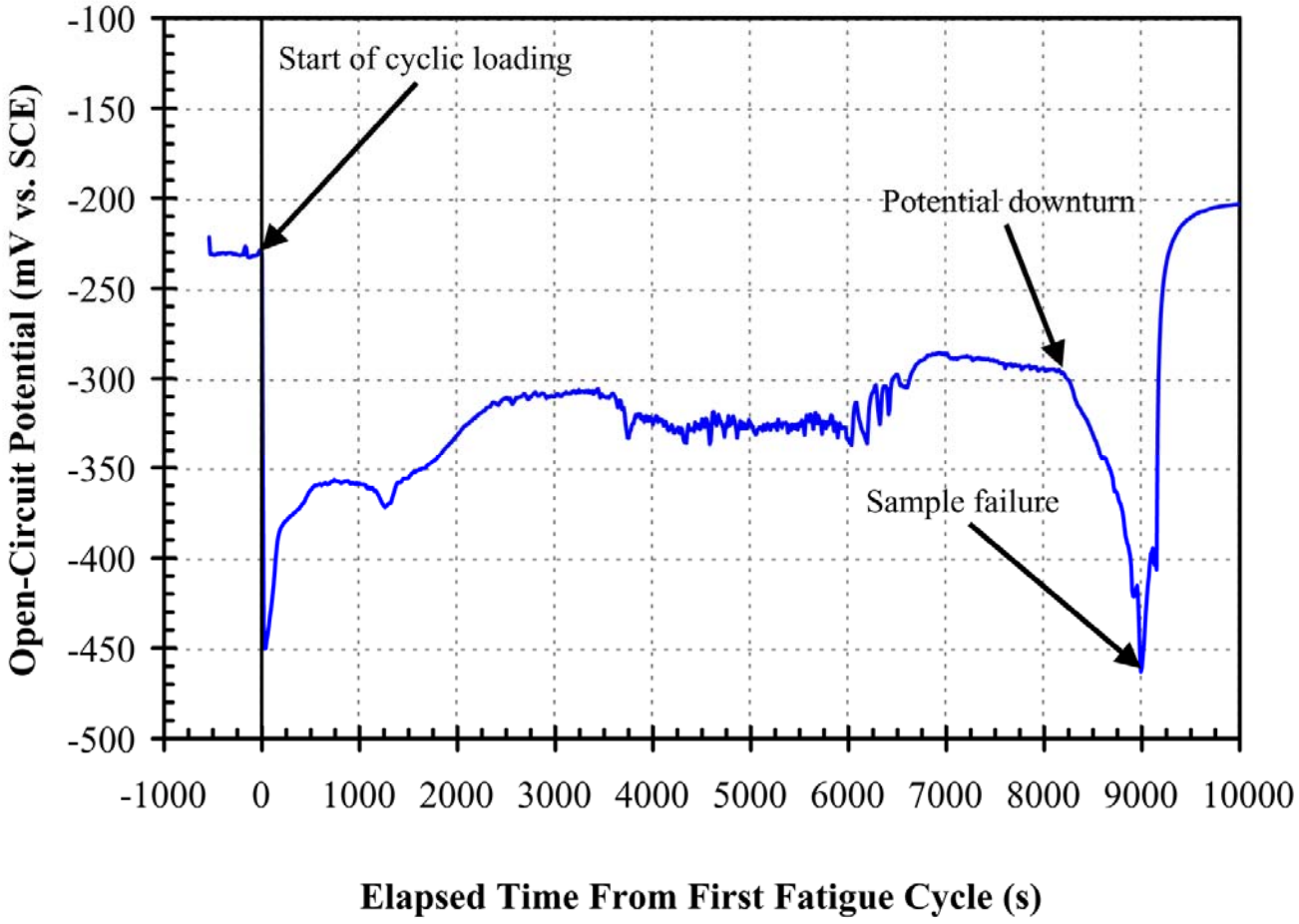

Figure 59. Typical plot of the open-circuit potential as a function of time during a corrosion-fatigue test.

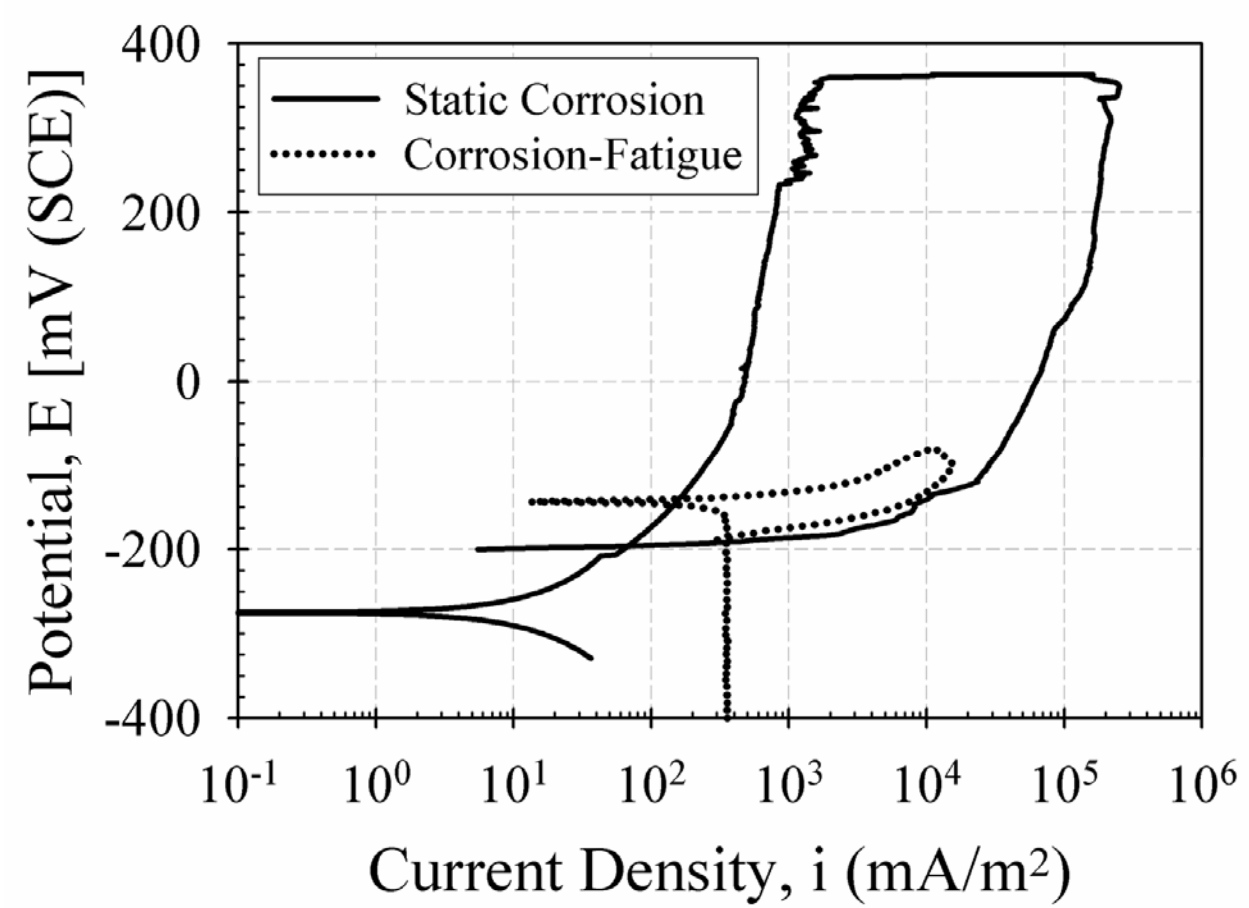

Figure 60. The average cyclic-anodic-polarization curves for the Vit 105 BMG alloy in 0.6 M NaCl without a load (static corrosion) and under fatigue loading at a stress range of 900 MPa (corrosion-fatigue).

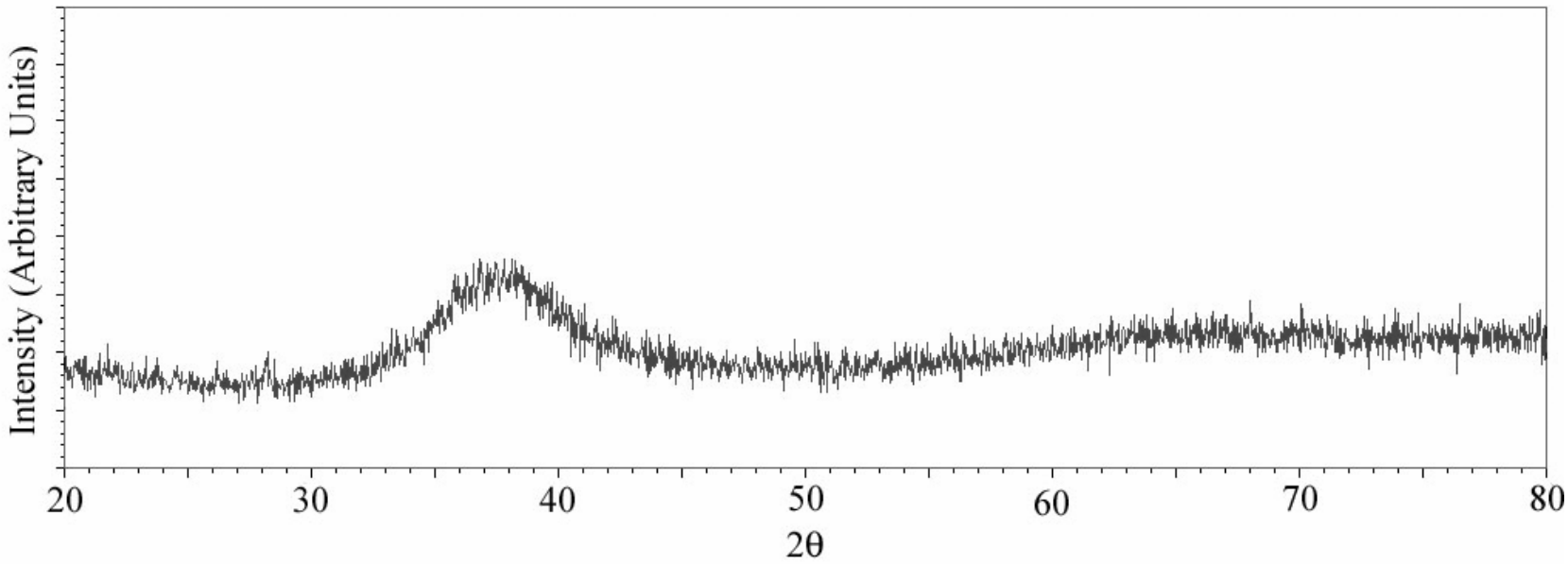

Figure 61. Typical x-ray diffraction spectrum of the Vit 105 BMG tensile specimens demonstrating a broad, diffuse peak characteristic of amorphous alloys.

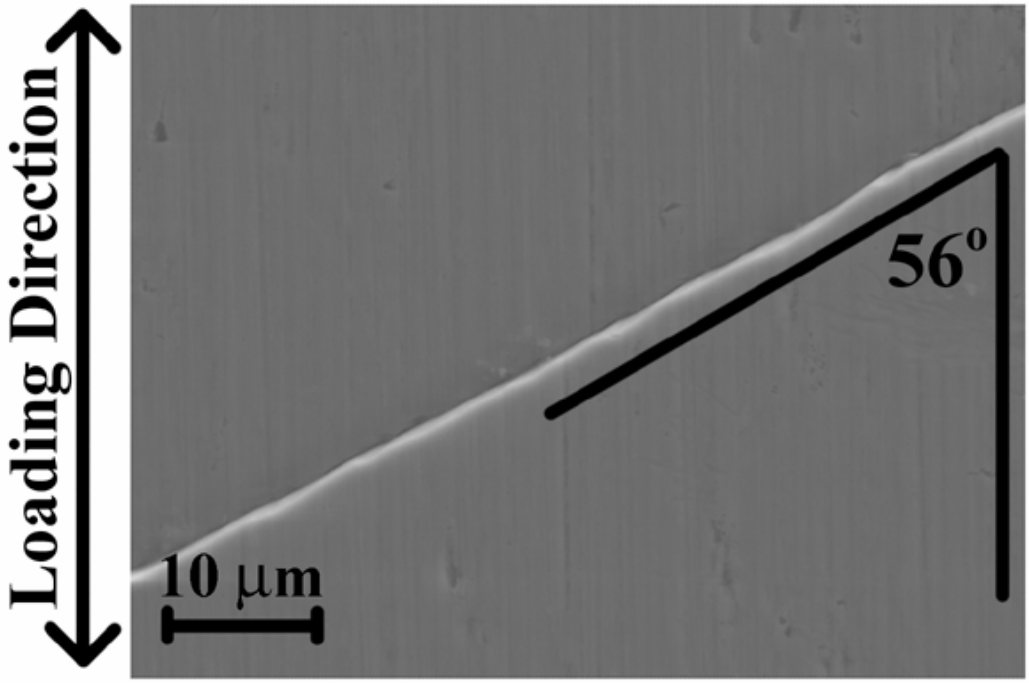

Figure 62. Scanning electron micrograph of a shear band illustrating the average 56° angle between the shear band plane and the loading direction.

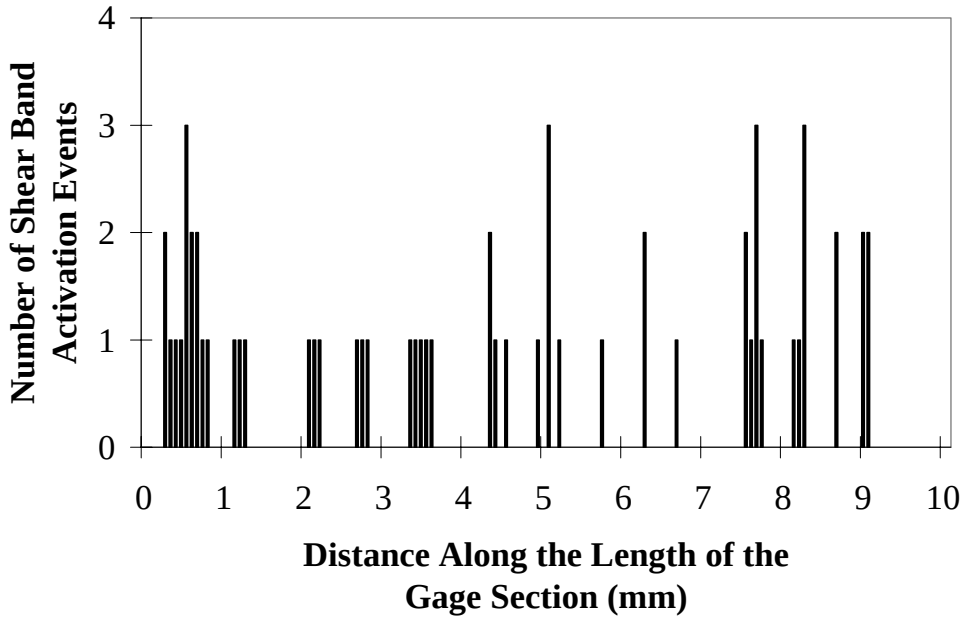

(a)

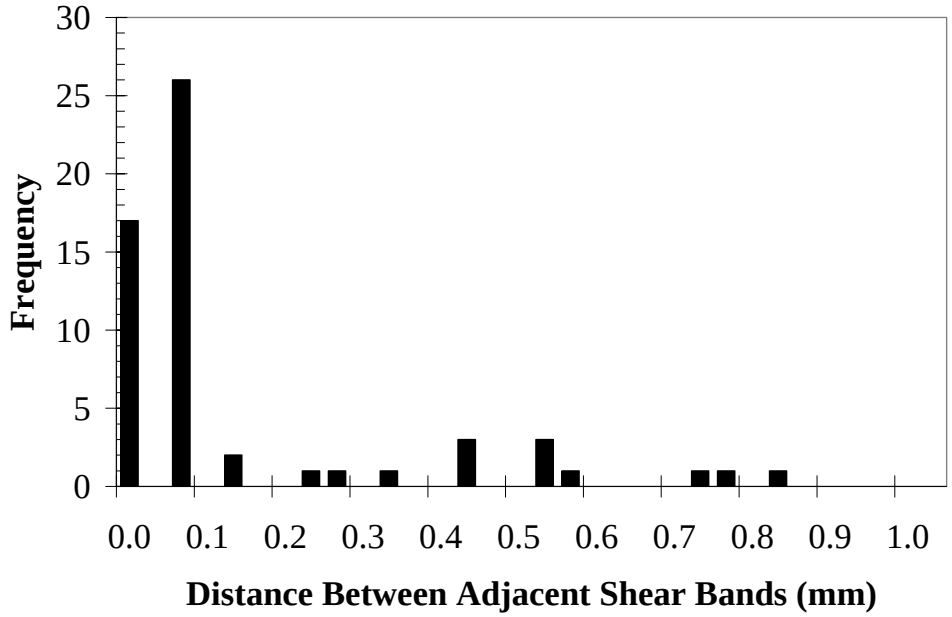

(b)

Figure 63. Analysis of shear-band locations. (a) Distribution of the shear bands as a function of the shear band location along the length of the gage section of the BMG tensile specimen, and (b) Distribution of the distance between adjacent shear bands.

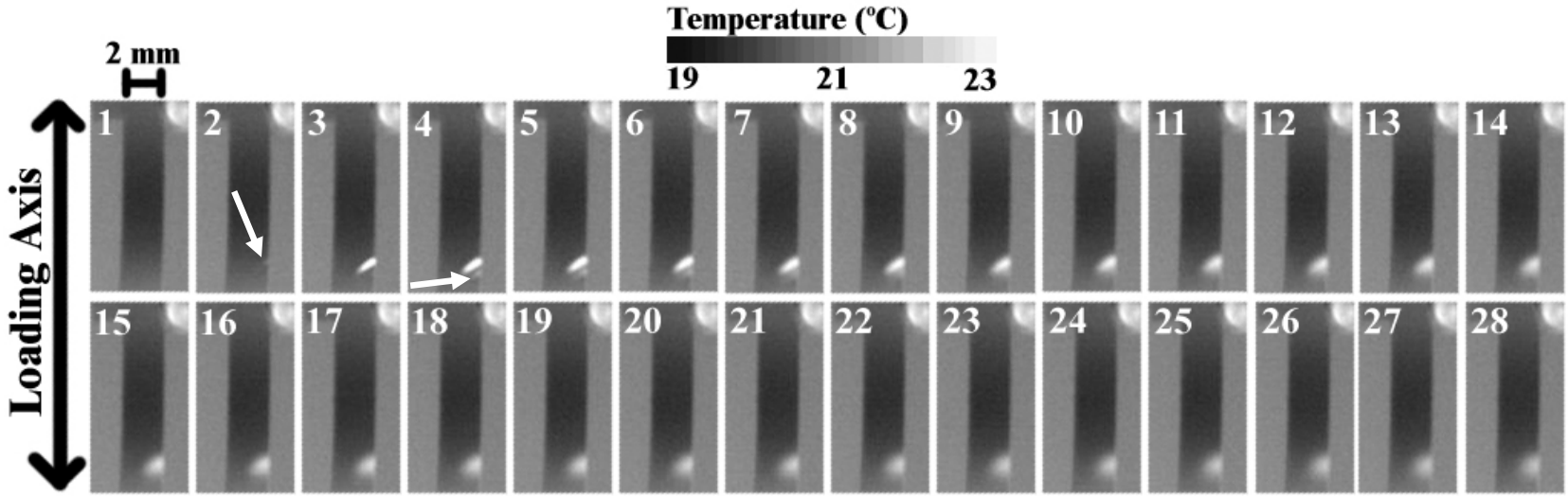

Figure 64. Sequential series of IR images demonstrating the initiation, propagation, and arrest of two shear bands at 1.62 GPa followed by heat dissipation from the region. The elapsed time between each image was 1.4 ms. The first shear band initiates between Frames 1 and 2 (denoted by an arrow), propagates, and arrests before Frame 3. The second shear band initiates, propagates and arrests between Frames 3 and 4, as denoted by an arrow. The remaining images demonstrate the heat conduction away from the shear bands following arrest.

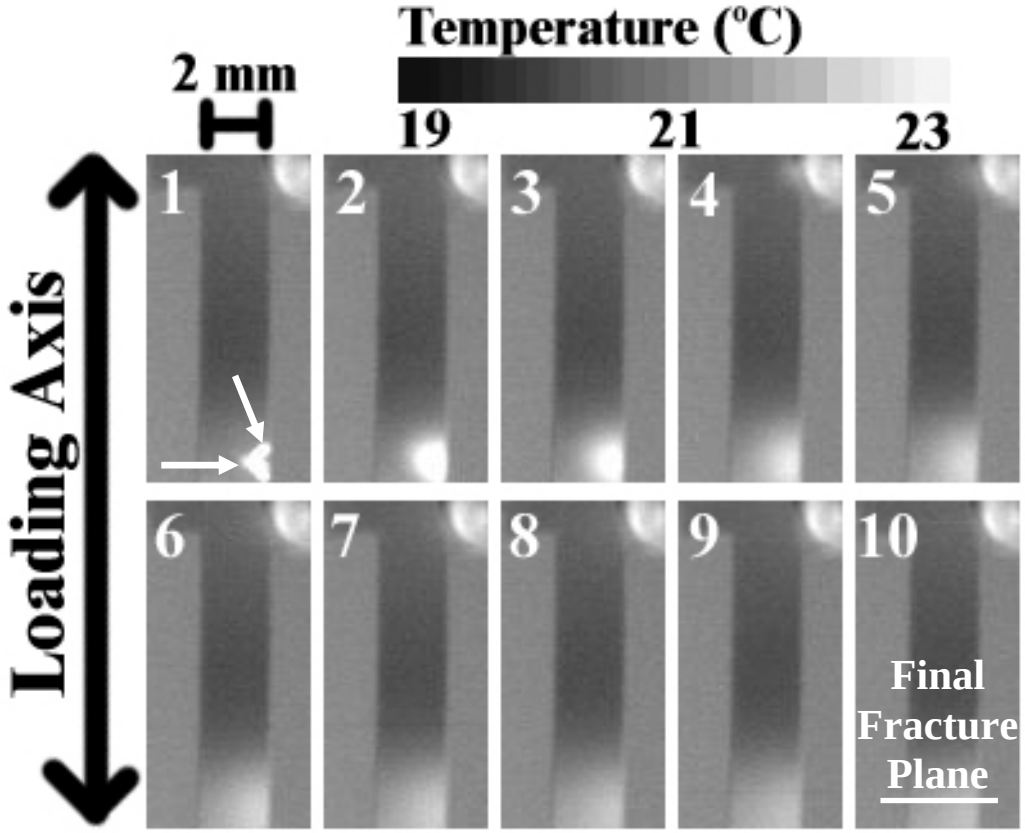

Figure 65. Series of non-sequential IR images from the final 280 ms before failure demonstrating a decreased rate of heat dissipation in the lower portion of the gage section where the fracture eventually occurred. The arrows in Frame 1 denote the location of two shear bands that formed at the same approximate time. The elapsed time between each frame was 28 ms. The stress in these images increased from 1.68 GPa in Frame 1 to 1.69 GPa in Frame 10, the final image obtained prior to failure.

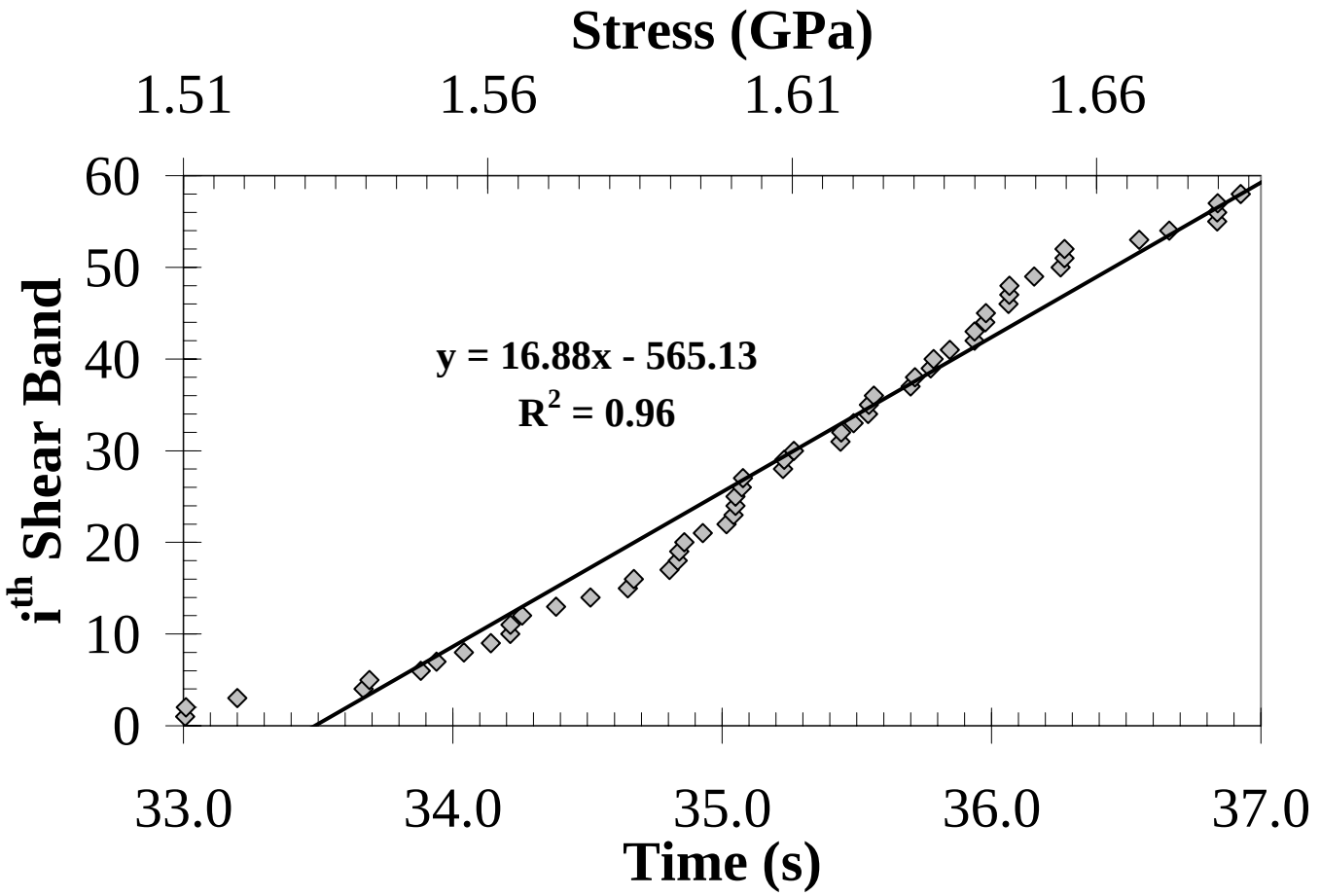

Figure 66. Scatter plot of the elapsed time and stress at the time of the i^{th} shear-band-activation event. Linear regression reveals a shear band initiation rate of approximately 17 shear bands per second after the occurrence of the first shear band.

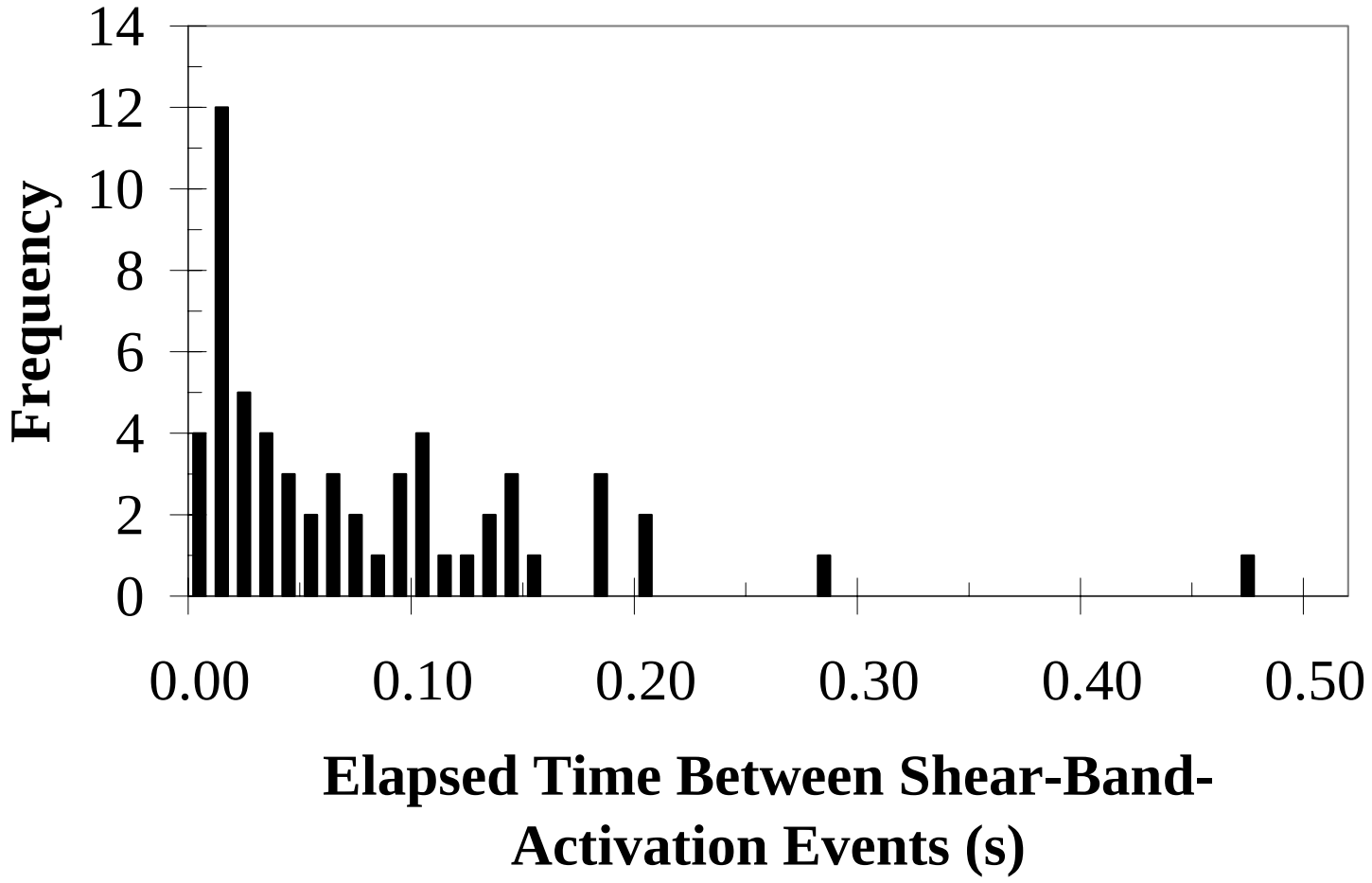

Figure 67. Distribution of the elapsed time between shear-band-activation events.

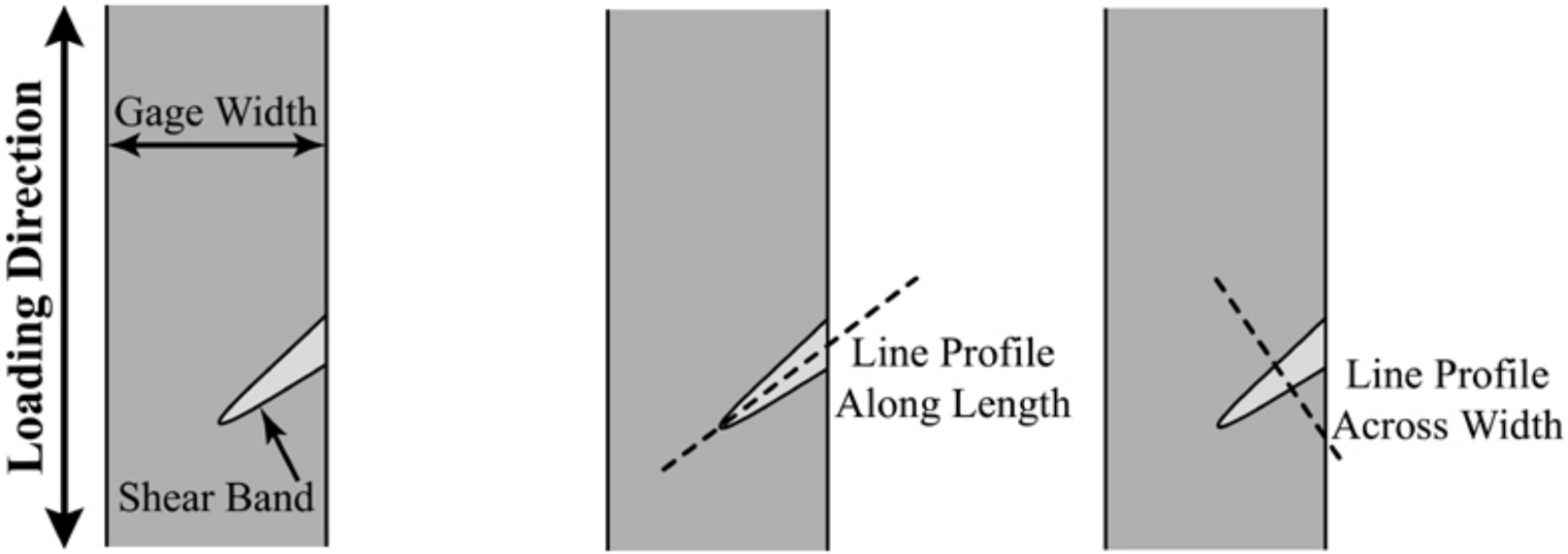

Figure 68. Schematic diagrams of the tensile gage section (a) with a shear band. Plots of temperature as a function of distance were obtained from the IR data by extracting line profiles, denoted by dashed lines, (b) along the lengths of the shear band axes, and (c) perpendicular to the axes of the shear bands. Images are not drawn to scale.

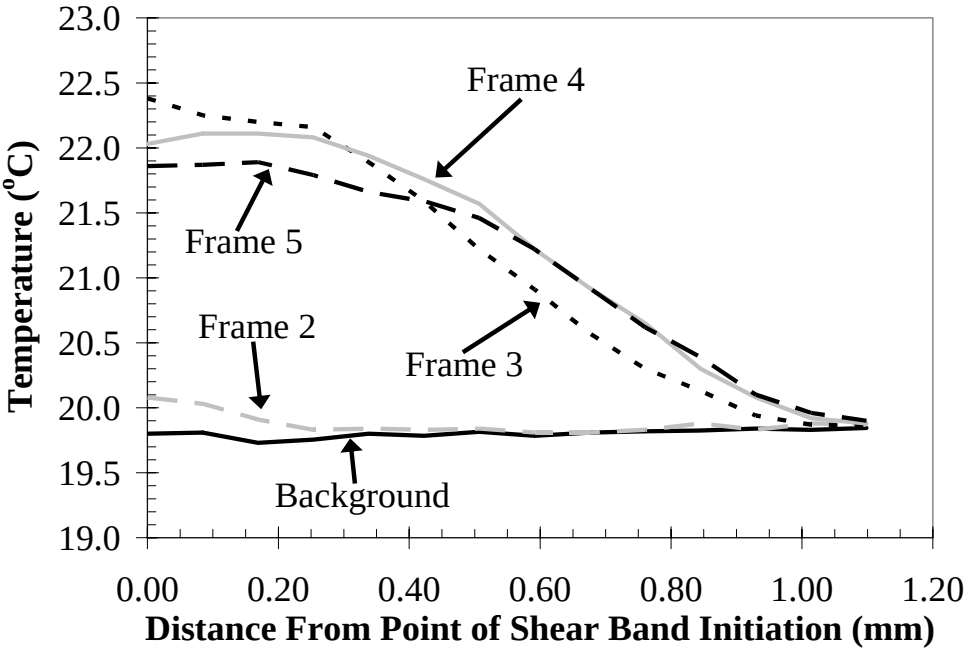

(a)

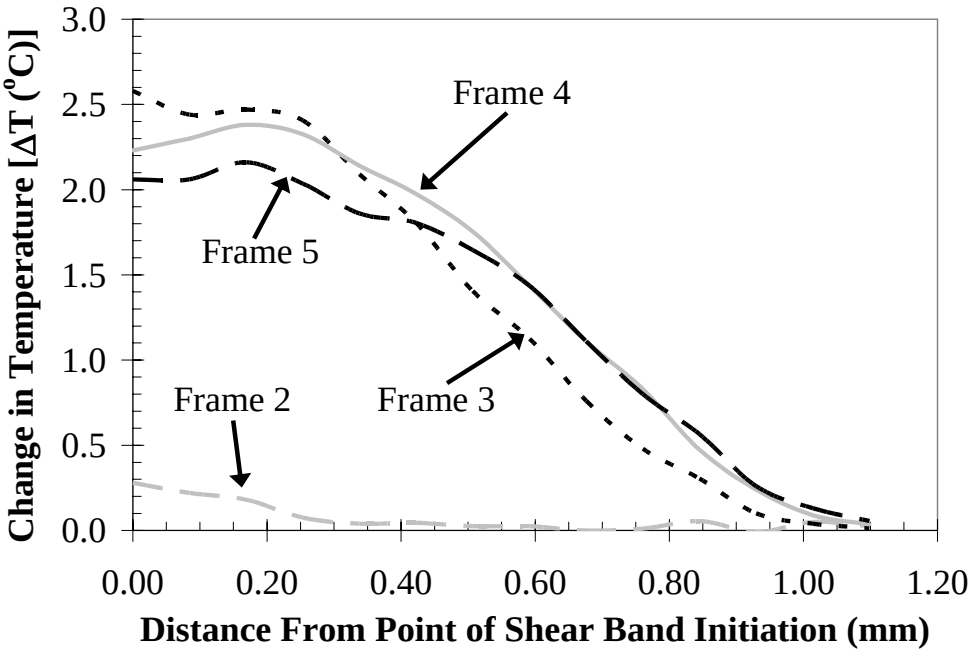

(b)

Figure 69. Shear band evolution along the axis of the primary shear band in Figure 4. (a) Temperature evolution, (b) Change in temperature. The frame numbers correspond to those in Figures 64 and 70. The elapsed time between each frame was 1.4 ms.

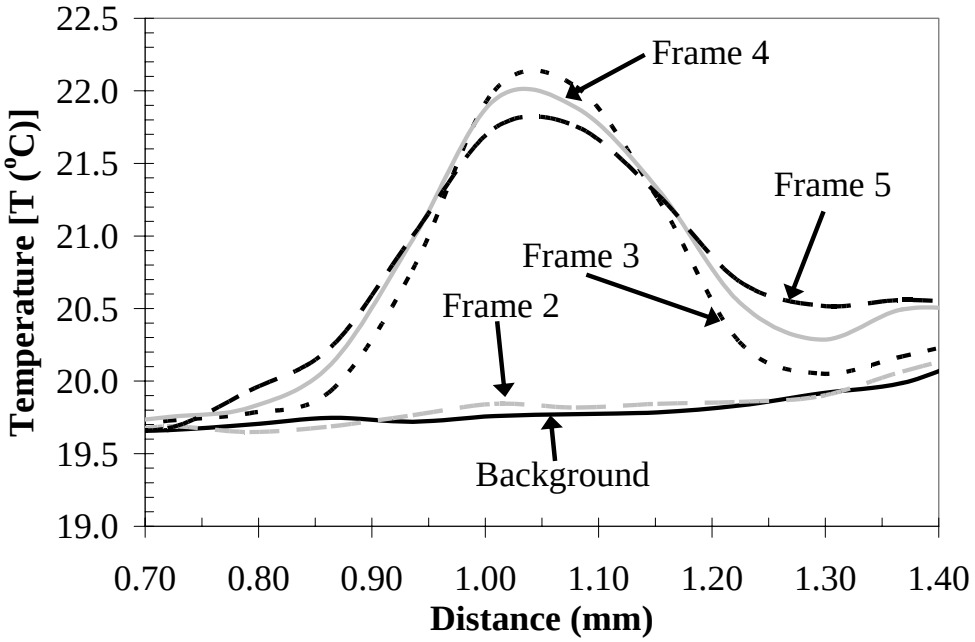

(a)

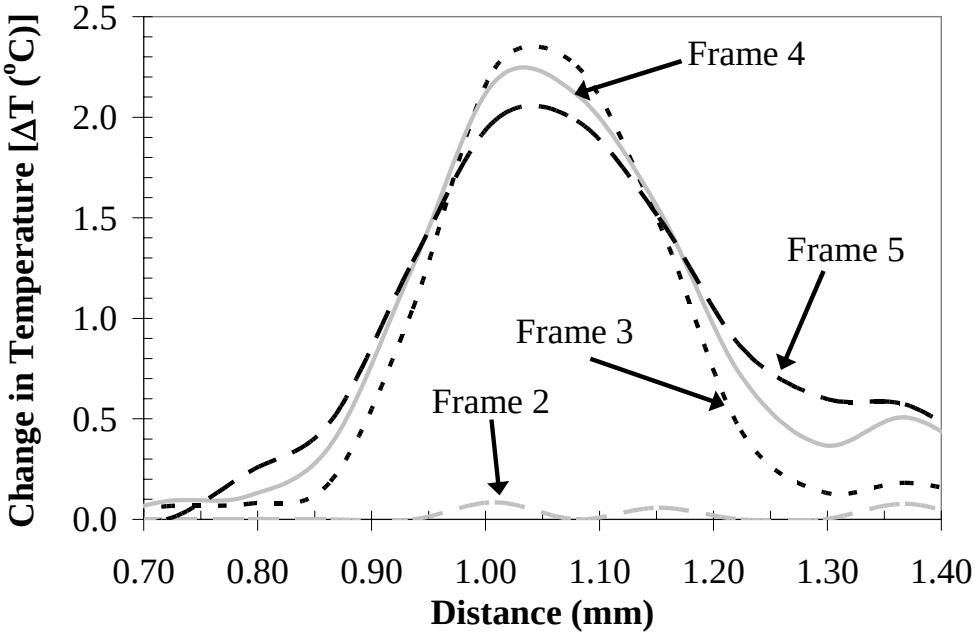

(b)

Figure 70. Shear band evolution perpendicular to the axis of the primary shear band in Figure 4. (a) Temperature evolution, (b) Change in temperature. The frame numbers correspond to those in Figures 64 and 69. The elapsed time between each frame was 1.4 ms.

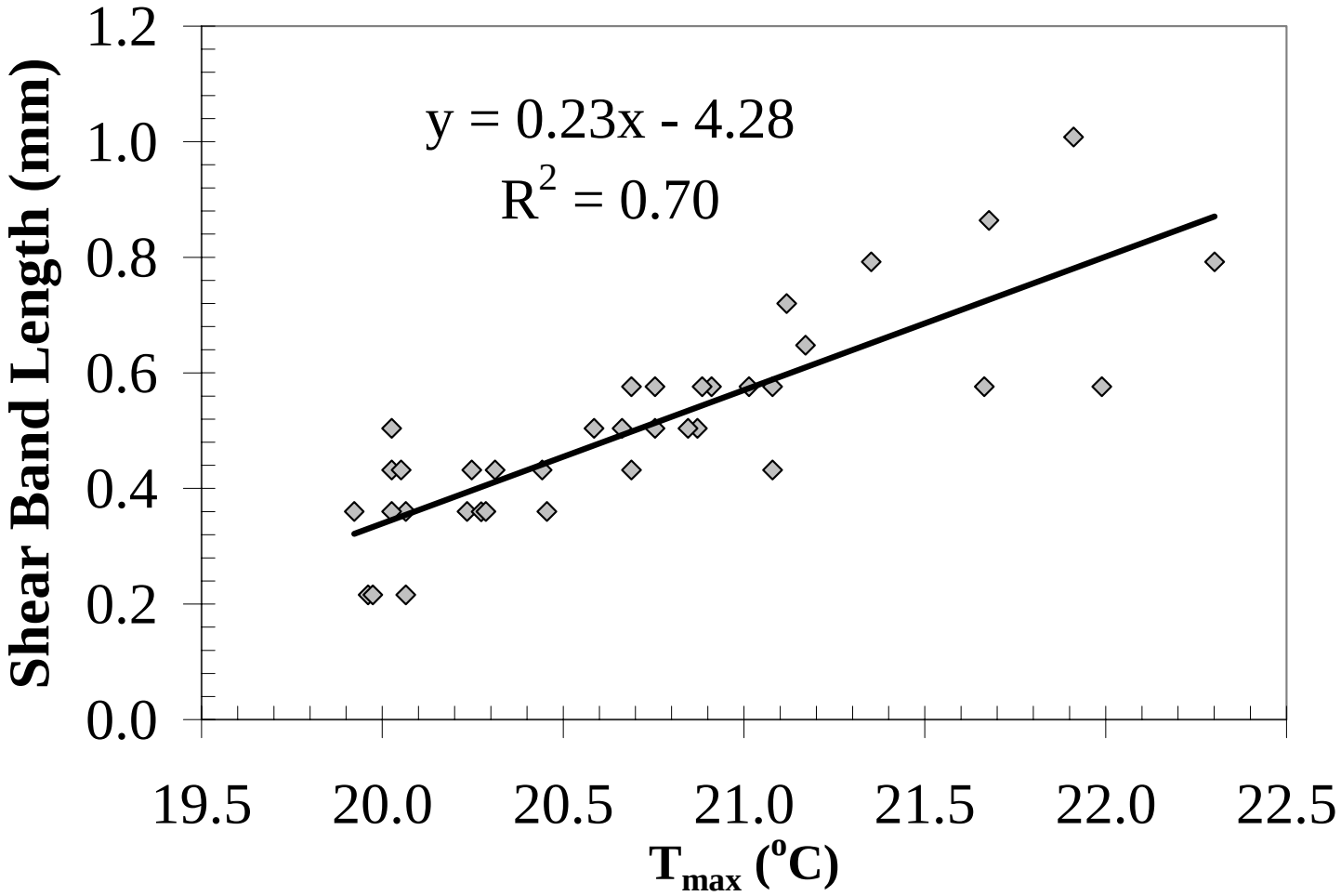

Figure 71. Scatter plot of shear band length as a function of maximum shear-band temperature demonstrating linear correlation.

VITA

Mark Morrison was born and raised in Memphis, TN, and graduated from Briarcrest High School in Memphis in 1994. He graduated with a B.S. degree in Materials Science and Engineering from The University of Tennessee in Knoxville in 1999. After graduation, Mark lived in Cork, Ireland, before returning to Knoxville for graduate school. He graduated with an M.S. degree in Materials Science and Engineering from The University of Tennessee in Knoxville in 2002. He spent the summer of 2002 working at The Institute for Materials Research at Tohoku University in Sendai, Japan. After returning from Japan, Mark completed his doctoral degree in Materials Science and Engineering in 2005 at The University of Tennessee in Knoxville.